Theoretical study of systems with interest in molecular magnetism and electronics.

Instituto de Ciencia Molecular

Universidad de Valencia

...

Memoria presentada por Salvador Cardona Serra para aspirar al grado de Doctor en Nanociencia y Nanotecnología (programa ref. 3045)

. . .

Dirigida por:
Dr. Eugenio Coronado Miralles, Dr. Juan Modesto Clemente Juan
y Dr. Alejandro Gaita Ariño.

D. Eugenio Coronado Miralles, catedrático del Departamento de Química Inorgánica de la Universidad de Valencia, D. Juan Modesto Clemente Juan, doctor por la misma Universidad y profesor titular del Departamento de Química Inorgánica de la Universidad de Valencia y D. Alejandro Gaita Ariño, doctor por la misma Universidad certifican:

Que la memoria presentada por D. Salvador Cardona Serra con título "Theoretical study of systems with interest in molecular magnetism and electronics" corresponde a su Tesis Doctoral y ha sido realizada bajo su dirección en el Instituto de Ciencia Molecular, autorizando mediante este escrito la presentación de la misma para optar al grado de Doctor.

En Paterna, a 16 de Septiembre de 2013.

Dr. Eugenio Coronado Miralles

Dr. Juan Modesto Clemente Juan

Dr. Alejandro Gaita Ariño

Salvador Cardona Serra

Agradecimientos

A mis padres.

A Eugenio Coronado, por darme la oportunidad de realizar esta tesis en su grupo, por confiar en mi desde el principio y tenerme siempre en cuenta, y por hacerme ver tanto mis fallos como mis virtudes.

A Modesto Clemente, por ser un gran director de tesis y compañero de trabajo, por enseñarme a trabajar de forma eficiente, por permitirme meter las manos en sus códigos de cálculo y por enseñarme los "rollitos nem" de Grenoble.

A Alejandro Gaita, por tantísimas conversaciones filosóficas a la hora de comer, por ser tan eficiente en sus correcciones, por ayudarme con todos y cada uno de los problemas que han surgido durante la tesis y por ser la persona más coherente con sus ideas que conozco.

A Efrén Navarro, por todos los años que lleva aguantándome, por ser mi compañero en el instituto, en la universidad y luego en el trabajo, por aguantar mis multiples preguntas sobre temas variados y por enseñarme las virtudes de la *Suite* de Adobe.

A Andrew Palii y Boris Tsukerblat, por darme siempre buenos consejos, por interesarse constantemente por mi tesis y mi trabajo y por unas conversaciones sobre tradiciones e historia muy interesantes.

A Concha, Julia, Elena, Mauri y Mónica, porque empezamos juntos en esto y por todos los momentos que hemos pasado desde entonces.

A José Jaime Baldoví, por ser excelentemente metódico, por su apoyo en los últimos años de la tesis y por ser el principal seguidor del "Cardonismo".

A Gonzalo Abellán, por enseñarme que nunca es demasiado tarde y que no hay más limitación que la que uno mismo se impone y por seguir deleitandome con su música.

A Antonio Pertegás y Alejandro Recuenco, por el tiempo que pasamos tanto en el trabajo como en Azeroth, espero que algún dia volvamos a coincidir por aquellos lares.

A Fernando Luis y Maria José Martínez, por ser unos excelentes investigadores, por enseñarme mucha física, directa o indirectamente, por aguantar mis retrasos sintéticos y por lo bien que me han tratado siempre que he estado en Zaragoza.

A todos los miembros del grupo de Materiales Moleculares del ICMOL por sus consejos en el día a día y su colaboración siempre que la he necesitado.

Table of Contents

	Agradecimientos	III
Chapter 0: Introduction		1
1.	From Molecular Magnetism to Molecular Spintronics.	3
2.	Motivation.	9
3.	Publications during this PhD.	11
Chapter 1: Computational approaches for Molecular Magnetism		15
1.	*State of the Art. Previous Work.*	17
1.1.	Magnetic clusters. MAGPACK.	17
1.2.	Mixed-Valence Clusters. MVPack.	19
2.	*Summary of the most relevant results.*	22
2.1.	Parallel implementation of the MAGPACK package.	22
2.2.	MVPACK, results.	25
3.	*Author's contribution to the publications.*	27
Chapter 2: Single Ion Magnets based on Polyoxometalates		33
1.	*State of the Art. Previous Work.*	35
1.1.	Early studies in Lanthanoid SIMs.	35
1.2.	Theoretical studies about SIMs.	37
2.	*Summary of the most relevant results.*	39
2.1.	Synthesis and Characterization.	39
2.2.	Theoretical approach.	40
2.3.	General conclusions.	42
3.	*Author's contribution to the publications.*	45
Chapter 3: Electrically switchable magnetic molecules		55
1.	*Introduction.*	57
2.	*Results and discussion.*	59
3.	*Conclusions.*	64
Chapter 4: Resumen de la Tesis Doctoral		69
Annex 1: Polyoxometalates		97

0
Introduction

"If one way be better than another, that you may be sure is nature's way."
-Aristotle.

1. From Molecular Magnetism to Molecular Spintronics

Molecular magnetism is a rapidly expanding field of research whose central theme is the design and study of magnetic molecules and materials with tunable properties. The development of this discipline started in the 1980s, with a main interest first in understanding and tuning the exchange interactions in molecules and low dimensional materials, and second in obtaining molecule-based magnetic solids that would order at high temperatures. This property was initially shown by two kinds of materials: The first one based on tetracyanoethylene (TCNE)[1] metal polymers and the second one based on bimetallic cyanides.[2] As a curiosity, the Prussian Blue, $Fe_4[Fe(CN)_6]_3 \cdot 14H_2O$, which was the first coordination compound and the first molecule-based magnetic solid, was discovered almost 300 years ago. It is remarkable that three centuries later, the scientific community is now realizing the potential of such coordination molecular materials.

Current trends in molecular magnetism revolve around two main classes of materials: multifunctional magnetic materials and molecular nanomagnets. Another important objective in the field is the organization of these magnetic molecules on surfaces. This is the first step to the fabrication of dispositives for the application of molecular nanomagnets in spintronics, quantum computing and medicine.

Multifunctional magnetic materials are those that combine magnetism with at least another property in a single molecule-based material. These solids hold promise for the realization of technologically important properties previously thought to be possible only with atom-based inorganic solids (e.g., magnetic ordering combined with conductivity, superconductivity, or ferroelectricity). One class of this type of compounds are *switching magnetic materials*. The magnetic properties of these materials are tuned by the application of external stimuli such as pressure, temperature or light.

1 (a) Miller, J. S.; Epstein, A. J.; Reiff, W. M.; Zhang J. H. *Mol. Cryst. Liq. Cryst.* **1985**, *120*, 27-34. (b) Miller, J. S.; Calabrese, J. C.; Epstein, A. J.; Bigelow, R. W.; Zhang, J. H.; Reiff, W. M. *J. Chem. Soc., Chem. Commun.* **1986**, 1026-1028. (c) Miller, J. S.; Calabrese, J. C.; Rommelmann, H.; Chittipeddi, S. R.; Zhang, J. H.; Reiff, W. M.; Epstein, A. J. *J. Am. Chem. Soc.* **1987**, *109*, 769-781. (d) Chittipeddi, S.; Cromack, K. R.; Miller, J. S.; Epstein, A. J. *Phys. Rev. Lett.* **1987**, *58*, 2695-2698. (e) Yee, G. T.; Miller, J. S. *In Magnetism-Molecules to Materials*; Miller, J. S., Drillon, M., Eds.; Wiley-VCH: Weinheim, Germany, 2004; Vol. 5, p 223. (f) Gama, V.; Duarte, M. T. *In Magnetism-Molecules to Materials*; Miller, J. S., Drillon, M., Eds.; Wiley-VCH: Weinheim, Germany, 2004; Vol. 5.

2 (a) Babel, D. *Comments Inorg. Chem.* **1986**, *5*, 285-320. (b) Dunbar, K. R.; Heintz, R. A. *Prog. Inorg. Chem.* **1997**, *45*, 283-391. (c) Verdaguer, M.; Bleuzen, A.; Marvaud, A. V.; Vaissermann, J.; Seuleiman, M.; Desplanches, C.; Scuiller, A.; Train, C.; Garde, R.; Gelly, G.; Lomenech, C.; Rosenman, I.; Veillet, P.; Cartier, C.; Villain, F. *Coord. Chem. Rev.* **1999**, *192*, 1023-1047. (d) Verdaguer, M.; Girolami, G. S. *Magn.: Mol. Mater. V* **2005**, 283-346. (e) Rebilly, J. N.; Mallah, T. *Struct. Bonding (Berlin)* **2006**, *122*, 103-131. (f) Shatruk, M.; Avendaño, C.; Dunbar, K. R. *Prog. Inorg. Chem.* **2009**, *56*, 155-334.

Archetypes of switching magnetic materials are molecular *spin-crossover compounds*[3] and tridimensional magnets based on Prussian Blue analogues.[4]

Chirality is also other important property that can be combined with magnetic systems to form *optomagnetic materials*. The interplay of chirality and ferromagnetism can result in the observation of novel physical properties such as magnetochiral dichroism.[5] Thus, many groups did a large effort in the synthesis and study of chiral magnets.

One final example of important multifunctional materials are those termed *dual-function materials.* These materials are formed by two structurally independent molecular networks which exhibit two different properties. A remarkable example of such a system is one in which molecular magnetism is combined with conductivity.[6] These materials are usually composed of a cationic conducting network (typically based on tetrathiafulvalene (TTF)-type organic molecules) and anionic metal complexes that serve as the magnetic components. Notable achievements in this area are the discovery of paramagnetic molecular metals and superconductors in the 1990s and the discovery of ferromagnetic molecular metals in 2000.[7] Importantly, the interplay between conductivity and magnetism has given rise to novel properties, for example, the observation of field-induced superconductivity.[8] One of the last frontiers that has been overcomed was the obtention of materials with the coexistence of either superconductivity and ferromagnetism or superconductivity with molecular nanomagnetism.[9]

Another class of materials, that has been revealed as of paramount importance in the field are the so called *molecular nanomagnets*.[10] these systems, usually called Single-molecule magnets (SMMs) are a class of molecules which show superparamagnetic behavior at the molecular scale. Indeed, in a certain temperature range the molecular solids based on these SMMs exhibit magnetic hysteresis of purely molecular origin, with

3 (a) Gaspar, A. B.; Ksenofontov, V.; Seredyuk, M.; Gütlich, P. *Coord Chem. Rev.* **2005**, *249*, 2661-2676. (b) Real, J. A.; Gaspar, A. B.; Niel, V.; Muñoz, M. C. *Coord. Chem. Rev.* **2003**, *236*, 121-141.

4 (a) Sato, O.; Iyoda, T.; Fujishima, A.; Hashimoto, K. *Science* **1996**, *272*, 704-705. (b) Coronado, E; Gimenez-Lopez, M. C.; Korzeniak, T.; Levchenko, G.; Romero, F. M.; Segura, A.; García-Baonza, V.; Cezar, J. C.; de Groot, F. M.; Milner, A.; Paz- Pasternak, M. *J. Am. Chem. Soc.* **2008**, *130*, 15519-15532.

5 (a) Rikken, G. L. J. A.; Raupach, E. *Nature (London)* **1997**, *390*, 493-494. (b) Rikken, G. L. J. A.; Raupach, E. *Phys. Rev. E* **1998**, *58*, 5081-5084. (c) Imai, H.; Inoue, K.; Kikuchi, K.; Yoshida, Y.; Ito, M.; Sunahara, T.; Onaka, S. *Angew. Chem., Int. Ed.* **2004**, *43*, 5618-5621. (d) Coronado, E.; Gómez-García, C. J.; Nuez, A.; Romero, F. M.; Waerenborgh, J. C. *Chem. Mater.* **2006**, *18*, 2670-2681. (e) Train, C.; Gheorghe, R.; Krstic, V.; Chamoreau, L. M.; Ovanesyan, N. S.; Rikken, G. L. J. A.; Grusselle, M.; Verdaguer, M. *Nat. Mater.* **2008**, *7*, 729-734.

6 Coronado, E.; Day, P. *Chem. Rev.* **2004**, *104*, 5419-5448.

7 Coronado, E.; Galán-Mascarós, J. R.; Gómez-García, C. J.; Lauhkin, V. L. *Nature (London)* **2000**, *408*, 447-449.

8 Uji, S.; Shinagawa, H.; Terashima, T.; Yakabe, Y.; Terai, Y.; Tokumoto, M.; Kobayashi, A.; Tanaka, H.; Kobayashi, H. *Nature (London)* **2001**, *410*, 908-910.

9 (a) Coronado, E.; Martí-Gastaldo, C; Navarro-Moratalla, E.; Ribera, A.; Blundell, S. J.; Baker, P. J. *Nat. Chem.* **2010**, *2*, 1031–1036. (b) Coronado, E.; Martí-Gastaldo, C.; Navarro-Moratalla, E.; Burzurí, E.; Camón, A.; Luis, F. *Adv. Mater.* **2011**, *23*, 5021–5026.

10 Gatteschi, D.; Sessoli, R.; Villain, J. *Molecular Nanomagnets*; Oxford University Press: Oxford, U.K., 2006.

prominent quantum effects.[11] Contrary to conventional bulk magnets and molecule-based magnets, collective long-range magnetic ordering of magnetic moments is not necessary to achieve memory effects.

Many examples of SMMs based on transition metal clusters are known. Nevertheless, the most quoted example is still the first one that was characterized as such: $[Mn_{12}O_{12}(O_2CMe)_{16}(H_2O)_4]$ (Mn12ac)[12] a molecule that combines a high axial anisotropy and a high spin ground state.[13] This molecule has been subjected to a high

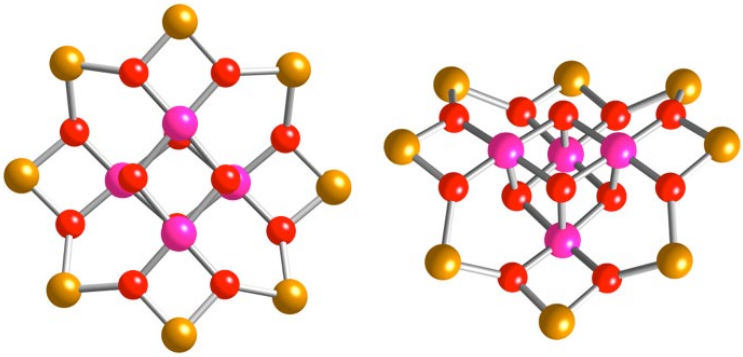

Figure 1. Stuctural representation of the Mn12ac. Some ligand atoms have been removed for clarity. Yellow: Mn^{3+}, Pink: $Mn^{4+,}$ Red: Oxygen.

number of magnetic and structural studies.[14] The cluster has eight ferromagnetically coupled Mn^{3+} ions (external ring, see Figure 1) and four Mn^{4+} ions in the central cube which are also ferromagnetically coupled. The coupling between these two moieties is antiferromagnetic, resulting in an S=10 total spin.

Owing to the uniaxial anisotropy of Mn12ac, characterized by a negative D value of D=-0.46 cm^{-1}, the ground spin multiplet splits into its Ms components in such a way that the Ms doublet = ±10 is stabilized and becomes the ground spin state of the cluster, while the rest of spin sublevels are at progressively higher energies as |Ms| decreases (see Figure 2). These level splitting explains the experimentally observed thermal barrier *U* to overcome the reversal of the magnetic moment (*U*= 43 cm^{-1}).

11 (a) Sessoli, R.; Gatteschi, D.; Caneschi, A.; Novak, M. A. *Nature (London)* **1993**, *365*, 141-143. (b) Castro, S. L.; Sun, Z. M.; Grant, C. M.; Bollinger, J. C.; Hendrickson, D. N.; Christou, G. *J. Am. Chem. Soc.* **1998**, *120*, 2365–2375. (c) Barra, A. L.; Caneschi, A.; Cornia, A.; de Biani, F. F.; Gatteschi, D.; Sangregorio, C.; Sessoli, R.; Sorace, L. *J. Am. Chem. Soc.* **1999**, *121*, 5302–5310. (d) Yoo, J.; Brechin, E. K.; Yamaguchi, A.; Nakano, M.; Huffman, J. C.; Maniero, A. L.; Brunel, L. C.; Awaga, K.; Ishimoto, H.; Christou, G.; Hendrickson, D. N. *Inorg. Chem.* **2000**, *39*, 3615–3623. (e) Berlinguette, C. P.; Vaughn, D.; Canada-Vilalta, C.; Galan-Mascaros, J. R.; Dunbar, K. R. *Angew. Chem., Int. Ed.* **2003**, *42*, 1523–1526.

12 Sessoli, R.; Tsai, H. L.; Schake, A. R.; Wang, S.; Vincent, J. B.; Folting, K.; Gatteschi, D.; Christou, G.; Hendrickson, D. N.; *J. Am. Chem. Soc.* **1993**, *115*, 1804-1816.

13 Gatteschi, D.; Sessoli, R. *Angew. Chem., Int. Ed.* **2003**, *42*, 268–297.

14 (a) Friedman, J.; Sarachik, M.; Tejada, J.; Ziolo, R. *Phys. Rev. Lett.* **1996**, *76*, 3830–3833. (b)Thomas, L.; Lionti, F.; Ballou, R.; Gatteschi, D.; Sessoli, R.; Barbara, B.; *Nature*, **1996**, *383*, 145-147. (c) Wernsdorfer, W.; Ohm, T.; Sangregorio, C.; Sessoli, R.; Mailly, D.; Paulsen, C.; *Phys. Rev. Lett.,* **1999**, *82*, 3903-3906.

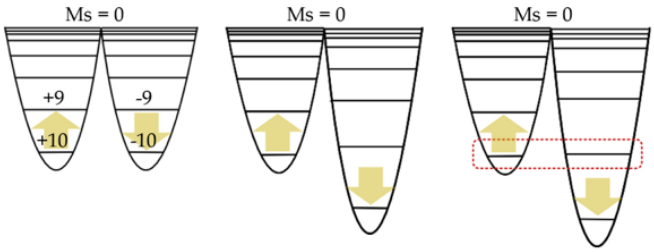

Figure 2. Well representation of the total spin states in Mn12ac. Centre and Right represent the effect of a magnetic external field (Zeeman effect)..

The studies about this manganese cluster set a roadmap based on two requirements for having molecules with low temperature magnetization blocking. The first was having a high spin ground state (S). The approach to achieve this was to couple as many magnetic ions as possible in the same cluster. The second requirement was a significant negative zero-field splitting (D) that stabilizes the highest M_S sublevel producing a total energy barrier ($U=DS^2$) for the reversal of the magnetization.

Shortly after the magnetic characterization of Mn12ac, SMM properties were found on an octanuclear iron complex ($[Fe_8O_2(OH)_{12}(tacn)_6]^{8+}$ with tacn representing 1,4,7-triazacyclononane).[15] This system has arguably been studied even in greater depth than Mn12ac, specially by the physics community to better understand the quantum tunneling effects in these systems.[16] Later, a rising number of lower nuclearity systems were reported to behave as SMMs, as for example, the tetranuclear complex $[Mn_4(O_2CMe)_2(pdmH)_6](ClO_4)_2$.[17] In this context, many examples of magnetic clusters with larger and larger nuclearities were reported in an attempt to increase the spin state of the cluster and hence, the superparamagnetic barrier.[18] However, the success of this approach has been very limited as demonstrated by the fact that Mn12 is still among one of the transition-metal systems exhibiting the highest effective barrier (ca. 45-50 cm-1). In fact, the abovementioned roadmap has been questioned as there are indications that a large magnetic anisotropy is not favoured by a high spin of the ground state.[19]

15 (a) Delfs, C.; Gatteschi, D.; Pardi, L.; Sessoli, R.; Wieghardt, K.; Hanke, D. *Inorg. Chem* **1993**, *32*, 3099–3103. (b) Barra, A. L.; Debrunner, P.; Gatteschi, D.; Schulz, C. E.; Sessoli, R.; *Europhys. Lett.*; **1996**, *35*, 133-138.

16 (a) Wernsdorfer, W.; Caneschi, A.; Sessoli, R.; Gatteschi, D.; Cornia, A.; Villar, V.; Paulsen, C.; *Phys. Rev. Lett.* **2000**, *84*, 2965-2968. (b) Wernsdorfer, W.; Caneschi, A.; Sessoli, R.; Gatteschi, D.; Cornia, A.; *Europhys. Lett.* **2000**, *50*, 552-558. (c) Takahashi, S.; Tupitsyn, I. S.; Van Tol, J.; Beedle, C. C.; Hendrickson, D. N.; Stamp, P. C. E. *Nature* **2011**, *476*, 76–79.

17 Yoo, J.; Brechin, E. K.; Yamaguchi, A.; Nakano, M.; Huffman, J. C.; Maniero, A. L.; Brunel, L. C.; Awaga, K.; Ishimoto, H.; Christou, G.; Hendrickson, D. N.; *Inorg. Chem.* **2000**, *39*, 3615-3623.

18 (a)Aubin, S. M. J.; Wemple, M.W.; Adams, D.M. ; Tsai, H.-L.; Christou, G.; Hendrickson, D.N. *J. Am. Chem. Soc.* **1996**, *118*, 7746-7754. King, P.; Wernsdorfer, W.; Abboud, K.A.; Christou, G. *Inorg. Chem.* **2004**, *43*, 7315-7323. Tasiopoulos, A.; Vinslava, A.; Wernsdorfer, W.; Abboud, K.A.; Christou, G. *Angew. Chem., Int. Ed.* **2004**, *43*, 2117-2121. Murugesu, M.; Takahashi, S.; Wilson, A.; Abboud, K.A.; Wernsdorfer, W.; Hill, S.; Christou, G. *Inorg. Chem.* **2008**, *47*, 9459-9470.

19 Ruiz, E.; Cirera, J.; Cano, J.; Alvarez, S.; Loose, C.; Kortus, J. *Chem. Comm.* **2008**, 52–54.

Fortunately, an entirely different paradigm for molecular nanomagnets was unearthed with the discovery of single-ion lanthanide SMM complexes.[20] This innovation represented a crucial step in the miniaturization of nanomagnets, namely the fact that a single anisotropic magnetic ion in an axial crystal-field environment is a sufficient condition for the establishment of a thermal barrier which slows down the reversing of the magnetization and allow observing quantum tunnelling effects.

Applications of the molecular nanomagnets under consideration include magnetic cooling due to the large magnetic entropy variations related to the high-spin value of the SMMs.[21] In biomedicine, magnetic nanoparticles, mostly in the form of metal oxides, have been shown to be useful as contrast agents in magnetic resonance imaging and in the hyperthermic treatment of tumors, to mention only two major achievements.[22] In this vein, magnetic nanoparticles based on molecules, particularly cyanide compounds, are gaining considerable ground. The prospect of being able to fine-tune the properties is a major driving force behind this line of research.

The increasing ability to design and obtain magnetic molecules and to control their properties by an external stimulus such as an electric field is a promising ingredient for *molecular spintronics*. Molecular Spintronics is a research area aimed at exploring the interaction between the spin of a magnetic molecule with an external electric current. One of the main objectives of this field is that of achieving a molecular spin-device.

Molecular electronics emerged a few decades ago as a new approach for complementing and even supplanting conventional inorganic electronics when technology reaches the nanoscale. In this context, a natural evolution of molecular electronics is the use of magnetic molecules as well as molecule-based magnetic materials as components for new spintronic devices.[23] There exist two major objectives in this new area, one is the design of molecular bulk spintronic structures while the other is that of single-molecule spintronics. For the former aspect, molecular magnetic conductors may prove to be useful, and, in fact, several materials have already been shown to exhibit interesting spintronic properties, for example, giant negative magnetoresistance.[24] There are two challenging goals in this area, namely, to raise the operating temperatures at which these phenomena occur and to prepare the materials as organized thin films and multilayers.

20 (a) Ishikawa, N.; Sugita, M.; Ishikawa, T.; Koshihara, S.; Kaizu, Y. *J. Am. Chem. Soc.* **2003**, *125*, 8694-8695. (b) Ishikawa, N.; Sugita, M.; Wernsdorfer, W. *J. Am. Chem. Soc.* **2005**, *127*, 3650-3651. (c) AlDamen, M. A.; Clemente-Juan, J. M.; Coronado, E.; Martí-Gastaldo, C.; Gaita- Ariño, A. *J. Am. Chem. Soc.* **2008**, *130*, 8874-8875. (d) AlDamen, M.; Cardona-Serra, S.; Clemente Juan, J. M.; Coronado, E.; Gaita-Ariño, A.; Martí-Gastaldo, C.; Luis, F.; Montero, O. *Inorg. Chem* **2009**, *48*, 3467–3479.

21 (a) Manoli, M.; Johnstone, R. D. L.; Parsons, S.; Murrie, M.; Affronte, M.; Evangelisti, M.; Brechin, E. K. *Angew. Chem., Int. Ed.* **2007**, *46*, 4456-4460. (b) Evangelisti, M.; Luis, F.; de Jongh, L. J.; Affronte, M. *J. Mater. Chem* **2006**, *16*, 2534-2549, and references cited therein.

22 Cheon, J.; Lee, J. H. *Acc. Chem. Res.* **2008**, *41*, 1630-1640.

23 Camarero, J.; Coronado, E. *J. Mater. Chem* **2009**, *19*, 1678–1684.

24 Matsushita, M. M.; Kawakami, H.; Sugawara, T.; Ogata, M. *Phys. Rev. B* **2008**, *77*, 195208.

For the second aspect, single molecule spintronics, most of the work developed until now remains theoretical with a few experimental examples of charge transport through SMMs and other magnetic molecules.[25] These measurements are at the very early stage, and many problems, which are intrinsic to the molecules (such as their chemical stabilities when they are deposited on a metallic surface) need to be solved to obtain reliable results. A second concern is that of controlling, as much as possible, the positioning of the magnetic molecules on surfaces.[26] Efforts are underway that employ both the "bottom-up" and "top-down" approaches as well as combinations of the two in order to control the position and the orientation of the molecule with nanoscale accuracy for applications such as information storage or quantum computing.[27]

The evolution of molecular magnetism from simple molecular species to complex architectures with remarkable new properties in nanomagnetism and to more intricate multifunctional materials with applications in molecular spintronics, medicine, and other related areas reflects the extraordinarily multidisciplinary nature of the field. Indeed, the collaborations between chemists and physicists that were absolutely essential for the development of magnetochemistry in general have expanded to include research in surface and materials science and engineering, medicine, biochemistry, and biophysics.

25 Bogani, L.; Wernsdorfer, W. *Nat. Mater.* **2008**, *7*, 179-186.

26 (a) Cavallini, M.; Gómez-Segura, J.; Ruiz-Molina, D.; Massi, M.; Albonetti, C.; Rovira, C.; Veciana, J.; Biscarini, F. *Angew. Chem., Int. Ed.* **2005**, *44*, 888-892. (b) Mannini, M.; Bonacchi, D.; Zobbi, L.; Piras, F. M.; Speets, E. A.; Caneschi, A.; Cornia, A.; Magnani, A.; Ravoo, B. J.; Reinhoudt, D. N.; Sessoli, R.; Gatteschi, D. *Nano Lett.* **2005**, *5*, 1435-1438. (c) Martínez, V.; García, F.; García, R.; Coronado, E.; Forment- Aliaga, A.; Romero, F. M.; Tatay, S. *Adv. Mater.* **2007**, *19*, 291-295.

27 (a) Lehmann, J.; Gaita-Ariño, A.; Coronado, E.; Loss, D. *Nat. Nanotechnol.* **2007**, *2*, 312-317. (b) Affronte, M.; Casson, I.; Evangelisti, M.; Candini, A.; Carretta, S.; Muryn, C. A.; Teat, S. J.; Timco, G. A.; Wernsdorfer, W.; Winpenny, R. E. P. *Angew. Chem., Int. Ed.* **2005**, *44*, 6496-6500. (c) Affronte, M.; Troiani, F.; Ghirri, A.; Carretta, S.; Santini, P.; Corradini, V.; Schuecker, R.; Muryn, C.; Timco, G.; Winpenny, R. E. P. *Dalton Trans.* **2006**, 2810-2817.

2. Motivation

The project described in this thesis is motivated by a particular interest in Molecular Magnetism from a theoretical point of view. Molecular Magnetism, is still a thriving research field where some problems remain unexplored:

- A large amount of molecular systems are still theoretically unmanageable due to their huge computational requirements, while the standard software package cannot profit from the power of multiprocessor supercomputers.
- The scientific community would require a computational code to calculate the magnetic properties of mixed-valence clusters.
- A new magnetic POM, which needs only one magnetic ion to behave as SMMs, has appeared. A rationalization of its behaviour and an extense study of other candidates is imperative.
- Considering molecular spintronics, the effect of an external electric field over magnetic molecules should be studied.

This thesis is divided in three main chapters. On each one, the author will describe the *state-of-the-art* before the start of this PhD, the most relevant results obtained and a detailed explanation about his specific contributions.

The first chapter, "**Computational approaches for Molecular Magnetism**", introduces the author's contribution to two tools developed for the theoretical understanding of magnetic clusters: The "*Parallel implementation of the MAGPACK package for the analysis of high-nuclearity spin clusters*" and "*MVPACK: A Package to Calculate Energy Levels and Magnetic Properties of High Nuclearity Mixed Valence Clusters*". For the first work the author coordinated a collaboration with the DSIC centre in the Polytechnic University of Valencia. The second code was being written when the author started his PhD, and his contribution was focused in programming the effect of the electric field over mixed-valence systems.

The second chapter "**Lanthanide Polyoxometalates as Single Ion Magnets**" deals with this family of SIMs, which was the second one after Ishikawa's molecules and the one that effectively opened the field to the current variety of ligand types and structures. The author presents in this chapter three relevant contributions. The first publication is "*Mononuclear Lanthanide Single Molecule Magnets Based on the Polyoxometalates* $[Ln(W_5O_{18})_2]^{9-}$ *and* $[Ln(\beta_2\text{-}SiW_{11}O_{39})_2]^{13-}$ *(*Ln^{III} *= Tb, Dy, Ho, Er, Tm and Yb)*" where the initial two series of compounds are synthesized, characterized and theoretically studied. The next is "*Lanthanoid Single-Ion Magnets Based on Polyoxometalates with a 5-fold Symmetry: The Series* $[LnP_5W_{30}O_{110}]^{12-}$ *(*Ln^{III} *= Tb, Dy, Ho, Er, Tm and Yb)*" where a lanthanoid complex with a exotic fivefold coordination was completely studied. This is relevant because originally it was thought that only square antiprismatic structures with 4-fold symmetry D_{4d} could be SIMs, and in fact it constituted the motivation for the last paper in this chapter "*Rational Design of Single-Ion Magnets and Spin Qubits Based on Mononuclear Lanthanoid Complexes*". There, a theoretical approach based on a point

charge model is developed, and suggestions are given for the rational design of both SIMs and spin qubits.

The third chapter, "**Electric field effects over mixed-valence molecules**" presents the application of MVPack to explore the possibilities of an electric control of the magnetic ground state of these molecules. Here, the full contribution "*Electrically switchable magnetic molecules: Inducing a magnetic coupling by means of an external electric field in a polyoxovanadate cluster*" is introduced.

3. Publications derived from this thesis.

1)Mononuclear lanthanide single molecule magnets based on the polyoxometalates $[Ln(W_5O_{18})_2]^{9-}$ and $[Ln(\beta_2\text{-}SiW_{11}O_{39})_2]^{13-}$ (Ln^{III}) Tb, Dy, Ho, Er, Tm, and Yb). AlDamen, M.; Cardona-Serra, S.; Clemente Juan, J. M.; Coronado, E.; Gaita-Ariño, A.; Martí-Gastaldo, C.; Luis, F.; Montero, O. *Inorg. Chem* **2009**, *48*, 3467–3479.

2)MVPACK: A package to calculate energy levels and magnetic properties of high nuclearity mixed valence clusters. Borrás-Almenar, J. J.; Cardona-Serra, S.; Clemente Juan, J. M.; Coronado, E.; Palii, A. V.; Tsukerblat, B. S. *J. Comput. Chem.* **2010**, *31*, 1321–1332.

3)Spin-lattice relaxation via quantum tunneling in an Er^{3+}-polyoxometalate molecular magnet. Luis, F.; Martínez-Pérez, M.; Montero, O.; Coronado, E.; Cardona-Serra, S.; Martí-Gastaldo, C.; Clemente Juan, J. M.; Sesé, J.; Drung, D.; Schurig, T. *Phys Rev B* **2010**, *82*, 060403.

4)Parallel implementation of the MAGPACK package for the analysis of high-nuclearity spin clusters. Ramos, E.; Roman, J. E.; Cardona-Serra, S.; Clemente Juan, J. M. *Comput. Phys.Comm.* **2010**, *181*, 1929–1940.

5)Assisted-assembly of coordination materials into advanced nanoarchitectures by Dip Pen nanolithography. Bellido, E.; Cardona-Serra, S.; Coronado, E.; Ruiz-Molina, D. *Chem. Comm.* **2011**, 47. 5175–5177.

6)Lanthanoid Single-Ion Magnets Based on Polyoxometalates with a Fivefold Symmetry: The series $[LnW_{30}O_{110}]^{12-}$ (Ln^{3+}= Tb, Dy, Ho, Er, Tm and Yb). Cardona-Serra, S.; Clemente Juan, J. M.; Coronado, E.; Gaita-Ariño, A.; Camón, A.; Evangelisti, M.; Luis, F.; Martínez-Pérez, M.-J.; Sesé, J. *J. Am. Chem. Soc.* **2012**, *134*, 14982–14990.

7) Multi-frequency EPR studies of a mononuclear holmium single-molecule magnet based on the polyoxometalate $[Ho^{III}(W_5O_{18})_2]^{9-}$. Ghosh, S.; Datta, S.; Friend, L.; Cardona-Serra, S.; Gaita-Ariño, A.; Coronado, E.; Hill, S. *Dalton Trans.* **2012**, *41*, 13697–13704.

8)Fragmenting Gadolinium: Mononuclear Polyoxometalate- Based Magnetic Coolers for Ultra-Low Temperatures. Martínez-Pérez, M.-J.; Montero, O.; Evangelisti, M.; Luis, F.; Sesé, J.; Cardona-Serra, S.; Coronado, E. *Adv. Mater.* **2012**, *24*, 4301–4305.

9)Gd-based single-ion magnets with tunable magnetic anisotropy: Molecular design of spin qubits. Martínez-Pérez, M.-J.; Cardona-Serra, S.; Schlegel, C.; Moro, F.; Alonso, P. J.; Prima-Garcia, H.; Clemente Juan, J. M.; Evangelisti, M.; Gaita-Ariño, A.; Sesé, J.; Van Slageren, J.; Coronado, E.; Luis, F. *Phys. Rev. Lett.* **2012**, *108*, 247213.

10)Rational Design of Single-Ion Magnets and Spin Qubits Based on Mononuclear Lanthanoid Complexes. Baldoví, J. J.; Cardona-Serra, S.; Clemente Juan, J. M.; Coronado, E.; Gaita-Ariño, A.; Palii, A. *Inorg. Chem* **2012**, *51*, 12565–12574.

11)The Use of Polyoxometalates in the Design of Layer-Like Hybrid Salts Containing Cationic Mn4 Single-Molecule Magnets. Cardona-Serra, S.; Clemente Juan, J. M.; Coronado, E.; Martí-Gastaldo, C.; Navarro-Moratalla, E. *Eur. J. Inorg. Chem.* **2013**, *2013*, 1903–1909.

12) Coherent manipulation of spin qubits based on polyoxometalates: the case of the single ion magnet $[GdW_{30}P_5O_{110}]^{12-}$. Baldoví, J. J.; Cardona-Serra, S.; Clemente Juan, J. M.; Coronado, E.; Gaita-Ariño, A.; Prima-García, H. *Accepted at Chem. Comm.*

13)Modelling electric field control of the spin state in the mixed-valence polyoxometalate $[GeV_{14}O_{40}]^{8-}$. Cardona-Serra, S.; Clemente Juan, J. M.; Gaita-Ariño, A.; Suaud, N.; Svobodab, O.; Coronado, E.; *Accepted at Chem. Comm.*

1

Computational approaches for Molecular Magnetism

"Look deep into nature, and then you will understand everything better."
-Albert Einstein.

1. State of the Art. Previous Work.

1.1. Magnetic clusters. MAGPACK.

Magnetic molecular clusters are polynuclear metal complexes which from the point of view of molecular magnetism can be described as a finite number of exchange coupled magnetic moments. They have received much attention in several areas of research such as coordination chemistry, magnetism, and biochemistry.[1] The exploration of this area between a mononuclear complex and the bulk state required the development of new theoretical concepts and techniques for investigation of their peculiar properties.[2]

For a long time, the study of this problem was restricted to treat comparatively simple clusters comprising a reduced number of exchange-coupled centers and special spin topologies, for which solutions can be analytically obtained. However, most interesting systems are of high nuclearity; often, they are also anisotropic and exhibit low symmetries. As the spin nuclearity of the cluster increases and, with the additional complication of considering the anisotropy of the cluster, the problem rapidly becomes unsolvable by analitical methods. Moreover, it is time-consuming to derive and obtain the solution numerically for each new problem. In that framework the development of the generalized spin Hamiltonian to treat those systems was worked out in Valencia some years ago.[3] This Hamiltonian takes into account direct Heisenberg-Dirac-Van Vleck (HDVV), biquadratic and anisotropic exchange as well as axial and rhombic single ion anisotropic terms.

$$\hat{H} = -2\sum_{if} J_{if}\hat{S}_i\hat{S}_f - \sum_{if} j_{if}(\hat{S}_i\hat{S}_f)^2 - 2\sum_{if}\sum_{\alpha} J_{if}^{\alpha}\hat{S}_i^{\alpha}\hat{S}_f^{\alpha} +$$
$$+\sum_i D_i\hat{S}_z^2(i) + \sum_i E_i(\hat{S}_x^2(i) - \hat{S}_y^2(i))$$

This research resulted in the development of the original MAGPACK package which implements this generalized spin Hamiltonian methodology to treat arbitrary topologies and nuclearities (up to a limit, see below) in a way that is transparent to the user.[4] This powerful and efficient computational code can be used to solve the exchange problem in high nuclearity spin clusters with all kinds of exchange interactions (isotropic, anisotropic, bicuadratic or antisymmetric), including the single-ion anisotropic effects. This package includes two main versions, one optimized for isotropic systems and another for anisotropic ions. Both codes work within an approach based on the use of the irreducible tensor operators (ITO) technique.[5] These codes have been freely

1 Blondin, G.; Girerd, J. J. *Chem. Rev.* **1989**, *90*, 1359.

2 Clemente, J. M.; Palii, A. V.; Tsukerblat, B. S.; Georges, R. *Molecular Magnetism: From Molecular Assemblies to the Devices;* NATO ASI E321; Kluwer Academic Publishers: Dordrecht, 1996.

3 Borrás-Almenar, J. J.; Clemente-Juan, J. M.; Coronado, E.; Tsukerblat, B. S. *Inorg Chem* **1999**, *38*, 6081-6088.

4 Borrás-Almenar, J. J.; Clemente Juan, J. M.; Coronado, E.; Tsukerblat, B. *J. Comput. Chem.* **2001**, *22*, 985–991.

5 (a) Tsukerblat, B. S.; Belinskii, M. I. *Magnetochemistry and Spectroscopy of Exchange Clusters*; Shtiintsa: Kishinev, 1983. (b) Tsukerblat, B. S.; Belinskii, M. I.; Fainzilberg, V. E. *Magnetochemistry and Spectroscopy of Transition Metal Exchange Cluster*; Horwood Academic Pub.: Amsterdam, 1987, vol. 9. (c) Varsalovich, D. A.; Moskalev, A. N.; Khersonskii, V. K. *Quantum Theory of Angular Momentum*; World Scientific: Singapor, 1988. (d) Silver, B. L.

distributed since their publication in 2001 and have been extensively used by the molecular magnetism community. As of July 2013, the original publication had been cited 482 times in topics such as single molecule magnets, interactions between 3d-4f ions and anisotropic 1D-chains.

While very efficient and productive, the original MAGPACK code has an important bottleneck, which is the diagonalization of the energy matrix. This obstacle has two aspects. The first is the RAM memory occupation which is a physical limit to the cluster size, the second is the diagonalization time, which can be a problem if the calculation has a time restriction. The diagonalization bottleneck sets a limit beyond which the system is not manageable by MAGPACK. For a standard computer specifications (1 microprocessor + 2Gb RAM), the code is able to calculate systems with traces of about 30000 elements. That means about 14 $S=^1/_2$ for anisotropic calculations [6] or 19 $S=^1/_2$ in the isotropic case.

To increase the system size, one can propose to increase the RAM memory, but that has proved not to be a real solution as, in this case, the limiting factor is the speed of the microprocessor. In this aspect, a supercomputer may not prove to be superior to a desktop workstation. Note that the diagonalization process is computed using the *DSPEV/ZHPEV* subroutines from the LAPACK package in a sequential way, that is: only one microprocessor takes the whole job. This means that the full power of a supercomputer with hundreds of cores is not accesible to the program.

This is to say, the original code lacked of an important computational feature which is crucial for increasing the maximum manageable size of a problem, namely Parallel Computation. Parallel Computation distributes the weight of a computational problem between two or more nodes. This is accomplished by breaking the problem into independent parts so that each processing element can execute its part of the algorithm simultaneously with the others. This lowers both calculation time and memory requirements.

For an efficient mathematical diagonalization that can profit from the computational power of multi-core (super)computers, a subroutine which can parallel process this problem should be used. These libraries do exist and indeed most of the commercial packages that are available in the market do use parallel processing subroutines. Coincidentally, the Department of Computer Systems and Computation of the Polytechnics University of Valencia (DSIC-UPV) hosts some of the cutting-edge researchers in parallel computation from Spain. In fact, they have programmed a code called SLEPc (Scalable Library for Eigenvalue Problem Computations) that is specifically designed for parallel diagonalization of large matrices.[7] This subroutine has been succesfully implemented in various scientific codes which needed to improve their calculation rates.[8] This code is based in the widely used PETSc (Portable, Extensible

Irreducible Tensor Methods; An Introduction for Chemists; Academic Press: London, 1988.

6 Ideal spin doublets are isotropic but anisotropy can appear e.g. due to dipolar interaction, or if a more complex system is effectively truncated to $S=^1/_2$

7 Hernández, V.; Román, J. E.; Vidal, V.; *Trans. Math. Software* **2005**, *31*, 351-362.

8 (a) Medvedev, D. M.; Gray, S. K.; Wagner, A. F.; Minkoff, M.; Shepard, R. *Journal of Physics: Conference Series*

Toolkit for Scientific Computation) a parallel framework for mathematical operations. SLEPc uses projection eigensolvers to obtain a discrete number of eigenvalues from the partial diagonalization of sparse matrices. This means that the total energy matrix is not diagonalized and that the user can only obtain the highest or lowest eigenvalues.

1.2. Mixed-Valence Clusters.

One particular case of spin clusters are those called mixed-valence (MV) magnetic clusters.[9] These complexes contain ions of the same transition metal in different oxidation states. There exists a large variety of mixed valence systems including clusters of biological relevance,[10] and rare earth manganates exhibiting giant magnetorresistance.[11]

Under some conditions, the extra electrons in these clusters can be delocalized over the metal structure. This delocalization was historically studied in a MV dimer called Creutz-Taube complex $[(NH_3)_5Ru^{II}(pyrazine)Ru^{III}(NH_3)_5]$.[12] In this case, one electron is delocalized over two diamagnetic metal sites. The simplicity of such a system allowed also to take into account, at the molecular level, the coupling of electronic and nuclear movements (vibronic interactions). The vibronic theory of MV dimers was formulated by Piepho, Krausz and Schatz and is referred to as PKS model.[13] Vibronic interactions are inherent for MV systems due to the strong deformation of the coordination sphere induced by the presence of an extra electron.[14] Usually it is too complex to treat explicitly, so it is taken into account effectively.

In magnetic systems, electronic delocalization strongly affects the magnetic coupling for example it gives rise to the so-called double-exchange, which couples the localized moments of each ion through extra electrons that can move between them. In Fig. 1 we show this mechanism in the case of a mixed valence d^2-d^3 dimer.

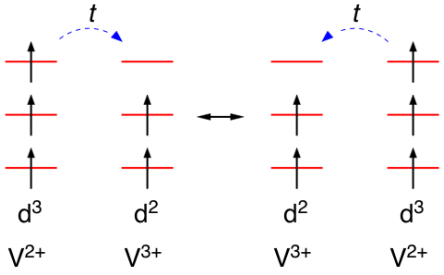

Figure 1. Model representation depicting the effect of double exchange in a d^2-d^3 MV system.

2005, *16*, 247–251. (b) Huang, T.-M.; Chang, W.-J.; Huang, Y.-L.; Lin, W.-W.; Wang, W.-C.; Wang, W. *J. Comput. Phys.* **2010**, *229*, 8684–8703.

9 (a) Demadis, K. D.; Hartshorn, C. M.; Meyer, T. J. *Chem. Rev.* **2001**, *101*, 2655–2685. (b) Launay, J.-P. *Chem. Soc. Rev.* **2001**, *30*, 386–397.

10 (a) Christou, G. *Acc. Chem. Res.* **1989**, 22, 328-335.(b)Blondin, G.; Girerd, J.J.; *Chem. Rev.* **1990**, *90*, 1359-1376.

11 Rao, C.N.R.; *Chem. Eur. J.* **1996,** *2,* 1499-1504.

12 (a) Creutz, C.; Taube, H. *J. Am. Chem. Soc.* **1969**, *91*, 3988. (b) Creutz, C.; Taube, H. *J. Am. Chem. Soc.* **1973**, *95*, 1086.

13 Piepho, S.; Krausz, E.; Schatz, P. *J. Am. Chem. Soc.* **1978**, *100*, 2996–3005.

14 Prassides, K. *Mixed Valency Systems: Applications in Chemistry, Physics and Biology.* NATO ASI Series C. Vol. 343 Kluwer Acad. Publ.

As the delocalized electron is known to mantain the orientation of the spin while being transfered, one would naively expect that double exchange usually results in a strong stabilization of the ferromagnetic state, but this is not necessarily true for arbitrary nuclearities or topologies. The first calculations of the energy pattern formed by the consideration of both double-exchange and Heisenberg exchange showed that even in the simplest cases (dimers, trimers or tetramers), the electron delocalization has different effects. As a consequence, it is important to note that the conclusions obtained for the relatively simple clusters cannot be extended to MV systems of higher nuclearity which involve localized and delocalized spins in complicated magnetic structures. In this context it was necessary to develop a new theory which took into account all the magnetic interactions (as for spin clusters) but also including the electron transfer.

With this aim, a theoretical approach to calculate the effect of electron delocalization in high-nuclearity MV clusters was published in 1996.[15] This theory was also based in the ITO technique mentioned in the previous section. There, the authors were able to derive closed form analytical expressions for the matrix elements of the full Hamiltonian which include four terms namely, orbital energy, transfer interaction, exchange interaction and Coulomb repulsion.

$$H = \sum_i \varepsilon_i \cdot n_i + \sum_{\langle i,j \rangle} t_{ij} \sum_\sigma (c_{i_\sigma}^\dagger c_{j_\sigma} + c_{j_\sigma}^\dagger c_{i_\sigma}) - \sum_{\langle i,j \rangle} 2 J_{ij} \vec{S}_i \cdot \vec{S}_j + \sum_{\langle i,j \rangle} V_{ij} \cdot n_i n_j$$

where, S_i is the local spin operator on site *i*, $c_{i\sigma}{}^\dagger$ (respectively $c_{i\sigma}$) are the usual creation (respectively annihilation) operators of an electron of spin projection σ on site *i*, n_i is the number operator on site *i*, ε_i is the energy of orbital *i*, t_{ij} is the electron transfer integral of a magnetic electron between sites *i* and *j*, J_{ij} is the exchange integral between sites *i* and *j*, and V_{ij} is the (intersite) electrostatic repulsion between two magnetic electrons on sites *i* and *j*.

In 2009, the possibility of including independent delocalization domains was reconsidered in the approach.[16] This modification resulted into two improvements that allowed the treatment of new systems: Firstly, making domains prevents the electrons to delocalize between them reducing the number of distributions and allowing the calculation of bigger systems, e. g. permitted the calculation of extended mixed valence systems such as dimeric phthalocianine chains where the electron delocalization is restricted to each dimer. The second improvement is that having domains permits to assign different spin cores for the centres on each domain. The feature allows us to calculate heteronuclear mixed-valence systems which where unaffordable before.

This approach was implemented as an efficient computational procedure that allowed us to calculate the bulk thermodynamic properties (magnetic susceptibility, magnetization, and specific heat) of high-nuclearity MV clusters but it was not completely adapted for its public distribution as was done for MAGPACK.

15 Borrás-Almenar, J. J.; Clemente, J. M.; Coronado, E.; Palii, A. V.; Tsukerblat, B. S.; Georges, R. *J. Chem. Phys.* **1996**, *105*, 6892–6909.

16 Clemente-Juan, J. M.; Borrás-Almenar, J. J.; Coronado, E.; Palii, A. V.; Tsukerblat, B. S.; *Inorg. Chem.* **2009**, *48*, 4557-4568.

The code has been widely used even before it was definitively published. In fact, this theory allowed the calculation of high-nuclearity MV clusters with many delocalized electrons, which were unapproachable before, i.e. the two electron reduced polyoxometalates $[XW_{12}O_{40}]^{n-}$ (Keggin)[17] and $[W_{10}O_{32}]^{6-}$.[18] (Figure 2)

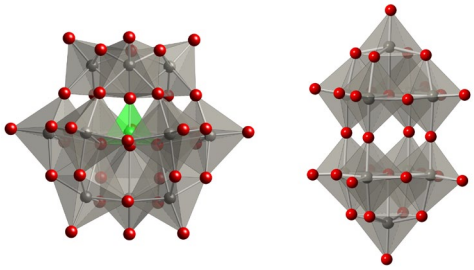

Figure 2. Molecular structure of the POM $[XW_{12}O_{40}]^{n-}$ (left) and $[W_{10}O_{32}]^{6-}$ (right)

In the first case, the Keggin anion is reduced by two electrons. The diamagnetism of this Keggin heteropolyblue was originally attributed to a multiroute superexchange mechanism. Later on it was demonstrated that the large spin-triplet gap could originate from the interplay between Coulombic repulsion and electron transfer, provided the transfer routes have a certain relation in sign and magnitude. Indeed, while the electrons are far away from each other at all times in the ground state, the possible electron transfer routes are different for singlets and triplets, and the result is a strong stabilization of the singlet.

The same behaviour was found for the second compound, the decawolframate structure. This POM is a dirreduced compound in which one can expect both electrons to be localized as far as possible from each other to minimize the Coulomb repulsion. This assumption can be questioned as the system behaves as a diamagnet. The calculation showed that the extra electrons are delocalized over the eight equatorial wolfram sites interacting antiferromagnetically. This delocalization is preferred in front of having the electrons slightly far from each other.

Compared with polywolframates, and due their lower LUMO's polyoxovanadates represent a remarkable class of high-nuclearity MV clusters providing good examples to study the chemical control of electron population. These compounds are therefore ideal systems for studying the influence of the number of delocalized electrons in the magnetic properties.

The $[V_{18}O_{48}]^{n-}$ cluster forms a family of compounds from 18 electrons, fully localized member for n=12, to mixed-valence member with 10 delocalized electrons for n=4.[19] This series of polyoxovanadates presents an unexpected magnetic behaviour: as the

17 Suaud, N.; Gaita-Ariño, A.; Clemente Juan, J. M.; Sánchez-Marín, J.; Coronado, E. *J. Am. Chem. Soc.* **2002**, *124*, 15134–15140.

18 Clemente Juan, J. M.; Coronado, E.; Gaita-Ariño, A.; Suaud, N. *J. Phys. Chem.* **2007**, *111*, 9969–9977.

19 Müller, A.; Sessoli, R.; Krickemeyer, E.; Bögge, H.; Meyer, J.; Gatteschi, D.; Pardi, L.; Westphal, J.; Hovemeier, K.; Rohlfing, R.; Döring, J.; Hellweg, F.; Beugholt, C.; Schmidtmann, M. *Inorg. Chem.* **1997**, *36*, 5239-5250.

electronic population is decreased, meaning a growing distance between unpaired electrons, an increasing antiferromagnetic coupling is measured. At first sight this was the opposite of what was expected. To understand it a complete study of the influence of the exchange and transfer parameters on the low-lying spin levels was performed. In this case, the previously explained combination of ab initio calculations with model t-J Hamiltonian was used to analyse the properties of this family. Unfortunately, the complete model for 10 electrons delocalized over the 18 vanadium atoms was very complex and time expensive to calculate. Then, the authors decided to use a simplified 10 centres 6 electrons model, which successfully explained the trend showed by the real complete system.

The main conclusion extracted was that the electron-transfer integral, calculated from *ab initio* calculations, plays the key role in the macroscopic AF properties of these MV polyoxovanadates. This was completely in agreement with previous studies. Additionally, both the structural effect of removing electrons from the initial spin-localized cluster on the amplitude of the magnetic coupling and on the number of counterions, and the effect of alleviating the spin frustration, only play a minor role.[20]

2. Summary of the most relevant results.

2.1. Parallel implementation of the MAGPACK package. (PAPER 1: *Parallel implementation of the MAGPACK package for the analysis of high-nuclearity spin clusters*).

General Considerations

The sequential package MAGPACK was partially rewritten and his workflow was parallelized to be optimally used on shared-memory computers with a message-passing paradigm (with the standard MPI). This was done by enriching the original FORTRAN77 code with some C++ preprocessing directives for including all the declarations required by the SLEPc library.

Henceforth, the parallelization strategy and the conclusions obtained are summarized:

Matrix generation, preallocation and storage

The first task of the parallelization strategy was to increase the size of the calculated system. Focusing on this, a main improvement would be to store the matrix elements in the most efficient way. The original package stores the energy matrix in a dense structure, that is, it keeps in memory the value of each matrix position, including the vast majority of zero values. This has been proved to be very inneficient both in memory consumption and in calculation time.

Thus, the sparse storage *sbaij,* which mainly consists in storing only the non-zero values, recording their positions in an optimized symmetric format, was selected to

20 Calzado, C.J.; Clemente-Juan, J. M.; Coronado, E.; Gaita-Ariño, A.; Suaud, N. *Inorg. Chem.* **2008**, *47*, 5889-5901.

replace the original dense scheme. Other schemes, as the *aijfull* (compute all elements without matrix symmetry considerations) or *aijhalf* (compute each element once, but storing them in two symmetrical positions) were considered but they proved to be less efficient than the former.

As the size of the problem increases, the generation of the energy matrix becomes very time consuming. Fortunately, such a process can be also parallelized by distributing blocks of rows between the available processing units. In this case, the total matrix size was initially calculated and each processor is assigned to calculate the percentage of non-zero elements that its local memory should store. This process is called Preallocation and accounts for the efficiency of the parallel distribution of work load. The preallocation is preferable as PETSc uses a dynamic memory scheme for flexible storage of matrices. Usually, for a correct preallocation it is enough to estimate roughly the number of non-zero elements. In this case, each value is explicitly calculated, thus, preallocation represents a considerable overhead but it pays off with respect to underestimating the real nonzero pattern.

Parallel distribution of the matrix solver

The SLEPc library provides a collection of parallel eigensolvers, most of which are based in mathematical projection methods. Thus, the Lanczos method as well as its more general variant for nonsymmetric problems called the Krylov-Schur method are implemented on it. Those approaches have been previosly optimized by the parallelization of three main operations:

- Matrix-vector product, which is specially optimized for a low number of nonzero elements. As in this case, this value is too large, it is not possible to expect perfect scalability.
- Vector operations which require global communications, such as inner product, orthogonalization, and norm. These operations should be avoided if possible as global communications play against efficiency.
- Other vector operations.

In addition to the solver details, there is a difference between the isotropic and the anisotropic case.

In the isotropic case, the total energy matrix can be divided into smaller submatrices, each one with a common total spin *S*. As there is no parameter which admixes Ms functions, each matrix can be separately diagonalized and its eigenvalues obtained independently. Note that in this case, not all the blocks are being calculated at the same time, but sequentially. Thus, a future improvement can be to redistribute the smaller matrices over a few processors while the others start the diagonalization of the larger ones. In the anisotropic case, the calculation is much more complicated as the Hamiltonian includes mixing terms and only one but huge diagonalization is needed.

As a result of this difference, it is always possible to calculate larger isotropic systems that those which include anisotropy.

Summary of Computational Improvements.

In general, the parallelization performance was sucessful, the new code allows to calculate much larger systems than before with a drastic reduction in the calculation time. In particular, with a parallel computer of 256 nodes and 2Gb per node, we have reach to calculate matrices of about 1,500,000 (the number of matrix elements considered has multiplied by 2,500). This means, approximately 20 $S=^1/_2$ for the anisotropic case and 25 $S=^1/_2$ for the isotropic. The test calculations demonstrate efficiencies near the unit (0.8 for 256 nodes) with quasi-linear speed-ups, which showed that the comunication processes are a minor problem and proved the validity of the parallelization.

The new matrix storage format has permitted to improve the memory consumption as the amount of RAM memory used for the partial diagonalization has been reduced. In addition, the preallocation task allows a fast-writing/reading process in the hard disk, which also reduces the calculation time.

The developed code has been evaluated with two moderate-sized test cases (with traces of about 60,000 elements), thus providing feedback about the correctness of the new program, giving an idea of scalability to large number of processors. The main conclusions are the following:

• The parallelization of the program has allowed to reduce drastically response time of the calculation compared to the original sequential code. This is a great advantage, e.g., in the solution of moderate-size problems with few processors. But more importantly, parallelization will make possible to solve much larger problems, those with real scientific interest, problems that would otherwise be impossible to address due to memory limitations or lack of computational power.

• The use of partial iterative eigensolvers available in SLEPc, which are intended for large-scale sparse matrices, is a major improvement over the original code. These methods allow for the computation of only the interesting part of the eigenvalues spectrum, thus saving a lot of computational effort. That ends in the possibility of addressing bigger problem sizes. In this particular application, the SLEPc solvers have proved to be very robust and efficient, with a very fast convergence.

•Computing only part of the spectrum can be a problem while calculating the thermodinamic properties because, if the energy levels are continuous, it is not trivial to determine where to truncate the eigenvalues. This can be solved by just calculating the low temperature part of the susceptibility considering anisotropy while the rest of the spectrum is calculated without it. In addition, when the optical properties such as Ineslastic Neutron Scattering are calculated, the huge size of the eigenvectors and the task of calculating the interaction between all the elements is an additional bottleneck with an enormous time consumption.

• The parallel performance has proved to be reasonably good in the analyzed test cases, especially in the anisotropic ones. This confirmed the accuracy of the method and proved that they are ready to cope with really big problems, provided that enough computational resources are available.

• Different matrix storage schemes and several strategies for handling matrices of the form $A + \gamma B$ have been evaluated. The main conclusion is that symmetric storage combined with an implicit representation of such matrices is very effective, both

sequentially and in parallel. The evaluation has also provided very valuable information concerning memory requirements, that will allow the users to make accurate estimations of memory consumption when solving huge problems.

As the viability of the approach has been demonstrated, the parallel code is now ready for production mode, that is, to address challenging problems with real scientific interest. Some preliminary results with large molecular clusters are very encouraging and it may be possible to achieve some significant breakthroughs in this area in a short term.

2.2. MVPACK, results (*PAPER 2: MVPACK: A package to calculate energy levels and magnetic properties of high nuclearity mixed valence clusters)*.

The resulting program accounts for the consideration of electron delocalization, isotropic exchange, orbital energies, Coulombic repulsion and Zeeman interactions. On the other hand this approach does not consider anisotropic interactions such as anisymmetric exchange, zero-field-splitting, or the anisotropy of the g factor. This is so because for efficiency reasons, the original theory did not consider the spin projection.

In relation to the electric field effect the properties of a two electron reduced polyoxovanadate have been calculated (see chapter 3). This molecule can act as a molecular switch undergoing a magnetic transition between a paramagnetic and a strongly antiferromagnetic ground state when an electric field is applied along its main molecular axis. Due to the importance of this result, a complete explanation of the calculations and the theoretical rationalizacion is presented in Chapter 3 "*Electrically Switchable Magnetic Molecules*". The main conclusions are summarized here for clearance. The studied molecule, $K_2Na_6[GeV_{14}O_{40}]$ has two "extra" electrons that are locatd in the to extreme vanadium ions along the z axis. Due to the high orbital energy of the central vanadium square, the electrons should overcome a barrier to magnetically interact with each other. An electric field can give the system enough energy to pass that barrier and permit the antiferromagnetic interaction, thus modifying the magnetic properties.

Additionally, other bicapped POM $[Ni(Phen)_2(H_2O)]_2[PMo_{12}O_{40}]$ has been studied using the MVPACK code. This POM structure is related to the one previosly studied $[PMo_{12}O_{40}(VO)_2]$. In this case, the molybden core is reduced by one electron, which is assumed to be, in principle, completely delocalized over the full structure. When the temperature decreases or when an electric field is applied in the main molecular axis such electron localizes in the molybden directly coupled with the nickel. Such interaction opens the possibility of achieving an electrical control of the spin interaction between itinerant and localized electrons. Unfortunately, these results stay in a preliminary stage and will not be presented in this thesis.

3. *Author's contribution to the publications.*

3.1. Contributions related to MAGPACK.

In this publication, the author has stablished an interdisciplinar collaboration between the scientific communities in the ICMol and the DSIC. Both groups had never met before and a intense collaboration has started since then with meetings taking place at least once a month.

The author improved his knowledge about parallel computation working with the original developers of SLEPc. During this collaboration, the author completely dissected the original MAGPACK and each part was improved by the means of computational efficiency and parallelization. The author learnt the most appropriated way to compute key mathematical operations such as the matrix-vector product and the optimal matrix distribution and storage.

Another task developed by the author was to implement the C++ commands on the original FORTRAN77 code to manage the options of the parallel solver and even to store the matrix energy efficiently. This was a complicated task which took up the first year of the collaboration and needed to be done very carefully because errors in the communication between the two programming languages are difficult to identify.

In addition the author has managed a project to obtain an account for computing in the "Supercomputing Spanish Network". Thanks to this project he performed dozens of test calculations during 2 years in "Tirant Supercomputer" in Valencia (Project: Magnetic properties of high nuclearity spin clusters and mixed-valence clusters, tirant_vlc52), while the DSIC researchers have focused on "Marenostrum" in Barcelona and "Caesar Augusta" in Zaragoza. For all the calculations, the author has choosen two Ni^{2+} and Mn^{2+} rings as examples for the anisotropic and isotropic codes respectively. These ring models have been widely used to simulate infinite chain systems.

3.2. Contributions related to MVPACK

In this publication, the author contributed adding the electric field simulation to the most actual version of the package. He did this by adding a subroutine which accounts of introducing the coordinates of the magnetic centres as well as any number of electric fields contributions with their direction and intensity. There the orbital energies of the metal centres are modified depending on their position along the direction of the field. In fact, an orbital is stabilized compared to another one when it is in a higher electric potential.

This was an interesting addition to the original code with the aim to stabilize or destabilize some electronic distributions with an external stimulus. This basic feature will provide useful information about the control of the spin states with the application of an external electric potential, which is an easy-to-manipulate stimulus.

As previously stated, in this last version, it is possible to apply independent electric fields simulating the effect of a gate potential with atomic resolution. This permits to

study the classical model of a cellular automaton but using as the grid cell one or more MV molecules.

In addition the author has managed the calculation of two mixed-valence POMs $K_2Na_6[GeV_{14}O_{40}]$ and $[Ni(Phen)_2(H_2O)]_2[PMo_{12}O_{40}]$. The former study is completed and will be presented in Chapter 3, while the latter stills in a preliminary development and will not be shown here.

PAPER 1:
Parallel implementation of the MAGPACK package for the analysis of high-nuclearity spin clusters

Computer Physics Communications, **2010**, *181*, 1929-1940.

Computer Physics Communications 181 (2010) 1929–1940

Contents lists available at ScienceDirect

Computer Physics Communications

www.elsevier.com/locate/cpc

Parallel implementation of the MAGPACK package for the analysis of high-nuclearity spin clusters

E. Ramos [a,*], J.E. Roman [a], S. Cardona-Serra [b], J.M. Clemente-Juan [b,c]

[a] Instituto ITACA, Universidad Politécnica de Valencia, Camino de Vera s/n, 46022, Valencia, Spain
[b] Instituto de Ciencia Molecular, Universidad de Valencia, Polígono de la Coma s/n, 46980, Paterna, Valencia, Spain
[c] Fundación General Universidad de Valencia, Amadeo de Saboya, 4, 46010, Valencia, Spain

ARTICLE INFO

Article history:
Received 1 February 2010
Received in revised form 18 June 2010
Accepted 15 September 2010

Keywords:
Molecular magnetism
Magnetic anisotropy
Magnetic isotropy
High spin clusters
MAGPACK
Large-scale eigenvalue problem
SLEPc
Message-passing parallelization

ABSTRACT

Molecular clusters are formed by a finite number of exchange-coupled paramagnetic centers and they are model systems between molecules and extended solids. In order to simulate their properties and extrapolate to solids, the size of the systems to be treated should be as large as possible. In this context, the use of efficient parallel codes is essential. We present the parallel programs PARANI and PARISO, for anisotropic and isotropic models, that enable the calculation of large energy matrices in parallel and the subsequent computation of the relevant spectral information. The evaluation of the matrix elements is based on the serial package MAGPACK that uses the irreducible tensor operators technique and takes into account all kinds of anisotropic and isotropic magnetic interactions. To obtain the eigenvalues, the energy matrix is partially diagonalized by means of the SLEPc library. The calculation of eigenvalues and eigenvectors of these spin clusters enables us to evaluate the bulk magnetic properties (magnetic susceptibility and magnetization) as well as the spectroscopic properties (inelastic neutron scattering spectra). The results are encouraging in terms of parallel efficiency and open the way to address very challenging problems.

1. Introduction

Molecular magnetism is a comparatively new research area aimed at the design and study of molecule-based magnetic materials which are interesting both from the point of view of their unusual physical properties and their importance for applications, including high-density information storage and quantum computing [1]. These compounds provide ideal opportunities to study basic concepts of magnetism and explore the new physical phenomena, such as quantum tunneling of magnetization, etc. Magnetic clusters, i.e., molecular assemblies formed by a finite number of exchange-coupled paramagnetic centers, are currently receiving much attention in several active areas of research such as molecular chemistry, magnetism or biochemistry.

As they are in between the small molecular systems and the bulk state, the limited number of interacting centers often allows us to model their properties with quantum mechanical approaches, avoiding the further approximations required to treat extended solids. From this point of view, they serve as model systems for in-depth understanding of the magnetic exchange interactions, providing, at the same time, a testing ground for theories.

For a long time, this problem has been mostly restricted to the treatment of comparatively simple clusters comprising a reduced number of exchange-coupled centers and special spin topologies, for which solutions can be obtained either analytically or numerically. However, upon increasing the nuclearity of the cluster, the problem rapidly becomes unapproachable due to the lack of translational symmetry within the cluster. An additional complication is the spin anisotropy of the cluster.

A very powerful and efficient computational approach for solving the exchange problem in high nuclearity spin clusters with anisotropic exchange interactions, including the single ion anisotropic effects, was proposed by some of the authors [2]. The clusters are formed by an arbitrary number of exchange-coupled centers which combine different spin values and arbitrary topology. This approach is based on the use of the irreducible tensor operators (ITO) technique. It permits the evaluation of both eigenvalues and eigenvectors of the system, and then, to interpret the magnetic susceptibility, magnetization and also the inelastic neutron scattering spectra.

However, the viability of this approach depends on the efficient solution of the associated algebraic problems, namely the diagonalization of the relevant matrices, whose dimension has a rapid growth with the size of the molecular cluster. Therefore, it is nec-

* Corresponding author.
E-mail addresses: ramos@dsic.upv.es (E. Ramos), jroman@dsic.upv.es (J.E. Roman), salvador.cardona@uv.es (S. Cardona-Serra), juan.m.clemente@uv.es (J.M. Clemente-Juan).

0010-4655/$ – see front matter
doi:10.1016/j.cpc.2010.09.007

essary to have recourse to advanced numerical methods as well as to exploit the computational power of large supercomputers.

In this paper we present an implementation of this computational approach that exploits the advantage of parallelization and makes use of efficient mathematical libraries to diagonalize the energy matrices. In particular, our code is based on SLEPc, the Scalable Library for Eigenvalue Problem Computations [3]. The combination of the ITO technique and the parallelization approach for both the evaluation of the matrix elements and the subsequent diagonalization results in one of the most powerful tools for the analysis of the magnetic properties in high nuclearity spin systems.

The rest of the paper is organized as follows. Section 2 gives some theoretical background describing the equations and the goal of the simulations. In Section 3 we provide details about the organization of the codes, in order to identify the main building blocks. Section 4 deals with the mathematical background related to sparse eigensolvers, and includes a brief description of the SLEPc library. In Section 5 we discuss the main issues related to parallelization of the codes, and in Section 6 we show results concerning the performance of the developed programs. We wrap up with some concluding remarks.

2. Theoretical background

The developed programs can consider spin clusters formed by an arbitrary number of magnetic sites, N, with local spins. The spin cluster basis functions are obtained by coupling the local spins in a successive way,

$$\left|S_1 S_2(\tilde{S}_2) S_3(\tilde{S}_3)\ldots S_{N-1}(\tilde{S}_{N-1}) S M\right\rangle = \left|(\tilde{S}) S M\right\rangle. \tag{1}$$

Once the basis set is created we apply the Hamiltonian in order to evaluate the eigenmatrix. This is achieved by the use of the ITO techniques, which allow us to fully take into account all kinds of magnetic exchange interactions between the metal ions comprised in clusters of arbitrary size.

It is possible to express all kinds of contributions to the spin Hamiltonian expressed in terms of the conventional spin operators, within function of this generalized Hamiltonian expressed in terms of ITO's. Next, we present the most common terms in the spin Hamiltonian: isotropic exchange ($\hat{H}_O$), biquadratic ($\hat{H}_{BQ}$), anisotropic ($\hat{H}_{AN}$) and zero-field splitting ($\hat{H}_{ZFS}$) interactions, respectively.

$$\hat{H}_O = -2\sum_{i,f} J_{if}\hat{\mathbf{S}}_i\hat{\mathbf{S}}_f = 2\sqrt{3}\sum_{i,f} J_{if}\hat{T}^{(0)}(11|if), \tag{2}$$

$$\begin{aligned}\hat{H}_{BQ} &= -\sum_{i,f} j_{if}(\hat{\mathbf{S}}_i\hat{\mathbf{S}}_f)^2 \\ &= -\sum_{i,f} j_{if}\left[\sqrt{5}\hat{T}^0(22|if) + \frac{\sqrt{3}}{2}\hat{T}^0(11|if)\right],\end{aligned} \tag{3}$$

$$\begin{aligned}\hat{H}_{AN} &= -2\sum_{i,f}\sum_{\alpha=x,y,z} J_{if}^{\alpha}\hat{S}_i^{\alpha}\hat{S}_f^{\alpha} \\ &= -2J_{if}^{x}\hat{S}_i^{x}\hat{S}_f^{x} - 2J_{if}^{y}\hat{S}_i^{y}\hat{S}_f^{y} - 2J_{if}^{z}\hat{S}_i^{z}\hat{S}_f^{z} \\ &= \frac{2}{\sqrt{3}}\sum_{i,f}\left[\left(J_{if}^{x}+J_{if}^{y}+J_{if}^{z}\right)\hat{T}^{(0)}(11|if)\right] \\ &\quad + \sum_{i,f}\left[\left(J_{if}^{y}-J_{if}^{x}\right)\left[\hat{T}_2^{(2)}(22|if)+\hat{T}_{-2}^{(2)}(11|if)\right]\right. \\ &\quad \left. + \frac{2}{\sqrt{6}}\left(J_{if}^{x}+J_{if}^{y}-2J_{if}^{z}\right)\hat{T}_0^{(2)}(11|if)\right],\end{aligned} \tag{4}$$

$$\hat{H}_{ZFS} = \sum_i D_i\left(S_i^z\right)^2 = \sum_i D_i\left[\frac{-1}{\sqrt{3}}\hat{T}^{(0)}(0|i) + \sqrt{\frac{2}{3}}\hat{T}_0^{(2)}(2|i)\right]. \tag{5}$$

In the above equations, $\hat{T}_q^{(k)}(k_i k_f|if)$ and $\hat{T}_q^{(k)}(k_i|i)$ are a simple notation of the complex ITO that contains all the information necessary to be evaluated [4].

Finally, using the Wigner–Eckart theorem and the successive decoupling procedure we can express the energy matrix elements as a function of single-spin matrix and several tabulated symbols as 9j-symbols.

$$\begin{aligned}&\left\langle(\tilde{S}')S'M'\middle|\hat{T}_q^{(k)}\left(k_1 k_2(\tilde{k}_2)\ldots k_{N-1}(\tilde{k}_{N-1})k_N\right)\middle|(\tilde{S})SM\right\rangle \\ &\quad = (-1)^{2k}(2S+1)^{-1/2}C_{SMkq}^{S'M'}\left\langle S_N\middle\|\hat{\mathbf{S}}^{(k_N)}\middle\|S'_N\right\rangle \\ &\qquad \times\prod_{i=1}^{N-1}\sqrt{(2\tilde{k}_{i+1}+1)(2\tilde{S}_{i+1}+1)\left(2\tilde{S}'_{i+1}+1\right)}\left\langle S_i\middle\|\hat{\mathbf{S}}^{(k_i)}\middle\|S'_i\right\rangle \\ &\qquad \times\begin{Bmatrix}\tilde{k}_i & k_{i+1} & \tilde{k}_{i+1}\\ \tilde{S}'_1 & S'_{i+1} & \tilde{S}'_{i+1}\\ \tilde{S}_1 & S_{i+1} & \tilde{S}_{i+1}\end{Bmatrix}.\end{aligned} \tag{6}$$

The diagonalization of this matrix gives us the eigenvalues and eigenvectors of the spin cluster.

In order to evaluate the different thermodynamic properties such as magnetic susceptibility and magnetization, we need to include in the Hamiltonian the term that takes into account the interaction between the external magnetic field and the spin functions. This interaction is the Zeeman term and can also be expressed in terms of ITO's, as

$$\begin{aligned}\hat{H}_{ZEE} &= \sum_i g_i^z\hat{S}_i^z H^z + g_i^{xy}\left(\hat{S}_i^x H^x + \hat{S}_i^y H^y\right) \\ &= \sum_i\left[g_i^z\hat{T}^0(0|i) + g_i^{xy}/\sqrt{2}\left(\hat{T}_{-1}^{(1)}(1|i) - \hat{T}_1^{(1)}(1|i)\right)H^{xy}\right].\end{aligned} \tag{7}$$

When the eigenvalues of the system at different magnetic fields or temperatures are available, it is possible to evaluate the partition function Z and the different thermodynamic properties of the system, as

$$M = NkT\frac{\partial \ln Z}{\partial H}, \tag{8}$$

$$\chi = \left(\frac{\partial M}{\partial H}\right)_{H\to 0}. \tag{9}$$

On the ground of the theoretical basis presented above and based on the sequential simulation codes developed in [2], we have implemented two parallel programs called ParAni and ParIso for calculating anisotropic and isotropic systems, respectively.

The isotropic systems are a special case where only the isotropic and biquadratic exchange terms are present in the spin Hamiltonian. These terms have the feature of not mixing functions with different quantum number S and not breaking the degeneracy of levels with the same S and different M. This decouples the energy matrix into several submatrices, one per each different S quantum number. Taking into account the ITO technique it is possible to eliminate this M quantum number and reduce the size of each S submatrix by a factor of $2S+1$.

3. Organization of the programs

ParAni and ParIso are programs based on the Ani and Iso subroutines form the Magpack package [2]. Both programs generate the spin functions of the system, calculate the energy matrix and diagonalize it in a parallel way to obtain the eigenvalues and

eigenvectors. The last part of the computation uses these data to evaluate the derived thermodynamic (specific heat, bulk susceptibility and magnetization) and spectroscopic properties (inelastic neutron scattering).

All the parameters describing the spin system and its properties (nuclearity, topology, exchange parameters, etc.) are provided by the user as input data. After execution, the program generates different output files containing all the information concerning the initialization, evaluation and simulation processes.

The programs are entirely written in FORTRAN77, enriched with some preprocessing directives for including all the declarations required by the SLEPc library, which will be described in Section 4.

3.1. Structure of ParAni

The ParAni program deals with the general anisotropic case. The main steps of the computation are the following:

(1) Setup of data containing the information of the cluster.
(2) Generation of starting spin functions.
(3) Evaluation of energy matrix, A. All nonzero elements are computed according to Eq. (6) and assembled into the matrix.
(4) First partial diagonalization. Given the eigenvalue relation $Ax = \lambda x$, a subset of the spectrum is computed, corresponding to the leftmost eigenvalues.
(5) Evaluation of Zeeman matrices. All nonzero elements are computed according to Eq. (7) and assembled into the matrices. To reduce the computational effort, only two matrices are computed, corresponding to parallel and perpendicular directions, $B_\parallel$ and $B_\perp$.
(6) Calculation of thermodynamic properties. This is done by computing a partial diagonalization of matrices $C_\parallel = A + \gamma B_\parallel$ and $C_\perp = A + \gamma B_\perp$ for three different values of the scalar γ. In total, six partial eigendecompositions are computed.
(7) Generation of final results, by combining all the previous results with a small computation.

All matrices mentioned above are symmetric. This fact can be exploited in the program, both in terms of storage requirements and computational effort, as will be discussed in Section 5. Another important aspect to be considered is that the matrices are sparse, i.e., the percentage of nonzero elements is rather small (around 1%). It is important to note that the sparsity pattern (i.e., the location of nonzero elements) is different in matrices A, $B_\parallel$ and $B_\perp$.

3.2. Structure of ParIso

In the case of isotropic systems, the energy matrix can be written as a block diagonal matrix,

$$A = \begin{bmatrix} A_1 & & & \\ & A_2 & & \\ & & \ddots & \\ & & & A_b \end{bmatrix}, \tag{10}$$

where each of the b blocks is a symmetric sparse matrix of different dimension. Finding the leftmost eigenvalues of A amounts to computing the leftmost eigenvalues of each of the blocks, A_i. Thus, the structure of the program ParIso is geared to this block structure, where one partial diagonalization is carried out per block (no Zeeman terms are present in this case).

(1) Setup of data containing the information of the cluster.
(2) For each diagonal block, $i = 1, \ldots, b$, do:
  (2.1) Generation of starting spin functions.
  (2.2) Evaluation of energy submatrix, A_i. All nonzero elements are computed according to Eq. (6) and assembled into the matrix.
  (2.3) Partial diagonalization of A_i.
(3) Generation of final results.

4. Projection methods for sparse eigenvalue problems

In this section, we discuss projection methods for solving the real symmetric standard eigenvalue problem,

$$Ax = \lambda x, \tag{11}$$

where $A \in \mathbb{R}^{n\times n}$, $\lambda \in \mathbb{R}$ (eigenvalue) and $x \in \mathbb{R}^n$ (eigenvector). Projection methods are appropriate when the matrix A is very large but its application to a vector is relatively cheap (e.g., it is sparse) and only part of the spectrum is required. If we number the eigenvalues consecutively from left to right, then we might want to compute the first k eigenpairs, (λ_i, x_i), $i = 1, \ldots, k$, usually with $k \ll n$. The basic principle of projection methods is to find the best approximations to the eigenvectors in a given subspace of small dimension. Let V be an $n \times m$ matrix, with $k \leqslant m \ll n$, whose columns v_i constitute an orthonormal basis of a given subspace $\mathcal{V}$, i.e., $V^T V = I_m$ and $\mathrm{span}\{v_1, v_2, \ldots, v_m\} = \mathcal{V}$. Then the eigenvalues of the so-called Rayleigh quotient matrix $T = V^T A V$ approximate eigenvalues of the original matrix. More precisely, if $T y_i = \theta_i y_i$ then the eigenpair approximations are $\tilde{\lambda}_i = \theta_i$ and $\tilde{x}_i = V y_i$. These approximate eigenvectors belong to subspace $\mathcal{V}$ and are the best possible approximations in that subspace. For background material on projection methods, the reader is referred to [5,6].

4.1. Restarted Krylov methods

The quality of the eigenpair approximations $(\tilde{\lambda}_i, \tilde{x}_i)$ depends on how the subspace $\mathcal{V}$ is built. A popular choice is to use the Krylov subspace associated with matrix A and a given initial vector v_1, $\mathcal{K}_m(A, v_1) = \mathrm{span}\{v_1, Av_1, A^2 v_1, \ldots, A^{m-1} v_1\}$. Without loss of generality, in the sequel we will assume that v_1 has unit length.

In the case of a symmetric matrix, we can use the Lanczos algorithm to compute an orthogonal basis of the Krylov subspace. This method also provides the projected matrix T, which is a symmetric tridiagonal matrix in this case. This computation is efficient and numerically stable, provided that an appropriate methodology is employed to guarantee a good quality of orthogonality among the basis vectors. In brief, the full-orthogonalization Lanczos method computes the basis vectors v_j in sequence, starting from v_2. Each vector v_j is the result of orthogonalizing Av_{j-1} with respect to the previous $j-1$ vectors, and then normalizing with respect to the Euclidean norm.

After m steps of the Lanczos algorithm, the computed quantities satisfy the relation

$$AV = VT + f_{m+1} e_m^T, \tag{12}$$

where f_{m+1} would yield the next basis vector (after normalization) if the process were to be continued, and e_m is the mth coordinate vector. As the number of columns in V grows, eigenvalues of T will tend to converge to eigenvalues of A. The rate of convergence will be fast provided that the initial vector v_1 is rich in the direction of the wanted eigenvectors. However, in practice this is usually not the case and consequently many iterations are likely to be required. This is a serious problem because increasing the number of iterations (m) implies a growth in storage requirements and, more importantly, a growth of computational cost per iteration (mainly because orthogonalization is increasingly expensive and also because the cost of computing eigenpairs of T becomes

non-negligible). A workaround for this is to *restart* the algorithm, that is, stop after m iterations and rerun the method with a new v_1 computed from the recently obtained spectral approximations. One possible approach is to explicitly compute v_1 as a linear combination of a subset of the current approximate eigenvectors. This is called explicit restart. The main difficulty with explicit restart is how to choose the parameters for building the new starting vector.

A better approach is to do some form of implicit restart, that avoids the need to explicitly compute a new starting vector v_1. In the context of Lanczos, one such technique is the so-called thick-restart Lanczos method [7]. In brief, this technique keeps ℓ approximate eigenvectors (those corresponding to eigenvalues in the wanted part of the spectrum) and discards the rest, then completes the basis with $m-\ell$ new Lanczos vectors (a typical choice is $\ell = m/2$). Apart from enhancing convergence between restarts, this technique allows the iteration to focus on a certain part of the spectrum, such as the leftmost eigenvalues.

The restart is also a good moment to keep track of already converged eigenvalues, so that they can be deflated. Deflating converged eigenvalues means modifying the iteration so that they do not reappear in the spectrum of T. This can be done in different ways, but the most effective one is called locking and consists in extracting the converged eigenvector from the active basis V but still consider it in the orthogonalization step. A schematic description of Lanczos with thick-restart and locking is shown below.

(1) Set $\tilde{X} = \emptyset$ (already converged eigenvectors).
(2) Run m steps of Lanczos.
(3) Restart loop (until k eigenpairs have converged):
  (3.1) Compute eigenpairs of T and check for newly converged eigenpairs.
  (3.2) Add newly converged eigenvectors to $\tilde{X}$.
  (3.3) Keep ℓ approximate eigenvectors in the basis.
  (3.4) Run $m-\ell$ steps of Lanczos.

Note that the number of columns of $\tilde{X}$ can grow as required. In this way, the iterative eigensolver can be used to compute more than m eigenpairs. For instance, if one wants to compute $k = 8000$ eigenpairs of a matrix of order $n = 50\,000$, then setting for instance $m = 10\,000$ would be too much computational effort for extracting eigenpairs of T, whereas with the above scheme it is possible to work with $m = 300$, say, and iterate until all wanted eigenpairs have been retrieved.

4.2. The SLEPc library

SLEPc, the Scalable Library for Eigenvalue Problem Computations [3], is a software package for the solution of large-scale eigenvalue problems on parallel computers. Apart from the standard eigenvalue problem of Eq. (11), it also addresses other types of problems such as the generalized eigenvalue problem or the singular value decomposition. SLEPc can work with either real or complex arithmetic, in single or double precision, and it is not restricted to symmetric (Hermitian) problems. It can be used from code written in C, C++, FORTRAN, and Python. SLEPc has been employed successfully in many different application areas such as nuclear engineering [8] or plasma physics [9].

SLEPc provides a collection of eigensolvers, most of which are based on the subspace projection paradigm described in the previous paragraphs. In particular, it includes a robust and efficient parallel implementation of the thick-restart Lanczos method, as well as its more general variant for nonsymmetric problems called the Krylov–Schur method [10]. The Lanczos solver includes the possibility to set the m parameter described in the previous subsection, thus allowing the computation of a large number of eigenpairs. This feature is missing in other software such as ARPACK [11]. In addition to Krylov solvers, other methods such as Davidson-type or conjugate-gradient solvers are under development.

SLEPc is built on top of PETSc (Portable, Extensible Toolkit for Scientific Computation [12]), a parallel framework for the numerical solution of partial differential equations, whose approach is to encapsulate mathematical algorithms using object-oriented programming techniques in order to be able to manage the complexity of efficient numerical message-passing codes. All the PETSc software is freely available and used around the world in many application areas. PETSc is object-oriented in the sense that all the code is built around a set of data structures and algorithmic objects. The application programmer works directly with these objects rather than concentrating on the underlying data structures. The three basic abstract data objects are index sets, vectors and matrices. Built on top of this foundation are various classes of solver objects, including linear, nonlinear and time-stepping solvers. SLEPc inherits all the good properties of PETSc, including portability to a wide range of parallel platforms, scalability to a large number of processors, and run-time flexibility giving full control over the solution process (one can for instance specify the solver at run time, or change relevant parameters such as the tolerance or the size of the subspace basis).

The solvers in PETSc and SLEPc have a data-structure neutral implementation. This means that the computation can be done with different matrix storage formats, and also even with a matrix that is not stored explicitly (this requires some user-defined operations such as the matrix–vector product). By default, a matrix in PETSc is stored in a parallel compressed-row sparse format (called `aij`), where each processor stores a subset of rows. Other formats include the symmetric variant (`sbaij`), where only the upper triangular part is stored, as well as the dense storage (both sequential and parallel).

5. Parallelization strategy

In this section, we provide some details about the implementation of the codes, by making use of the parallel capabilities of the SLEPc and PETSc frameworks. We put especial emphasis on optimization issues, such as efficient memory management and reduction of memory requirements.

5.1. How SLEPc eigensolvers are parallelized

We start by describing the parallelization strategy used by SLEPc eigensolvers. Both PETSc and SLEPc are oriented to large-scale computation on distributed memory parallel computers with a message-passing paradigm (with the MPI standard). As mentioned before, matrices in PETSc are generally stored by blocks of rows. Vectors also follow the same data distribution, so every processor owns a contiguous chunk of the vector elements. According to the description of the Lanczos algorithm in Section 4, we can discuss the parallelization of the main operations:

- Matrix–vector product, Av_{j-1}. In PETSc, this operation is implemented with mesh-based computations in mind, so that it is particularly efficient in finite-element applications, for example. In our particular application, the matrices do not arise from a computational mesh and the number of nonzero elements is relatively large, so one should not expect perfect scalability.
- Vector operations that require global communication, such as orthogonalization, inner product and norm. Global communication should be avoided whenever possible, and SLEPc implementations are carefully developed with this issue in mind [13].
- Trivially parallelizable vector operations, such as addition.

- Operations on the small projected matrix, T. These operations are carried out sequentially, in a replicated way (all processors perform the same computation). This is usually positive for to parallel performance, provided that the size of the projected problem is not large. This is one of the reasons why using a small value of m compared to k can be beneficial. The other reason is memory requirement as described next.

In order to determine the memory requirements of the eigensolver, we have to focus on Eq. (12). We assume that matrix A is of dimension n. Apart from the matrix A (whose storage will be discussed later) and minor workspace, the memory requirements can be summarized as follows:

- Storage of basis vectors V and eigenvectors $\tilde{X}$: the number of columns of V grow up to the maximum, m (`mpd` in SLEPc's terminology), and there is also need to store the eigenvectors as they converge, up to the requested number, k (`nev` in SLEPc's terminology). So we need to store at least $m+k$ vectors, that is $n_{\text{local}}(m+k)$ floating-point numbers per processor (assuming the local dimension is $n_{\text{local}} = n/p$, and p is the number of processors).
- Storage of the projected matrix: for this we need two square arrays, one for T and the other for its eigenvectors, both of dimension $m \times m$. This memory is replicated in all processors, not distributed. This amount of memory is negligible except in the case that m is too large.

As an example, suppose we have a problem of order $n = 80\,000$ and we want to solve it with $p = 8$ processors, computing $k = 1000$ eigenvalues with $m = 500$. The local part of the vectors would be $n_{\text{local}} = 10\,000$. The memory in each processor would be:

- Basis vectors and eigenvectors: $n_{\text{local}}(m+k) = 15\,000\,000$.
- Projected problem: $2m^2 = 500\,000$.
- Total: 15 500 000 floating-point numbers, that is roughly 120 Mbytes (in double precision).

As quoted above all the code is prepared to work correctly in single precision arithmetic. In the following, we use double precision throughout.

5.2. Matrix generation

Apart from the partial diagonalization, the most computationally expensive part is the generation of matrix A (step 3 in the algorithm of Section 3.1). This matrix is real, symmetric, sparse, and very large, so for best efficiency all these properties have to be considered when generating and storing it.

The percentage of nonzero elements is considerably larger than in other classes of applications. Still, sparse storage (that is, storing only nonzero elements) represents a huge advantage compared to a dense storage, both in terms of memory savings and reduction of computational cost. We consider that a matrix entry a_{ij} is nonzero if $|a_{ij}| > 10^{-12}$. With this threshold, the percentage of nonzero elements is typically about 1% or less.

Together with the sparse storage, distributing the matrix across several processes makes it possible to increase the size of the molecular cluster under study, which is crucial for analyzing problems of real scientific interest. In our application, matrix generation is trivially parallelizable, meaning that each process can compute its assigned rows without intervention of the other processes (assuming that all processes compute the starting spin functions redundantly, in step 2 in the algorithm of Section 3.1). However, it is possible to enhance the properties related to parallelization by using an appropriate ordering, as will be discussed below. Before that, we treat two important issues: memory preallocation and exploitation of symmetry.

Matrix preallocation is necessary because PETSc uses a dynamic memory scheme for flexible storage of matrices (the used memory grows as new nonzero elements are added). Since allocation of memory is time-consuming, this scheme is very inefficient especially for very large matrices with many nonzero elements. The solution is to preallocate, that is, to do an a priori estimation of the number of nonzero elements and reserve a sufficiently large chunk of memory for them. Sometimes, it is sufficient to estimate nonzero elements very roughly for preallocation. In our case, we have opted for performing a very accurate estimation: each processor counts nonzero elements in each row by computing the potentially nonzero values. This represents a considerable overhead, but it pays off with respect to underestimating the real nonzero pattern.

Regarding the symmetry of the matrix, we have three options:

- `aijfull`: Compute all matrix elements, without taking symmetry into account.
- `aijhalf`: Compute half of the elements only (e.g., the upper triangular part), but store each element twice (both in the original position and the symmetric one). The drawback of this option is that it requires explicit interprocessor communication during matrix assembly.
- `sbaij`: Compute half of the elements only and use a special symmetric storage format.

The first two schemes differ only when generating the matrix but are equivalent in the rest of the code.

For a matrix with n_{nz} nonzero elements, the total storage requirement is about n_{nz} floating point numbers and $n + n_{\text{nz}}$ integers. In the case of the special `sbaij` format, the memory usage is reduced roughly by half. By default, we use the symmetric storage format, because it saves a lot of memory and it is the best one in terms of matrix generation time (we will also see in Section 6 that the parallel performance of the matrix–vector product does not degrade with respect to the other options).

Although the number of matrix rows assigned to each process is roughly the same, the different number and position of nonzero elements in each row can lead to load imbalance and excessive communication overhead in the matrix–vector product. For best performance, it may be necessary to perform an appropriate reordering of the unknowns, and permute the matrix accordingly. As it is well known, in this context a good ordering can be computed by partitioning the adjacency graph associated to the nonzero structure of the matrix, where the goal is to obtain p partitions of almost equal size while minimizing the edge-cut between partitions. For this aim, we have used ParMETIS [14]. Fig. 1 shows the resulting nonzero pattern after permutation for the case of 2 and 16 partitions. The diagonal blocks represent the binding of unknowns within a partition, whereas the off-diagonal blocks represent edges connecting one partition to another (since some nonzero elements have been dropped, it is possible to obtain totally disconnected partitions when the number of partitions is small).

5.3. Computation of magnetic susceptibility

In case of anisotropic systems, for the calculation of the magnetic susceptibility, several consecutive diagonalizations are needed at different fields, both its intrinsic magnitude and its orientation with regard to the axis of anisotropy is changed. The values obtained in each of these diagonalizations are translated later to obtain only one file of results and using them as the

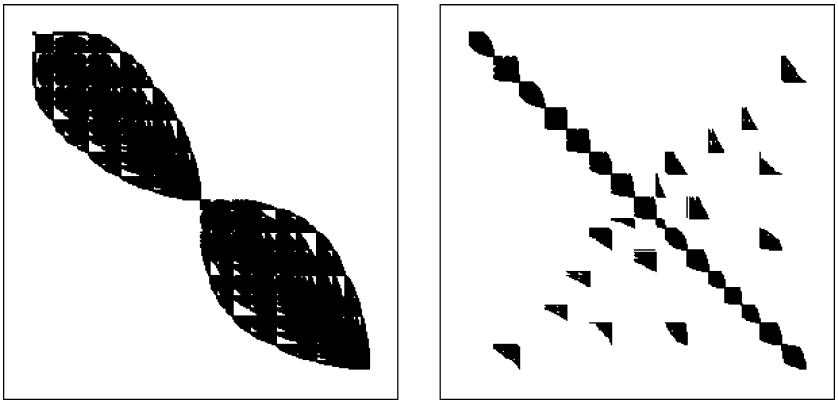

Fig. 1. Pattern of nonzero elements of matrix A for the case of 2 and 16 partitions.

molecule energy levels allows us to calculate the magnetic susceptibility of the compound under study.

Using the notation of Section 3.1, a partial diagonalization is required for matrices $C_\parallel = A + \gamma B_\parallel$ and $C_\perp = A + \gamma B_\perp$ for three different values of the scalar γ. Next, we discuss the implementation details associated to these matrices.

In PETSc, the operation $C = A + \gamma B$ (usually referred to as matrix *axpy*) is very efficient provided that A and B have the same sparsity pattern (or alternatively one pattern is a subset of the other). Otherwise, the overhead of this operation can be extremely high, mainly due to memory management reasons discussed previously. In our case, neither $B_\parallel$ nor $B_\perp$ have a sparsity pattern similar to that of A. As a consequence, the matrix *axpy* should be avoided whenever possible in order to get reasonable efficiency. We address this issue with two different strategies: (1) do accumulative matrix *axpy*s, and (2) avoid them completely by making use of implicit (*shell*) matrices.

For the accumulative matrix *axpy*s, we have reorganized the computation in such a way that the three $C_\parallel$ matrices are processed before, then the three $C_\perp$ matrices. Also, their computation has been rearranged so that the second and third ones can be obtained additively from the previous one. In matrix notation, $C_1 = A + \gamma_1 B$, then $C_2 = C_1 + \gamma_2 B$ and $C_3 = C_2 + \gamma_3 B$. In this way, only the first matrix *axpy* will be inefficient, because in the other two we can assure that the sparsity pattern of B is a subset of C_1 and C_2. Overall, we are avoiding 4 inefficient *axpy*s.

The other strategy makes use of implicit matrices, which are called *shell* matrices in PETSc. These are matrices that do not store matrix elements explicitly. Instead, they interoperate with the rest of the code components by providing some user-defined operations consisting on a subroutine that operates with user-defined data. In our case, we define a *shell* matrix that contains A, B, and γ as data, and implements the matrix–vector product operation as $y = Cx = (A + \gamma B)x = Ax + \gamma Bx$. No other matrix operations are required because Lanczos eigensolvers are based on matrix–vector products exclusively. With this approach, we eliminate the need of matrix *axpy*s completely, but as a consequence we are increasing the cost of the eigensolver since we now perform two matrix–vector products whenever the solver needs to do a matrix–vector product with C.

5.4. Optimizations for the isotropic case

The parallelization of the calculation in the isotropic case is very similar, except for avoiding the complication associated to the Zeeman matrices that are not present in this case. The matrices have the block structure described in Section 3.2. If we consider matrix A as a whole, its percentage of nonzero elements is just 0.1%, but all the individual submatrices have 1–2% elements or more. The generation of the matrix is very similar to the anisotropic case, with the difference that the individual blocks are stored separately. Not all blocks need to be in memory simultaneously, since after generating one block it is possible to compute its partial diagonalization and then the matrix is no longer needed and can be destroyed. For all these reasons, we are able to calculate much larger systems than in the anisotropic case.

It would be possible to carry out further optimizations in order to improve the parallel efficiency in ParIso. For example, since typically one or two of the blocks have a very small dimension (50 or less), these blocks could be fully diagonalized with a dense eigensolver in each processor in a replicated way. This would avoid the parallel overhead associated to distributing such a small computation among all the available processors.

6. Code evaluation

We have carried out a number of numerical experiments in order to validate the correctness of the parallel codes, as well as to assess their parallel efficiency.

The computer system used for the computational experiments is Caesar Augusta, an IBM cluster consisting of 256 JS20 blade computing nodes, each of them with two 64-bit PowerPC 970FX processors running at 2.2 GHz, interconnected with a low latency Myrinet network. In all tests, we have used two processors per node, up to 64 nodes. When discussing the parallel performance, we will evaluate speedup and efficiency with respect to nodes, not processors. For instance, the speedup for two nodes, S_2, is defined as the ratio between the execution time with one node (two processors) and two nodes (four processors). The ideal speedup in this case is 2, so the efficiency for two nodes is defined as $E_2 = S_2/2$. These quantities are defined analogously for larger number of nodes.

6.1. Test cases and validation of numerical results

For the ParAni code, the experiments we report in this paper are related to the simulation of a ring of 10 centers of nickel(II) ions, where the associated problem dimension is $N = 59\,049$. The objective is to calculate the magnetic properties of infinite chains

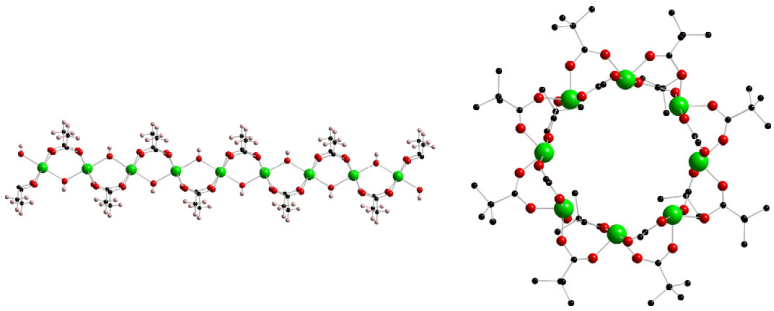

Fig. 2. Chain of atoms of nickel (left) and its representation as a ring (right).

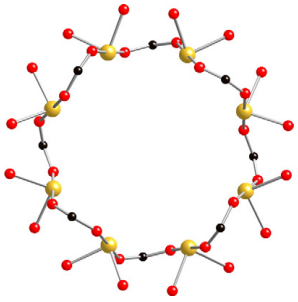

Fig. 3. Scheme of the eight manganese ring model.

of Ni atoms with antiferromagnetic interaction between them. In order to simulate the fact that the chains are infinite and to avoid the lack of interaction in the edges, the calculation has been done using closed rings. Fig. 2 illustrates the chain of atoms of nickel and its model through a ring of 8 members.

The model used in PARISO is an eight manganese ring with antiferromagnetic coupling. As in the other example, calculating rings is a correct approximation for simulating infinite chains. In Fig. 3 we can see this model.

In order to validate the correctness of the computations, we compare the results from the parallel versions with the results from the original sequential MAGPACK codes. This comparison is feasible for rings of small nuclearity, with matrix size less than 20 000 for which the serial code is still viable. For the antiferromagnetic rings the reduced susceptibility curve (susceptibility divided by the number of centers) with $2N$ centers tends to a constant value as N goes to infinity. The way of verifying the results for high nuclearity rings calculated by the parallel version is to see that they are the upper limit of the low nuclearity curves calculated accurately by MAGPACK. As N gets larger, the difference with respect to the curve corresponding to $N-1$ is reduced. To calculate the susceptibility, it is necessary to have a large number of computed levels, so this comparison is made for low temperatures where a smaller number of levels is required.

6.2. Performance of the matrix generation

We now proceed to analyze the matrix generation in terms of parallel performance. In Table 1 we show the times spent in the parallel generation of the energy matrix (step 3 in the algorithm of Section 3.1) for the anisotropic case in the nickel ring for different number of nodes. Fig. 4 depicts the speedup and efficiency with respect to nodes. From these results, we see that `sbaij` is sequentially almost twice as fast as the `aijfull` case, whereas the `aijhalf` alternative is somewhere midway. In parallel, the performance of `sbaij` is the worst, and the reason is that it is the case where load imbalance is more marked. The performance of `aijhalf` is worse than `aijfull`, as expected by the required communication. We can conclude that the matrix generation stage is quite scalable, because even the worst case achieves more than 75% efficiency with 64 nodes.

Table 1
Comparison of the matrix generation time (in seconds) for the nickel ring with the three considered methods.

Nodes	`aijfull`	`aijhalf`	`sbaij`
1	36 121	29 279	22 549
2	18 736	15 001	12 849
4	9393	7850	6590
8	4820	4034	3356
16	2419	2041	1783
32	1229	1050	890
64	620	531	454

6.3. Tuning of eigensolver parameters

In this section, we analyze the impact of SLEPc's `mpd` parameter on the performance of the eigensolver in this particular application. The maximum projected dimension (`mpd`) is what was referred to as m in the description of Section 4. The smaller the value of this parameter is, the less memory will be required. However, setting a too low value may hinder convergence thus increasing overall computing time. Therefore, it is important to make a reasonably good a priori estimation of the optimal value.

For this, we carry out a study varying the `mpd` parameter when computing 100, 200, 1000 and 2000 eigenvalues of the nickel ring with 8 nodes (16 processors). We tried values of `mpd` ranging from 25 to 1200 (although practical experience shows that values larger than $2 \cdot$ `nev` are usually wasteful).

Table 2 shows the execution time required in each case. These times are plotted graphically in Fig. 5, together with the number of iterations required by the eigensolver. The plots have a logarithmic scale in order to emphasize the differences.

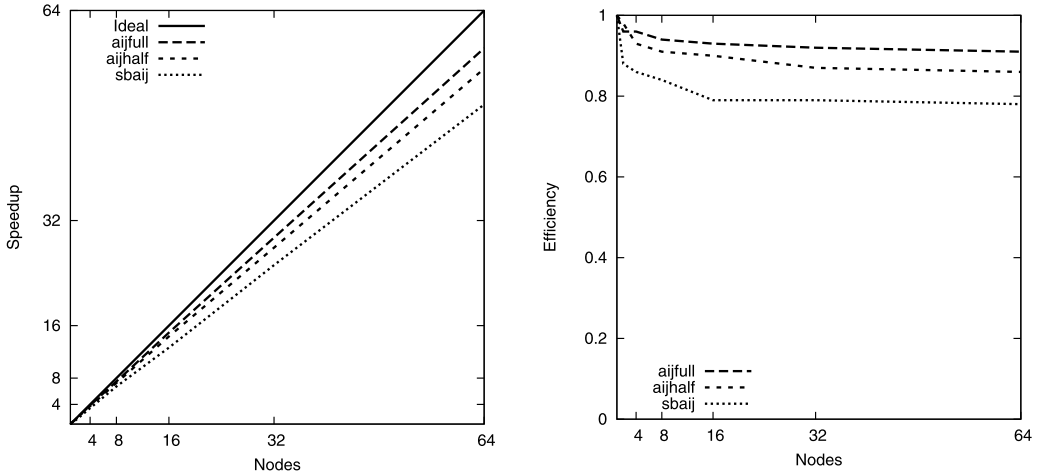

Fig. 4. Speedup (left) and parallel efficiency (right) of the matrix generation for the nickel ring, for the three considered methods.

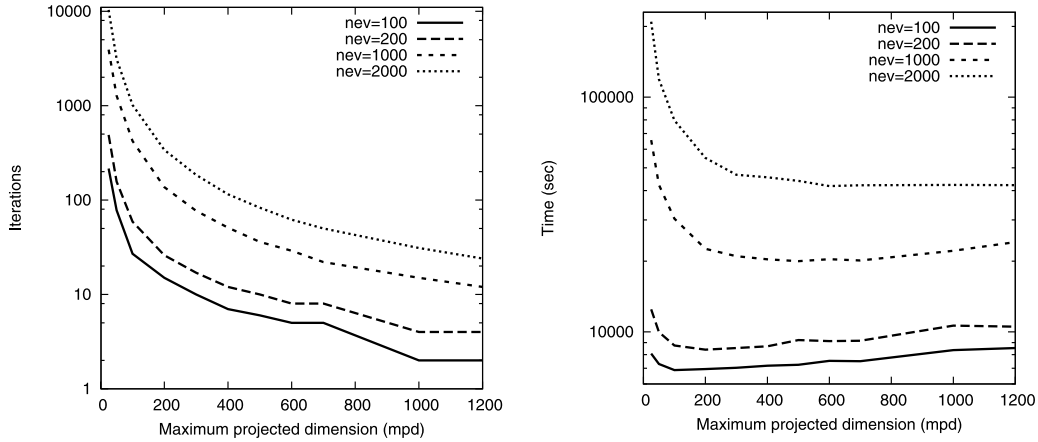

Fig. 5. Number of iterations of the eigensolver (left) and execution time (right) with varying values of the `mpd` parameter when computing 100, 200, 1000 and 2000 eigenvalues of the nickel ring with 8 nodes.

Table 2
Execution time (in seconds) with varying values of the `mpd` parameter when computing 100, 200, 1000 and 2000 eigenvalues of the nickel ring with 8 nodes.

`mpd`	`nev` = 100	`nev` = 200	`nev` = 1000	`nev` = 2000
25	8083	12 480	65 604	209 494
50	7297	9980	42 302	119 194
100	6871	8753	30 372	79 676
200	6943	8397	22 584	55 108
300	7032	8539	21 003	46 705
400	7173	8682	20 382	45 535
500	7244	9231	20 010	43 959
600	7523	9136	20 395	41 772
700	7504	9163	20 146	42 139
1000	8360	10 639	22 156	42 265
1200	8530	10 525	24 112	42 155

Results show that the number of iterations always decrease for larger values of `mpd`. However, these iterations become more and more expensive, and as a result it comes a point when the overall time stagnates or even starts to increase. We are interested in using a value close to this optimal `mpd`. For small `nev`, it seems that setting `mpd` = `nev` is a reasonable choice, whereas for larger values of `nev`, we can conclude that `mpd` = 300 is a good compromise between memory consumption and run time. From now on, we will use this value for all the tests.

We have repeated the analysis for the isotropic case, and the conclusions are very similar. Fig. 6 shows the corresponding times. Maybe in this case the optimal value of `mpd` is slightly smaller, because the dimension of the matrix blocks is smaller than the size of the whole anisotropic matrix. Anyway, a value of `mpd` = 300 is still reasonable.

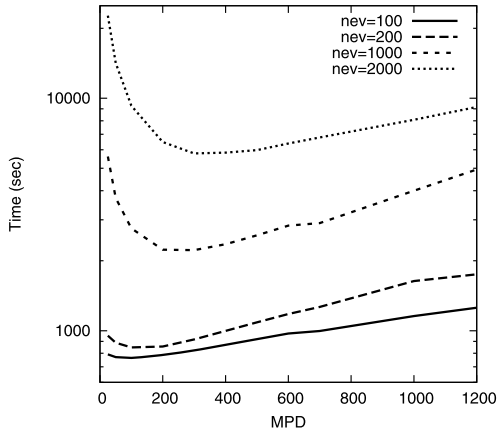

Fig. 6. Execution time with varying values of the `mpd` parameter when computing 100, 200, 1000 and 2000 eigenvalues of the manganese ring with 8 nodes.

Table 3
Breakdown of execution time (in seconds) for the whole computation (algorithm of Section 3.1) for the nickel ring with 8 nodes and `sbaij` storage.

Step	Time	Percentage
(1)–(2) Setup & spin functions	0	0%
(3) Generation of energy matrix	3356	27%
(4) First diagonalization	828	7%
(5) Generation of Zeeman matrices	2078	17%
(6) Thermodynamic properties	5942	49%
Total	12 204	100%

6.4. Parallel performance – anisotropic case

We now turn our attention to the parallel performance analysis of the overall computation in the anisotropic code. In view of the algorithm sketched in Section 3.1, we notice that apart from the matrix generation of step 3, the main computations are the diagonalization of step 4, the evaluation of Zeeman matrices in step 5, and the calculation of thermodynamic properties in step 6. In order to have a clearer idea of the individual cost of each stage, we show in Table 3 the breakdown of the execution time for a fixed number of processes.

The parallel performance of the evaluation of Zeeman matrices will be very similar to the case of the energy matrix, already discussed in Section 6.2. Also, the performance of the diagonalizations required in step 6 will be analogue to that of step 4. Thus, we focus our analysis on the first diagonalization, on one hand, and the total computation, on the other. The latter possibly includes the matrix *axpy* operations discussed in Section 5.

We will use the terms `aijfull`, `aijhalf`, and `sbaij` to refer to the cases where explicit matrix *axpy* operations are used for creating $C_\parallel$ and $C_\perp$, with the three matrix storage strategies considered in Section 6.2. Apart from these, we will also consider the case in which these matrices are handled implicitly via PETSc shell matrices, as discussed in Section 5. We call this the `sbaijshell` case. Note that in this case we have chosen a symmetric storage format for matrices A, $B_\parallel$ and $B_\perp$. Finally, we have considered an additional strategy also based on shell matrices, that differs from `sbaijshell` in that computations are reordered in such a way that it is possible to reuse the storage space of $B_\parallel$ for $B_\perp$, since only one of them is required at a time. We call this last option `sbaijreuse`, which is the most memory efficient one but involves some added computational overhead due to not creating $B_\parallel$ and $B_\perp$ at the same time.

Table 4
Breakdown of execution time (in seconds) for the steps 4 and 6 combined (all diagonalizations plus the required matrix *axpy* operations), for the nickel ring with 8 nodes and `sbaij` storage.

Operation	Time	Percentage
Matrix–vector product	4516	67%
Orthogonalization and restart	1837	27%
Matrix *axpys*	417	6%
Total	6770	100%

Table 5
Execution time (in seconds) corresponding to the first partial diagonalization of the nickel ring with `mpd` = 300 and `nev` = 600 with increasing number of nodes.

Nodes	`aijhalf`	`aij-parmetis`	`sbaij`	`sbaijshell`
1	5525	4948	5922	6030
2	2743	2353	3117	3063
4	1353	1293	1478	1491
8	746	689	828	803
16	388	376	423	428
32	237	210	274	254
64	117	117	149	157

When analyzing the parallel performance of the diagonalization operation, it is important to know which percentage of the computation is devoted to the matrix–vector multiplication, compared to the rest of the operations discussed in Section 4. Table 4 further decomposes the time of steps 4 and 6, combined, into the main building blocks of the thick-restart Lanczos method (plus the matrix *axpys* required only in explicit storage schemes). We can see that most of the time is spent in the matrix–vector multiplication. Thus, it is important to optimize this operation and it may be beneficial to apply the permutation technique discussed in Section 5.

Table 5 shows execution times corresponding to the first partial diagonalization (computing 600 eigenvalues) with four considered strategies: `aijhalf` (`aijfull` is equivalent to this in this analysis), `aij-parmetis`, `sbaij` and `sbaijshell` (`sbaijreuse` is equivalent to this in this analysis). The second one corresponds to the matrix stored in nonsymmetric format after permutation with ParMETIS. Fig. 7 represents speedups and efficiencies obtained in this test. The first comment is that parallel efficiency is reasonably good, although a bit worse than in the generation of the matrix. We can attribute this behavior to the fact that the problem dimension ($n = 59\,049$) is too small for such a large number of processors. Preliminary results with much larger problems indicate that the eigensolver scales well to 256 processors or more. From the results, we see that `sbaij` is slower than the nonsymmetric counterparts, as expected since the symmetric storage format has the same floating-point operations with a different memory access pattern. On the other hand, although the shell matrix approach requires more floating-point operations than the rest (two matrix–vector products instead of one), its performance is comparable to that of `sbaij`. Finally, comparing the permuted variant (`aij-parmetis`) with the one with default ordering (`aijhalf`), we can see that for many processors speedup decays instead of improving. We conclude that for this particular application it is not worth reordering the matrix, so we have not considered permutations in the symmetric storage cases.

Total execution times are listed in Table 6. These times cover all the computation, including the generation of all matrices, all the required partial diagonalizations, and matrix *axpys* if necessary. The corresponding speedup and efficiency are depicted in Fig. 8.

From the results, we see that in general the parallel performance is better in the total computation, with respect to the di-

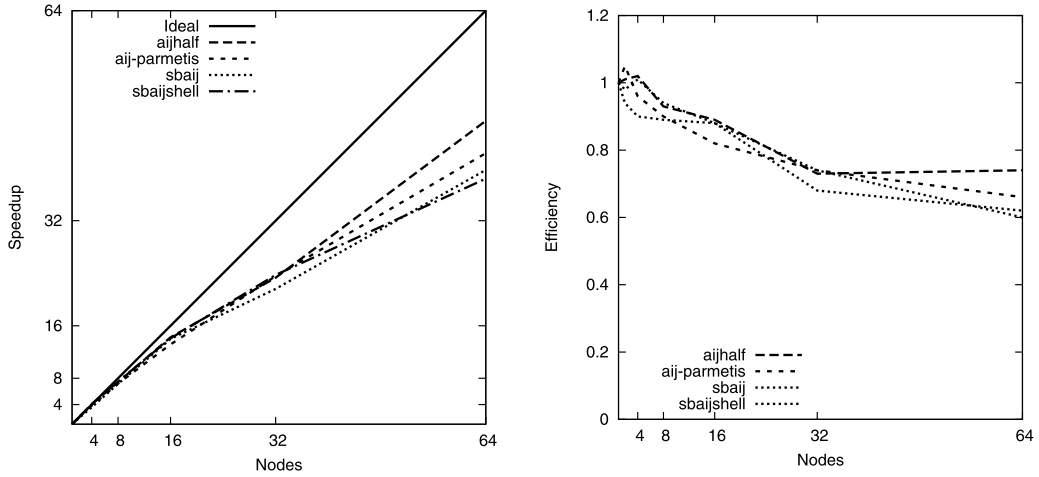

Fig. 7. Speedup (left) and parallel efficiency (right) of the first diagonalization for the nickel ring, for four matrix storage schemes.

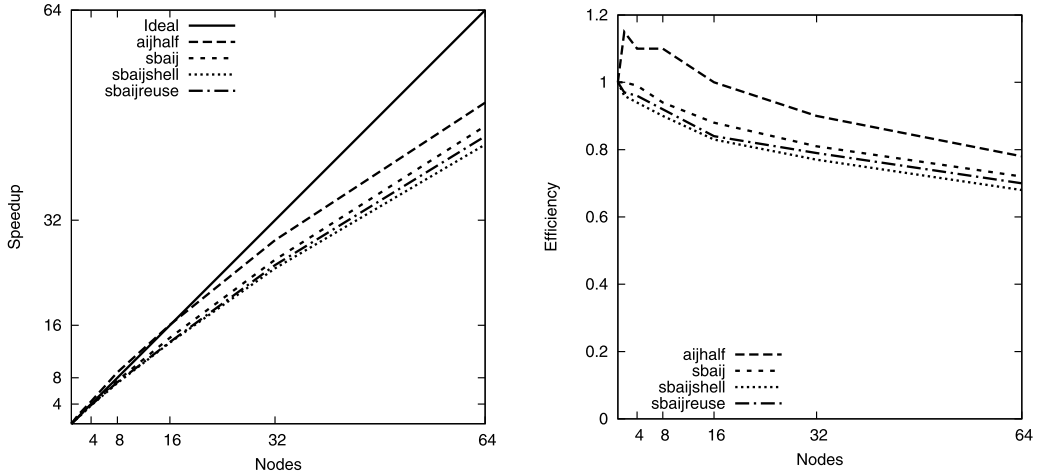

Fig. 8. Speedup (left) and parallel efficiency (right) of the whole computation for the nickel ring, for four matrix storage schemes.

Table 6
Execution time (in seconds) corresponding to the whole computation of the nickel ring with `mpd` = 300 and `nev` = 600 with increasing number of nodes.

Nodes	`aijhalf`	`sbaij`	`sbaijshell`	`sbaijreuse`
1	117 341	92 183	80 538	88 974
2	50 846	46 151	42 057	45 829
4	26 623	23 187	21 323	23 180
8	13 293	12 204	11 186	12 133
16	7308	6539	6034	6618
32	4052	3550	3265	3536
64	2351	1989	1850	1987

agonalization. One reason for this is that matrix generation has very good efficiency, and it represents a considerable percentage of the computation. Another reason is that the inefficiency of matrix *axpy* operations is due to the overhead associated to memory management, but this becomes more benign as the number of processors increase, since the amount of data stored in each processor is smaller. In any case, the parallel efficiency for 64 nodes is always above 68%.

In terms of actual response time, we can observe that `aijhalf` is slower in absolute terms, although it scales better than the symmetric variants (for large problems, it could eventually become faster but it is limited by memory requirements). The `sbaijshell` approach is significantly faster than the rest, both sequentially and in parallel. This can be attributed to avoiding all matrix *axpys*. The `sbaijreuse` strategy is slower but the most memory efficient approach, since it is based on symmetric storage and allows for the suppression of one of the matrices. For these

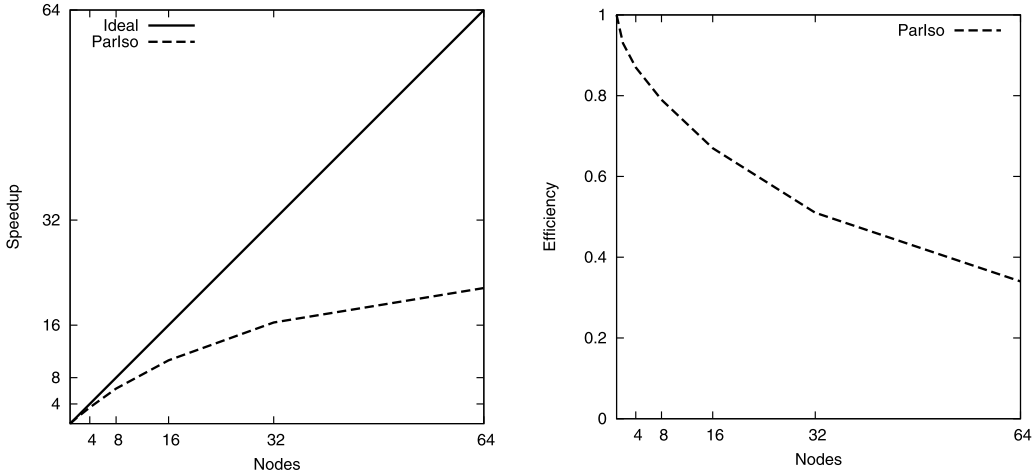

Fig. 9. Speedup (left) and parallel efficiency (right) of the whole computation for the manganese ring with the isotropic code.

Table 7
Execution time (in seconds), speedup and efficiency corresponding to the whole computation of the manganese ring with `mpd` = 300 and `nev` = 1000.

Nodes	`Time`	`Speedup`	`Efficiency`
1	13 013	1.00	1.00
2	7011	1.86	0.93
4	3755	3.47	0.87
8	2055	6.33	0.79
16	1222	10.65	0.67
32	793	16.41	0.51
64	601	21.65	0.34

reasons, we have opted for setting `sbaijreuse` as the default for production runs.

6.5. Parallel performance – isotropic case

As commented before, ParIso enables the solution of larger problems. In the selected test case, the problem size is $n = 135\,954$, but since the computation in ParIso is block-oriented, the size of the blocks will be much smaller. In particular, in this test case we have 21 blocks, the largest one being of order 16 576 whereas the smallest blocks have dimensions 84, 28, 7, and 1. Therefore, the large blocks are very small compared to the dimension of the test case used in the evaluation of ParAni. Furthermore, as mentioned in Section 5, we have no special provision for the efficient handling of tiny blocks. For all these reasons, the parallel efficiency in this subsection should be expected to be worse than in the previous analyses.

We analyze a run in which we have requested `nev` = 1000 eigenvalues in each block (of course, in the blocks of order $n < 1000$ we compute only n eigenvalues). In Table 7 we can observe the obtained execution times. These times correspond to the totality of the computation: generation of the matrices and diagonalizations. The speedups and efficiencies for up to 64 nodes are depicted in Fig. 9.

From the results, we can conclude that, as expected, the parallel performance is not as good as in the previous analyses. The problem size is too small to justify the use of 64 or even 32 nodes. However, in ParIso we could expect a parallel performance similar to ParAni for problems where the blocks are comparable in size to the nickel test case considered in the anisotropic runs.

7. Conclusions and future work

In this paper we have presented the parallelization of the MagPack package, that includes codes for anisotropic and isotropic simulation of molecular clusters with the ITO computational technique. The critical part of the computation, namely the partial diagonalization of large-scale sparse matrices, is carried out by means of the SLEPc library. We have evaluated the developed codes with two moderate-sized test cases, that provide us with feedback about the correctness of the new programs, and give us an idea of scalability to large number of processors. The main conclusions that we can draw are the following:

- The parallelization of the programs allows the drastic reduction of the response time of the calculation, compared to the original sequential programs. This is a great advantage, e.g., in the solution of moderate-size problems with few processors. More importantly, parallelization will make it possible to solve much larger problems, those with real scientific interest, that would otherwise be impossible to address due to memory limitations or lack of computational power.
- The use of state-of-the-art iterative eigensolvers available in SLEPc, which are intended for large-scale sparse matrices, is a major improvement over the original codes. These methods allow for the computation of just the part of the spectrum of interest, thus saving a lot of computational effort, and can address huge problem sizes. In this particular application, the SLEPc solvers have proved to be very robust and efficient, with a very fast convergence.
- The parallel performance is reasonably good in the analyzed test cases, especially in the anisotropic ones. This makes us confident that the codes will be able to cope with really big problems, provided that enough computational resources are available.
- We have evaluated different matrix storage schemes and several strategies for handling matrices of the form $A + \gamma B$. We have found that symmetric storage combined with an implicit

representation of such matrices is very effective, both sequentially and in parallel. The evaluation has also provided us with very valuable information concerning memory requirements, that will allow us to make accurate estimates of memory consumption when solving huge problems.

Once we have demonstrated the viability of our approach, the next step is to use the PARISO and PARANI programs in production mode, that is, to address challenging problems with real scientific interest. Some preliminary results with large molecular clusters are very encouraging and we foresee to achieve some significant breakthroughs in this area in a short term.

We also plan to continue enhancing the programs. In the next months, we will evaluate some new eigensolvers that are under development in SLEPc, in particular the Davidson-type methods.

A more broad view of the future work is to apply the same methodology to other codes and applications in related areas. The use of the SLEPc library opens the possibility of parallelizing various programs in computational chemistry whose scientific advantages are very relevant. This paradigm shift is going to allow us to solve problems that until now were impossible to address, since sequential computation is inviable due to the amount of time and memory required.

Acknowledgements

The authors are grateful for the computing resources provided by the Spanish Supercomputing Network (RES). The simulations were carried out on two nodes of the network: the supercomputer Caesar Augusta at BIFI (Universidad de Zaragoza) and the supercomputer Tirant at Universidad de Valencia, working group vlc52. The work was partially supported by the Spanish Ministry of Science and Innovation (MICINN): the first and second authors with project number TIN2009-07519, and the third and fourth authors with projects CSD2007-00010 – Consolider-ingenio in molecular nanoscience, CTQ-2008-06720. The Generalitat Valenciana (Promoteo Program) is gratefully acknowledged. S.C.-S. thanks the MICINN for a predoctoral grant.

References

[1] E. Coronado, K.R. Dunbar, Preface for the forum on molecular magnetism: The role of inorganic chemistry, Inorg. Chem. 48 (2009) 3293–3295.
[2] J.J. Borras-Almenar, J.M. Clemente-Juan, E. Coronado, B.S. Tsukerblat, MAGPACK: A package to calculate the energy levels, bulk magnetic properties, and inelastic neutron scattering spectra of high nuclearity spin clusters, J. Comput. Chem. 22 (9) (2001) 985–991.
[3] V. Hernandez, J.E. Roman, V. Vidal, SLEPc: A scalable and flexible toolkit for the solution of eigenvalue problems, ACM Trans. Math. Software 31 (3) (2005) 351–362.
[4] J.J. Borras-Almenar, J.M. Clemente-Juan, E. Coronado, B.S. Tsukerblat, High-nuclearity magnetic clusters: Generalized spin Hamiltonian and its use for the calculation of the energy levels, bulk magnetic properties, and inelastic neutron scattering spectra, Inorg. Chem. 38 (1999) 6081–6088.
[5] B.N. Parlett, The Symmetric Eigenvalue Problem, Prentice–Hall, Englewood Cliffs, NJ, 1980, reissued with revisions by SIAM, Philadelphia, 1998.
[6] Z. Bai, J. Demmel, J. Dongarra, A. Ruhe, H. van der Vorst (Eds.), Templates for the Solution of Algebraic Eigenvalue Problems: A Practical Guide, Society for Industrial and Applied Mathematics, Philadelphia, PA, 2000.
[7] K. Wu, H. Simon, Thick-restart Lanczos method for large symmetric eigenvalue problems, SIAM J. Matrix Anal. Appl. 22 (2) (2000) 602–616.
[8] D. Gilbert, J.E. Roman, W.J. Garland, W.F.S. Poehlman, Simulating control rod and fuel assembly motion using moving meshes, Ann. Nucl. Energy 35 (2) (2008) 291–303.
[9] J.E. Roman, M. Kammerer, F. Merz, F. Jenko, Fast eigenvalue calculations in a massively parallel plasma turbulence code, Parallel Comput. 36 (5–6) (2010) 339–358.
[10] G.W. Stewart, A Krylov–Schur algorithm for large eigenproblems, SIAM J. Matrix Anal. Appl. 23 (3) (2001) 601–614.
[11] R.B. Lehoucq, D.C. Sorensen, C. Yang, ARPACK Users' Guide, Solution of Large-Scale Eigenvalue Problems by Implicitly Restarted Arnoldi Methods, Society for Industrial and Applied Mathematics, Philadelphia, PA, 1998.
[12] S. Balay, K. Buschelman, V. Eijkhout, W. Gropp, D. Kaushik, M. Knepley, L.C. McInnes, B. Smith, H. Zhang, PETSc users manual, Tech. Rep. ANL-95/11, Revision 3.0.0, Argonne National Laboratory, December 2008.
[13] V. Hernandez, J.E. Roman, A. Tomas, Parallel Arnoldi eigensolvers with enhanced scalability via global communications rearrangement, Parallel Comput. 33 (7–8) (2007) 521–540.
[14] G. Karypis, V. Kumar, Parallel multilevel k-way partitioning scheme for irregular graphs, SIAM Rev. 41 (2) (1999) 278–300.

PAPER 2:
MVPACK: A Package to Calculate Energy Levels and Magnetic Properties of High Nuclearity Mixed Valence Clusters.

Journal of Computational Chemistry, **2010**, *31*, 1321-1332.

Software and News Update

MVPACK: A Package to Calculate Energy Levels and Magnetic Properties of High Nuclearity Mixed Valence Clusters*

J. J. BORRÁS-ALMENAR,[1] S. CARDONA-SERRA,[1] J. M. CLEMENTE-JUAN,[1,2] E. CORONADO,[1] A. V. PALII,[3] B.S. TSUKERBLAT[4]

[1]*Instituto de Ciencia Molecular, Universidad de Valencia, Polígono de la Coma, s/n 46980 Paterna, Spain*

[2]*Fundació General de la Universitat de València (FGUV), Plaza del Patriarca, 4-1, 46002, Valencia, Spain*

[3]*Institute of Applied Physics, Academy of Sciences of Moldova, Academy Street 5, MD 2028 Kishinev, Moldova*

[4]*Chemistry Department, Ben-Gurion University of the Negev, Beer-Sheva 84105, Israel*

Received 22 April 2009; Revised 16 July 2009; Accepted 31 July 2009
DOI 10.1002/jcc.21400
Published online 31 December 2009 in Wiley InterScience (www.interscience.wiley.com).

Abstract: We present a FORTRAN code based on a new powerful and efficient computational approach to solve the double exchange problem for high-nuclearity MV clusters containing arbitrary number of localized spins and itinerant electrons. We also report some examples in order to show the possibilities of the program.

 J Comput Chem 31: 1321–1332, 2010

Key words: molecular magnetism; mixed-valence compounds; double-exchange; Heisenberg exchange; electron delocalization; magnetic properties; software

Introduction

Molecular magnetism is a comparatively new research area aimed at the design and the study of molecule-based magnetic materials which are interesting both from the point of view of their unusual physical properties and their importance for applications including high-density information storage and quantum computing (see ref. 1 and references therein). These compounds provide ideal opportunities to study basic concepts of magnetism and explore the new physical phenomena, such as quantum tunneling of magnetization, etc. The magnetic clusters containing the delocalized electrons [mixed-valence (MV) systems[2]] are of particular interest in this area. As compared with the magnetic clusters in which all spins are localized, the MV systems are much less studied because of their complexity and the lack of the adequate theoretical models for their description. These systems are composed of ions of the same transition metal in different oxidation states. Under some conditions the extra electrons can be delocalized over the network of metal sites giving rise to the so-called double exchange[3–5] that couples the localized magnetic moments through the itinerant electrons.

Until recently the calculation of the energy pattern of MV compounds exhibiting electron delocalization has been restricted to comparatively simple systems comprising one or two itinerant electrons/holes delocalized over a small number (two, three, or four) of exchange-coupled metal sites (see ref. 2 and references therein). At the same time at least two classes of higher nuclearity MV systems are of current interest in molecular magnetism, namely, large MV clusters and MV chains. Important representatives of the first class are the polynuclear iron–sulfur clusters[6] which form active metal sites of iron–sulfur proteins. The other representatives of this class are the so-called polyoxometalates.[2,7–13] These metal oxide molecular clusters have the ability to accept various specific numbers of electrons, which can be delocalized over a large number of metal sites, as well as the

*The package is available from the authors upon request by e-mail: juan.m.clemente@uv.es

Correspondence to: J. M. Clemente-Juan; e-mail: juan.m.clemente@uv.es and A. V. Palii; e-mail: Andrew.Palii@uv.es

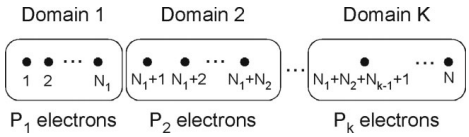

Figure 1. Scheme of the MV systems under consideration.

possibility to accommodate into these structures paramagnetic metal ions with localized magnetic moments. As a result these compounds can be viewed as model systems to study the interplay between electron transfer and exchange interactions.[11,13–19] The second class contains the MV chain compounds[20] in which we also face the problem of the interaction between localized and delocalized electrons.

In this article we present a powerful and efficient computational approach to solve the double exchange problem for high-nuclearity MV clusters containing arbitrary number of localized spins and itinerant electrons. The isotropic magnetic exchange between the localized spins is also included in the computation procedure that is aimed at the evaluation of the eigenvalues and thermodynamic properties of complex MV systems. This approach is based on the use of the theory of the angular momenta and irreducible tensor operator technique.

The program package we present here is a new contribution to solve the problem of systems with spin delocalization. It is a further development of our previous package (MAGPACK)[21] which only allows the evaluation of properties of large exchange coupled clusters comprising localized spins. These two complementary packages are assumed to provide an efficient computational tool for the modeling of the majority of systems of interest in molecular magnetism.

In the following sections we will present both the theoretical background in a concise manner and the FORTRAN program called MVPACK. In the last section some examples are worked out in order to demonstrate the abilities of the program.

Theoretical Background

A general approach to the problem of double exchange in high nuclearity clusters containing a large number of localized spins and itinerant electrons has been worked out in a previous article.[22] Here we present a brief survey of these results adapted to the general case of magnetic MV compounds. The system under the study consists of N metal sites and arbitrary number P of delocalized electrons as schematically shown in Figure 1. For the sake of simplicity we will consider the case of a strong one-site Coulomb repulsion, so that the configurations with two (or more) electrons on the same site are excluded. In this sense we imply the restriction $P < N$ that can be removed in the framework of the developed procedure provided that a more sophisticated consideration is required. We assume also that under certain reasonable physical conditions the whole system can be divided into K mixed-valence domains each one containing N_r ($r = 1, 2, \ldots K$) metal sites ($N_1 + N_2 + \cdots + N_K = N$). Each domain contains arbitrary number P_r of delocalized electrons ($P_1 + P_2 + \cdots + P_K = P$), so that the domains are represented by the MV clusters of the type of $P_r d^{n_r+1} + (N_r - P_r)\, d^{n_r}$ containing P_r ions in d^{n_r+1} configuration and $[N_r - P_r]$ ions in the d^{n_r} configuration. The electron transfer processes without excitation of the system are assumed to be possible only within each delocalized domain. On the contrary, the interdomain electron hopping is assumed to lead to a strong enhance in the energy (second-order effect). Such second-order electron transfer gives rise to the kinetic exchange coupling between the ions belonging to different domains.

An interesting and physically important situation occurs when one or several P_r vanish. If $P_r = 0$ we are dealing with a domain possessing ions with the definite numbers of the electrons in the unfilled shells (fixed valences). These domains are not involved in the electron transfer processes so we will refer them to as localized domains. In general, the localized domains can be heteronuclear, that is, they can contain different ions (spins). The systems containing both localized and delocalized domains can be termed as mixed valence systems with partial electron delocalization (examples of such kinds of systems are the polyoxovanadates clusters[14–16]).

This general scheme of MV system and the meaning of the notations can be illustrated by considering the particular case shown in Figure 2 for an instant distribution of the extra electrons over the metal sites. This systems comprises twelve sites ($N = 12$) and four itinerant electrons ($P = 4$). We assume that the structure of this cluster is such that it can be divided into three ($K = 3$) domains. The three sites ($N_1 = 3$) with the numbers 1, 2, and 3 (domain 1) are occupied by the localized spins so that the number of the delocalized electrons for this domain is zero ($P_1 = 0$). The domain 2 contains one extra electron ($P_2 = 1$) delocalized over four sites ($N_2 = 4$). Finally, in domain 3 three electrons ($P_3 = 3$) are delocalized over five ($N_3 = 5$) sites.

For the sake of definiteness we describe the case when $n_r + 1 \leq 5$, that is, all metal sites (with and without extra electrons) possess less than half-filled d-shells. An active orbital space of each metal (let say, for that with the number f) contains $n_r + 1$ orbitals, with n_r of these orbitals being singly occupied forming the high-spin Hund state with $s_0^r = n_r/2$. Conventionally, these d^{n_r} ions will be referred to as spin cores. The remaining (highest in energy) orbital is singly occupied when the site f contains the

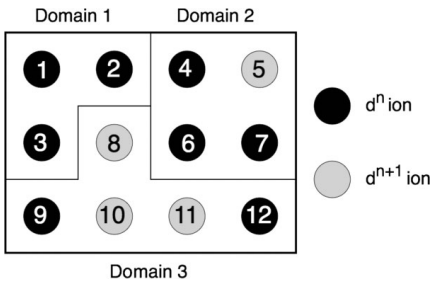

Figure 2. Illustrative example of complex MV system comprising of three domains.

d^{n_r+1} ion, or empty if the position f is occupied by the d^{n_r} ion. The d^{n_r+1} ions are also assumed to be the high-spin ones, so the spins of the constituent ions in the r-th delocalized domain will be either $s_f = s_0^r$ for $d_f^{n_r}$ ion or $s_f = s_0^r + 1/2$ for $d_f^{n_r+1}$ ion. Both kinds of ions (d^{n_r} and d^{n_r+1}) are supposed to possess orbitally nondegenerate ground terms that means that the low-symmetry crystal field completely removes the orbital degeneracy in both d^{n_r} and d^{n_r+1} ions and the energy gaps between the ground and excited states are much bigger when compared with the values of the electron transfer integrals. We consider a common case assuming that the domains can be physically different (different ions, local crystal fields, etc.). In our notations the number n of the core's electrons are allowed to depend on the symbol r and hence the core's spin can be different for different domains. There are $N_r!/[P_r!(N_r - P_r)!]$ possibilities to distribute P_r extra electrons among N_r sites in the r-th domain. Then the total number of the electronic distributions in the whole cluster is calculated as follows:

$$\prod_{r=1}^{K} N_r![P_r!(N_r - P_r)!]^{-1} \tag{1}$$

It is convenient to number the extra electrons in the whole system from 1 to P and then to indicate the sites, which can be occupied by the electron with a given number. For example, each electron with the number $1 \le v \le P_1$ can occupy the positions 1, 2, ... N_1 (first delocalized domains), meanwhile the remaining positions for such electron are forbidden. Of course, such assignment has a formal character and introduced here in order to facilitate the process of generating the allowed electronic distributions in the system. It is convenient to firstly generate all $N!/[P!\ (N - P)!]$ electronic distributions and then to exclude the forbidden distributions with the aid of the above introduced correspondence between the electron's number and the allowed sites for this number. In this way we arrive at the number of the electronic distributions given by eq. (1).

Each electronic distribution D defines the set of the spins of the constituent metal ions $(s_1, s_2, \ldots, s_N)$. We use the $\{D(\tilde{S})SM_S\}$-representation for the wave-functions in which the spins of the individual ions (for a given D) are coupled in a successive way to give the total spin S of the cluster; $(\tilde{S}) \equiv \{\tilde{S}_2, \tilde{S}_3, \ldots, \tilde{S}_{N-1}\}$ are the possible sets of the intermediate spins ($\tilde{S}_2 \equiv \tilde{S}_{12}$, $\tilde{S}_3 \equiv \tilde{S}_{123}$, etc.), finally M_S is the total spin projection. Note that the intermediate spins and total spin depend not only on the local spins within the delocalized domains but also on the set of local spins belonging to the localized domain.

The electron hopping from the site i to the site k is described by the following double exchange Hamiltonian:

$$H_{tr}(i \to k) = t_{ik} \sum_{\sigma} c_{k\sigma}^{+} c_{i\sigma}, \tag{2}$$

where the operator $c_{k\sigma}^{+}(c_{i\sigma})$ creates (annihilates) an electron on the site $k(i)$ with the spin projection σ, and t_{ik} is the transfer integral. Such Hamiltonian connects the states belonging to different electronic distributions. Provided that the sites i and k belong to the r-th delocalized domain, the matrix element of the operator H_{tr} $(i \to k)$ is calculated as follows:

$$\begin{aligned}
&\left\langle \left(s'_\beta = s_\beta, \beta \ne i,k\right)\left(s'_i = s_0^r, s'_k = s_0^r + \frac{1}{2}\right)\right. \\
&\times \left.(\tilde{S}')S'M'_s|H_{tr}(i \to k)|\left(s_\beta, \beta \ne i,k\right)\left(s_i = s_0^r + \frac{1}{2}, s'_k = s_0^r\right)(\tilde{S})SM_S\right\rangle \\
&\quad = (-1)^{2s'_0} t_{ik}\delta_{SS'}\delta_{M_sM'_s} Z_{i\to k}\left[\left(s'_\beta = s_\beta, \beta \ne i,k\right)\right. \\
&\quad \times \left.\left(s_i = s_0^r + \frac{1}{2}, s'_i = s_0^r, s_k = s_0^r, s'_k = s_0^r + \frac{1}{2}\right)(\tilde{S})(\tilde{S}')S\right], \quad (3)
\end{aligned}$$

where $Z_{i\to k}[\cdots]$ is the function of local spins s_i, s_k, and s'_i s'_k for the initial and final electronic distributions, the corresponding sets of intermediate spins $(\tilde{S})$ and $(\tilde{S}')$, and total spin S. Providing $i < k$ the function $Z_{i\to k}[\cdots]$ is given by:

$$\begin{aligned}
&Z_{i\to k}^{(i<k)}\left[(s'_\beta = s_\beta, \beta \ne i,k)(s_i, s'_i, s_k, s'_k)(\tilde{S})(\tilde{S}')S\right] \\
&\quad = (-1)^{1+(1/2)(k-i)+2(s_i+s_k)+s'_i+s'_k-\tilde{S}_{i-1}-\tilde{S}_i-\tilde{S}'_{k-1}-\tilde{S}_k} \\
&\quad \times \sqrt{(2s_i+1)(2s'_k+1)(2\tilde{S}'_i+1)(2\tilde{S}'_{k-1}+1)} \\
&\quad \times \delta_{\tilde{S}_2\tilde{S}'_2}\delta_{\tilde{S}_3\tilde{S}'_3}\cdots\delta_{\tilde{S}_{i-1}\tilde{S}'_{i-1}}\delta_{\tilde{S}_k\tilde{S}'_k}\delta_{\tilde{S}_{k+1}\tilde{S}'_{k+1}}\cdots\delta_{\tilde{S}_{N-1}\tilde{S}'_{N-1}} \\
&\quad \times \begin{Bmatrix} s'_i & 1/2 & s_i \\ \tilde{S}_i & \tilde{S}_{i-1} & \tilde{S}'_i \end{Bmatrix}\begin{Bmatrix} s_k & 1/2 & s'_k \\ \tilde{S}'_{k-1} & \tilde{S}_k & \tilde{S}_{k-1} \end{Bmatrix} \\
&\quad \times \prod_{f=1}^{k-i-1}(-1)^{-s_{i+f}+\tilde{S}'_{i+f}+\tilde{S}_{i+f-1}} \\
&\quad \times \sqrt{(2\tilde{S}_{i+f-1}+1)(2\tilde{S}'_{i+f}+1)}\begin{Bmatrix} \tilde{S}'_{i+f-1} & 1/2 & \tilde{S}_{i+f-1} \\ \tilde{S}_{i+f} & s_{i+f} & \tilde{S}'_{i+f} \end{Bmatrix}. \quad (4)
\end{aligned}$$

Expressions, eqs. (3) and (4), represent the generalization of the results obtained in ref. 22 to a more common case of systems exhibiting partial delocalization and containing several delocalized domains. In contrast to the early theories of the double exchange these formulas contain the products of 6*j*-symbols only and does not include higher order *nj*-symbols and also Clebsch-Gordan coefficients (from a general symmetry concept the latter should not appear in the physical values in a properly designed theory that involves isotropic interactions only). This advantage reduces essentially the time required for the evaluation and therefore allows to efficiently treat high nuclearity systems. The values $\tilde{S}_0, \tilde{S}'_0, \tilde{S}_1, \tilde{S}'_1, \tilde{S}_N$ and $\tilde{S}'_N$ in eqs. (3) and (4) require additional definitions. More detailed considerations show that one should use the following rules: $\tilde{S}_0 = S'_0 = 0$, $\tilde{S}_1 = s_1$, $\tilde{S}'_1 = s'_1$, $\tilde{S}_N = S$, $S'_N = S'$. Besides, in the particular case when $k = i + 1$ the product in eq. (4) should be substituted by 1.

Although eq. (3) relates to the case of less than half-filled *d*-shells, it can be also used for the case of more than half-filled *d*-shells because the matrices of the double exchange for the "complementary" systems $P_r d^{9-n_r} + (N_r - P_r)d^{10-n_r}$ and $P_r d^{n_r+1} + (N_r - P_r)d^{n_r}$ differ only in its sign.[22]

Along with the double exchange, one should take into account the Heisenberg—Dirac—Van Vleck (HDVV) exchange interaction. This interaction can couple both the spins located in the same domain and those belonging to different domains. As a

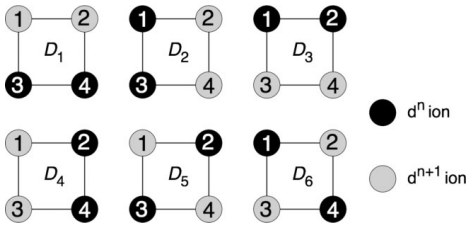

Figure 3. Electronic distributions for a square planar $2d^{n+1}-2d^n$ cluster.

matter of fact, the HDVV exchange acts within each localization (electronic distribution) and therefore does not connect the states belonging to different distributions. For this reason the exchange Hamiltonian, i.e., local spins and exchange parameters, should be defined for each electronic distribution. For a certain electonic distribution D the Hamiltonian is given by:

$$H_{ex}(D) = -2\sum_{i=1}^{N-1}\sum_{j=i+1}^{N} J_{ij}(D)s_i s_j, \tag{5}$$

where J_{ij} (D) are the exchange integrals, which are dependent on the electronic distribution. The dependence of the exchange parameters on the distribution D can be illustrated by considering a square planar $2d^{n+1} - 2d^n$ cluster (two itinerant electrons per four sites) for which six electronic distributions are possible as shown in Figure 3 from which one can see also the values of the local spins. One can see that depending on the electronic distribution the exchange integral J_{12} can take three different values related to the following three physically different kinds of interaction: $d^{n+1}-d^{n+1}$ (distribution D_1), d^n-d^n (distribution D_3), and $d^{n+1}-d^n$ (distributions D_2, D_4, D_5, D_6). The remaining exchange integrals can be classified similarly.

The matrix element of $H_{ex}(D)$ can be calculated with the aid of irreducible tensor operator technique.[23–25] Using the same basis as in eq. (3) we obtain:

$$\begin{aligned}\langle (s_f)(\tilde{S}')S'M'_s|H_{ex}(D)|(s_f)(\tilde{S})SM_s\rangle &= \delta_{ss'}\delta_{M_sM'_s}(2S+1)^{-1/2}\sum_{k_1k_2\ldots k_N}\left\langle s_N\middle\|s^N_{k_N}\middle\|s_N\right\rangle \\ &\times \sum_{\tilde{k}_2\tilde{k}_3\ldots\tilde{k}_{N-1}} G[k_1k_2(\tilde{k}_2)k_3(\tilde{k}_3)\ldots k_{N-1}(\tilde{k}_{N-1})k_N] \\ &\times \prod_{i=1}^{N-1}\sqrt{(2\tilde{k}_{i+1}+1)\,(2\tilde{S}_{i+1}+1)(2\tilde{S}'_{i+1}+1)} \\ &\times \begin{Bmatrix} \tilde{k}_i & k_{i+1} & \tilde{k}_{i+1} \\ \tilde{S}'_i & s_{i+1} & \tilde{S}'_{i+1} \\ \tilde{S}_i & s_{i+1} & \tilde{S}_{i+1}\end{Bmatrix}\left\langle s_i\middle\|s^f_{k_i}\middle\|s_i\right\rangle,\end{aligned} \tag{6}$$

where the set (s_f) of the local spins corresponds to the electronic distribution D. The values $\tilde{k}_2, \tilde{k}_3, \ldots$ obey the same addition rules as the spin quantum numbers, that is, $|k_1 - k_2| \le \tilde{k}_2 \le k_1 + k_2$, $|\tilde{k}_2 - k_3| \le \tilde{k}_3 \le \tilde{k}_2 + k_3, \ldots |\tilde{k}_{N-1} - k_N| \le k \le \tilde{k}_{N-1} + k_N$. Only the following coefficients $G[\cdots]$ are nonvanishing:

$$G[k_i = k_j = 1 (i \neq j), k_f = 0\ (f \neq i,j), k = 0] = 2\sqrt{3}J_{ij}. \tag{7}$$

The condition $k = 0$ has appeared in eq. (7) because only isotropic exchange interaction is considered. In eq. (6) the rules $\tilde{S}_1 = \tilde{S}'_1 \equiv s_1$, $\tilde{S}_N = \tilde{S}'_N \equiv S, \tilde{k}_1 \equiv k_1$ and $\tilde{k}_N = k$ are assumed to be fulfilled. Only the one-center reduced matrix elements with $k_f = 0, 1$ are present in eq. (6), they are given by:

$$\left\langle s_f\middle\|s^f_0\middle\|s_f\right\rangle = \sqrt{2s_f+1},\ \left\langle s_f\middle\|s^f_1\middle\|s_f\right\rangle = \sqrt{s_f(s_f+1)(2s_f+1)}. \tag{8}$$

Equations (3), (4), and (6)–(8) form a set of equations providing a theoretical background for the design of the computer program that is able to calculate the energy pattern of complex MV systems.

Along with the HDVV exchange and the electron transfer the Coulomb intercenter repulsion should also be included in the Hamiltonian. This contribution, that is in general strong, arises from the fact that different electronic distributions possess, in general, different intercenter interelectronic Coulomb repulsion energies. Thus turning back to the case of square planar system shown in Figure 3 one can see that the Coulomb repulsion between the extra electrons located at the nearest sites (edge of the square) is stronger than that in the case when they are located on the remote sites (diagonal of the square). Therefore, there are two different Coulomb energies $U(D_1) = U(D_2) = U(D_3) = U(D_4) \equiv U_e$ and $U(D_5) = U(D_6) \equiv U_d$ with $U_e > U_d$.

Finally, an additional contribution into the Hamiltonian appears if the metal sites belonging to the delocalized domains are nonequivalent, for example, because of difference in the local crystal fields. Then the sum of the orbital energies of the extra electrons becomes dependent on the electronic distribution D. The full orbital energy of the system corresponding to a cer-

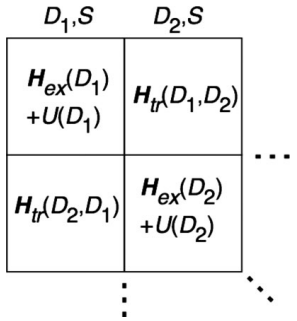

Figure 4. Scheme of the structure of the matrix of the Hamiltonian $H_{tr} + H_{ex}$ (D_1 and D_2 are different in the position of one electron).

tain distribution D can be simply added to the intercenter Coulomb energy for this distribution to get an effective parameter $U(D)$, which includes both contributions.

The structure of the matrix of the Hamiltonian that includes the electron transfer, HDVV exchange and an effective Coulomb repulsion is schematically shown in Figure 4. The exchange interaction and Coulomb terms form the diagonal blocks with respect to the basis functions belonging to the definite electronic distributions, meanwhile the electron transfer gives rise to the off-diagonal blocks connecting the electronic distributions, which are different in the position of one extra electron. As far as the full Hamiltonian is isotropic it is also diagonal with respect to the value of the total spin S that allows to additionally reduce the sizes of the matrices to be diagonalized as shown in Figure 4.

Once we have the energy levels, we can evaluate different thermodynamic properties of the system as magnetization, magnetic susceptibility, and magnetic specific heat. Because anisotropic interactions are not included, the magnetic properties of the MV system do not depend on the direction of the magnetic field. For this reason one can consider the magnetic field directed along arbitrary axis Z of the molecular coordinate frame that is chosen as a spin quantization axis. In this case the energies of the system will be $E_\mu(S) + g_e\ \beta\ M_S\ H_Z$, where $E_\mu(S)$ are the eigenvalues of the Hamiltonian containing magnetic exchange and double exchange contributions (index μ runs over the energy levels with given total spin S). Then the partition function in the presence of the external magnetic field is given by:

$$Z(H_z) = \sum_{S\mu} \exp\left[\frac{-E_\mu(S)}{(kT)}\right] \sum_{M_s} \exp\left[\frac{-g_e \beta M_s H_z}{(kT)}\right]. \qquad (9)$$

Using this expression one can evaluate the magnetic susceptibility, magnetization, and specific heat with the aid of the standard thermodynamical definitions.

Organization of the Program

The MVPACK, a package to calculate energy levels and magnetic properties of high nuclearity mixed valence clusters, is based on the theory so far presented. This program generates all possible distributions of P extra electrons over N_d spin cores with the subsequent exclusion of the forbidden distributions as described in Section 2. Then, for each allowed distribution D all intermediate spins and the total spin are calculated with the aid of the successive spin-coupling scheme. The generated basis is used for the evaluation of the matrix of the full Hamiltonian including the one-electron transfer (double exchange) and isotropic exchange interactions, and to diagonalize this matrix. In the final step the energy levels are used to evaluate the thermodynamic properties of the polynuclear MV clusters.

In order to give to the program the parameters involved in the model of spin system (nuclearity, division into subsystems, transfer and exchange parameters, etc.) and in the evaluation of the properties the program uses two FORTRAN INCLUDE files. After execution, the program generates different output files containing all the information concerning the initialization, evaluation, and simulation processes.

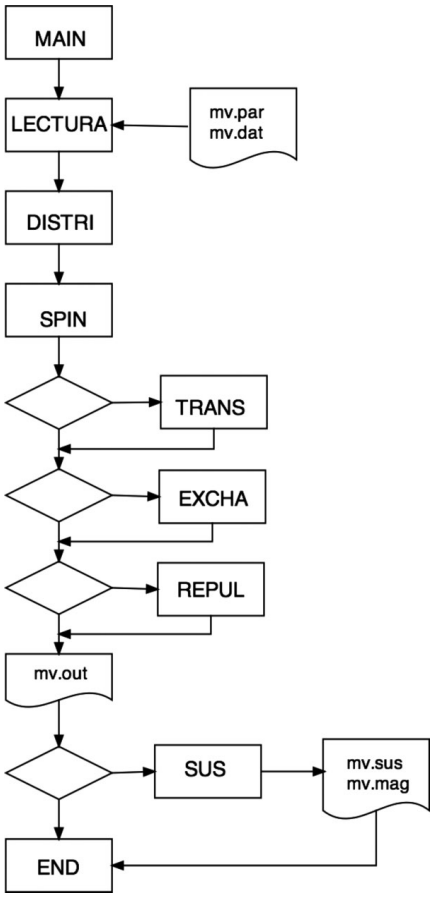

Figure 5. General organization of the MVPACK package showing the different programs.

The program is entirely written in Standard portable FORTRAN77. Figure 5 shows a schematic chart for the whole program. Here, the main program first call the subroutines to evaluate the electronic distributions and spin functions, and then evaluate energy matrices and diagonalize them and finally the subroutines to calculate properties.

The LECTURA subroutine reads the INCLUDE files and verifies their information; it reorganizes this information and initialize a large common block areas containing the data handed to run a calculation. An output file is created (MV.OUT) con-

taining all the information obtained from INCLUDE files concerning definition of the system, the errors, and warnings generated at the different steps of the initialization process.

After this initialization process, the program enters in DISTRI and SPIN, where it first calculates the electronic distributions and second finds the spin functions for each distribution. The energy matrix elements are calculated by a successive addition of the different interaction contributions. Each contribution is associated to an independent subroutine: TRANS is for the electron transfer interactions, EXCHA is for the isotropic exchange interactions, and REPUL is for Coulomb repulsion or to introduce the difference in the one-site energies that appears because the different symmetry of each metal center. The TRANS subroutine uses the general expression, eq. (4), to evaluate the energy matrix elements, and for the case of EXCHA subroutine the eq. (6). To evaluate the mathematical functions involved in this expression (Clebsch-Gordan coefficients, 6*j* and 9*j* symbols, etc.), different EXTERNAL FUNCTIONs have been defined. Finally, to obtain the eigenvalues, the energy matrix is diagonalized by a standard subroutine DSPEV of the LAPACK Mathematical Library.[26]

To evaluate the properties of the spin cluster, the different subroutines associated to these properties are called from SPIN. These subroutines are SUS and MAG. They calculate magnetic susceptibility and heat capacity, and magnetization, respectively. The program returns from SUS and MAG different output files (MV.SUS and MV.MAG) containing the evaluated properties in a column text type format that allows an easy plot for graphic package.

Application of the Program

Example 1. Hexanuclear Octahedral MV Clusters $[P]d^5-[6-P]d^4$ *(P = 1, 2, 3, 4, 5)*

The structure of these clusters is shown in Figure 6. Neglecting the interactions between the remote centers (diagonal of octahedron) one can describe the double exchange in these clusters by a single transfer integral *t*. We also assume that the magnetic exchange can be described by a single parameter *J*, neglecting thus the differences between d^4-d^4, d^5-d^5, and d^4-d^5 interactions. In this case the exchange between any two metal ions occupying positions *i* and *j* is described by the Hamiltonian $H_{ex} = -2J\ s_i\ s_j$, where the spins s_i and s_j are dependent on *D*. For the simplest case of the d^5-5d^4 cluster the network of the exchange and transfer parameters are shown in Figure 6 in which one possible localization of the extra electron (on the site 1) is presented.

Figure 7 shows the energy patterns of the double exchange splittings calculated for $[P]d^5-[6-P]d^4$ clusters providing $J = 0$ and $U = 0$. One can see that all energy patterns are dependent on the sign of the transfer parameter, and on the number of itinerant electrons. For example, the ground state of cluster with one delocalized electron ($P = 1$) is highly degenerate with respect to *S* and comprises all *S* values from 1/2 to 25/2 providing $t > 0$, meanwhile for $t < 0$ it is ferromagnetic ($S_{gr} = 25/2$). On the contrary in cluster with $P = 2$ the ground state is ferromagnetic for $t > 0$ and quasidegenerate (with weak antiferromagnetic splitting) for $t < 0$. The energy pattern of the cluster

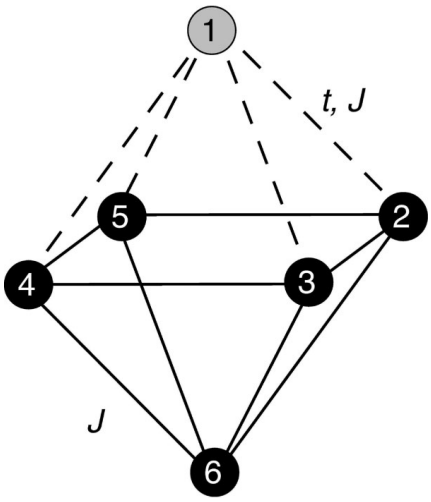

Figure 6. The network of the exchange and transfer integrals for the d^5-5d^4 cluster.

with $P = 3$ is quasisymmetric with respect to the change of the sign of the transfer parameter. In this case irrespectively of the sign of *t* the double exchange produces weak ferromagnetic effect. Finally, the energy patterns of the clusters with $P = 4$ and $P = 5$ calculated with $t > 0$ ($t < 0$) prove to be similar to those obtained for clusters with $P = 2$ and $P = 1$ providing $t < 0$ ($t > 0$). One can see that these clusters are quite different from the MV dimmers in which the double exchange always stabilizes the ferromagnetic ground state.[4] On the other hand these systems are similar to triangular MV trimmers,[27–29] tetrahedral MV tetramers,[30–32] and hexanuclear octahedral d^2-5d^1 clusters[33] exhibiting transfer frustration that seems to be a common feature of all MV clusters with symmetric triangular faces (for a more detailed discussion see ref. 2). It is to be noted that the energy patterns of the $Pd^5-(6-P)d^6$ clusters for $t > 0$ ($t < 0$) are exactly the same as the energy patterns of the $Pd^5-(6-P)d^4$ clusters providing $t < 0$ ($t > 0$). This means that the obtained results can be applied to the discussion of the magnetic behavior of the series of iron–sulfur superclusters $[Fe_6S_6]^{n+}$.[34–37]

The effect of the magnetic exchange for the octahedral d^5-5d^4 cluster is illustrated by Figure 8, where the temperature dependences of the magnetic susceptibilities (in the form χT vs. *T*) calculated with different sets of *t* and *J* are shown. One can see (Fig. 8a) that in the case of $t < 0$ and $J > 0$ the ground state is ferromagnetic independently of the magnitude of *J*. For this reason for two upper curves in Figure 8a the low temperature limit $\chi T|_{T\to 0} = 84.375$ emu.K/mol that corresponds to $S_{gr} = 25/2$. On the contrary providing $t < 0$ and $J < 0$ the interplay between antiferromagnetic exchange and double exchange can stabilize different spin states. For example the state with $S_{gr} =$

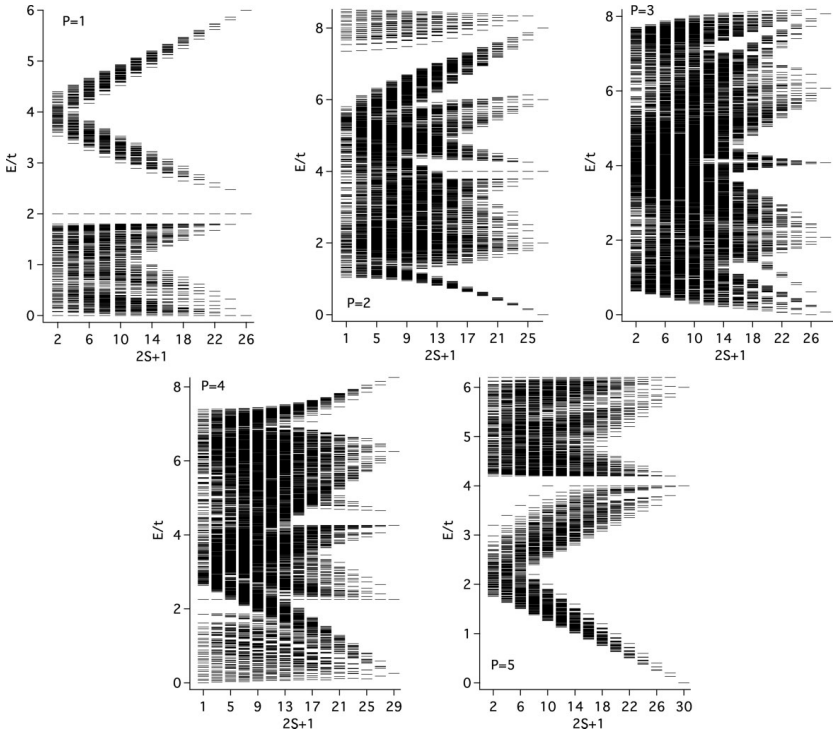

Figure 7. Energy patterns of the double exchange splittings for the octahedral $Pd^5-(6-P)d^4$ clusters.

17/2 proves to be the ground state ($\chi T/_{T\to 0}$ = 40.375 emu·K/mol) for $J = -0.01$ |*t*| (Fig. 8a, lower curve). The larger is |*J*| the lower is the spin of the ground state. Finally, when the antiferromagnetic exchange is much stronger than the double exchange the ground state proves to be antiferromagnetic. Quite different situation occurs if $t > 0$. In this case the ground state

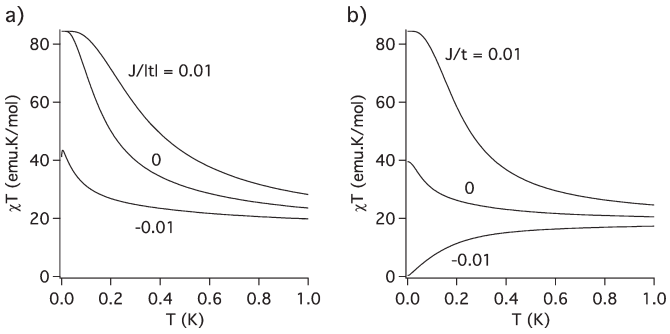

Figure 8. Effect of HDVV exchange on the χT vs. T curves for the octahedral d^5-5d^4 cluster: (a) $t <$ 0, (b) $t > 0$.

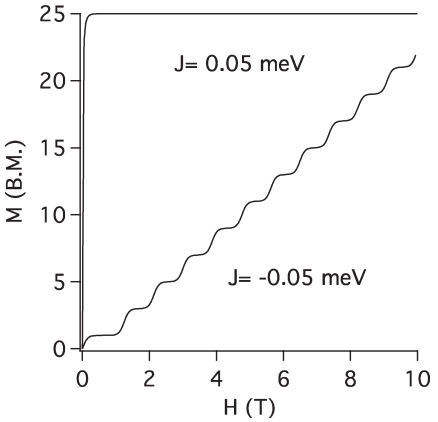

Figure 9. The low-temperature ($T = 0.1$ K) magnetization for the octahedral d^5-5d^4 cluster calculated for the case of strong positive double exchange ($t \gg |J|$).

at $J = 0$ represents the paramagnetic mixture of different spin states. Providing $t > 0$ and $J \neq 0$ the ground state can be either ferro- or antiferromagnetic depending of the sign of the exchange parameter. Thus, $\chi T_{T\to 0} = 84.375$ emu·K/mol for $J > 0$ ($S_{gr} = 25/2$), and $\chi T_{T\to 0} \approx 0.37$ emu·K/mol for $J < 0$ ($S_{gr} = 1/2$). No ground state with intermediate value of S is possible in this case.

The effect of weak exchange interaction for the octahedral d^5-5d^4 cluster in the case of positive t is also evidenced by the curves showing the dependence of the magnetization on the applied magnetic field H (see Fig. 9). At low temperature the magnetization versus field curve for antiferromagnetic exchange ($J < 0$) shows several steps, which correspond to the change of the quantum number M_S of the ground state when H is increasing. Providing ferromagnetic exchange ($J > 0$) the magnetization is described by a Brillouin function and reach a saturation value of about 25 μ_B that corresponds to the ground state with the maximum spin value $S = 25/2$.

The combined effect of positive double exchange ($t > 0$) and interelectronic Coulomb repulsion on the energy pattern of the $2d^5-4d^4$ cluster containing two itinerant electrons is shown in Figure 10. In this case the two kinds of dispositions of the electronic pair corresponding to the two distances in the octahedron are different in the Coulomb repulsion energy U (Fig. 10a). This gives rise to the electron trapping effect. In fact two electrons tend to be as separated as possible in order to minimize the Coulomb repulsion energy, meanwhile the electron transfer leads to the increase of this energy. As a result the ferromagnetic effect caused by the double exchange is strongly suppressed (compare Fig. 7 for $P = 2$ and Fig. 10b).

Another possibility of the program is to calculate the magnetic specific heat. Figure 11 shows the magnetic heat capacity curves calculated for a series of $Pd^5-(6-P)d^4$ clusters providing $t > 0$ and $J = U = 0$. For $P = 1, 2, 5$ the C_p vs. kT/t curve presents a single round maximum, which is shifted to the higher

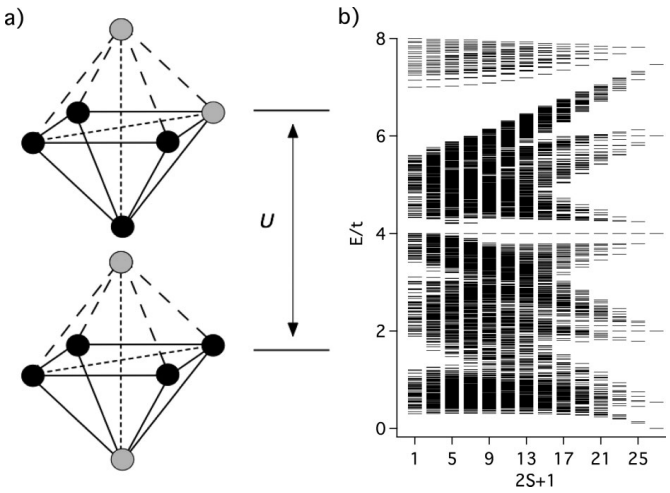

Figure 10. Effect of Coulomb repulsion on the energy pattern of the octahedral $2d^5-4d^4$ cluster: (a) two kinds of dispositions of the electronic pair in a O_h cluster with two moving electrons; (b) Energy pattern of the square-planar $2d^5-4d^4$ cluster calculated with $U = 2t > 0$.

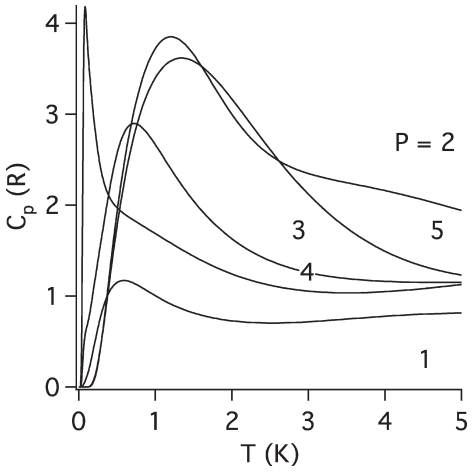

Figure 11. Magnetic specific heat for the octahedral $Pd^5-(6-P)d^4$ clusters calculated with $t > 0$, $J = 0$, and $U = 0$.

temperature region with the increase of t. For $P = 4$ the curve possesses the sharp low-temperature maximum, which appears because of the proximity of the ground level with $S = 0$ and first excited level with $S = 1$. Finally, for $P = 3$ the curve presents a round maximum at $kT \approx 0.058t$ and sharp maximum at $kT \approx 0.007t$.

Example 2. Reduced Polyoxoanions with Keggin Structure

The Keggin anion can be described by the formula $[XM_{12}O_{40}]^{n-}$, where M = Mo or W, and X = B^{III}, Si^{IV}, P^{V}, Co^{2+}, Co^{3+}, Fe^{3+}, Cu^{2+}, etc.[38] For the α-isomer, its structure consists of four edge-sharing triads of MO_6 octahedra arranged around the heteroatom X, by sharing corners in such a way that the resulting cluster has a tetrahedral symmetry (see Fig. 12).

An important property of the anion with the Keggin structure is that it can be reversibly reduced by addition of various specific numbers of electrons, which are delocalized over the 12 metal sites. Experimentally, it has been found that when a heteropoly complex contains a pair of delocalized electrons, their spins are always completely paired, even at room temperature. This result was initially attributed to a very strong antiferromagnetic coupling via a multiroute superexchange mechanism,[39] but more recently it was suggested[17–19] that the electron delocalization can stabilize the diamagnetic ground state and it was proved[18,19,40,41] (see also review[2]) that a combination of Coulomb repulsion between the electrons and electron delocalization is an efficient mechanism of a spin pairing in the ground state. The cited works[18,19,40,41] dealt with the case of 2e-reduced polyoxoanion containing delocalized electronic pair. Here we present the calculations of the energy patterns for a series of polyoxoanions with Keggin structure containing different even numbers $P = 2, 4, 6, 8, 10, 12$ of itinerant electrons. In these calculations we use the set of parameters obtained from the *ab initio* study of the double reduced polyoxoanion with delocalized electronic pair.[40,41] The set of parameters includes the three one-electron transfer integrals $t = -530$ meV, $t' = -522$ meV, $t^d = -154$ meV, two exchange integrals $J = -75$ meV, $J' = -95$ meV and five intercenter Coulomb repulsion integrals $U = 2535$ meV, $U' = 2600$ meV, $U^d = 1745$ meV, $V = 300$ meV, and $V' = 65$ meV. These parameters are associated with the different metal–metal distances within the Keggin structure as schematized in Figure 13, in which only the Coulomb repulsion parameters are shown.

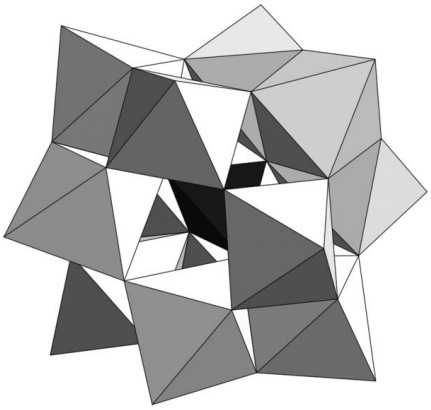

Figure 12. Schematic structure of a Keggin anion.

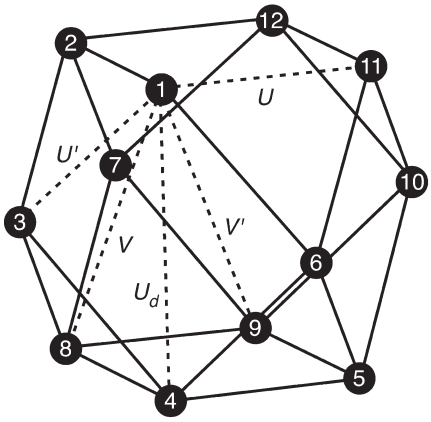

Figure 13. Nonvanishing Coulomb repulsion parameters for the Keggin structure.

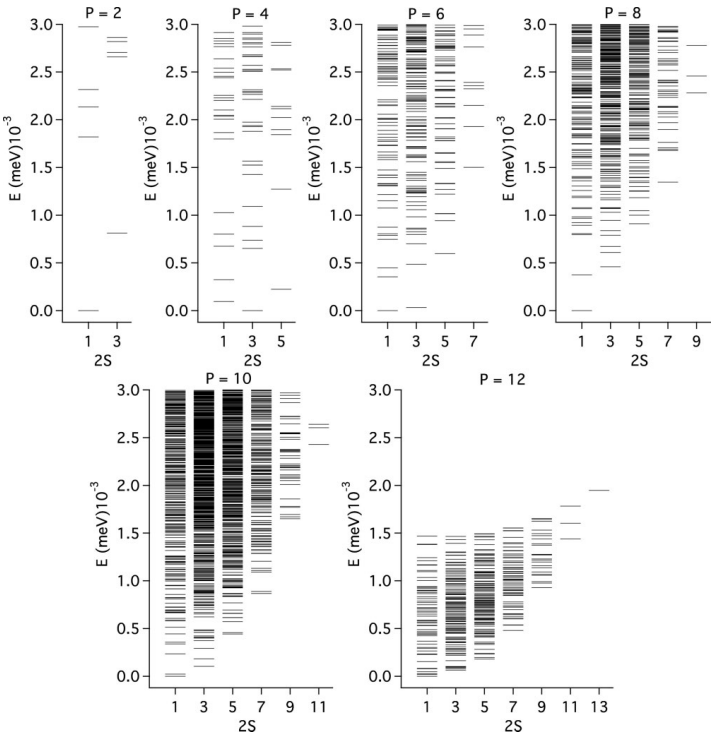

Figure 14. Energy schemes for the reduced Keggin polyoxoanions with different even numbers of delocalized electrons.

The energy patterns calculated with MVPACK are shown in Figure 14. One can see that for all even numbers P except $P = 4$ the ground state proves to be diamagnetic. This is a well known result for the 2e reduced polyoxoanion.[18,19,40,41] Present calculation shows that the spin pairing resulting in the diamagnetic ground state is rather common phenomenon in polyoxoanion species with different numbers of delocalized electrons. The case of four delocalized electrons represents an exception from this general trend because in this case the spin triplet state proves to be the ground one. At the same time the energy gaps between the ground spin-triplet and excited spin-singlet states is not too large so the conclusion about the ground spin-triplet state for the 4e-reduced polyoxoanion is probably the result of the usage of the set of parameters obtained from the *ab initio* study of 2e-reduced polyoxoanion. To date no experimental data are available for the 4e-reduced polyoxoanion so the question about the spin of the ground state of this system remains open.

Concluding Remarks

In this article we have presented a package that allows to calculate the energy levels and the magnetic properties of MV systems of high nuclearity. The model employed in the program includes electron transfer processes and isotropic magnetic exchange and Zeeman interactions. Within this model we have used closed form expressions for the matrix elements of the full Hamiltonian containing only products of 6j-symbols (double exchange part) and 9j-symbols (exchange part) that are generated in the program. It is important that these expressions contain neither high-order recoupling coefficients nor 3j-symbols. The elaborated representative examples illustrate the efficiency of the program. Although the model of a MV system is rather general we have not taken into account anisotropic interactions, like antisymmetric exchange and zero-field splitting, as well as the anisotropy of g-tensors. The theoretical background so far used and the program already designed provide possibility of

extension with due account of these factors that could be important for applications.

This program can be used not only for MV systems formed by transition metal ions but also for MV organic compounds as graphenes, fullerenes or conjugated polymers which provide also magnetic spin systems because of the electron hopping.

For the future extension of the package, we are working to make tractable other properties of interest for MV clusters such as inelastic neutron scattering, electron paramagnetic resonance and Mössbauer spectra. Other important point to implement is the elaboration of a more powerful subroutine to deal with electron and spin density distributions in order to extract information about electronic correlation.

It should be also noted that the problem of mixed valency is inherently related to the vibronic pseudo Jahn-Teller interaction (see, for instance refs. 42–47). In general, the vibronic problem includes two steps, namely the evaluation of the wave-functions and eigenvalues relating to a high symmetry fixed nuclear configuration and then evaluation of the vibronic matrix with the subsequent diagonalization of the full vibronic Hamiltonian.[48,49] The MVPACK provides a solution of the first step of the vibronic problem that is it gives the electronic wave-functions (basis set) and the electronic energy pattern that can be further used for the evaluation of the adiabatic potentials and vibronic energy levels. Such kind of calculations will be considered in the future versions of MVPACK. Finally, in the proposed approach only the spin-symmetry has been employed, whereas the point symmetry of the cluster is not exploited. One can expect that the use of point symmetry for high-symmetric clusters could simplify considerably the procedure of diagonalization of large matrices of the double exchange. Efficiency of the combined spin and point symmetries has been recently demonstrated in the evaluation of the localized systems.[50] Such kind of the group-theoretical consideration of MV systems will be also included in the future versions of MVPACK.

Acknowledgments

Financial support by Spanish MICINN (CSD2007-00010-consolider-ingenio in Molecular Nanoscience, MAT2007-61584, CTQ-2008-06720 and CTQ-2005-09385), Generalitat Valenciana (PROMETEO/2008/128), and the UE STREP MolSpinQIP. AVP thanks University of Valencia for a visiting grant.

References

1. Coronado, E.; Dunbar, K. R. Inorg Chem 2009, 48, 3293–3295.
2. Borrás-Almenar, J. J.; Clemente-Juan, J. M.; Coronado, E.; Palii, A. V.; Tsukerblat, B.S. In Magnetism: Molecules to Materials, Miller J.; Drillon M., Eds.; Willey-VCH: Weinheim, 2001, 155–210.
3. Zener, C. Phys Rev 1951, 82, 403–405.
4. Anderson, P. W.; Hasegawa, H. Phys Rev 1955, 100, 675–681.
5. De Gennes, P.-G. Phys Rev 1960, 118, 141–154.
6. Blondin, G.; Girerd, J.-J. Chem Rev 1990, 90, 1359–1376.
7. Coronado, E.; Gomez-García, C. J. Comments Inorg Chem 1995, 17, 255–281.
8. Coronado, E.; Gómez-Garcìa, C. J. Chem Rev 1998, 98, 273–296.
9. Klemperer, W. G.; Wall, C. G. Chem Rev 1998, 98, 297–306.
10. Pope, M. T.; Müller, A. Polyoxometalates: From Platonic Solids to Anti-RetroViral Activity; Kluwer Academic Publishers: Dordrecht, The Netherlands, 1994.
11. Clemente-Juan, J. M.; Coronado, E. Coord Chem Rev 1999, 193–195, 361–394.
12. Müller, A.; Sessoli, R.; Krickemeyer, E.; Bögge, H.; Meyer, J.; Gatteschi, D.; Pardi, L.; Westphal, J.; Hovemeier, K.; Rohlfing, R.; Doring, J.; Hellweg, F.; Beugholt, C.; Schmidtmann, M. Inorg Chem 1997, 36, 5239–5250.
13. Müller, A.; Peters, F.; Pope, M. T.; Gatteschi, D. Chem Rev 1998, 98, 239–272.
14. Gatteschi, D.; Tsukerblat, B. S. Chem Phys 1996, 202, 25–37.
15. Gatteschi, D.; Tsukerblat, B. S.; Barra, A. L.; Brunel, L. C.; Müller, A.; Doring, J. Inorg Chem 1993, 32, 2114–2117.
16. Gatteschi, D.; Tsukerblat, B. S. Mol Phys 1993, 79, 121–143.
17. Borshch, S. A.; Bigot, B. Chem Phys Lett 1993, 212, 398–402.
18. Borrás-Almenar, J. J.; Clemente-Juan, J. M.; Coronado, E.; Tsukerblat, B. S. Chem Phys 1995, 195, 1–15.
19. Borrás-Almenar, J. J.; Clemente-Juan, J. M.; Coronado, E.; Tsukerblat, B. S. Chem Phys 1995, 195, 17–28.
20. Williams, J. M.; Ferraro, J. R.; Thorn, R. J.; Carlson, K. D.; Geiser, U.; Wang, H. H.; Kini, A. M.; Ehangbo, M. H. In Organic Superconductors, Synthesis, Structure, Properties, and Theory; Crimes, R. N., Ed.; Prentice-Hall Inc.: Englewood Cliffs, NJ, 1992.
21. Borrás-Almenar, J. J.; Clemente-Juan, J. M.; Coronado, E.; Tsukerblat, B. S. J Comput Chem 2001, 22, 985–991.
22. Borrás-Almenar, J. J.; Clemente-Juan, J. M.; Coronado, E.; Georges, R.; Palii, A. V.; Tsukerblat, B. S. J Chem Phys 1996, 105, 6892–6909.
23. Warshalovich, D. A.; Moskalev, A. N.; Khersonskii, V. K. Quantum Theory of Angular Momentum; World Scientific: Singapore, 1988.
24. Tsukerblat, B. S.; Belinskii, M. I. Magnetochemistry and Radiospectroscopy of Exchange Clusters; Stiintsa Publ.: Kishinev, 1983.
25. Bencini, A.; Gatteschi, D. Electron Paramagnetic Resonance of Exchange Coupled Systems, Springer-Verlag, 1990.
26. Anderson, E.; Bai, Z.; Bishof, C.; Blackford, S.; Demmel, J.; Dongarra, J.; Croz, J. D.; Greenbaum, A.; Hammarling, S.; McKenney, A.; Sorensen, D., Eds. LAPACK User's Guide; Society for Industrial and Applied Mathematics, 3rd ed., SIAM: Philadelphia, 1999.
27. Belinskii, M. I. Sov Phys Solid State 1985, 27, 1057–1067.
28. Belinskii, M. I. Mol Phys 1987, 60, 793–819.
29. Gomez-Garcia, C. J.; Coronado, E.; Pourroy, G. J Appl Phys 1990, 67, 5992–5994.
30. Borrás-Almenar, J. J.; Coronado, E.; Georges, R.; Gomez-Garcia, C. J. Chem Phys 1992, 166, 139–144.
31. Belinskii, M. I.; Tsukerblat, B. S.; Zaitsev, S. A.; Belinskaya, I. S. New J Chem 1992, 16, 791–799.
32. Palii, A. V.; Ostrovskii, S. M.; Tsukerblat, B. S. New J Chem 1992, 16, 943–952.
33. Bencini, A.; Palii, A. V.; Ostrovsky, S. M.; Tsukerblat, B. S.; Uyterhoeven, M. G. Mol Phys 1995, 86, 1085–1097.
34. Coucouvanis, D.; Kanatzidis, M. G.; Dunham, W. R.; Hagen, W. R. J Am Chem Soc 1984, 106, 7998–7999.
35. Kanatzidis, M. G.; Dunham, W. R.; Hagen, W. R.; Coucouvanis, D. J Chem Soc Chem Commun 1984, 356–358.
36. Kanatzidis, M. G.; Hagen, W. R.; Dunham, W. R.; Lester, R. K.; Coucouvanis, D. J Am Chem Soc 1985, 107, 953–961.
37. Czervinski, M.; Dabrowski, J. Mol Phys 1997, 90, 445–464.
38. Keggin, J. F. Electron Polarisation, Nature 1933, 131 908.
39. Casãn-Pastor, N.; Baker, L. C. W. J Am Chem Soc 1992, 114, 10384–10394.

40. Suaud, N.; Gaita-Ariño, A.; Clemente-Juan, J.M.; Coronado, E. Chem Eur J 2004, 10, 4041–4053.
41. Suaud, N.; Gaita-Ariño, A.; Clemente-Juan, J.M.; Sánchez-Marín, J.; Coronado, E. J Am Chem Soc 2002, 124, 15134–15140.
42. Wong, K. Y.; Schatz, P. N. Prog Inorg Chem 1981, 28, 369–449.
43. Launay, J. P.; Babonneau, F. Chem Phys 1982, 67, 295–300.
44. Borshch, S. A.; Bominaar, E. L.; Blondin, G.; Girerd, J.-J. J Am Chem Soc 1993, 115, 5155–5168.
45. Marks, A. J.; Prassides, K. New J Chem 1993, 17, 59–65.
46. Piepho, S. B. J Am Chem Soc 1988, 110, 6319–6326.
47. Borras-Almenar, J. J.; Coronado, E.; Ostrovsky, S. M.; Palii, A. V.; Tsukerblat, B. S. Chem Phys 1999, 240, 149–161.
48. Bersuker, I. B.; Polinger, V. Z. Vibronic Interactions in Molecules and Crystals; Springer-Verlag: Berlin, 1989.
49. Bersuker, I. B. The Jahn-Teller Effect; Cambridge University Press: Cambridge, 2006.
50. Schnalle, R.; Schnack, J. Phys Rev 2009, B79, 104419.

2

Single Ion Magnets based on Polyoxometalates

"Nature knows no pause in progress and development, and attaches her curse on all inaction."
-Johann Wolfgang von Goethe.

1. State of the Art. Previous Work.

1.1. Early studies in Lanthanoid SIMs.

For many years since the discovery of the first SMM the strategy followed by chemists with the aim of increasing the blocking temperature of these nanomagnets has combined two requirements. The increase in the total spin *S*, and the increase in the axial anisotropy *D*. Eventually, it was suggested that these requirements could not be optimized simultaneously.[1] But even before this was formally proved, a novel path emerged with the discovery of the Single Ion Magnets (SIMs).

SIMs are mononuclear magnetic molecules that exhibit slow relaxation of the magnetization at low temperatures. Actually, they are the mononuclear analogues of the well-known SMMs. In these nanomagnets the splitting of the low lying magnetic levels determines their behaviour. Thus, in a lanthanoid ion, the ground state J is splitted in its M_J sublevels by the effect of a ligand field (LF) produced by its coordination sphere. If the symmetry is axial, the LF effect avoids the M_J mixing in the wavefunctions and therefore supresses the fast relaxation of the magnetization achieved by quantum tunneling.[2]

For most coordination schemes, the LF introduces anisotropic high order terms or even distortions from axiality, thus the sublevel scheme does not present the parabolic shape derived from the term DS_z^2 as do most of the transition metal based SMMs. In these cases, the anisotropy is much more complicated to visualize and can only be properly estimated considering the full symmetry of the coordination. It is also important to note that such systems the barrier can not be calculated as the difference between highest and lowest spin state as, often, it is just the energy of the first excited state.

The first example of a SIM was the terbium bis-phthalocyaninato ($TbPc_2$) double decker with coordination symmetry D_{4d} (square antiprism, see Figure 1) described by Ishikawa.[3]

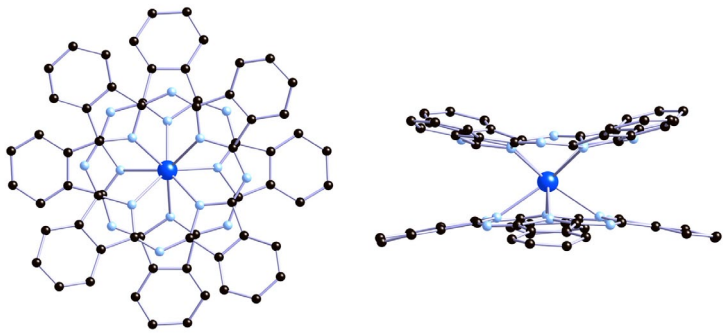

Figure 1. Structure of $Ln(Pc)_2TBA$.(Pc=Phthalocyaninate, TBA=Tetrabutylammonium) Left: Top view. Right: Side view.

1 Waldmann, O. *Inorg. Chem.* **2007**, *46*, 10035-10037.
2 Sorace, L.; Benelli, C.; Gatteschi, D. *Chem. Soc. Rev.* **2011**, *40*, 3092-3104.
3 Ishikawa, N.; Sugita, M.; Ishikawa, T.; Koshihara, S. Y.; Kaizu, Y. *J. Am. Chem. Soc.* **2003**, *125*, 8694-8695.

Its magnetic characterization was based the same procedure that the used in SMMs i.e. dynamic susceptibility measurements.[4] In this technique an oscillating magnetic field is applied to a nanomagnet at a particular frequency, and, while possible, the orientation of its magnetic moment changes to follow it. At low frequencies, the system has enough time to invert its spin, either by tunnelling or by overcoming the barrier, and is able to follow completely the external field. When the temperature is low enough and the frequency is high enough, the system gradually starts to be unable to follow the external dynamic field, and the oscillation of the magnetization acquires a phase compared with the oscillation of the driving field. As the temperature decreases further, or at higher frequencies, there exists a point at which the natural frequency for the relaxation of the system matches the frequency of the applied external field. In this moment a maximum peak in the out-of-phase susceptibility is achieved. Any further lowering of the temperature or an increase in the frequency leads to a decrease in both the in-phase and out-of-phase signals, and in the limit the magnetization is completely blocked and remains independent from the oscillating field. The mechanism for this spin relaxation has been studied for SMMs and it is commonly assumed to follow a classical Arrhenius law (as it needs to overcome a thermal barrier).

In the case of $TbPc_2$ the ac dynamical susceptibility measurements showed that the magnetic moment of this complex exhibits slow relaxation of the magnetization below 40K with and an effective barrier of more than 400 cm^{-1}. $TbPc_2$ has been largely studied,[5] and a large number of derivatives were prepared with the goal of increasing the blocking temperature.[6] For instance, a particular successful derivative takes advantage of the possibility to oxidize the ligand, to increase the ligand field felt by the lanthanoid ion.[7]

The contributions of Ishikawa constituted a turning point for molecular nanomagnets research. From this point, many magnetic studies appear using compounds with only one magnetic center coordinated with ligands in a pseudoaxial symmetry. Indeed, POM-lanthanoid complexes have been proposed as SIMs.[8] As in $LnPc_2$ complexes, the "sandwich" structure provides the lanthanoid ion with a D_{4d} coordination symmetry. In this first communication, the authors presented $[Er(W_5O_{18})_2]^{9-}$ (see Fig 2) and its magnetic characterization.

The magnetic measurements demonstrated that, in the case of POM the erbium derivative showed a clear SIM behaviour. This is in contrast with that observed in the $LnPc_2$ series where terbium derivative was the optimum choice. Such divergence was suposed to come from differences in the coordination nature between both compounds.

4 (a) Caneschi, A.; Gatteschi, D.; Sessoli, R.; Barra, A.-L.; Brunel, L. C.; Guillot, M. *J. Am. Chem. Soc.* **1991**, *113*, 5873–5874. (b) Novak, M. A.; Sessoli, R.; Caneschi, A.; Gatteschi, D. *J. Magn. Magn. Mater.* **1995**, *146*, 211–213.

5 (a) Gómez-Segura, J.; Díez-Pérez, I.; Ishikawa, N.; Nakano, M.; Veciana, J.; Ruiz-Molina, D. *Chem. Comm.* **2006**, 2866–2868. (b) Katoh, K.; Kajiwara, T.; Nakano, M.; Nakazawa, Y.; Wernsdorfer, W.; Ishikawa, N.; Breedlove, B.; Yamashita, M. *Chem Eur J* **2010,** *17*, 117–122.

6 (a) Ishikawa, N.; Otsuka, S.; Kaizu, Y. *Angew. Chem. Int. Ed.* **2005**, *44*, 731–733. (b) Ishikawa, N.; Sugita, M.; Wernsdorfer, W. *J. Am. Chem. Soc.* **2005,** *127*, 3650–3651.

7 Takamatsu, S.; Ishikawa, T.; Koshihara, S.; Ishikawa, N. *Inorg. Chem.* **2007**, *46*, 7250-7252.

8 AlDamen, M.; Clemente Juan, J. M.; Coronado, E.; Martí-Gastaldo, C.; Gaita-Ariño, A. *J. Am. Chem. Soc.* **2008**, *130*, 8874–8875.

The study of such diferences motivated the theoretical study of different coordination schemes to rationalize the correlation between structure and properties.

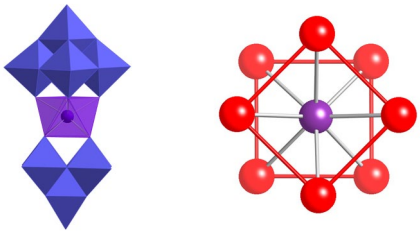

Figure 2. Left: Molecular structure of $[Er(W_5O_{18})_2]^{9-}$. Right: Detailed view of the coordination centre.

1.2. Theoretical studies about SIMs.

The first studies about nanomagnets were only empirical: they just tried to analyse the dynamic susceptibility in order to parameterize the behaviour. The simplest approximation considers a unique relaxation process which is impeded by a thermal barrier. Within this approximation, the behaviour can be fitted to an Arrhenius law and is described completely by two parameters: effective barrier height (U_{eff}) and preexponential factor (τ_0). Going one-step further, but still in an empirical approach, the existence of multiple relaxation pathways can be acknowledged. In this case, the Cole-Cole fitting parameter (α), which is a magnitude that correlates in-phase with out-of-phase signals, contains information about the number of active relaxation processes.

More complex studies about SMMs and SIMs are carried within very different theoretical approximations, including *ab initio* and density functional theory.[9]

More relevant for the present work, ligand field theory deals with the effect of the coordination on the ground state splitting of SIM. Initially, simple studies to obtain ideal LF-parameters have been done for the $TbPc_2$ complex.[10] The method consisted of a simultaneous fit of the dc magnetic susceptibilities and NMR data for a series of mononuclear complexes. And this was the state of the art at the beginning of this thesis.

Some years after, our group has proposed a model based on effective point charges models to predict the LF-parameters. This model is directly connected with the structural features of the mononuclear complex.[11] These qualitative descriptions cannot give precise details about the energy level scheme but can be used as a starting point to clarify which derivatives are expected to show slow magnetic relaxation. The final conclusion about theoretical models is that even with the most complex calculation, no

9 Long, J.; Habib, F.; Lin, P.-H.; Korobkov, I.; Enright, G.; Ungur, L.; Wernsdorfer, W.; Chibotaru, L. F.; Murugesu, M. *J. Am. Chem. Soc.* **2011**, *133*, 5319–5328.

10 Ishikawa, N.; Sugita, M.; Okubo, T.; Tanaka, H.; Iino, T.; Kaizu, Y. *Inorg. Chem.* **2003**, *42*, 2440-2446.

11 Baldoví, J. J.; Cardona-Serra, S.; Clemente-Juan, J. M.; Coronado, E.; Gaita-Ariño, A.; Palii, A.; *Inorg. Chem.* **2012**, *51*, 12565–12574.

unimolecular description is able to predict relaxation phenomena.

Thus, much theory about molecular magnets was focused on the understanding of the relaxation processes.[12] This phenomenon caused a great interest in the physicists' community which tried to develop a general theory to understand the effect of the surrounding crystal in the magnetic blockade. A successful study included the decoherence effects of the nuclear spin bath, phonons and magnons.[13]

12 Szallas, A.; Troiani, F. *Phys. Rev. B.* **2010**, *82*, 224409.

13 Takahashi, S.; Tupitsyn, I. S.; van Tol, J.; Beedle C. C.; Hendrickson, D. N.; Stamp, P. C. E. *Nature*, **2011**, *476*, 76-79.

2. *Summary of the most relevant results.*

The aim of this work was to obtain purely POM-based SIM to measure and to analyse their magnetic properties. An additional goal was to magnetically dilute the system in a diamagnetic matrix to study the single ion propeties. These complexes can be very interesting due to the isolation provided by the diamagnetic metal oxide which lessens the direct dipolar interaction without introducing magnetic disorder. POMs also present a huge variety of coordination symmetries that can be explored from the point of view of constructing SIMs.

In this thesis three polyoxowolframate "families" have been synthesized and characterized. These are: $Na_9Ln(W_5O_{18})_2$ [LnW10], $K_{13}Ln(\beta_2\text{-}SiW_{11}O_{39})_2$ [LnW22] and $K_{12}LnP_5W_{30}O_{110}$ [LnW30]. Ln = Gd^{3+}, Tb^{3+}, Dy^{3+}, Ho^{3+}, Er^{3+}, Tm^{3+},Yb^{3+}. The work is completed with an exhaustive theoretical analysis and rationalization of the magnetic behaviour.[14, 15]

2.1. Synthesis and Characterization.

All products have been synthesized with all the late lanthanoid ions from Tb^{3+} to Yb^{3+} except the LnW10 series. In these compounds, the smaller size of Tm^{3+} and Yb^{3+} made their derivatives unstable and not isolable in pure phases. All the compounds have been identified by EPMA (Electron Probe Microanalysis) performed in a Philips SEM XL30 equipped with EDAX DX-4 microsonde. IR Spectra were also recorded in a FT-IR Nicolet 5700 spectrometer in the 4000-400cm^{-1} range using powdered crystals in KBr pellets.

Magnetic susceptibility measurements were performed with a commercial magnetometer equipped with a SQUID sensor and a commercial Physical Properties Measurement System (PPMS). Direct current (dc) data were collected in the range 2-300 K with an applied field of 1000 G. The susceptibility data were corrected from the diamagnetic contributions as deduced by using the Pascal's constant tables. Alternate current (ac) data were collected in the range 2-15 K with an applied alternating field of 3.95 G at different frequencies in the range 1-10000 Hz.

For some of the compounds the magnetic characterization was extended to very low temperatures with a combination of non commercial experimental set-ups in collaboration with Dr. Fernando Luis (ICMA, Zaragoza). Magnetization hysteresis loops were measured, between 350 mK and 7 K, using a homemade micro-Hall magnetometer working in a ^{3}He refrigerator. The sample, mixed with Apiezon N grease to ensure its proper thermalization at these very low temperatures, was deposited directly on the edge

14 (a) Aldamen, M. A.; Cardona-Serra, S.; Clemente-Juan, J. M.; Coronado, E.; Gaita-Ariño, A.; Martí-Gastaldo, C.; Luis, F.; Montero, O.; *Inorg. Chem*. **2009**, *48*, 3467-3479. (b) Luis, F.; Martínez-Pérez, M.; Montero, O.; Coronado, E.; Cardona-Serra, S.; Martí-Gastaldo, C.; Clemente-Juan, J. M.; Sesé, J.; Drung, D.; Schurig, T. *Phys. Rev. B* **2010**, *82*, 060403

15 Cardona-Serra, S.; Clemente Juan, J. M.; Coronado, E.; Gaita-Ariño, A.; Camón, A.; Evangelisti, M.; Luis, F.; Martínez-Pérez, M.-J.; Sesé, J. *J. Am. Chem. Soc*. **2012**, *134*, 14982–14990.

of one of the two Hall crosses. In these conditions, the ac susceptibility was measured, from 333 Hz up to 13 kHz, using a home-built mutual inductance susceptometer thermally anchored to the mixing chamber of a ^{3}He-^{4}He dilution refrigerator, which gives access to temperatures ranging from 0.09 K up to 3.5 K. Finally, specific heat data were obtained between 350 mK and 20 K on compact pellets using a commercial PPMS.

In the case of the dynamic ac measurements, the results are quite different in each series. For LnW10, the Er^{3+} complex exhibits clear frequency-dependent signals at low temperatures. Upon cooling, a maximum is observed at high frequencies (1000-10000 Hz) between 4 - 6 K. Also an interesting signal is obtained for the Ho^{3+} derivative, which shows a shoulder around 5 K.

For LnW22 not only Er^{3+} but also Dy^{3+} and Ho^{3+} and Yb^{3+} complexes display a frequency dependent signal in their out-of-phase measurements. Unfortunately, only a smooth shoulder can be detected in these cases. This shows the comparatively faster relaxation rate of these compounds.

In the case of LnW30, the Dy^{3+} complex shows the best-defined dependence, with a worse resolved signal appearing in Ho^{3+}. In this series, the peak is not observed while decreasing the temperature down to 80 mK; that is, no complete superparamagnetic blocking occurs. This behaviour indicates that the paramagnetic relaxation rate τ-1, depends very weakly on temperature.

Additional Inelastic Neutron Scattering (INS) experiments were performed for LnW10 (Ln = Ho^{3+}, Er^{3+}) and LnW30 (Ln = Dy^{3+}, Ho^{3+}). Deuterated samples of the four compounds were measured in IN4 at Institute Laue-Langevin (Grenoble, France). The measurements were done at wavelengths λ= 1.1, 2.2 and 3.6 Å, which correspond to energy windows of 5-60, 2-15 and 1-5 meV respectively. INS can give precise information about the low energy levels of a magnetic molecule. Unfortunately, we found that the spectra were dominated by very intense phonon transitions (the baseline has a cubic increase with temperature due to vibrations) that obscure any magnetic signal of the lanthanoid ion.

2.2. Theoretical approach.

The Ligand Field (LF) Theory describes the effect of the electric field due to the surrounding ligands acting on a given paramagnetic metal ion. This crystal field results in the splitting of the ground electronic multiplet of the lanthanoid ion, described by its total angular momentum J into the M_J multiplet.

The LF Hamiltonian (H_{LF}) can be expressed in terms of different operators: spherical

harmonics,[16] Stevens' operators[17] or irreducible tensors operators.[18] The different notational conventions of this Hamiltonian are related to each other by equivalence coefficients. We generally used the extended Stevens operators, O_k^q, which are the most extensively adopted operators in LF calculations.[19] For a given J-multiplet the LF Hamiltonian based on the Stevens formalism takes the general form:

$$\hat{H}_{LF}(J) = \sum_{k=2,4,6} \sum_{q=0}^{k} B_k^q O_k^q = \sum_{k=2,4,6} \sum_{q=0}^{k} a_k A_k^q \left\langle r^k \right\rangle O_k^q$$

where k is the operator order, $\langle r^k \rangle$ is the expectation value of r^k, a_k are the α, β, γ Stevens equivalent coefficients for $k=2, 4, 6$. α, β, γ are tabulated for the ground state of each lanthanoid ion. Hence, the LF parameters, A_k^q and B_k^q, are referred to the ground state as well.

For pseudoaxial systems, like LnW10 and LnW22, only the terms with q=0 are not vanishing. Distortions from the pseudo-axial ideal symmetric structure will add q≠0 terms. In our systems, only those with a 5-fold rotation axis, like LnW30, include one q≠0 term , even for the idealized symmetry.

In order to elucidate the products, we made use of the effective fitting of dc magnetic susceptibility data measured as a function of the temperature. To minimize the number of parameters, this method assumes that the LF parameters have a linear variation with the number of *f* electrons as was proposed by Ishikawa. Under these conditions, the A_k^q can be expressed as:

$$A_k^q \left\langle r^k \right\rangle = a_k^q + b_k^q (n_f - 7)$$

where n_f varies from 8 to 13 when moving from Tb^{3+} to Yb^{3+}.

To automatize the susceptibility fitting, a general FORTRAN77 code was developed. This program simultaneously fits the all the experimental $\chi_m T$ data for all different member of a series, calculating each with a limited number of LF parameters defined by the user. An external code named MINUITT.F [20] was implemented in order to minimize the least squares error for each point varying the desired parameters. In addition, two extra parameters to account for both the TIP (Temperature Independent Paramagnetism) and the misscaling of the curves (e.g. weighting errors on incomplete substitution) were included. This program was used for the fitting of all the compounds presented.

In addition to the previous code, the author contributed to the development of a point charges model to obtain the ligand field parameters from a simple consideration of the symmetry arround the lanthanoid. Starting from the position vector of the coordination

16 Elliott, R. J.; Stevens, K. W. H. *Proc. Roy. Soc. A*, **1952**, *215*, 437–453.
17 Stevens, K. W. H. *Proc. Phys. Soc. A,* **1952**, *65*, 209-215
18 Morrison, C. A.; Wortman, D. E.; Karayianis, N.; *.J. Phys. C: Solid State Physics*, **1976**, *9*, L191-194
19 (a) Buckmaster, H. A. *Can. J. Phys.,* **1962**, *40*, 1670–1677; (b) Rudowicz, C.; *J. Phys. C: Solid State Physics,* **1985**, *18*, 1415–1430. (c) Ryabov, I.D.; *J. Mag. Res*. **1999**, *140*, 141. Ibid., *Appl. Magn. Reson*., **2009**, *35*, 481-494.
20 James, F.; Roos, M. *Comput. Phys. Commun.* **1975**, *10*, 345.

atoms, this approach can calculate which would be the most important LF terms and even estimate qualitatively his magnitude. This theory departs from the consideration of a LF Hamiltonian that is expressed in terms of spherical harmonics:

$$A_k^q = \frac{4\pi}{2k+1} c_{kq} (-1)^q \sum_{i=1}^{N} \frac{z_i e^2 Y_{k-q}(\theta_i, \ _i)}{R_i^{k+1}}$$

where φ_i, θ_i, R_i, are the polar coordinates of the effective point charge z_i which represent the ith ligand with the lanthanoid at the origin of the coordinates system; e is the electron charge and ckq is a tabulated numerical factor that relates spherical harmonics Y_{k-q} and the Stevens operators. This was also computationally implemented in a sequential code called SIMPRE.

2.3. General conclusions.

In general, the polyoxometalate-lanthanoid complexes have proved to be promising candidates to study the single ion magnet behaviour. They have been used to obtain magnetically diluted, robust crystals that can be studied with a large amount of techniques. Those complexes can even be synthesized varying the nuclear spin of the lanthanoid which is a factor that participates in the quantum tunnelling relaxation. This has been helpful in many other theoretical and experimental studies about these systems. Additional work has been done about the theoretical proposal of the Ln-POM complexes as spin qubits. In particular EPR studies were done to determine the zero-field tunnelling gap for the case of HoW10, a key parameter for quantum manipulations.[21]

Experimentally, Gd^{3+} derivatives have also been presented as magnetic coolers at very low temperatures.[22] About the development of Ln-POM based devices, dip-pen nanolithography was used to obtain crystalline nanostructures that can be precisely deposited with the tip of an atomic force microscope.[23]

Finally, some remarkable ideas can be extracted combining the analysis of the experimental results.

- First, **the coordination scheme determines which lanthanoids behave as SIMs.** There is a great difference between the phthalocyaninate and the POM complexes behaviour. In the case of the $LnPc_2$ complexes, Tb^{3+} was the cation with the better magnetic behaviour (higher blocking temperatures and larger energy barriers); otherwise, for the LnW10 series Er^{3+} was the most promising candidate. Our magnetic calculations started from the consideration of the opposite sign of the Steven's coefficient α (α<0 for Tb^{3+} and α>0 for Er^{3+}). Thus, the observed stabilization of the higher MJ sublevel should be achieved by differences in

21 Ghosh, S.; Datta, S.; Friend, L.; Cardona-Serra, S.; Gaita-Ariño, A.; Coronado, E.; Hill, S. *Dalton Trans.* **2012**, *41*, 13697-13704.

22 Martínez-Pérez, M.-J.; Montero, O.; Evangelisti, M.; Luis, F.; Sesé, J.; Cardona-Serra, S.; Coronado, E. *Adv. Mater.* **2012**, *24*, 4301–4305.

23 Bellido, E.; Cardona-Serra, S.; Coronado, E.; Ruiz-Molina, D. *Chem. Comm*. **2011**, *47*, 5175-5177.

the coordination scheme. As was described in the crystal description, the distances between the coordinating oxygen planes (Ln-POM) is smaller than the distance between the nitrogen planes ($LnPc_2$). Thus gives a compression effect for the polyoxometalate complex while the phthalocyaninate sandwich can be considered elongated. The main difference of this characteristic is the change in the sign of the second order CF term.

- **Very different, and non axial, coordination schemes can result in SIMs.** Comparing the two main series LnW10 and LnW30, both systems show single ion magnet behaviour in spite of the huge differences in their coordination structure (axial vs equatorial). In the LnW10, the main contribution to the stabilization of the maximum M_J is the (proportional to the typically called Zero Field Splitting 'D') term while the presence of a high q=5 term defines the magnetic properties in the case of the LnW30 series. This parameter that mixes magnetic functions with different M_J is not enough to rule out the possibility of a blocking in the magnetization. The explanation to this phenomenon is based in the fact that the mixture is not always active and the ground state eigenvector does not contain both the $+M_J$ and $-M_J$. In this way, the system cannot find a way to tunnel via its own ground wavefunction and can only relax through a thermally activated Orbach process, as usual. It is important to notice that even with such differences both complexes can be considered as systems with slow relaxation of the magnetization.[24]

- **Within a similar coordination scheme, little distortions can be correlated with the relaxation rates.** The similar pattern in the energy levels for $Na_9Ln(W_5O_{18})_2$ and $K_{13}Ln(\beta_2\text{-}SiW_{11}O_{39})_2$ suggest that both would have approximately the same relaxation phenomena. Despite of this, it is observed that the former shows slower relaxation times than the latter. This can be explained taking into account that the initial hypothesis was to consider both series as completely axial complexes with no deviations from the ideal D_{4d}. Experimentally, the $K_{13}Ln(\beta_2\text{-}SiW_{11}O_{39})_2$ is more distorted, and this is reflected in extradiagonal terms which are a source of relaxation.

- **The divergences of low temperature ac signal reveals a very efficient tunnelling process.** The observed divergence of the out-of-phase dynamic susceptibility below the blocking temperature is not observed in the Transition-Metal SMMs such as Mn12ac, in which the signal tends to disappear below this blocking limit. This phenomenon shows the existence of a very fast tunnelling process that takes place at very low temperatures. This behaviour was deeply studied in collaboration with Dr. Fernando Luis. Just summarizing the results, the conclusion was that dipolar interaction was quasi-inexistent and the tunnelling process should arise

24 Martínez-Pérez, M. J.; Cardona-Serra, S.; Schlegel, C.; Moro, F.; Alonso, P. J.; Prima-García, H.; Clemente-Juan, J. M.; Evangelisti, M.; Gaita-Ariño, A.; Sesé, J.; van Slageren, J.; Coronado, J.; Luis, F. *Phys. Rev. Lett.* **2012**, *108*, 247213.

from a cooperative spin-lattice relaxation effect. For this work, the experimental contribution was to synthesize magnetically diluted samples using $Na_9Y(W_5O_{18})_2$ as the diamagnetic matrix and cocrystalize both systems in an single crystal structure.

- **In general, Ln-POMs complexes are excepctional systems for practical applications such as quantum computing or as magnetic coolers.** Thus, having a high $q \neq 0$ term provides interesting systems also attractive for its use as solid-state spin qubits. In this way, some of these systems show a large tunnelling gap between their lowest energy states that can be accessible by using the correct frequency irradiation in a pulsed EPR setup. Besides this, the magnetic ordering in these materials only occurs at very low temperatures (below 0.01K), which allows the use of the Gd derivatives as magnetic coolers in the very low temperature range, studies that scientists were not able to perform in transition metal clusters.

- **It is possible to stablish a general theory which calculates the LF terms from the crystallografic structure.** This opens the possibility of going beyond the late rationalization of the properties and permits to address the rational design. Moreover, using DFT methods it is possible to improve the only geometric description while taking into account covalent effects.

3. Author's contribution to the publications.

3.1. Contributions related to PAPER 3: "*Mononuclear Lanthanide Single Molecule Magnets Based on the Polyoxometalates* $[Ln(W_5O_{18})_2]^{9-}$ *and* $[Ln(\beta_2\text{-}SiW_{11}O_{39})_2]^{13-}$ *(*Ln^{III} *= Tb, Dy, Ho, Er, Tm and Yb)***"**

In this publication, the author completed the synthesis of the series $[Ln(W_5O_{18})_2]^{9-}$ and $[Ln(\beta_2\text{-}SiW_{11}O_{39})_2]^{13-}$ with their full characterization. Previously, only the erbium derivative of each complex had been studied. When this thesis started, the author noticed the importance of such compounds and decided to study the rest of the series. His experimental contribution to the publication allowed him to rationalize the magnetic behaviour of each compound using Ishikawa's approach (*vide supra*). With this goal, the author collaborated in the development of a computational code which was able to fit simultaneously all the magnetic susceptibilities and magnetization using an effective Hamiltonian which considers the symmetrically appropiate LF terms.

The author also contributed in the synthesis of pure isotopic erbium complexes to study the effect of the lanthanoid nuclear spin in the decoherence times which was published separately.[14b] Additionally, the possibility of preparing magnetically diluted samples was developed by the author. Using a diamagnetic matrix based on the yttrium derivative, the dipolar interactions can be avoided, thus improving the study of the single ion property.

3.2. Contributions related to PAPER 4: "*Lanthanoid Single-Ion Magnets Based on Polyoxometalates with a 5-fold Symmetry: The Series* $[LnP_5W_{30}O_{110}]^{12-}$ *(*Ln^{III} *= Tb, Dy, Ho, Er, Tm and Yb).***"**

In this publication, the author studied both experimentally and theoretically the series $[LnP_5W_{30}O_{110}]^{12-}$. The exotic symmetry of the coordination centre, pseudo-C_5 aim to redesign all the previously studies in lanthanoid LF to consider odd non-axial terms.

The author started with the synthesis of the full series using a previously described hydrothermal process. He slightly modified this method by increasing the time and temperature of the synthesis and, in some cases, obtained a remarkable higher yield. All the samples were characterized with various techniques before their magnetic measurements.

The autor also modified the computational code to include the 5-fold terms (in fact, now the program is able to include up to any sixth order term) and rationalized the results of the susceptibility fittings.

As for the previous series, the author developed the method to obtain magnetically diluted samples which were subsequently studied by his colleagues from the Luis' group.

Additionally, he participated in the study to understand the anisotropy details of a "non-axial" SIM and to develop a comparative study of the magnetic low-temperature blocking phenomenon between $[Gd(W_5O_{18})_2]^{9-}$ and $[GdP_5W_{30}O_{110}]^{12-}$. The latter has been recently found to display extraordinary coherence properties, in yet another work where the author contributed but which is not a major part of this thesis.

3.3. Contributions related to PAPER 5: "*Rational Design of Single-Ion Magnets and Spin Qubits Based on Mononuclear Lanthanoid Complexes.*"

In this publication, the author collaborated with the initial programming of the computational code that, starting from the atomic coordinates of each ligand, calculates the qualitative value of the ligand field terms. This code was initially developed to study the previous series $[LnP_5W_{30}O_{110}]^{12-}$ due to the complex symmetry of the coordination centre. The author extrated LF key parameters from the consideration of an ideal C_5 structure, thus offering a simplified Hamiltonian where the B_5^6 term plays a crucial role in the understanding of the low energy levels and the magnetic properties at very low temperatures.

Afterwards, the author contributed with a direct comparison of the point charges LF method versus the direct susceptibility fitting. Here the author performed a large quantity of calculations for many systems with various symmetries (with trigonal, tetragonal and pentagonal axis) and discussed the results with the other participants. These results were the basis to stablish a direct correlation between the two methods and, while only considering the ligand coordinates, try to predict the magnetic behaviour of a mononuclear lanthanoid complex.

PAPER 3:
Mononuclear Lanthanide Single Molecule Magnets Based on the Polyoxometalates $[Ln(W_5O_{18})_2]^{9-}$ and $[Ln(\beta_2\text{-}SiW_{11}O_{39})_2]^{13-}$ (Ln^{III} = Tb, Dy, Ho, Er, Tm and Yb)

Inorganic Chemistry, **2009**, *48,* 3467-3479.

Inorg. Chem. **2009**, *48*, 3467−3479

Forum

Mononuclear Lanthanide Single Molecule Magnets Based on the Polyoxometalates $[Ln(W_5O_{18})_2]^{9-}$ and $[Ln(\beta_2\text{-}SiW_{11}O_{39})_2]^{13-}$ (Ln^{III} = Tb, Dy, Ho, Er, Tm, and Yb)

Murad A. AlDamen,[†] Salvador Cardona-Serra,[†] Juan M. Clemente-Juan,[†,‡] Eugenio Coronado,*[,†] Alejandro Gaita-Ariño,[†,§] Carlos Martí-Gastaldo,[†] Fernando Luis,[||] and Oscar Montero[||]

Instituto de Ciencia Molecular, Universidad de Valencia, Polígono la Coma s/n, 46980 Paterna, Spain, Department of Physics and Astronomy, University of British Columbia, 6224 Agricultural Road, Vancouver, British Columbia V6T 1Z1, Canada, Instituto de Ciencia de Materiales de Aragón, CSIC, Universidad de Zaragoza, Plaza San Francisco s/n, 50009 Zaragoza, Spain, and Fundación General Universidad de Valencia (FGUV), Plaça del Patriarca, 46002 Valencia, Spain

Received August 26, 2008

The first two families of polyoxometalate-based single-molecule magnets (SMMs) are reported here. Compounds of the general formula $[Ln(W_5O_{18})_2]^{9-}$ (Ln^{III} = Tb, Dy, Ho, and Er) and $[Ln(SiW_{11}O_{39})_2]^{13-}$ (Ln^{III} = Tb, Dy, Ho, Er, Tm, and Yb) have been magnetically characterized with static and dynamic measurements. Slow relaxation of the magnetization, typically associated with SMM-like behavior, was observed for $[Ln(W_5O_{18})_2]^{9-}$ (Ln^{III} = Ho and Er) and $[Ln(SiW_{11}O_{39})_2]^{13-}$ (Ln^{III} = Dy, Ho, Er, and Yb). Among them, only the $[Er(W_5O_{18})_2]^{9-}$ derivative exhibited such a behavior above 2 K with an energy barrier for the reversal of the magnetization of 55 K. For a deep understanding of the appearance of slow relaxation of the magnetization in these types of mononuclear complexes, the ligand-field parameters and the splitting of the *J* ground-state multiplet of the lanthanide ions have been also estimated.

Introduction

Most single-molecule magnets (SMMs) are polynuclear complexes formed by magnetic clusters of exchange-coupled metal ions with high-spin ground states and predominant uniaxial anisotropy.[1,2] The possibility of constructing SMMs using a single lanthanide ion has been recently demonstrated by Ishikawa in phthalocyaninatolanthanide complexes with a "double-decker" structure, $[LnPc_2]^-$.[3] In these complexes, a trivalent lanthanide ion, Ln^{III}, is encapsulated by two π-conjugated planar ligands (Pc = phthalocyanine dianion; Ln^{III} = Tb, Dy, Ho, Er, Tm, and Yb). These ligands present four coordinating pyrrole nitrogen atoms in a square-planar symmetry. When two tetradentate ligands encapsulate the Ln^{III} ion, each moiety is twisted ca. 45° with respect to the other, generating a D_{4d} ligand-field (LF) symmetry around the lanthanide.

* To whom correspondence should be addressed. E-mail: eugenio.coronado@uv.es. Tel: +34-963544415. Fax: +34-963543273.
[†] Universidad de Valencia.
[‡] Fundación General Universidad de Valencia.
[§] University of British Columbia.
[||] Universidad de Zaragoza.

(1) (a) Sessoli, R.; Gatteschi, D.; Caneschi, A.; Novak, M. A. *Nature* **1993**, *365*, 141–143. (b) Gatteschi, D.; Sessoli, R. *Angew. Chem., Int. Ed.* **2003**, *42*, 268–297. (c) Gatteschi, D.; Sessoli, R.; Villain, J. *Molecular Nanomagnets*; Oxford University Press: Oxford, U.K., 2006.

(2) For examples, see: (a) Mallah, T.; Auberger, C.; Verdaguer, M.; Veillet, P. *J. Chem. Soc., Chem. Commun.* **1995**, *61*, 62. (b) Castro, S. L.; Sun, Z. M.; Grant, C. M.; Bollinger, J. C.; Hendrickson, D. N.; Christou, G. *J. Am. Chem. Soc.* **1998**, *120*, 2365–2375. (c) Barra, A. L.; Caneschi, A.; Cornia, A.; de Biani, F. F.; Gatteschi, D.; Sangregorio, C.; Sessoli, R.; Sorace, L. *J. Am. Chem. Soc.* **1999**, *121*, 5302–5310. (d) Barra, A. L.; Caneschi, A.; Gatteschi, D.; Goldberg, D. P.; Sessoli, R. *J. Solid State Chem.* **1999**, *145*, 484–487. (e) Yoo, J.; Brechin, E. K.; Yamaguchi, A.; Nakano, M.; Huffman, J. C.; Maniero, A. L.; Brunel, L. C.; Awaga, K.; Ishimoto, H.; Christou, G.; Hendrickson, D. N. *Inorg. Chem.* **2000**, *39*, 3615–3623. (f) Sokol, J. J.; Hee, A. G.; Long, J. R. *J. Am. Chem. Soc.* **2002**, *124*, 7656–7657. (g) Berlinguette, C. P.; Vaughn, D.; Canada-Vilalta, C.; Galan-Mascaros, J. R.; Dunbar, K. R. *Angew. Chem., Int. Ed.* **2003**, *42*, 1523–1526.

(3) Ishikawa, N.; Sugita, M.; Ishikawa, T.; Koshihara, S.; Kaizu, Y. *J. Am. Chem. Soc.* **2003**, *125*, 8694–8695.

10.1021/ic801630z CCC: $40.75
Published on Web 04/13/2009

In this class of single-atom nanomagnets, the magnetic anisotropy required for observing slow relaxation of the magnetization arises from the splitting of the J ground state of the Ln^{III} ion when it is submitted to a LF. For certain LF symmetries, such a splitting can stabilize sublevels with a large $|M_J|$ value, thus achieving an easy axis of the magnetization.[4] Some years ago, Ishikawa developed a convenient procedure to determine the LF parameters and the sublevel structure of the phthalocyaninatolanthanide complexes.[5] The approach involves a simultaneous least-squares fit of the magnetic susceptibility data and ^{1}H NMR paramagnetic shifts for the whole set of compounds. The best set of LF parameters gave large positive values for $A_0^2r^2$ and large negative values for $A_0^4r^4$ in the phthalocyaninato complexes.[6] Under these conditions, the ground-state sublevels for Tb, Dy, and Ho turned out to be doublets with large $|M_J|$ values, for Tb reaching the maximum value ($M_J = \pm 6$). Furthermore, in this case, the ground-state sublevel is well isolated from the first excited one (by more than 400 cm^{-1}). The ground-state sublevels of the other lanthanides turned out to be doublets with low $|M_J|$ values. For example, in the Er case, this sublevel corresponds to that with the minimum $|M_J|$ value ($\pm^1/_2$). Accordingly, from the six members of the family, only Tb and Dy derivatives exhibited SMM behavior, with frequency-dependent out-of-phase alternating current (ac) susceptibility peaks at 40 and 10 K, respectively. In these nanomagnets, the relaxation processes were associated with a thermally activated Orbach process involving excited sublevels of the ground J multiplet. Resonant quantum tunneling of the magnetization, which is a characteristic feature of SMMs, was also observed in the Ho derivative.[7]

Still, few studies on the mononuclear lanthanide-based complexes exhibiting SMM behavior, apart from the phthalocyaninatolanthanide complexes, have been reported. In this context, we have shown in a previous communication that polyoxometalates (POMs) encapsulating lanthanides with coordination geometries similar to those of bis(phthalocyaninato)lanthanide complexes can also exhibit SMM behavior.[8] This was firstly demonstrated in the sodium salt of the polyanion $[Er(W_5O_{18})_2]^{9-}$. In the present work, we report a detailed magnetostructural characterization for the whole family $[Ln(W_5O_{18})_2]^{9-}$ (Ln^{III} = Tb, Dy, Ho, and Er) and extend this study to the series $[Ln(SiW_{11}O_{39})_2]^{13-}$ (Ln^{III} = Tb, Dy, Ho, Er, Tm, and Yb).

Experimental Section

Synthesis. All reagents and solvents were of commercially available grade and used without any previous purification. $LnCl_3 \cdot 6H_2O$ and $Er_2(CO_3)_2 \cdot xH_2O$ are highly hygroscopic compounds; for that reason, they were stored in desiccators. The monolacunary Keggin precursor, $K_8[(\beta_2\text{-}SiW_{11}O_{39}] \cdot 14H_2O$, was prepared according to a previously described procedure[9] and identified by electron probe microanalysis (EPMA) and FT-IR techniques (SI 1 and SI 2 in the Supporting Information).

$Na_9[Tb(W_5O_{18})_2] \cdot xH_2O$ (**1**) was prepared following a previously described procedure[10]with slight modifications. A total of 8.3 g (25 mmol) of $Na_2WO_4 \cdot 2H_2O$ was dissolved in 20 mL of water. The resulting solution was adjusted to pH 7.4−7.5 with acetic acid. Subsequently, an aqueous solution (2 mL) containing 0.921 (2.5 mmol) of $TbCl_3 \cdot 6H_2O$ was added dropwise to the above-mentioned solution under continuous stirring and heated up to 85 °C. Crude crystals were isolated when this solution was left to stand at room temperature. FT-IR data in cm^{-1}: 935 (s), 845 (s), 798 (m), 706 (m), 586 (w), 545 (m), 490 (w).

$Na_9[Dy(W_5O_{18})_2] \cdot xH_2O$(**2**) was prepared as previously described for **1** but using 0.930 g (2.5 mmol) of $DyCl_3 \cdot 6H_2O$. FT-IR data in cm^{-1}: 933 (s), 847 (s), 804 (m), 705 (m), 584 (w), 549 (m), 490 (w).

$Na_9[Ho(W_5O_{18})_2] \cdot xH_2O$(**3**) was prepared as previously described for **1** but using 0.940 g (2.5 mmol) of $HoCl_3 \cdot 6H_2O$. FT-IR data in cm^{-1}: 933 (s), 847 (s), 804 (m), 708 (m), 596 (w), 546 (m), 422 (w).

$Na_9[Er(W_5O_{18})_2] \cdot xH_2O$(**4**) was prepared following a previously described method.[11] In a first stage, $Er_2(CO_3)_2 \cdot xH_2O$ (2.180 g, 3.8 mmol) was dissolved in 30 mL of HCl (0.1 M) and heated at 80 °C for 30 min, giving rise to a colorless solution (A). Simultaneously, $Na_2WO_4 \cdot 2H_2O$ (50 g, 152 mmol) was dissolved in distilled water (100 mL) with continuous stirring; the pH was adjusted to 7.2 with acetic anhydride, and the resulting solution (B) was heated to 90 °C. Then, A was dropwise added to the hot stirred wolframate solution (B). After being vigorously stirred for 1 h, the mixture was filtered rapidly and left to evaporate at room temperature. A total of 3 weeks later needle-shaped pale-pink crystals of **4**, suitable for single-crystal X-ray diffraction, were obtained. FT-IR data for **1** in cm^{-1}: 935 (s), 845 (s), 798 (m), 706 (m), 586 (w), 545 (m), 490 (w).

$K_{13}[Tb(\beta_2\text{-}SiW_{11}O_{39})_2] \cdot xH_2O$ (**5**) was prepared by following a previously described method.[12] A total of 0.5 g (0.15 mmol) of $K_8[\beta_2\text{-}SiW_{11}O_{39}] \cdot 14H_2O$ and 0.0319 g (0.085 mmol) of $TbCl_3 \cdot 6H_2O$ were added to 20 mL of 1 M KCl. The resulting mixture was adjusted to pH 4.4−5.0 by the dropwise addition of 0.1 M HCl. Afterward, the solution was mechanically stirred at 50 °C for 30 min and allowed to stand at room temperature. Rapid filtration, followed by slow evaporation in an open container at room temperature, yielded crystals suitable for X-ray diffraction, after 3 days. FT-IR data in cm^{-1}: 1003 (m), 957 (m), 910 (s), 872 (s), 837 (m), 789 (s), 725 (s).

$K_{13}[Dy(\beta_2\text{-}SiW_{11}O_{39})_2] \cdot xH_2O$ (**6**) was prepared as previously described for **5** but using 0.032 g (0,085 mmol) of $DyCl_3 \cdot 6H_2O$. FT-IR data in cm^{-1}: 1005 (m), 953 (m), 910 (s), 877 (s), 837 (m), 793 (s), 727 (s).

$K_{13}[Ho(\beta_2\text{-}SiW_{11}O_{39})_2] \cdot xH_2O$ (**7**) was prepared as previously described for **5** but using 0.032 g (0,085 mmol) of $HoCl_3 \cdot 6H_2O$. FT-IR data in cm^{-1}: 1008 (m), 954 (m), 915 (s), 877 (s), 838 (m), 794 (s), 720 (s);.

(4) Ishikawa, N.; Sugita, M.; Ishikawa, T.; Koshihara, S.; Kaizu, Y. *J. Phys. Chem. B* **2004**, *108*, 11265–11271.
(5) Ishikawa, N.; Iino, T.; Kaizu, Y. *J. Phys. Chem. A* **2002**, *106*, 9543. Ishikawa, N.; Iino, T.; Kaizu, Y. *J. Am. Chem. Soc.* **2002**, *124*, 11440.
(6) Ishikawa, N.; Sugita, M.; Okubo, T.; Takana, N.; Iino, T.; Kaizu, Y. *Inorg. Chem.* **2003**, *42*, 2440.
(7) (a) Ishikawa, N.; Sugita, M.; Wernsdorfer, W. *Angew. Chem., Int. Ed.* **2005**, *22*, 2931. (b) Ishikawa, N.; Sugita, M.; Wernsdorfer, W. *J. Am. Chem. Soc.* **2005**, *127*, 3650.
(8) Aldamen, M.; Clemente-Juan, J. M.; Coronado, E.; Martí-Gastaldo, C.; Gaita-Ariño, A. *J. Am. Chem. Soc.* **2008**, *130*, 8874–8875.
(9) Tézé, A.; Hervé, G. *Inorg. Chem.* **1990**, *27*, 88.
(10) Ozeki, T.; Yamase, T. *Acta Crystallogr.* **1994**, *C50*, 327.
(11) Shiozaki, R.; Inagaki, A.; Nishino, A.; Nishio, E.; Maekawa, M.; Kominami, H.; Kera, Y. *J. Alloys Compd.* **1996**, *234*, 193.
(12) Bassil, B. S.; Dickman, M. H.; Von der Kammer, B.; Kortz, U. *Inorg. Chem.* **2007**, *46*, 2452.

Table 1. Summary of the Structural Data of **4**[a]

formula	$Na_9ErW_{10}O_{71}H_{68}$
mol wt	3348.6
T [K]	173(2)
λ [Å]	0.710 73
cryst syst	triclinic
space group	$P\bar{1}$
a [Å]	12.744(3)
b [Å]	13.071(3)
c [Å]	20.470(4)
α [deg]	82.89(3)
β [deg]	74.53(3)
γ [deg]	88.80(3)
V [Å^3]	3260.8(11)
Z	2
ρ_{calcd} [g cm^{-3}]	3.411
2θ limit [deg]	2.18−30.09
GOF	0.984
R1	0.0714
R2	0.1905

[a] R1 = $\sum(F_o - F_c)/\sum(F_o)$. R2 = $[\sum[w(F_o^2 - F_c^2)^2]/\sum[w(F_o^2)^2]]^{1/2}$; $w = 1/[\sigma^2(F_o^2) + (0.0343P)^2 + 2.4502P]$; $P = (F_o^2 + 2F_c^2)/3$.

$K_{13}[Er(\beta_2\text{-}SiW_{11}O_{39})_2]\cdot xH_2O$ (**8**) was prepared as previously described for **5** but using 0.0326 g (0,085 mmol) of $ErCl_3\cdot 6H_2O$. FT-IR data in cm^{-1}: 1008 (m), 958 (m), 915 (s), 878 (s), 836 (m), 790 (s), 724 (s).

$K_{13}[Tm(\beta_2\text{-}SiW_{11}O_{39})_2]\cdot xH_2O$ (**9**) was prepared as previously described for **5** but using 0.0326 g (0,085 mmol) of $TmCl_3\cdot 6H_2O$. FT-IR data in cm^{-1}: 1009 (m), 957 (m), 912 (s), 876 (s), 837 (m), 789 (s), 723 (s).

$K_{13}[Yb(\beta_2\text{-}SiW_{11}O_{39})_2]\cdot xH_2O$ (**10**) was prepared as previously described for **5** but using 0.039 g (0,085 mmol) of $YbCl_3\cdot 6H_2O$. FT-IR data in cm^{-1}: 1007 (m), 957 (m), 914 (s), 879 (s), 837 (m), 787 (s), 723 (s).

X-ray Data Collection. Crystals were collected by hand, fixed on a 200 μm MicroMount,[13] and mounted on a Nonius-Kappa CCD single-crystal diffractometer equipped with graphite-monochromated Mo Kα radiation (λ = 0.710 73 Å) at 293(2) or 173(2) K. Data collection was performed by using the program *Collect*.[14] Data reduction and cell refinement were performed with the programs *Denzo* and *Scalepack*.[15] The crystal structure was solved by direct methods using the program *SIR97*,[16] followed by Fourier synthesis, and refined on F^2 with *SHELXL-97*.[17] Anisotropic least-squares refinement of all non-disordered heavy atoms (Ln, W, Si, Na, and O) was performed. All crystallographic plots were obtained using the *CrystalMaker* program.[18] Tables 1 and 3 summarize the crystal data collection and refinement parameters.

ICSD 419267, 419778, and 419779 files contain the supplementary crystallographic data for this paper. They can be obtained free of charge via http://www.fiz-karlsruhe.de/obtaining_crystal_structure_data.html or from the Inorganic Crystal Structure Database (ICSD, FIZ Kalsruhe, Hermann-von-Helmholtz-Platz 1, Eggenstein-Leopoldshafen, 76344, Germany; phone (+49) 7247-808-555, fax (+49) 7247-808-259).

Table 2. Structural Parameters Concerning the Lanthanide Coordination Sphere in the Series $[Ln^{III}W_{10}O_{36}]^{9-}$

$[Ln^{III}W_{10}O_{36}]^{9-}$	countercation	d_{pp}[b] [Å]	d_{in}[a] [Å]	φ[c] [deg]	ref
Pr	3 K^+, 4 Na^+, 2 H^+	2.667	2.955	41.4	27
Nd	3 K^+, 4 Na^+, 2 H^+	2.615	2.948	43.2	27
Sm	6 Na^+, 3 H^+	2.575	2.921	46.9	28
Sm	3 K^+, 4 Na^+, 2 H^+	2.695	2.926	46.9	27
Eu	9 Na^+	2.356	2.608	46.7	29
Eu	4 Sr^{2+}, 1 Na^+	2.556	2.878	41.2	30
Gd	3 K^+, 4 Na^+, 2 H^+	2.635	2.892	43	31
Gd	8 Na^+, 1 H^+	2.539	2.898	39.1	32
Dy	9 Na^+	2.496	2.876	44.0	33
Dy	3 K^+, 4 Na^+, 2 H^+	2.551	2.864	43.1	27
Er	9 Na^+	2.469	2.856	44.5	this work

[a] d_{in} is the average O−O distance within the oxygen-based square planes. [b] The d_{pp} parameter defines the average distance between the two oxygen-based square planes. [c] φ is defined as the relative orientation between the two squares defined by the coordinating oxygen atoms (see the text).

Table 3. Summary of the Structural Data of **8** and **9**[a]

formula	$K_{13}ErW_{22}O_{103}H_{50}$	$K_{13}TmW_{22}O_{103}H_{50}$
mol wt	6474.5	6476.2
T [K]	173(2)	293(2)
λ [Å]	0.710 73	0.710 73
cryst syst	monoclinic	monoclinic
space group	$P21/c$	$P21/c$
a [Å]	20.208(4)	20.196(7)
b [Å]	20.535(3)	20.522(7)
c [Å]	27.294(5)	27.232(8)
α [deg]	90	90
β [deg]	113.805(7)	113.791(1)
γ [deg]	90	90
V [Å^3]	10362.6(2)	10327.5(4)
Z	4	4
ρ_{calcd} [g cm^{-3}]	4.09	3.80
2θ limit [deg]	2.51−27.48	1.46−30.02
GOF	1.028	1.030
R1	0.0817	0.0948
R2	0.2084	0.2889

[a] R1 = $\sum(F_o - F_c)/\sum(F_o)$. R2 = $[\sum[w(F_o^2 - F_c^2)^2]/\sum[w(F_o^2)^2]]^{1/2}$; $w = 1/[\sigma^2(F_o^2) + (0.0343P)^2 + 2.4502P]$; $P = (F_o^2 + 2F_c^2)/3$.

Physical Measurements. The metallic composition of bulk samples was determined by EPMA performed in a Philips SEM XL30 equipped with an EDAX DX-4 microsonde. IR spectra were recorded on a FT-IR Nicolet 5700 spectrometer in the 4000−400 cm^{-1} range using powdered, hand-collected crystal samples in KBr pellets. Magnetic susceptibility measurements were performed on previously ground, hand-collected crystals with a Quantum Design MPMS-XL-5 magnetometer equipped with a SQUID sensor and a Quantum Design model PPMS-9. The susceptibility data were corrected from the diamagnetic contributions as deduced by using Pascal's constant tables. Direct current (dc) data were collected in the range 2−300 K with an applied field of 1000 G. Alternate current (ac) data were collected in the range 2−12 K with an applied alternating field of 3.95 G at different frequencies in the range 1−10000 Hz.

Results and Discussion

Structural Characterization. Here we report the magnetostructural study of two series of mononuclear lanthanide-based complexes obtained by encapsulation of the lanthanide metal by two monolacunary POM anions acting

(13) Thorne, R. E.; Stum, Z.; Kmetko, J.; O'Neill, K.; Gillilan, R. *J. Appl. Crystallogr.* **2003**, *36*, 1455–1460.
(14) Collect, Nonius BV, 1997−2000.
(15) Otwinowsky, Z.; Minor W. In *Processing of X-ray diffraction data collected in oscillation mode*; Carter, C. W., Jr., Sweet, R. M., Eds.; Academic Press: New York, 1997.
(16) Altomare, A.; Burla, M. C.; Camalli, M.; Cascarano, G. L.; Giacovazzo, C.; Guagliardi, A.; Moliterni, A. G. G.; Polidori, A.; Spagna, G. *J. Appl. Crystallogr.* **1999**, *32*, 115–119.
(17) Sheldrick, G. M. *SHELXL-97*; University of Göttingen: Göttingen, Germany, 1997.
(18) *CrystalMaker Software*; CrystalMaker Software Limited: Oxfordshore, U.K., 2006.
(19) (a) Ostendorp, G.; Werner, J. P.; Homborg, H. *Acta Crystallogr., Sect. C: Cryst. Struct.* **1995**, *51*, 1125–1128. (b) Koike, N.; Uekusa, H.; Ohashi, Y.; Harnoode, C.; Kitamura, F.; Ohsaka, T.; Tokuda, K. *Inorg. Chem.* **1996**, *35*, 5798–5804.
(20) Stevens, K. W. H. *Proc. Phys. Soc. A* **1952**, *65*, 209–215.
(21) (a) Orbach, R. *Proc. Phys. Soc. A* **1961**, *264*, 458–484. (b) Rudowicz, C. *J. Phys. C: Solid State Phys.* **1985**, *18*, 1415–1430.

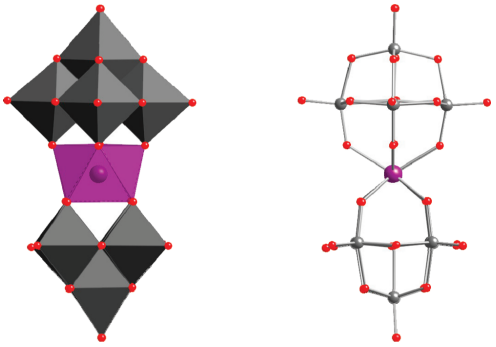

Figure 1. Polyhedral (left) and ball-and-stick (right) representations of the $[Ln(W_5O_{18})_2]^{9-}$ cluster (oxygen, red; tungsten, gray; lanthanide, purple). This structure can be considered representative of the whole set of compounds: Ln^{III} = Tb (**1**), Dy (**2**), Ho (**3**), and Er (**4**).

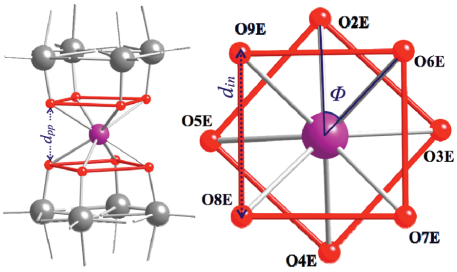

Figure 2. Perspective showing the square-antiprismatic coordination of the central Ln^{3+} ion and the d_{pp} parameter in $[Ln(W_5O_{18})_2]^{9-}$ (left). Perspective showing the d_{in} and ϕ structural features (right).

as tetradentate ligands. When the monolacunary $[W_5O_{18}]^{6-}$ anion derived from the Lindqvist anion $[W_6O_{19}]^{2-}$ is used, one obtains the series $[Ln(W_5O_{18})_2]^{9-}$ [Ln^{III} = Tb (**1**), Dy (**2**), Ho (**3**), and Er (**4**); see Figure 1). On the other hand, when the monolacunary $[\beta_2\text{-}SiW_{11}O_{39}]^{8-}$ anion derived from the Keggin anion $[SiW_{12}O_{40}]^{4-}$ is used, one obtains the series $[Ln(\beta_2\text{-}SiW_{11}O_{39})_2]^{13-}$ [Ln^{III} = Tb (**5**), Dy (**6**), Ho (**7**), Er (**8**), Tm (**9**), and Yb (**10**); Figure 3). Notice that the synthesis and structures of the first series were already reported for the derivatives Ln^{III} = Pr,[27] Nd,[27] Sm,[27,28] Eu,[29,30] Gd,[31,32] Tb,[27] and Dy.[27,33] Among them,

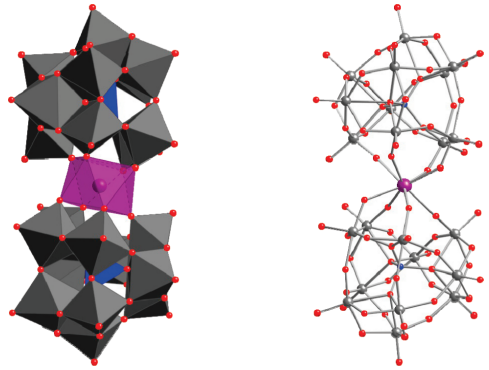

Figure 3. Polyhedral (left) and ball-and-stick (right) representations of the $[Ln(\beta_2\text{-}SiW_{11}O_{39})_2]^{13-}$ cluster (oxygen, red; silicon, blue; tungsten, gray; lanthanide, purple). This structure can be considered representative of the whole set of compounds: Ln^{III} = Tb (**5**), Dy (**6**), Ho (**7**), Er (**8**), Tm (**9**), and Yb (**10**).

only the Eu and Dycompounds were isolated as sodium salts (see Table 2). Concerning the second series, the synthesis and structures of their potassium salts were first reported by Bassil et al. for the derivatives Ln^{III} = La, Ce, Sm, Eu, Gd, Tb, Yb, and Lu.[12] The compounds described in this work have been isolated as hydrated eneasodium (**1**−**4**) and tridecapotassium salts (**5**−**10**), respectively, and characterized by FT-IR and EPMA. Although important efforts have been devoted to obtain the decawolframelanthanoatothulim and -ytterbium derivatives, we could not isolate them as pure phases. Because the SMM behavior observed in mononuclear lanthanide-based POMs is strongly dependent on the exact coordination geometry around the metal, important attention has been devoted to the analysis of their crystal structures.

$[Ln(W_5O_{18})_2]^{9-}$ Series [Ln^{III} = Tb (1), Dy (2), Ho (3), and Er (4)]. Considering that all the synthesized compounds are isostructural, we have only determined the crystal structure of the Er complex. It is formed by two anionic $[W_5O_{18}]^{6-}$ moieties sandwiching the central lanthanide ion (Figures 1 and 2). The anionic clusters are surrounded by sodium cations that are octahedrally coordinated by oxygen atoms, with Na−O distances in the range 2.235−2.684 Å (average 2.429 Å), apart from Na6, which exhibits square-pyramidal coordination, with Na−O distances in the range 2.280−2.362 Å (average 2.326 Å). These NaO_n (n = 5 and 6) clusters are connected by edge- and corner-sharing linkages. These hydrated Na^+ cations interact with the highly charged $[Er(W_5O_{18})_2]^{9-}$ anions for electroneutrality, thus introducing a large number of water molecules in the lattice, as has been previously observed in other sodium salts of decawolframolanthanoate. This fact, together with

(22) (a) Fedotov, M. A.; Samokhvalova, E. P.; Kazansky, L. P. *Polyhedron* **1996**, *15*, 3341–3351. (b) Shiozaki, R.; Inagaki, A.; Nishino, A.; Nishio, E.; Maekawa, M.; Kominami, H.; Kera, Y. *J. Alloys Compd.* **1996**, *234*, 193–198.
(23) (a) Cole, K. S.; Cole, R. H. *J. Chem. Phys.* **1941**, *9*, 341–351. (b) Dekker, C.; Arts, A. F. M.; Dewijn, H. W.; Vanduyneveldt, A. J.; Mydosh, J. A. *Phys. Rev. B* **1989**, *40*, 11243–11251.
(24) (a) Clemente-Juan, J. M.; Coronado, E. *Chem. Rev.* **1999**, *193*, 361–394. (b) Coronado, E.; Gómez-García, C. J. *Chem. Rev.* **1998**, *98*, 273–296. (c) Müller, A.; Peters, F.; Pope, M. T.; Gatteschi, D. *Chem. Rev.* **1998**, *98*, 239–272. (d) Calzado, C. J.; Clemente-Juan, J. M.; Coronado, E.; Gaita-Arino, A.; Suaud, N. *Inorg. Chem.* **2008**, *47*, 5889–5901, and references cited therein. .
(25) (a) Lehmann, J.; Gaita-Arino, A.; Coronado, E.; Loss, D. *Nature Nanotechnol.* **2007**, *2*, 312–317. (b) Bertaina, S.; Gambarelli, S.; Mitra, T.; Tsukerblat, B.; Müller, A.; Barbara, B. *Nature* **2008**, *453*, 203–206.
(26) Ritchie, C.; Ferguson, A.; Nojiri, H.; Miras, H. N.; Song, Y. F.; Long, D. L.; Burkholder, E.; Murrie, M.; Kogerler, P.; Brechin, E. K.; Cronin, L. *Angew. Chem., Int. Ed.* **2008**, *47*, 5609–5612.
(27) Ozeki, T.; Yamase, T. *Acta Crystallogr.* **1994**, *B50*, 128.
(28) Ozeki, T.; Yamase, T. *Acta Crystallogr.* **1994**, *C50*, 327.
(29) Sugeta, M.; Yamase, T. *Bull. Chem. Soc. Jpn.* **1993**, *66*, 444.
(30) Ozeki, T.; Yamase, T.; Kosaka, M. *Acta Crystallogr.* **1993**, *C50*, 1849.

the presence of the bulky POM ligand $[W_5O_{18}]^{6-}$, results in good isolation of the anisotropic Ln^{3+} ions in the solid state (shortest Er−Er distance of 11.225 Å).

Regarding the lanthanide inner coordination sphere, the skew angle (ϕ) can be defined either as the rotation angle between the two rotating triads, each of them belonging to different $[W_5O_{18}]^{6-}$ moieties, or as the offset between the two squares defined by the mean planes through the coordinating oxygen atoms (O2E, O3E, O4E, O5E and O6E, O7E, O8E, O9E; Figure 2). In this particular case, each anionic moiety is twisted 44.2° with respect to the other. This angle is very close to that expected for an ideal D_{4d} symmetry ($\phi = 45°$). Therefore, the coordination site can be described as slightly distorted square-antiprismatic (Figure 2). Er−O distances also support this minor distortion because they range from 2.339(3) to 2.387(3) Å (average value 2.367(7) Å). This geometry corresponds to an approximate D_{4d} LF symmetry, which is also that exhibited by the series of "double-decker" phthalocyanine complexes. However, in this last case, the geometry around the Er^{3+} ion is more distorted with a skew angle of 41.4°. In addition, in the reported compound, the ratio between the interplanar distance $d_{pp} = 2.47(1)$ Å, calculated as the distance between the upper and lower planes containing the four oxygen atoms, and the average distance between the four neighboring oxygen atoms placed in each plane, $d_{in} = 2.86(5)$ Å, is indicative of a certain axial compression of the square antiprism built up by the 8-fold-coordinated Er^{3+} ion. This fact contrasts with the axial elongation exhibited by the "double-decker" phthalocyanine complexes.[19] Concerning the above-mentioned oxygen-based square planes, the φ angle can be defined as well. This parameter, estimated as the angle between the planes' normal vectors, is useful to check the distortion, if any, from perfect coplanarity between the coordinating planes. In the Er complex, φ was found to be 0°, thus confirming minimum deviation from the ideal D_{4d} symmetry.

All of these geometrical differences in the lanthanide coordination sites with respect to the phthalocyaninate complexes, although small, seem to be sufficient to completely change the magnetic relaxation properties of these lanthanide-based complexes.

$[Ln(\beta_2\text{-}SiW_{11}O_{39})_2]^{13-}$ [Ln^{III} = Tb (5), Dy (6), Ho (7), Er (8), Tm (9), and Yb (10)]. Taking into account that all the synthesized compounds were isostructural, crystal structures have only been determined for derivatives **8** and **9**. The identities of **5**−**10** were confirmed by FT-IR and EPMA. These dimeric polyanionic species are composed of a central Ln^{3+} encapsulated by two $(\beta_2\text{-}SiW_{11}O_{39})^{8-}$ units in a distorted square-antiprismatic coordination (pseudo-D_{4d} symmetry; Figure 3). The anionic POM moieties are surrounded by potassium cations for charge balance. Average K−O_W distances are found to be 2.837 and 2.812 Å for **8** and **9**, respectively. As previously indicated for the $[Ln(W_5O_{18})_2]^{9-}$ family, the large number of water molecules present in the crystalline lattice, together with the presence of the bulky POM ligands (β_2-$SiW_{11}O_{39})^{8-}$, results in a good isolation of the anisotropic Ln^{3+} ions in the solid state (shortest Ln−Ln distance of 12.624 and 12.625 Å for Er and Tm derivatives). Ln^{3+} ions are connected to four oxygen atoms belonging to each monolacunary Keggin unit with Ln−O_W and Ln−W distances together with a O_W−Ln−O_W angle strongly affected by the size of the central atom (see Table 4). As expected, when the atomic number of the lanthanide is increased, a decrease of the average Ln−O_W and Ln−W distances is observed. This same effect has been observed for the other structural parameters such as the interplanar distance (d_{pp}), calculated as the distance between the upper and lower square planes containing the four oxygen atoms, and the average in-plane O_W−O_W distance (d_{in}), concerning the four neighboring oxygen atoms within each plane. Figure 5 shows the linear variation of these structural parameters with the Ln^{3+} ionic radius.

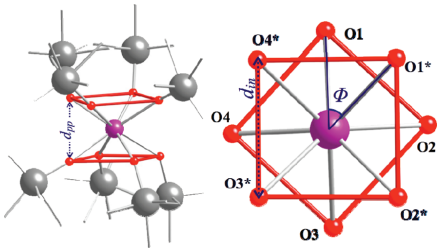

Figure 4. Perspective showing the square-antiprismatic coordination of the central Ln^{3+} ion and the d_{pp} parameter in $[Ln(\beta_2\text{-}SiW_{11}O_{39})_2]^{13-}$ (left). Perspective showing the d_{in} and ϕ structural features (right).

Focusing now on the coordination geometry of the metal complexes (Figure 4), one notices that the ratio between d_{pp} and d_{in} distances is indicative of the presence of a certain compression of the square antiprism, similar to what has been observed in the $[Ln(W_5O_{18})_2]^{9-}$ series. The other parameters (ϕ and φ angles), however, indicate larger distortions from the regular square-antiprismatic D_{4d} symmetry, as compared with the $[Ln(W_5O_{18})_2]^{9-}$ series. Indeed, the skew angle value (ϕ) has been found to be 47.5° and 48.0° for **8** and **9**, respectively. Besides, important deviations from coplanarity between the two coordinating planes have been observed with an average $\varphi = 2.8°$ value (see Table 4). These geometrical differences between the two families are general and should affect the LF parameters and, hence, the magnetic properties.

A final point that deserves to be mentioned concerns the chirality of the $(\beta_2\text{-}SiW_{11}O_{39})^{8-}$ anion. As previously described for the $[Ln(\beta_2\text{-}SiW_{11}O_{39})]^{13-}$ (Ln^{3+} = La, Ce, Sm, Eu, Gd, Tb, Yb, and Lu) series,[12] important attention must be paid to the absolute configuration of the molecular cluster resulting from the relative chirality of the two $(\beta_2\text{-}SiW_{11}O_{39})^{8-}$ moieties. Bassil et al. described these configurations as A, when the relative chirality of one lacunary Keggin unit with respect to the other was (*R*,*R*) or (*S*,*S*) and B for (*S*,*R*) and (*R*,*S*) relative configurations. Note that the A configuration is defined by a C_2 space group,

Table 4. Structural Parameters Concerning the Lanthanide Coordination Sphere in the Series $[Ln(\beta_2\text{-}SiW_{11}O_{39})]^{13-}$

$K_{13}[Ln(\beta_2\text{-}SiW_{11}O_{39})_2]$	Ln^{3+} radius[a] [Å]	d(Ln−O_W) [Å]	d(Ln−W) [Å]	d_{in}[b] [Å]	d_{pp}[c] [Å]	ϕ[d] [deg]	φ[e] [deg]	ref
La	1.061	2.49	4.050	2.964	2.681	39.9	4.1	12
Ce	1.034	2.46	4.028	2.937	2.653	40.8	3.1	12
Sm	0.964	2.41	3.989	2.872	2.583	41.3	2.9	12
Eu	0.950	2.40	3.982	2.863	2.566	44.4	0	12
Gd	0.938	2.40	3.975	2.863	2.566	42.9	2.8	12
Tb	0.923	2.37	3.961	2.833	2.458	44.6	2.8	12
Er	0.881	2.36	3.929	2.832	2.478	47.5	2.8	this work
Tm	0.869	2.60	3.919	2.850	2.477	48.0	2.8	this work
Yb	0.858	2.33	3.918	2.787	2.473	48.3	2.3	12
Lu	0.848	2.32	3.909	2.785	2.458	47.6	2.3	12

[a] Data were extracted from: Cotton, F. A.; Wilkinson, G. *Advanced Inorganic Chemistry*; Limusa: Madrid, Spain, 1998. [b] The d_{pp} parameter defines the average distance between the two oxygen-based square planes. [c] The d_{in} is the average O−O distance within the oxygen-based square planes. [d] ϕ is defined as the relative orientation between the two squares defined by the coordinating oxygen atoms (see the text). [e] φ is defined as the angle between the normal vectors of the oxygen-based square planes (see the text).

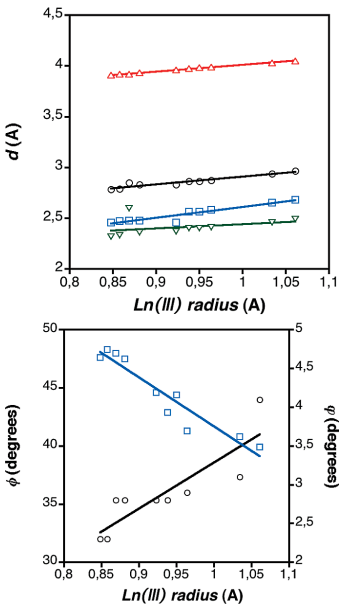

Figure 5. Dependence of the structural parameters concerning the lanthanides' coordination spheres with the Ln^{3+} ionic radius (see Table 4). Plotted data belong to the $[Ln(\beta_2\text{-}SiW_{11}O_{39})_2]^{9-}$ family and have been extracted from ref 12 and the present work. Solid thin lines represent the best linear fitting. (Top) d(Ln−W): red triangles. d_{in}: black circles. d_{pp}: blue squares. d(Ln−O): inverted green triangles. (Bottom) ϕ angle: blue squares. φ angle: black circles. The Eu derivative exhibited an anomalous φ value, and it has been omitted.

while the B configuration corresponds to C_1. For compounds **6**−**9**, only configuration B is observed. This fact is in good agreement with the previous observation that the chirality of the surrounding Keggin units depends on the size of the lanthanide. Indeed, these authors claimed that early lanthanide ions, attending to their bigger size, favor the A configuration, whereas when shifting to a smaller ionic radius, a gradual transition from the A to B configuration is favored. In this context, they observed that the $[Ln(\beta_2\text{-}SiW_{11}O_{39})_2]^{13-}$ systems encapsulating the

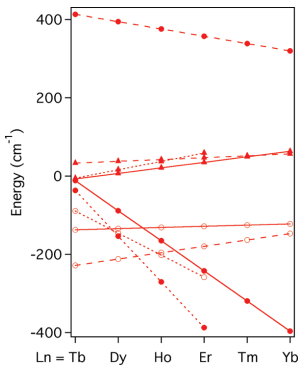

Figure 6. LF parameters $A_2^0\ r^2$ (●), $A_4^0\ r^2$ (○) and $A_6^0\ r^6$ (▲) of $Na_9[Ln(W_5O_{18})_2]\bullet xH_2O$ (dot lines), $K_{13}[Ln(\beta_2\text{-}SiW_{11}O_{39})_2]\bullet xH_2O$ (solid lines) and $[Pc_2Ln]TBA$ families (dashed lines).

smaller lanthanide ions, Yb and Lu, exhibited 100% of the B configuration.

dc Susceptibility Measurements. The magnetic properties of powdered samples of the four members of the $[Ln^{III}(W_5O_{18})_2]^{9-}$ family (Ln = Tb^{3+}, Dy^{3+}, Ho^{3+}, and Er^{3+}) in the form of the χ_mT product versus T are shown in Figure 7. At room temperature, all samples show χ_mT values close to those expected for the free trivalent ion: χ_mT = 11.92 emu K^{-1} mol^{-1} for Tb^{3+} (J = 6, g = $^3/_2$, $\chi_mT_{free\ ion}$ = 11.81), 13.31 emu K^{-1} mol^{-1} for Dy^{3+} (J = $^{15}/_2$, g = $^4/_3$, $\chi_mT_{free\ ion}$ = 14.17), 14.05 emu K^{-1} mol^{-1} for Ho^{3+} (J = 8, g = $^5/_4$, $\chi_mT_{free\ ion}$ = 14.06), and 10.85 emu K^{-1} mol^{-1} for Er^{3+} (J = $^{15}/_2$, g = $^6/_5$, $\chi_mT_{free\ ion}$ = 11.475). When the temperature decreases, the χ_mT value gradually decreases because of depopulation of the highest crystal-field levels.

Figure 8 shows the χ_mT versus Tplots for the six members of the $[Ln(\beta_2\text{-}SiW_{11}O_{39})]^{13-}$family (Ln = Tb^{3+}, Dy^{3+}, Ho^{3+}, Er^{3+}, Tm^{3+}, and Yb^{3+}). Again, at room temperature, the χ_mT values are close to free ion values: χ_mT = 11.16 emu K^{-1} mol^{-1} for Tb^{3+}, 13.71 emu K^{-1} mol^{-1} for Dy^{3+}, 14.21 emu K^{-1} mol^{-1} for Ho^{3+}, 11.56 emu K^{-1} mol^{-1} for Er^{3+}, and 6.82 emu K^{-1} mol^{-1} for Tm^{3+} (J = 6, g = $^7/_6$, $\chi_mT_{free\ ion}$ = 7.15), 2.68 emu K^{-1} mol^{-1} for Yb^{3+} (J = $^7/_2$, g = $^8/_7$, $\chi_mT_{free\ ion}$ = 2.57).

Determination of LF Parameters. The LF describes the effect of the electric field due to the surrounding ligands acting on a given paramagnetic metal ion. For the C_4 point group, the

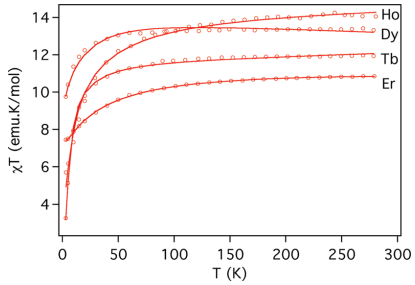

Figure 7. Plots of the $\chi_m T$ product versus T for the four members of the $Na_9[Ln(W_5O_{18})_2]\cdot xH_2O$ family (Ln = Tb, Dy, Ho, and Er). Solid lines are the best simultaneous fits obtained using the Hamiltonian in eq 2 and the conditions in eq 3.

LF Hamiltonian can be written taking into account the operator equivalent as

$$\hat{H} = A_2^0 r^2 \alpha \hat{O}_2^0 + A_4^0 r_4 \beta \hat{O}_4^0 + A_4^4 r^4 \beta \hat{O}_4^4 + A_6^0 r^6 \gamma \hat{O}_6^0 + A_6^4 r^6 \gamma \hat{O}_6^4 \quad (1)$$

where α, β, and γ coefficients are the constants tabulated by Stevens for each lanthanide,[20] $\hat{O}_k^q$ are the operator equivalents and can be expressed as polynomials of the total angular momentum operators,[21] r^k are radial factors, and A_k^q are numerical parameters. The products $A_k^q\ r^k$ are the parameters to be determined.

In the $[Ln^{III}(W_5O_{18})_2]^{9-}$ family, each anionic $[W_5O_{18}]^{6-}$ moiety is twisted 44.2° with respect to the other. This skew angle is very close to that expected for an ideal D_{4d} symmetry ($\phi = 45°$). Hence, an idealized D_{4d} symmetry can be assumed in this case. For this symmetry, the two LF terms with $q \neq 0$ ($A_4^4 r^4$ and $A_6^4 r^6$) vanish, and the LF Hamiltonian can be simplified to give

$$\hat{H} = A_2^0 r^2 \alpha O_2^0 + A_4^0 r^4 \beta O_4^0 + A_6^0 r^6 \gamma O_6^0 \quad (2)$$

In the $[Ln(\beta_2\text{-}SiW_{11}O_{39})]^{13-}$ family, this assumption may still be valid and, even if the distortions in the square antiprism are larger, the two LF terms with $q \neq 0$ are expected to be small and can be neglected. Ishikawa demonstrated that the LF parameters of an isomorphic series of lanthanide complexes could be determined by a simultaneous fit of all of the $\chi_m T$ values under the assumption that the LF parameters from the f^8 system to the f^{13} system show a linear variation.[6] Under these conditions, the $A_k^q r^k$ coefficients can be expressed as a linear function of the number of f electrons, n_f:

$$A_k^q r^k = a_k^q + b_k^q (n_f - 10.5) \quad (3)$$

where n_f values range from 8 to 13 when moving from Tb^{3+} to Yb^{3+}. The constant 10.5 represents the average value of n_f for the full series.

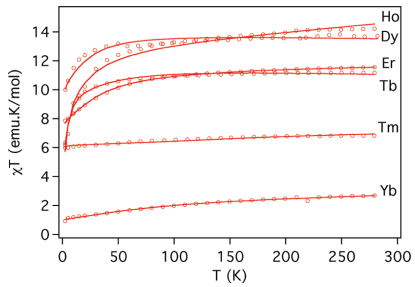

Figure 8. Plots of the $\chi_m T$ product versus T for the six members of the $K_{13}[Ln(\beta_2\text{-}SiW_{11}O_{39})_2]\cdot xH_2O$ family (Ln = Tb, Dy, Ho, Er, Tm, and Yb). Solid lines are the best simultaneous fits obtained using the Hamiltonian in eq 2 and the conditions in eq 3.

Table 5. LF Parameters Determined for the $[LnW_{10}]^{9-}$ and $[LnW_{22}]^{13-}$ Families (in cm^{-1})

	$[LnW_{10}]^{9-}$ series			$[LnW_{22}]^{13-}$ series		
Ln	$A_2^0 r^2$	$A_4^0 r^4$	$A_6^0 r^6$	$A_2^0 r^2$	$A_4^0 r^4$	$A_6^0 r^6$
Tb	−36.8	−89.0	−5.2	−11.3	−137.4	−7.1
Dy	−153.6	−145.5	16.3	−88.3	−134.4	7.0
Ho	−270.4	−202.0	37.7	−165.2	−131.3	21.1
Er	−387.2	−258.5	59.2	−242.2	−128.2	35.2
Tm				−319.2	−125.2	49.2
Yb				−396.1	−122.1	63.3

Following the Ishikawa procedure, we have estimated the best set of LF parameters in both families of rare-earth POMs (Figure 6 and Table 5). These values are extracted from a simultaneous fit of 40 $\chi_m T$ values per compound from 2 K up to room temperature. Figures 7 and 8 show the excellent agreement between the experimental values and the theoretical expectations. If we compare these two sets of LF parameters with those derived from the phthalocyaninatolanthanide complexes (Figure 6), the most important difference is the sign of the $A_0^2 r^2$ parameter, which is negative in the two rare-earth POM families but positive in the phthalocyaninatolanthanide family (see Table 5). We can associate this change in the sign with differences in the axial distortion of the coordination site. In fact, while the POM derivatives exhibit an axial compression, axial elongation of the square antiprism is observed in the phthalocyaninatolanthanide complexes. This different sign has important consequences in the structure of the low-lying energy levels and in the dynamic magnetic properties of these complexes, as we will discuss in the next sections.

A simultaneous fit of the susceptibility data and ^{17}O and ^{183}W NMR paramagnetic shifts has been performed for the $[Ln^{III}(W_5O_{18})_2]^{9-}$ family. The room temperature ^{17}O and ^{183}W NMR chemical shifts have been extracted from different works.[22] This simultaneous fit does not have a good and unique solution, and the result depends on how the weight of each experimental>property data is treated. NMR fit gives a solution with positive values of $A_0^2 r^2$, whereas the opposite is obtained from the susceptibility fit. These differences may come from different causes. First, the NMR experiments are performed in solution, whereas susceptibility measurements are performed on powdered samples. In solution, even if the general configuration of the complex is unchanged, changes in the bond lengths and angles can occur. On the other hand, in POMs, an important electron delocalization from the paramagnetic center to oxygen and wolfram

atoms has been proven, and important contact contributions to the chemical shift can be possible even for apical atoms. For this reason we have decided not to use the NMR data but more reliable techniques such as electron paramagnetic resonance (EPR) and specific heat.

Electronic Structure of $[Ln(W_5O_{18})_2]^{9-}$ and $[Ln(\beta_2\text{-}SiW_{11}O_{39})_2]^{13-}$. The electronic structure of the ground-state multiplet of each lanthanide complex expressed in terms of the LF parameters can be obtained from a diagonalization of the $(2J + 1)$-dimension eigenmatrix. Figure 9 shows the $2J + 1$ energy sublevels of the ground state of each system as a function of the M_J values.

a. $[Tb(W_5O_{18})_2]^{9-}$ (1) and $[Tb(\beta_2\text{-}SiW_{11}O_{39})_2]^{13-}$ (5) Systems. In both systems, the ground substate is that with the lowest M_J value, 0. In the case of the Lindqvist derivative, the first excited level, $M_J = \pm 1$, is around 15 cm^{-1} above the singlet ground substate, while in the Keggin derivative, the $M_J = \pm 1$ doublet is almost degenerate with the ground substate. The structure of the energy level pattern is very similar in both systems. For the low $|M_J|$ values, one can observe the distribution of levels expected for a positive axial zero-field splitting (ZFS) of order 2, $A_2^0r^2\alpha > 0$. The highest $|M_J|$ value, ± 6, is stabilized because of the negative axial ZFS of order 4, $A_4^0r^4\beta < 0$, and the doublet $M_J = \pm 6$ can become the ground substate for big values of the $A_2^0r^2/A_4^0r^4$ ratio. In fact, for **5**, this ratio is large enough to place the levels $M_J = 0$ and ± 6 very close in energy. In the Ishikawa complex, the $M_J = \pm 6$ doublet is even more stabilized and becomes the ground substate because of the fact that $A_2^0r^2\alpha < 0$.

b. $[Dy(W_5O_{18})_2]^{9-}$ (2) and $[Dy(\beta_2\text{-}SiW_{11}O_{39})_2]^{13-}$ (6) Systems. The lowest Kramers doublet for both systems corresponds to $M_J = \pm^{11}/_2$. The first excited doublet $M_J = \pm^9/_2$ is very close in energy to the ground substate in both systems (with gaps of ca. 4 and 2 cm^{-1}, respectively).

c. $[Ho(W_5O_{18})_2]^{9-}$ (3) and $[Ho(\beta_2\text{-}SiW_{11}O_{39})_2]^{13-}$ (7) Systems. For the Ho^{3+} complexes, the ground substate is the doublet $|M_J| = \pm 4$, and the first excited level is the doublet $M_J = \pm 5$ with energy gaps of 16 and 6 cm^{-1}, respectively.

d. $[Er(W_5O_{18})_2]^{9-}$ (4) and $[Er(\beta_2\text{-}SiW_{11}O_{39})_2]^{13-}$ (8) Systems. The ground substate is the $M_J = \pm^{13}/_2$ doublet in both systems. For **4**, the $M_J = \pm^1/_2$ doublet is very close in energy, around 3 cm^{-1}, and the $M_J = \pm^{15}/_2$ doublet is at 17 cm^{-1}. In **8**, the ground substate is more stabilized and the doublets with $M_J = \pm^1/_2$ and $\pm^{15}/_2$ are at 24 and 33 cm^{-1}, respectively. These three doublets are well isolated from the rest of the doublets. This scheme results from an opposite effect of the different LF terms. High $|M_J|$ values are the usually stabilized by a negative second-order LF term ($A_2^0r^2\alpha$), but in this case, the higher order LF terms stabilize the $M_J = \pm^1/_2$ doublet. Notice that this energy level scheme is completely different from that reported for the Ishikawa complex. In fact, in this complex, the $M_J = \pm^1/_2$ doublet becomes the ground substate because it is strongly stabilized as a result of a positive second-order LF term.

e. $[Tm(\beta_2\text{-}SiW_{11}O_{39})_2]^{13-}$ (9) System. The ground substate for this complex is the doublet with the highest $|M_J|$ value ($=\pm 6$). The energy gap between this doublet and the first excited doublet, $M_J = \pm 3$, is around 400 cm^{-1}. This large energy gap makes the ground substate the most populated level even at room temperature with a population ratio of 80%. The constant value of $\chi_m T$ in all ranges of temperature is due to this small depopulation of the other LF sublevels.

f. $[Yb(\beta_2\text{-}SiW_{11}O_{39})_2]^{13-}$ (10) System. In this complex, the ground substate is the doublet with $M_J = \pm^5/_2$, with the first excited sublevel ($M_J = \pm^7/_2$) placed at 100 cm^{-1}. The energy pattern is the result of a high and negative second-order LF term, which stabilizes the $M_J = \pm^7/_2$ doublet, and positive fourth- and sixth-order LF terms, which stabilize the $M_J = \pm^5/_2$.

Low-Lying Energy Levels in 4. Using the indirect information provided by the study of the thermal dependence of the magnetic susceptibility, the LF parameters and the resulting energy splittings of the ground-state multiplets of the 10 POM lanthanide complexes have been estimated. This method has been employed to determine the ground substates of these complexes. However, the resulting splitting structures contain one or various excited sublevels that are very close in energy, or even degenerate, to the ground sublevel. In these conditions, the energy splitting of these low-lying energy levels can only be considered approximate, and other techniques are required to obtain more quantitative information. Let us illustrate this point with the $[Er(W_5O_{18})_2]^{9-}$ derivative (**4**), which shows a complex splitting structure of the low-lying levels, with three levels separated by less that 20 cm^{-1}. As complementary techniques, we have used EPR and specific heat.

The powder X-band EPR spectrum of the sodium salt of **4**, performed at low temperatures, shows a strong signal around 800 G (Figure 10). The intensity of this signal increases when the temperature increases from 8 to 25 K. This indicates that the transition associated with this signal has its origin in an excited state. Taking into account the energy levels obtained for **4** with an ideal D_{4d}-symmetry LF Hamiltonian, only the transition within the excited doublet $M_J = \pm^1/_2$ is allowed. Evaluation of the energy levels, including Zeeman interaction for different orientations of the external magnetic field, places this transition within the experimental range of magnetic fields available in the X band. The temperature dependence of the intensity of this signal can be reproduced by assuming a three-level energy pattern, as derived from the susceptibility analysis. In this model, the doublet $\pm^1/_2$ is an excited state that has to be situated 17.5 cm^{-1} above the ground doublet $\pm^{13}/_2$ and 11.1 cm^{-1} below the next excited doublet $\pm^{15}/_2$. The powder EPR spectra for the other members of the family have also been

(31) Ozeki, T.; Yamase, T. *Acta Crystallogr.* **1993**, *C49*, 1577.
(32) Ozeki, T.; Yamase, T.; Ueda, K. *Acta Crystallogr.* **1993**, *C49*, 1572.
(33) Sawada, K.; Yamase, T. *Acta Crystallogr.* **2002**, *C58*, 149.

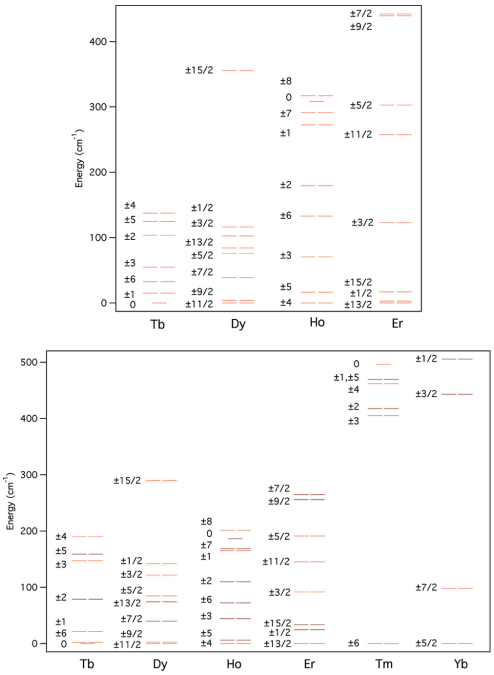

Figure 9. Energy level diagrams of the ground-state multiplets for $Na_9[Ln(W_5O_{18})_2]\cdot xH_2O$ and $K_{13}[Ln(\beta_2\text{-}SiW_{11}O_{39})_2]\cdot xH_2O$ families derived from the susceptibility data.

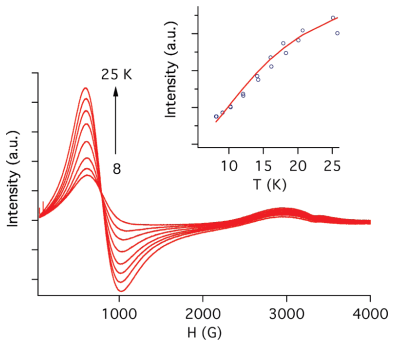

Figure 10. X-band EPR spectra for complex **4** at different temperatures from 8 to 25 K. Inset: Evolution of the intensity of the signal as a function of the temperature. The solid line is the theoretical intensity for a three-level model (see the text for further discussion).

performed, but the very complex structure observed has prevented us from extracting useful information on the low-lying energy spectrum.

Specific heat measurements support that the energy gap between the ground doublet and the first excited one is not smaller than ca. 17 cm^{-1} in **4**, in full agreement with the EPR data. The measurements, performed down to 0.35 K and under zero magnetic field, are shown in Figure 11. They are compared with data measured, under identical conditions,

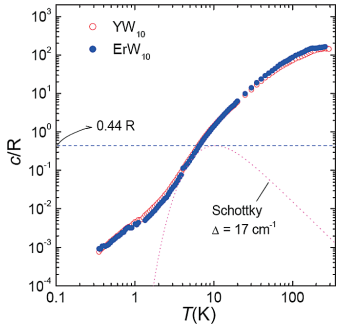

Figure 11. Specific heat of **4** at zero field. Thin lines show the different contributions.

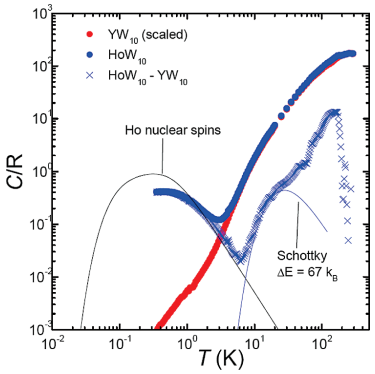

Figure 12. Specific heat of **3** at zero field compared with the data measured on the $[Y(W_5O_{18})_2]^{9}$ nonmagnetic compound.

on the nonmagnetic derivative containing $[Y(W_5O_{18})_2]^{9-}$. We observe that the two sets of data overlap, within the experimental uncertainties, over the whole temperature range. This is a clear indication that the specific heat is fully dominated by contributions that are equally present in the two compounds. These arise from (a) vibrations of the lattice (acoustic and optical phonons), which dominate above 2 K, and (b) the hyperfine split levels of ^{183}W (14.3% in natural W) nuclear spins ($I = {}^1/_2$). In the temperature range between 2 and 8 K, the specific heat is approximately proportional to T,^{3} in agreement with the Debye model for the specific heat of acoustic phonons. The fit gives a Debye temperature $\Theta_D = 57(2)$ K. Concerning the electronic levels of the erbium ions, we can estimate from these data a lower bound for the energy difference between the ground state and the first excited doublet. For two doublets separated an energy of Δ, the Schottky shows a peak at a temperature $T_{max} = 0.42\Delta/k_B$, where $c_{max} = 0.44R$. Because no such contribution is observed below 10 K, the gap Δ should not be smaller than 17 cm^{-1}. An illustrative example of this magnetic contribution is provided by the dotted line in Figure 11.

Specific heat measurements have also been performed on **3** (Figure 12). As described above for **4**, we have included the data measured on the nonmagnetic $[Y(W_5O_{18})_2]^{9-}$ compound as a reference. In this case, though, we have

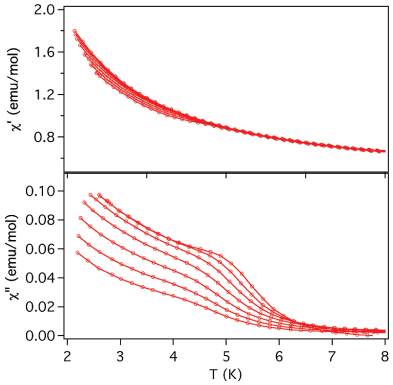

Figure 13. In-phase and out-of-phase dynamic susceptibility of **3**. High-frequency measurements from left to right: 1000, 1500, 2200, 3200, 4600, 6800, and 10000 Hz.

rescaled the latter data by a factor 1.2 to make them overlap with the data obtained for $[Ho(W_5O_{18})_2]^{9}$ above 250 K (where only lattice vibrations contribute). This factor might arise from the effect that the molecular mass has on the energies of the vibration modes or from a small error in the determination of the sample's mass. As observed for **4**, lattice vibrations dominate above 5 K. Yet, there is a small difference between the curves measured on the two compounds (blue crosses in Figure 12), which might be compatible with the presence of a Schottky anomaly centered near 25 K. This would correspond to an energy-level splitting on the order of 67 k_B. The additional contribution observed at even higher temperatures is probably an artifact related to the large contribution introduced by the apiezon grease. Therefore, what we see might be caused by a nonperfect subtraction of the addenda. The curves measured on the magnetic and nonmagnetic compounds deviate below 4 K. This contribution suggests the presence of low energy levels (energy splitting on the order of 1 k_B), which probably arise from the hyperfine split levels of the holmium nuclear spins (see the prediction in Figure 12). Therefore, and in contrast with the situation observed in the case of erbium nuclei, the holmium nuclear spins remain in thermal equilibrium down to very low temperatures. The different behavior of the nuclear specific heat might be associated with the different spin−lattice relaxation times (or spin-tunneling times) measured for the electronic magnetic moments of erbium and holmium: $\tau \approx 10^{-3}$ s and $\tau \approx 10^{-4}$ s, respectively.

ac Magnetic Susceptibility Measurements. Dynamic magnetic susceptibility measurements have been performed at low temperatures (down to 2 K) for the 10 salts of the two series of POM complexes.

In the $[Ln(W_5O_{18})_2]^{9-}$ series, only Ho (**3**) and Er (**4**) derivatives exhibit clear frequency-dependent out-of-phase signals (χ'') at low temperatures. Thus, upon cooling, a maximum or a shoulder is observed at high frequency (1000−10000 Hz), followed by sharp increases in χ'' at lower temperatures (Figures 13 and 14). In turn, the Dy derivative (**2**) only shows an increase in χ'' below 4 K (SI 5 in the Supporting Information), while Tb (**1**) does not show any χ'' signal down to 2 K (SI 4 in the Supporting Information). In the $[Ln(\beta_2\text{-}SiW_{11}O_{39})_2]^{13-}$ series, Er (**8**) and Yb (**10**) derivatives show a shoulder at high frequencies and a divergence in χ'' at lower temperatures (Figure 5 and SI 10 in the Supporting Information). In turn, Dy (**6**) and Ho (**7**) derivatives only show an increase in χ'' below 6 K (SI 7 and SI 8 in the Supporting Information), while Tb (**5**) and Tm (**9**) do not show any χ'' signal down to 2 K (SI 5 and SI 9 in the Supporting Information).

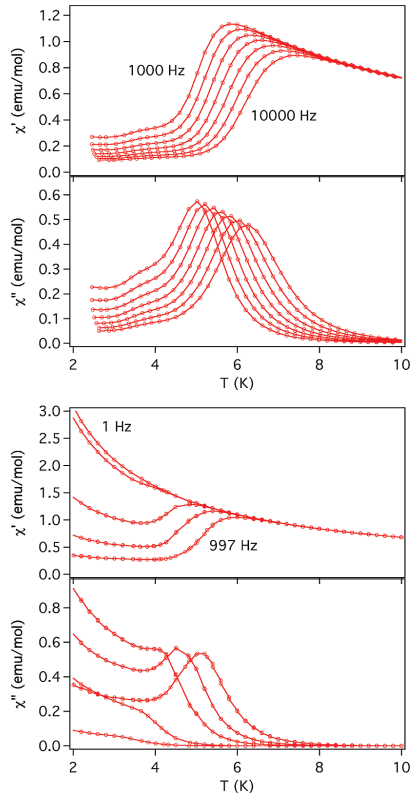

Figure 14. In-phase and out-of-phase dynamic susceptibility of **4**. (Top) High-frequency measurements from left to right: 1000, 1500, 2200, 3200, 4600, 6800, and 10000 Hz. (Bottom) Low-frequency measurements from top to bottom: 1, 10, 110, 332, and 997 Hz.

$[Ho(W_5O_{18})_2]^{9-}$. In compound **3**, one observes a shoulder in χ'' situated at ca. 5 K (for a frequency of 10 000 Hz), which is strongly frequency-dependent and tends to disappear when the frequency is reduced, and a divergence at lower temperatures (Figure 13). This behavior closely resembles that of the Er derivative (**4**) when studied at low frequencies.

$[Er(W_5O_{18})_2]^{9-}$. The magnetic properties of **4** reveal the typical features associated with the SMM behavior. Thus, both χ' and χ'' show strong frequency dependencies, which indicate the presence of a slow relaxation process involving

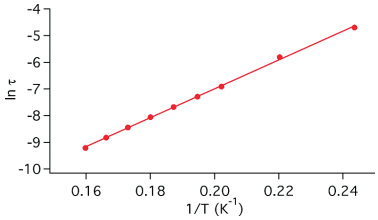

Figure 15. Relaxation-time fitting to the Arrhenius law in the 110−10000 Hz interval for **4**.

an energy barrier for the reversal of the magnetization. Depending on the frequency of the applied ac field, χ' presents a maximum between 5.5 and 7.5 K, while χ'' has also a maximum between 5 and 6.2 K for 1000 and 10 000 Hz, respectively (Figure 14). Below the blocking temperature, the susceptibility increases as the system is cooled down and this increase becomes more pronounced as the frequency is decreased. In this situation, the maximum, which shifts toward lower temperatures when the frequency is decreased, becomes closer to the divergence, appearing only as a shoulder. The divergence may be indicative of a fast relaxation process within the ground-state doublet $M_J = \pm^{13}/_2$ because it is the only populated at these temperatures according to the EPR and specific heat data (Figures 10 and 11).

Analyses of the frequency dependence of the χ'' peaks through an Arrhenius plot permits the estimation of the magnetization−relaxation parameters in this system (Figure 15). Best fitting affords a barrier height (U_{eff}/k_B) of 55.2 K with a preexponential factor (τ_O) of 1.6×10^{-8} s. Given the good insulation of Er^{3+} ions provided by the diamagnetic polyoxowolframate framework (the shortest Er−Er distance in the crystal structure is 11.225 Å), the slow relaxation process exhibited by **4** should be considered as a single-molecule property.

To discard the presence of magnetic impurities that might be responsible for the "anomalous" increase of the magnetic susceptibility below the blocking temperature, the frequency dependence of the ac susceptibility of **4** was measured at different temperatures (Figure 16). The fitting of the experimental data to a Cole−Cole function suggests the presence of a very narrow distribution of relaxation times (least-squares fittings yielded $\alpha = 0.82$). Besides, no additional out-of-phase peaks are observed, indicating that at any temperature there is only one dominating relaxation process related to a single magnetic species.

To understand the apparently "strange" behavior of the dynamic susceptibility, we must bring into play the definition of the Cole−Cole function.[23] According to it, χ'' can be defined as

$$\chi'' = (\chi_T - \chi_S)\frac{(\omega\tau)^{\alpha}\sin(\alpha\pi/2)}{1 + (\omega\tau)^{2\alpha}} \qquad (4)$$

This expression simplifies to the well-known Debye equation when $\alpha = 1$. The χ_T and $\chi_S$susceptibilities stand for the equilibrium and high-frequency (or adiabatic) limits, respectively. When measured as a function of the frequency, these

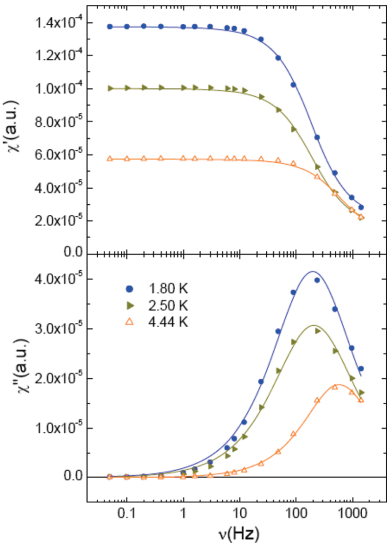

Figure 16. ac susceptibility of **4** measured as a function of the frequency at the temperatures indicated by the caption. Top: Real component. Bottom: Imaginary component. Solid lines represent the best fitting of the experimental data to a Cole−Cole function, yielding $\alpha = 0.82$.

two parameters remain constant and a maximum of χ'' is observed when the τ product is equal to 1, exactly as is experimentally observed in this case. On the other hand, things are quite different when χ'' is measured as a function of the temperature. Then, not only τ but also χ_T (and to a much lesser extent χ_S) depend on the temperature. Usually (e.g., in the case of Mn12 and many other SMMs), these parameters remain almost constant because the relaxation time depends exponentially on the temperature in the temperature range accessible to ac susceptibility experiments. On the contrary, in this particular case, the relaxation time tends to become independent of the temperature below approximately 3 K. This can be seen from the fact that the maxima of χ'' do not shift to lower frequencies as T decreases. In other words, there is a crossover from a thermally activated relaxation mechanism, above 3 K, to a direct (or pure tunneling) mechanism below 3 K. This temperature-independent tunneling mechanism is very fast compared to what is usually observed in other SMMs: from the Cole−Cole fits, we infer relaxation times on the order of milliseconds. Still, at any temperature, one or the other is dominating (i.e., provides the fastest relaxation channel). Therefore, when we measure χ'' as a function of the temperature at fixed frequency, the susceptibility does not get fully blocked because the relaxation time remains very small and it does not change with decreasing T. As a result, and according to the Cole−Cole equation, the imaginary component "inherits" the variation with temperature of the equilibrium susceptibility, which is approximately proportional to the reciprocal temperature. The ratio of χ'' to the equilibrium susceptibility depends on the frequency, and for this reason, χ'' still depends on the frequency.

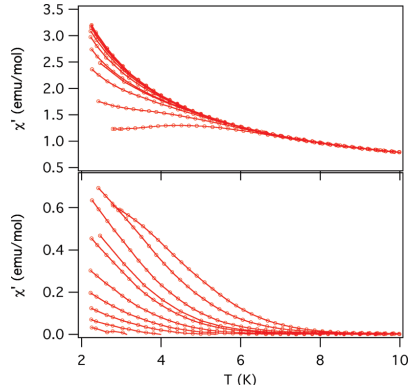

Figure 17. In-phase (top) and out-of-phase (bottom) dynamic susceptibility of **8**. High-frequency measurements from left to right: 1000, 1500, 2200, 3200, 4600, 6800, and 10 000 Hz.

In summary, the observed temperature dependence of χ'' reflects the existence of a fast tunneling relaxation channel. This relaxation mechanism becomes dominant over thermally activated processes already below approximately 3 K. In this particular case, it is so fast that the superparamagnetic blocking (i.e., the condition $\tau \gg 1$) is only attained for very high frequencies and prevents χ'' from vanishing completely.

The two relaxation processes, which are clearly seen in **4**, are still present in **3**. The main difference is that the tunneling process dominates the low-temperature behavior and, therefore, the thermally activated relaxation process can only be observed for the higher frequencies.

$[Dy(\beta_2\text{-}SiW_{11}O_{39})_2]^{13-}$. Compound **6** exhibits a strong frequency dependence of the out-of-phase signal below 10 K (SI 6 in the Supporting Information). Nevertheless, no blocking is observed down to 2 K, preventing extraction of the dynamical parameters.

$[Ho(\beta_2\text{-}SiW_{11}O_{39})_2]^{13-}$. In compound **7**, χ'' increases continuously below 6 K without showing any blocking down to 2 K (SI 7 in the Supporting Information). As previously observed in the Er derivative of the Keggin series (**8**) and in the Ho derivative of the Keggin series (**7**), the slow relaxation process characteristic of the SMM behavior is faster than that in the Lindqvist Ho analogue (**3**) and therefore lower temperatures are needed to fully characterize **7**.

$[Er(\beta_2\text{-}SiW_{11}O_{39})_2]^{13-}$. The ac susceptibility curves of **8** are shown in Figure 17. In this derivative, strong frequency dependencies in χ'' and χ' are also observed, which are indicative of a SMM behavior. However, the maxima in the χ'' peak are not observed even at 2 K, indicating that the magnetization relaxes much faster in this compound than in **4**. Thus, in **8**, the blocking temperature has to be situated below this temperature. Lower temperatures are now required to complete the characterization of this molecular nanomagnet.

$[Yb(\beta_2\text{-}SiW_{11}O_{39})_2]^{13-}$. A strong frequency dependence of the out-of-phase signal of **10** below 10 K is also observed (SI 9 in the Supporting Information). As commented on above, additional lower temperature magnetic characterization is required to extract information concerning the dynamical parameters.

Final Discussion. In the last years, POM chemistry has motivated an increasing interest in molecular magnetism by providing ideal examples to study the exchange interactions and the electron hopping in high-nuclearity magnetic and mixed-valence clusters.[24] Very recently, new possibilities in the emerging area of quantum computing have been foreseen for these magnetic complexes.[25] In a recent communication, we have shown that POM complexes containing a single lanthanide ion can provide examples of SMMs.[8] Almost simultaneously, the first example of a polynuclear magnetic cluster assembled by POMs exhibiting SMM behavior has also been reported.[26] These novel properties of POMs enhance the relevance of these inorganic molecules in molecular magnetism because a plethora of a new series of SMMs can be foreseen by a suitable choice of POM ligands.

We have shown in this work that POM complexes containing a single lanthanide ion in an antiprismatic geometry with approximately D_{4d} symmetry can exhibit SMM behavior. This has been demonstrated in the families $[Ln(W_5O_{18})_2]^{9-}$ (Ln^{III} = Tb, Dy, Ho, and Er) and $[Ln(\beta_2\text{-}SiW_{11}O_{39})_2]^{13-}$ (Ln^{III} = Tb, Dy, Ho, Er, Tm, and Yb). Magnetic relaxation properties typical of SMMs have been observed in various members of the two families, namely, the Ho and Er derivatives of the former series (compounds **3** and **4**) and the Dy, Ho, Er, and Yb derivatives of the second series (compounds **6**−**8** and **10**). In the $[Er(W_5O_{18})_2]^{9-}$ derivative (**4**), the presence of a frequency-dependent maximum in χ'' has enabled us to estimate the energy barrier for the reversal of the magnetization (U_{eff} = 55.2 K). Although the other members also show frequency-dependent χ'' signals, this energy barrier seems to be smaller and thus the blocking temperatures are expected to be situated below 2 K.

To understand why these six compounds exhibit this behavior, we have estimated the LF parameters for all of the reported complexes and the resulting splitting of the J ground-state multiplet of the lanthanide ion. We can observe that these compounds have ground-state doublets with large $|M_J|$ values, thus achieving an easy axis of the magnetization (in the Dy derivatives with $J = {}^{15}/_2$, $M_J = \pm{}^{11}/_2$ is the ground state; in the Ho derivatives with $J = 8$, $M_J = \pm 4$ is the ground state; in the Er derivatives with $J = {}^{15}/_2$, $M_J = \pm{}^{13}/_2$ is the ground state; in the Yb derivative with $J = {}^{7}/_2$, $M_J = \pm{}^{5}/_2$ is the ground state). With these LF parameters, the ground state of the Tb derivatives (**1** and **5**) turns out to be a singlet $M_J = 0$. This explains why these last two compounds do not behave as SMMs.

If we compare these POM lanthanide derivatives with the phthalocyaninatolanthanide complexes reported by Ishikawa et al.,[7] one can find significant differences and similarities in the magnetic relaxation properties:

Thus, while in POM complexes, the Er derivatives behave as SMMs, in the phthalocyaninato complexes, they do not show any sign of SMM behavior. In turn, the Tb derivative behaves as a SMM in the phthalocyaninato complexes but not in the POMs. These differences come from the different LF splittings as a consequence of the different structural

distortions observed in the lanthanide site. Thus, while POM complexes show an axial compression of the lanthanide coordination site, in the phthalocyaninato family, an axial elongation is observed. This small structural change leads to different LF parameters and, in particular, to a change of the sign of the axial ZFS parameter of order 2, $A_2^0\langle r^2\rangle$. As a consequence, the lowest-lying energy levels for erbium and terbium are very different and almost reversed in the two classes of complexes. In fact, while in the case of erbium the POM ligands stabilize larger $|M_J|$ values, the phthalocyaninato ligand stabilizes the lowest value, $M_J = \pm 1/2$. In a similar way, in the terbium case, the POM derivatives stabilize the singlet $M_J = 0$, while the doublet with the largest J value, $M_J = \pm 6$, becomes the ground state in the phthalocyaninato derivative.

On the other hand, one can notice that the magnetic relaxation processes are faster in POMs than in the phthalocyaninato complexes showing SMM behavior. The reason can be related with the smaller separation between the lower-lying energy levels caused by the LF splitting, which in POM derivatives often contain two or more levels separated by less than 30 cm^{-1}. Another related question is the observation that, in general, for a given lanthanide, the magnetization of the Keggin-type series relaxes faster than that for the Lindqvist one. One observes in Figure 9 that in both series the LF leads to a similar pattern for the lower-lying energy levels. Therefore, similar magnetic relaxation properties should be expected. However, the sublevel structures have been determined under the assumption of a purely axial D_{4d} symmetry, when nonaxial distortions are clearly present in the Keggin-type derivatives (the two coordinating planes are not parallel). This type of distortion, which is absent in the Lindqvist-type derivatives, may account for the faster magnetic relaxation observed in the Keggin-type derivatives. In fact, apart from having a non-negligible influence on the sublevel structures, this distortion can also mix the different wave functions.

A final point that deserves to be discussed concerns the divergence in χ'' observed in this class of mononuclear lanthanide SMMs at temperatures below the blocking temperature. Such a behavior is specific for this class of SMMs and is in sharp contrast to that observed in the cluster-based SMMs (Mn_{12}, for example) in which χ'' tends to vanish below the blocking temperature. In the mononuclear lanthanide SMMs, both processes, the thermally activatd relaxation process giving rise to the observation of a maximum in χ'' due to the superparamagnetic blocking of the magnetic moments and a very fast tunneling process giving rise to a divergence in χ'', seem to coexist. This is clearly observed in **4** but also appears in other derivatives, such as, for example, in **3** and **10**, although in these compounds, the maximum in χ'' is less pronounced and is often masked by the divergence. Notice that this kind of behavior was already observed in the phthalocyaninatolanthanide complexes. In that case, the divergence was attributed to the presence of intermolecular magnetic interactions between adjacent complexes. However, in our case, the large intermolecular distances provided by the bulky POM clusters keep the lanthanides well-insulated (the shortest Er−Er distance in **4** is 11.225 Å) and only the magnetic dipolar interactions are possible. In these conditions, the divergence seems to be rather associated with a single-molecule property. A preliminary investigation on the low-temperature spin dynamics of these systems suggests that this divergence corresponds to a very fast quantum tunneling process within the $\pm M_J$ ground-state doublet. Moreover, this anomalous behavior appears as the most attractive feature of these materials because for the first time it enables the direct study of the crossover between thermally activated relaxation and direct tunneling by means of a single, and simple, experimental technique: linear ac susceptibility.

Acknowledgment. Financial support from the European Union (NoE MAGMANet and MolSpinQIP), the Spanish Ministerio de Ciencia e Innovación (Project Consolider-Ingenio in Molecular Nanoscience, CSD2007-00010, and Projects MAT2007-61584, CTQ-2005-09385, and NAN2004 09270C03-03), the Generalitat Valenciana, and the Gobierno de Aragón (Project PM012) is gratefully acknowledged. M.A. and S.C. thank the AECI-MAE and MCI for scholarships. We also acknowledge the help of J. M. Martínez-Agudo with the magnetic and EPR measurements.

Supporting Information Available: Crystal structure files in CIF format (files 1 and 2 correspond to compounds **8** and **9**, respectively), FT-IR spectrum and EPMA data for the whole set of compounds together with the ac magnetic susceptibility data for **1**, **2**, **5**−**7**, **9**, and**10**. This material is available free of charge via the Internet at http://pubs.acs.org.

IC801630Z

Supplementary Information

Mononuclear Lanthanide Single-Molecule Magnets Based on the Polyoxometalates $[Ln(W_5O_{18})_2]^{9-}$ and $[Ln(\beta_2\text{-}SiW_{11}O_{39})_2]^{13-}$ (Ln^{III} = Tb, Dy, Ho, Er, Tm and Yb)

Murad A. AlDamen, Salvador Cardona-Serra, Juan M. Clemente-Juan, Eugenio Coronado,* Alejandro Gaita-Ariño, Carlos Martí-Gastaldo, Fernando Luis and Oscar Montero.

Table of Contents

SUPPLEMENTARY INFORMATION **1**
SI 1. FT-IR SPECTRA FOR THE $[Ln(W_5O_{18})_2]^{-9}$ FAMILY WHERE LN=TB, DY, HO AND ER. 2
SI 2. FT-IR SPECTRA FOR THE $[Ln(\beta_2\text{-}SiW_{11}O_{39})_2]^{13-}$ FAMILY WHERE LN=TB, DY, HO, ER, TM AND YB. 4
SI 3. ELECTRON PROBE MICROANALYSIS (EPMA) DATA FOR THE $[Ln(W_5O_{18})_2]^{-9}$ AND $[Ln(\beta_2\text{-}SiW_{11}O_{39})_2]^{13-}$ FAMILIES. 6
SI 4. IN-PHASE (UP) AND OUT-OF-PHASE (DOWN) DYNAMIC SUSCEPTIBILITY OF 1 AT 1467, 2154, 3162, 4641, 6813 AND 10000 HZ. 7
SI 5. IN-PHASE (UP) AND OUT-OF-PHASE (DOWN) DYNAMIC SUSCEPTIBILITY OF 2 AT 1000, 1467, 2154, 3162, 4641, 6813 AND 10000 HZ. 8
SI 6. IN-PHASE (UP) AND OUT-OF-PHASE (DOWN) DYNAMIC SUSCEPTIBILITY OF 5 AT 1 AND 110 HZ. 9
SI 7. IN-PHASE (UP) AND OUT-OF-PHASE (DOWN) DYNAMIC SUSCEPTIBILITY OF 6. HIGH FREQUENCY MEASUREMENTS FROM LEFT TO RIGHT: 1, 10, 110, 332 AND 1000 HZ. 10
SI 8. IN-PHASE (UP) AND OUT-OF-PHASE (DOWN) DYNAMIC SUSCEPTIBILITY OF 7. HIGH FREQUENCY MEASUREMENTS FROM LEFT TO RIGHT: 1000, 1467, 2154, 3162, 4641, 6813 AND 10000 HZ. 11
SI 9. IN-PHASE (UP) AND OUT-OF-PHASE (DOWN) DYNAMIC SUSCEPTIBILITY OF 9 AT 332 HZ. 12
SI 10. IN-PHASE (UP) AND OUT-OF-PHASE (DOWN) DYNAMIC SUSCEPTIBILITY OF 10 UNDER NO EXTERNAL APPLIED FIELD. HIGH FREQUENCY MEASUREMENTS FROM LEFT TO RIGHT: 56, 133, 316, 750, 1800, 4200 AND 10000 HZ. 13

SI 1. FT-IR spectra for the $[Ln(W_5O_{18})_2]^{-9}$ family where Ln=Tb, Dy, Ho and Er.

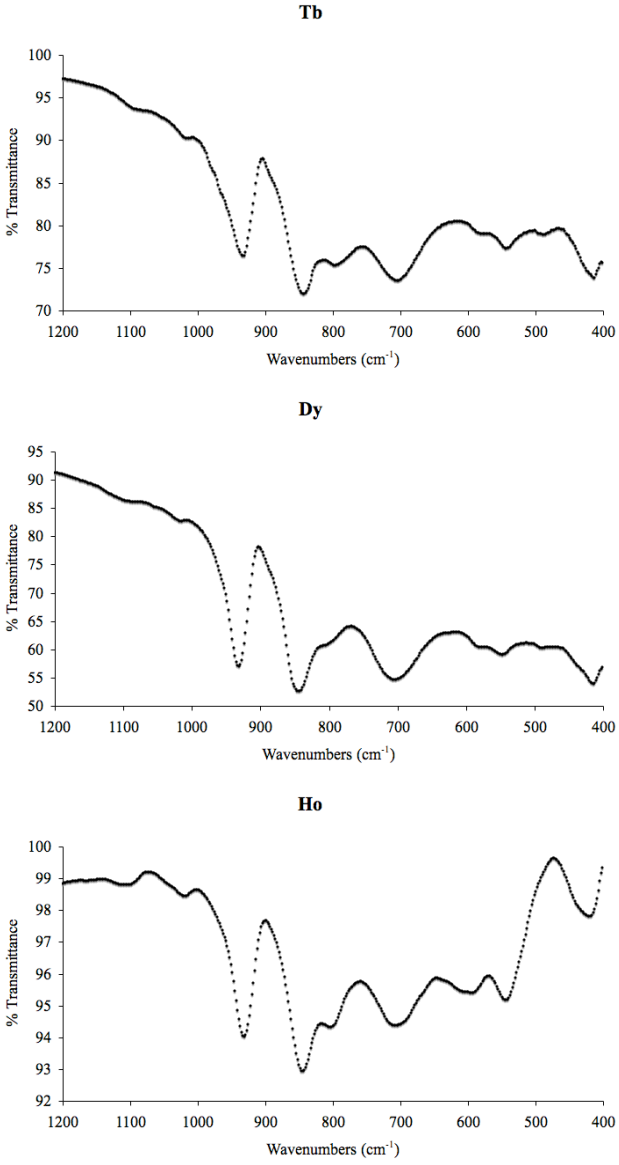

Er

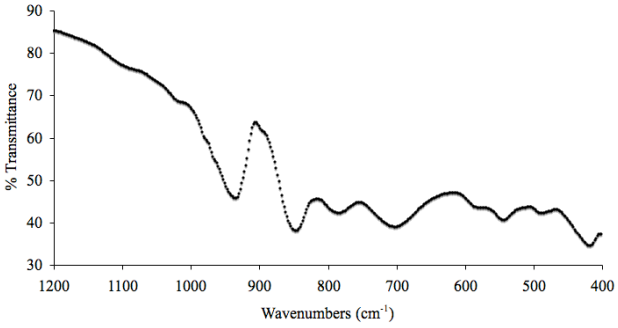
90
80
70
60
50
40
30
% Transmittance
1200
1100
1000
900
800
700
600
500
400
Wavenumbers (cm-1)

SI 2. FT-IR spectra for the $[Ln(\beta_2\text{-}SiW_{11}O_{39})_2]^{13-}$ family where Ln=Tb, Dy, Ho, Er, Tm and Yb.

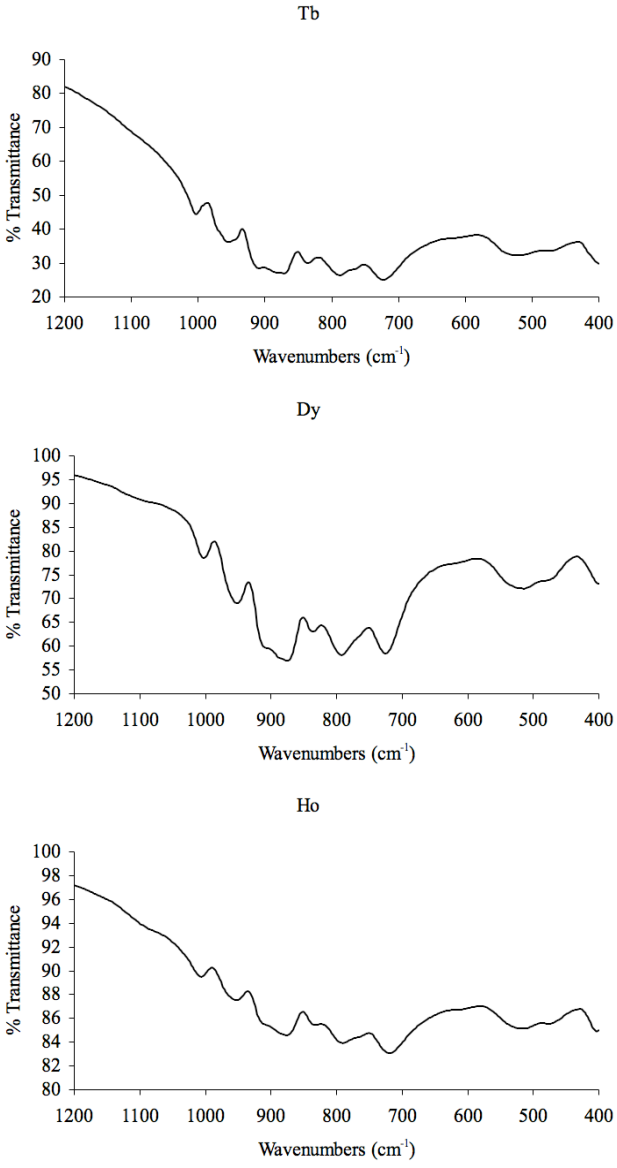

Er

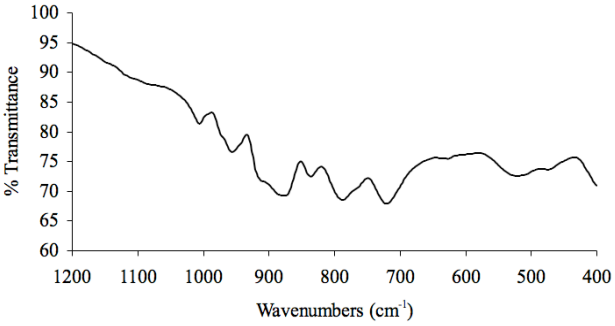
100
95
90
85
80
75
70
65
60
% Transmittance
1200
1100
1000
900
800
700
600
500
400
Wavenumbers (cm-1)

Tm

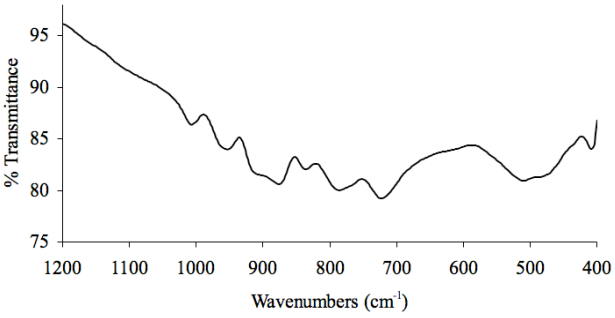
95
90
85
80
75
% Transmittance
1200
1100
1000
900
800
700
600
500
400
Wavenumbers (cm-1)

Yb

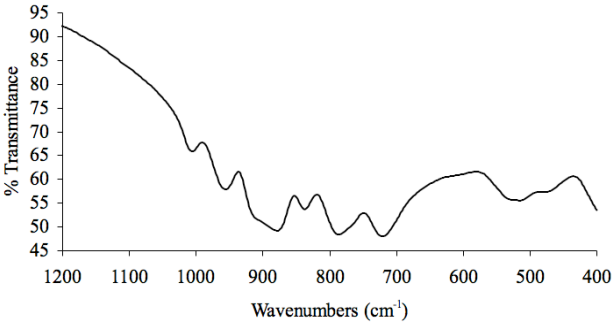
95
90
85
80
75
70
65
60
55
50
45
% Transmittance
1200
1100
1000
900
800
700
600
500
400
Wavenumbers (cm-1)

SI 3. Electron probe microanalysis (EPMA) data for the $[Ln(W_5O_{18})_2]^{-9}$ and $[Ln(\beta_2\text{-}SiW_{11}O_{39})_2]^{13-}$ families.

	$[Ln(W_5O_{18})_2]Na_9$					*$[Ln(\beta_2\text{-}SiW_{11}O_{39})_2]K_{13}$*						
	Er	**Tb**	**Dy**	**Ho**	**Theor.**	**Er**	**Tb**	**Dy**	**Ho**	**Yb**	**Tm**	**Theor.**
%W	4.9	5.4	5.4	5.3	5	3.0	3.2	2.9	3.0	2.8	3.0	2.8
%Ln	49.8	50.1	51.2	49.6	50	60.8	62.1	61.0	60.3	61.3	60.8	61.1
%Na/K	45.3	44.5	43.4	45.1	45	36.2	34.7	36.1	36.7	35.9	36.2	36.1

SI 4. In-phase (up) and out-of-phase (down) dynamic susceptibility of **1** at 1467, 2154, 3162, 4641, 6813 and 10000 Hz.

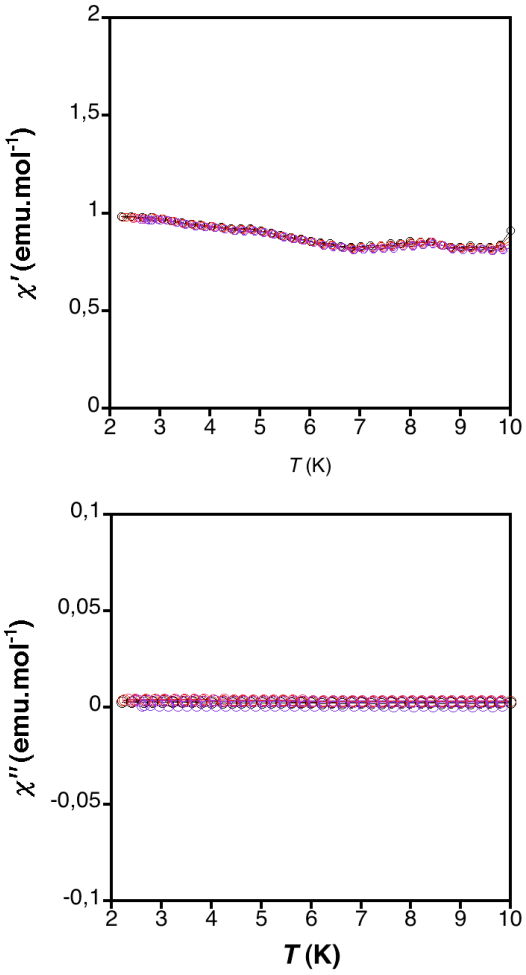

SI 5. In-phase (up) and out-of-phase (down) dynamic susceptibility of **2** at 1000, 1467, 2154, 3162, 4641, 6813 and 10000 Hz.

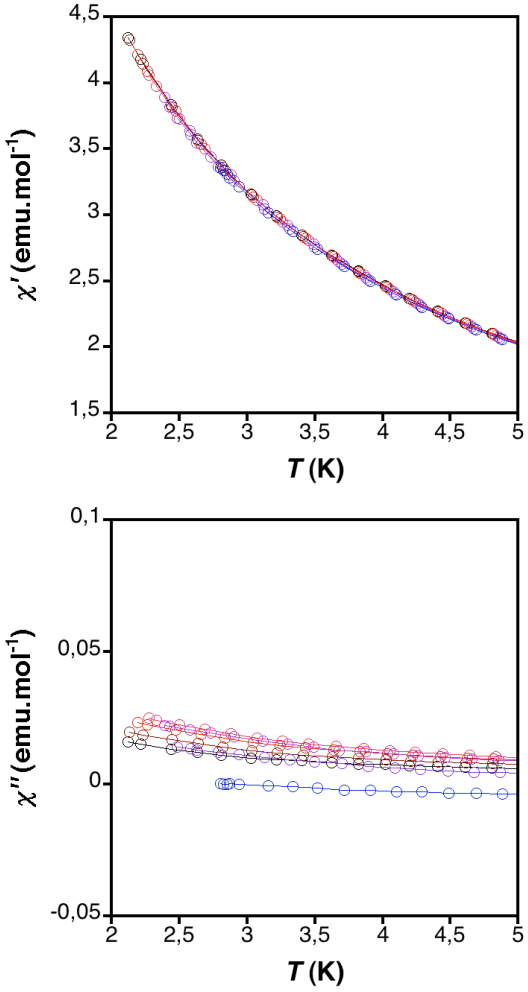

SI 6. In-phase (up) and out-of-phase (down) dynamic susceptibility of **5** at 1 and 110 Hz***.***

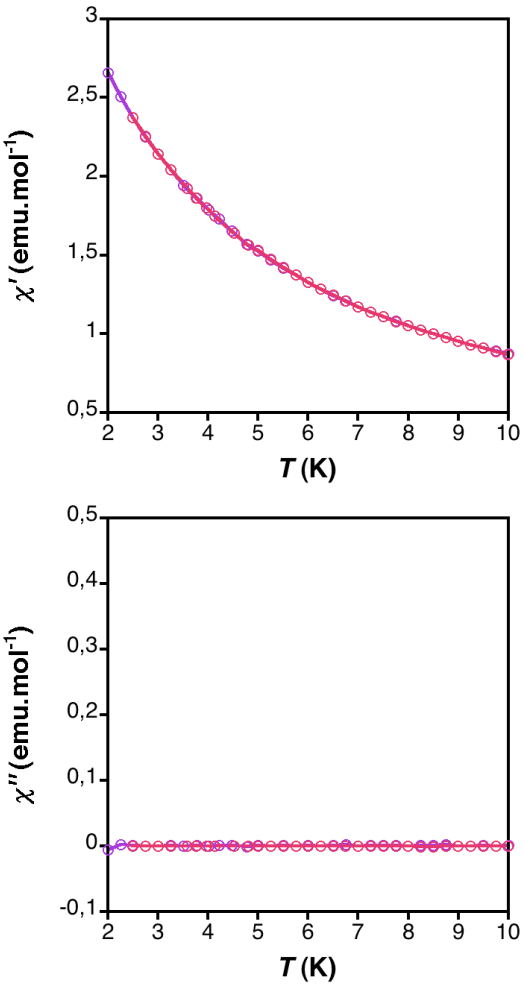

***SI* 7.** In-phase (up) and out-of-phase (down) dynamic susceptibility of **6**. High frequency measurements from left to right: 1, 10, 110, 332 and 1000 Hz.

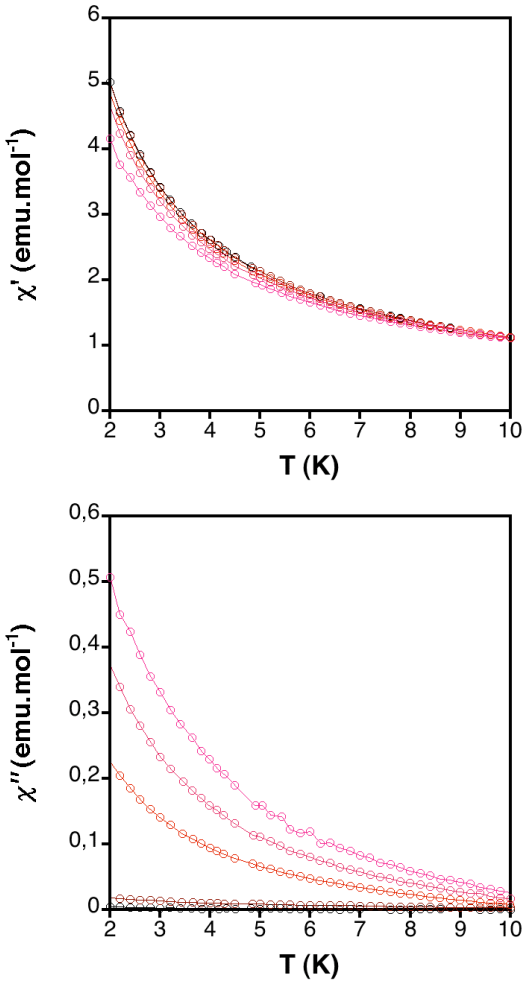

***SI* 8**. In-phase (up) and out-of-phase (down) dynamic susceptibility of **7**. High frequency measurements from left to right: 1000, 1467, 2154, 3162, 4641, 6813 and 10000 Hz.

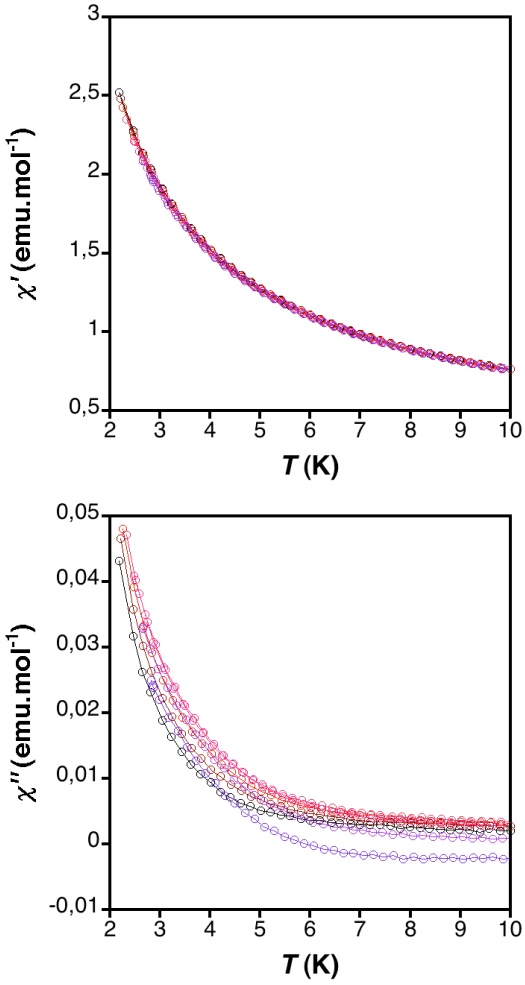

SI 9. In-phase (up) and out-of-phase (down) dynamic susceptibility of **9** at 332 Hz.

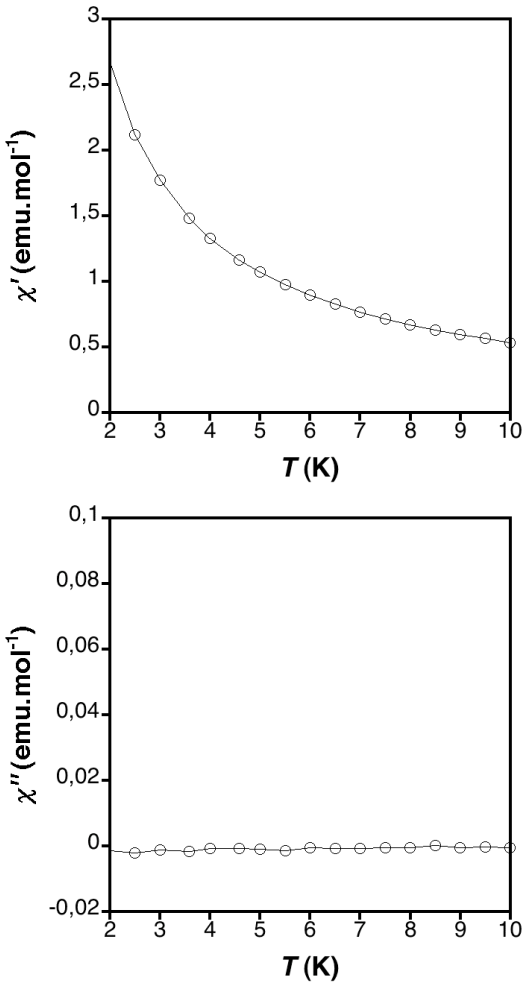

***SI* 10.** In-phase (up) and out-of-phase (down) dynamic susceptibility of **10** under no external applied field. High frequency measurements from left to right: 56, 133, 316, 750, 1800, 4200 and 10000 Hz.

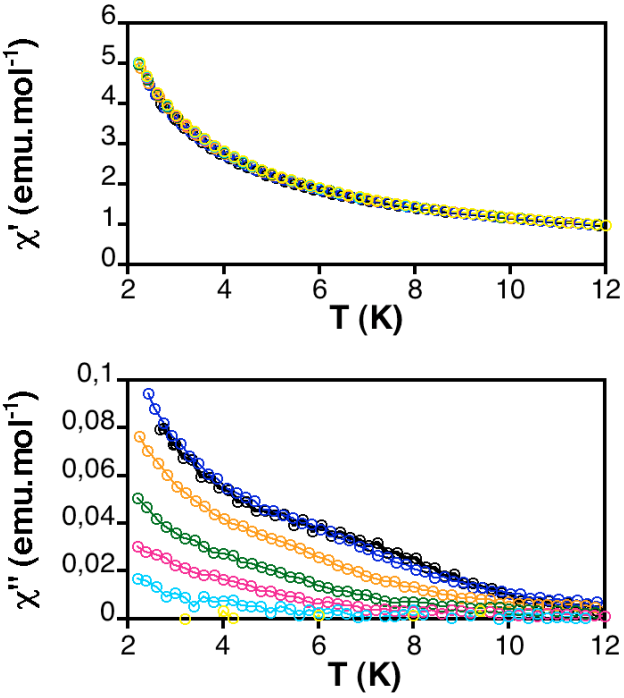

PAPER 4:

Lanthanoid Single-Ion Magnets Based on Polyoxometalates with a 5-fold Symmetry: The Series $[LnP_5W_{30}O_{110}]^{12-}$ (Ln^{III} = Tb, Dy, Ho, Er, Tm and Yb)

Journal of the American Chemical Society, **2012**, *134,* 14982-14990.

JACS
JOURNAL OF THE AMERICAN CHEMICAL SOCIETY

Article

pubs.acs.org/JACS

Lanthanoid Single-Ion Magnets Based on Polyoxometalates with a 5-fold Symmetry: The Series $[LnP_5W_{30}O_{110}]^{12-}$ (Ln^{3+} = Tb, Dy, Ho, Er, Tm, and Yb)

S. Cardona-Serra,[†] J. M. Clemente-Juan,[†] E. Coronado,[†,*] A. Gaita-Ariño,[†] A. Camón,[‡] M. Evangelisti,[‡,§] F. Luis,[‡,§,*] M. J. Martínez-Pérez,[‡,§] and J. Sesé[§,⊥]

[†]Instituto de Ciencia Molecular (ICMol), Universidad de Valencia, Catedrático José Beltrán Martínez No. 2, 46980 Paterna, Spain

[‡]Instituto de Ciencia de Materiales de Aragón (ICMA), CSIC-Universidad de Zaragoza, Plaza San Francisco s/n, 50009 Zaragoza, Spain

[§]Departamento de Física de la Materia Condensada, Universidad de Zaragoza, Plaza San Francisco s/n, 50009 Zaragoza, Spain

[⊥]Instituto de Nanociencia de Aragón (INA), Universidad de Zaragoza, Edificio I+D, Campus Río Ebro, 50018 Zaragoza, Spain

Supporting Information

ABSTRACT: A robust, stable and processable family of mononuclear lanthanoid complexes based on polyoxometalates (POMs) that exhibit single-molecule magnetic behavior is described here. Preyssler polyanions of general formula $[LnP_5W_{30}O_{110}]^{12-}$ (Ln^{3+} = Tb, Dy, Ho, Er, Tm, and Yb) have been characterized with static and dynamic magnetic measurements and heat capacity experiments. For the Dy and Ho derivatives, slow relaxation of the magnetization has been found. A simple interpretation of these properties is achieved by using crystal field theory.

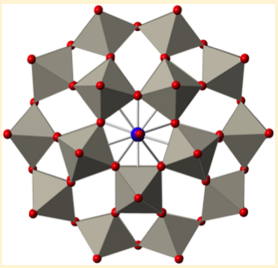

INTRODUCTION

The relevance of polyoxometalates (POMs) in molecular magnetism is based on the ability of these metal-oxide clusters to act as chelating ligands incorporating a large number of magnetic centers at specific sites of their molecular structures.[1] Magnetic POMs can be divided into three broad families. A first class consists of POMs encapsulating a number of 3d-transition metal ions, which can be connected through oxo bridges forming magnetic clusters of variable nuclearities and high symmetries, often enabling exchange interactions between the magnetic centers. A second family is formed by POMs encapsulating one or more lanthanoid ions in order to give rise to a lanthanoid complex in which the 4f-magnetic ions are submitted to the crystal field created by the POM ligands. Finally, a third family incorporates a mixed-valence POM framework hosting a number of electrons that are usually hopping over all the framework structure. The result is a mixed-valence magnetic POM in which the localized magnetic moments coming from the encapsulated 3d or 4f metal ions are coexisting or even interacting with the delocalized electrons coming from the POM framework.[2,3]

In all these cases, the rigidity and large size of the generally nonmagnetic POM framework lead to magnetic systems possessing highly symmetric topologies and coordination sites, while keeping an effective magnetic isolation between them and a remarkable stability in solution as well as in the solid state.[4] Owing to all these electronic, structural, and chemical features, the studies of magnetic POMs give precise and unique answers to the questions of magnetic interactions.[1,5−7]

Taking advantage of all this previous knowledge, we are now in position of using these polyanions as platforms for designing magnetic molecules exhibiting useful properties such as magnetic bistability or switching, which can open new perspectives in molecular spintronics and quantum computing.[8−10] A key result in this context was the discovery in 2008 of the first examples of mononuclear lanthanoid POMs behaving as single-molecule magnets (SMMs).[11] Thus, it was demonstrated that the sodium salt of the polyanion $[Er(W_5O_{18})_2]^{9-}$ exhibits a slow relaxation of the magnetization at low temperatures, which agrees with the presence of an energy barrier for the reversal of the magnetization very close to that observed for the archetypical Mn_{12} cluster ($U_{eff}/k_B \approx 60$ K), and a very rich physics at very low temperature connected with quantum tunneling effects.[12] This kind of POM possesses an octacoordinated coordination site close to the antiprismatic D_{4d} symmetry. It represents the second example of a mononuclear

Received: June 1, 2012
Published: August 15, 2012

dx.doi.org/10.1021/ja305163t | J. Am. Chem. Soc. 2012, 134, 14982−14990

lanthanoid complex behaving as a SMM. The first example was discovered by Ishikawa et al. in 2003 in the Tb derivative of the bis-phthalocyaninato complexes formulated as $[LnPc_2]^-$, also possessing a D_{4d} symmetry.[13] In this class of mononuclear nanomagnets, also known as single-ion magnets (SIMs), the magnetic anisotropy required for observing this barrier arises from the splitting of the J ground state of the Ln^{III} when it is submitted to a crystal field (CF). For certain CF symmetries, such splitting can stabilize sublevels with a large $|M_J|$ value, thus achieving an easy axis of the magnetization.[14] In these two cases, the different distortion of the antiprismatic site (axially compressed for POMs and axially elongated for the $[LnPc_2]^-$ complexes) leads to a different splitting of the $\pm M_J$ levels. Thus, these coordination sites stabilize the higher M_J values in the Er derivative encapsulated by POMs or in the Tb derivative encapsulated by phtalocyanines. That explains why these two mononuclear complexes behave as SMMs. In these systems, the slow relaxation of the magnetization is ensured by the highly symmetrical coordination symmetry around the lanthanoid, such as the pseudoaxial D_{4d} symmetry, which favors the purity of the ground doublet. It seems obvious that many other lanthanoid complexes should satisfy these structural and electronic requirements. Still, most of the known examples of SIMs reported so far are restricted to the antiprismatic D_{4d} symmetry.

Other coordination geometries different from the D_{4d} need now to be explored. In fact, other axial symmetries around the lanthanide, such as D_{2d},[15a] D_{3h},[15b] and C_{∞}[15c] have also shown to exhibit a SMM behavior. In the present paper, we will extend this study to other geometries taking advantage of the unique ability of POMs to act as rigid ligands offering a powerful tool for the design of metal complexes with tailored symmetries. We here focus on the well-known $[LnW_{30}O_{110}]^{12-}$ family of complexes in which its very unusual C_5 axial symmetry allows us to study both experimentally and theoretically the possibilities of preparing new SIMs having 5-fold symmetry.

EXPERIMENTAL SECTION

Synthesis. All reactants and solvents were of commercially available grade and used without any previous purification. $LnCl_3{\cdot}6H_2O$ are highly hygroscopic and should be stored in desiccators. The mixed potassium/sodium Preyssler salt, where a sodium ion is encapsulated, was prepared according to a well-known procedure[16] and identified by FT-IR techniques.

$K_{12}LnP_5W_{30}O_{110}{\cdot}nH_2O$ (Ln^{3+} = Tb, Dy, Ho, Er, Tm, and Yb) was prepared following the previously described method.[16]

In a typical experiment, $K_{12.5}Na_{1.5}[NaP_5W_{30}0_{110}]{\cdot}15H_2O$ (1 g, 0.12 mmol) was dissolved in 12 mL of water, and the solution was heated to 60−70 °C. To this solution, 2 equiv of the lanthanoid ion, as the chloride salt dissolved in water, was added dropwise (3 mL). The mixture was placed in a Parr model 4746 or model 4748 sample preparation bomb and heated to 160 °C overnight. After the solution had cooled to room temperature, the product was isolated by the addition of 4 g of solid KCl. The product was identified by FT-IR: 1159(s), 1064(s), 1020(m), 939(s), 914(s), 777(s), 568(w), 539(m), 468(w).

Physical Measurements. IR spectra were recorded on a FT-IR Nicolet 5700 spectrometer in the 4000−400 cm^{-1} range using powdered sample in KBr pellets. Magnetic susceptibility, χ_m, data were measured between 2 and 300 K with a commercial magnetometer equipped with a SQUID sensor and a commercial physical properties measurement system (PPMS). The diamagnetic contributions to the susceptibility were corrected using Pascal's constant tables. Direct current (dc) data were collected with an applied field of 1000 Oe. Alternate current (ac) were collected in the range 2−12 K with an applied alternating field of 3.95 Oe at different frequencies in the range 1−10000 Hz. The magnetic characterization was extended to very low temperatures with a combination of noncommercial experimental set-ups. Magnetization hysteresis loops were measured between 350 mK and 7 K using a homemade micro-Hall magnetometer working in a ^{3}He refrigerator. The sample, mixed with Apiezon N grease to ensure its proper thermalization at these very low temperatures, was deposited directly on the edge of one of the two Hall crosses. The ac susceptibility of a powdered DyW_{30} sample was measured from 333 Hz to 13 kHz using a home-built mutual inductance susceptometer thermally anchored to the mixing chamber of a ^{3}He−^{4}He dilution refrigerator, which gives access to temperatures ranging from 0.09 to 3.5 K. The ac susceptibility of a HoW_{30} single crystal was measured, from 0.03 Hz to 200 kHz, using an integrated microSQUID susceptometer, recently developed by some of us,[17] which works in the temperature region from 13 mK to 3 K. Inelastic neutron scattering experiments were performed on the IN4 instrument of the Institut Laue-Langevin at wavelengths 1.1, 2.2, and 3.6 Å. Finally, specific heat data were also measured between 350 mK and 20 K on compact pellet samples using a commercial PPMS.

RESULTS AND DISCUSSION

Here we report the magnetic study of a series of mononuclear lanthanoid-based complexes formulated as $K_{12}LnP_5W_{30}O_{110}{\cdot}nH_2O$ (Ln^{3+} = Tb, Dy, Ho, Er, Tm, and Yb), which are usually called "Preyssler anions" (see Figure 1a). In these complex systems the structural details depend on the experimental data available. We base our description of the structure on single-crystal X-ray results.[18]

In this POM structure, the lanthanoid cation can occupy two equivalent coordination sites, which show a very unusual 5-fold geometry formed by five phosphate oxygens ($d_{Ln-Op} \approx 2.7$ Å) and five bridging oxygens between two tungsten atoms (d_{Ln-Ow}

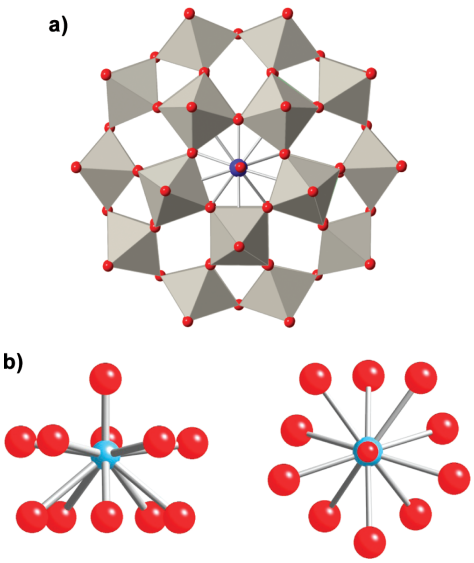

Figure 1. (a) Complete structure of the $[LnP_5W_{30}O_{110}]^{12-}$ anion. (b) Scheme showing the coordination of the lanthanoid ion in a 5-fold environment.

dx.doi.org/10.1021/ja305163t | J. Am. Chem. Soc. 2012, 134, 14982−14990

≈ 2.9 Å). The result is a pentagonal antiprism coordination site (Figure 1b). The lanthanoid cation is not placed at the center of this antiprism but closer to the plane formed by the phosphate oxygens. A water molecule placed in an axial position close to the other coordination site completes the coordination sphere ($d_{Ln-O} \approx 2.2$ Å). The coordination number of the lanthanoid cation is 11 (monocapped pentagonal antiprism, shown in Figure 1b). Based on these structural considerations, we assign an ideal C_5 symmetry to the coordination of the lanthanoid ion in the whole series of $[LnP_5W_{30}O_{110}]^{12-}$ POMs (in short LnW_{30}). These anionic molecules are surrounded by potassium cations for charge balance. Given the size of the POM ligands that are encapsulating the lanthanoid, an extremely good isolation of the anisotropic Ln^{3+} ions in the solid state is observed (shortest Ln−Ln distance of 13.2 Å).

It is important to note that, despite the differences of the cited X-ray description with indirect techniques like spectroscopic lifetime measurements or EXAFS studies,[25] our geometrical reasoning is robust and does not change with fine details. In particular, and as discussed below, the 5-fold symmetry, which has not been put in doubt by any technique, is what produces A_6^5 as only extradiagonal parameter. The diagonal terms A_2^0, A_4^0, and A_6^0 can similarly be interpreted in terms of polar angles and independently of small variations in the metal−ligand distance.

Determination of Crystal Field Parameters. Direct current magnetic measurements have been used to determine the CF parameters and the resulting splitting of the ground electronic state of the lanthanoid ions caused by the crystal field. One has to note that the substitution proportion x of sodium by lanthanoid cations in the structure is often not complete, with usual values in the range $0.85 < x < 0.95$. As already shown by Creaser et al.,[19] this effect is to be expected specially for Tm^{3+} and Yb^{3+}, with $0.4 < x < 0.6$. We account for this effect by a scaling factor of the whole $\chi_m T$ curve, which, as shown in Table 1, produces a good agreement between the room temperature $\chi_m T$ value and the value expected for free ions. This procedure guarantees that we use the corrected values for the determination of the CF parameters. Because the interactions between magnetic centers are very weak in this system, this moderate dilution is not expected to have any measurable effect on the static magnetic properties and to produce only a small perturbation on the dynamical behavior compared with a nondiluted crystal.

Table 1. Total Angular Momentum of the Lanthanoid Cations, as Given by Hund's Rules, and $\chi_m T$ Values for LnW_{30} Family

lanthanoid ion	J	$\chi_m T$ of the free ion (emu·K/mol)	$\chi_m T$ of the LnPOM complex (emu·K/mol)
Tb^{3+}	6	11.81	11.48
Dy^{3+}	15/2	14.17	14.41
Ho^{3+}	8	14.06	14.386
Er^{3+}	15/2	11.475	11.37
Tm^{3+}	6	7.15	7.22
Yb^{3+}	7/2	2.57	2.51

The CF describes the effect of the electric field due to the surrounding ligands acting on the lanthanoid ion. It splits the electronic ground state multiplet of the free ion, described by its total angular momentum, J, into M_J doublets and singlets. For C_5 symmetry, the CF Hamiltonian can be expressed in terms of the operator equivalents as follows:

$$\hat{H} = \alpha A_2^0 r^2 \hat{O}_2^0 + \beta A_4^0 r^4 \hat{O}_4^0 + \gamma A_6^0 r^6 \hat{O}_6^0 + \gamma A_6^5 r^6 \hat{O}_6^5 \quad (1)$$

where α, β, and γ are the Stevens constants for each lanthanoid,[20] $\hat{O}_k^q$ are the operator equivalents expressed as polynomials of the total angular momentum operators,[21] $\langle r^k \rangle$ expectation values of the radial factor r^k, and A_k^q are numerical parameters that depend on the nature of the ligand shell.

Unlike pseudoaxial systems, where only the $A_k^q\langle r^k\rangle$ terms with $q = 0$ ($A_2^0\langle r^2\rangle$, $A_4^0\langle r^4\rangle$, $A_6^0\langle r^6\rangle$) are different from zero, the C_5 symmetry allows a term with $q = 5$ ($A_6^5\langle r^6\rangle$), which mixes magnetic states $|J,M_J\rangle$ with different M_J. Therefore, M_J is no longer a good quantum number. This term appears also in higher symmetries containing axes of order 5, such as the icosahedral symmetry.[22]

As shown in Figure 2, below 50−100 K, the $\chi_m T$ value of all the samples begins to decrease due to the thermal depopulation of the excited electronic levels. Thus, in order to determine experimentally the $A_k^q r^k$ products, we will make use of the dc magnetic susceptibility data measured as a function of temperature. Ishikawa et al. proposed that the CF parameters of an isomorphic series of lanthanoid complexes could be determined by a simultaneous fit of the all $\chi_m T$ values under the assumption that the CF parameters from the f^8 to the f^{13} system show a linear variation.[23] Under these conditions, the $A_k^q\langle r^k\rangle$ coefficients can be expressed with eq 2.

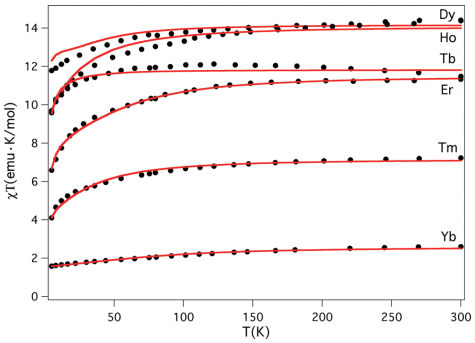

Figure 2. $\chi_m T$ data measured on powdered samples of the LnW_{30} series under a magnetic field $H = 1000$ Oe. The lines are least-squares simultaneous fits of all these curves obtained by the method described above using the CF Hamiltonian (1).

$$A_k^q \langle r^k \rangle = a_k^q + b_k^q (n_f - 7) \quad (2)$$

where n_f goes from 8 to 13 when moving from Tb^{3+} to Yb^{3+}.

Using this procedure, a good fit of all the magnetic curves has been obtained from a unique set of crystal field parameters (Table 2). The fitting has been made over a set of 40 $\chi_m T$ values per compound. The experimental data were chosen to be approximately equally spaced on a logarithmic temperature scale from 2 K to room temperature in order to give more weight in the fit to the contribution of low energy levels. Figure 2 shows the agreement between the experimental values and the fits.

Table 2. CF Parameters Determined for the LnW_{30} Series (in cm^{-1})

Ln^{3+}	f^n	$A_2^0\langle r^2\rangle$	$A_4^0\langle r^4\rangle$	$A_6^0\langle r^6\rangle$	$A_6^5\langle r^6\rangle$
Tb^{3+}	8	69.3	34.3	6.7	-1.08×10^3
Dy^{3+}	9	49.7	43.6	11.3	-1.16×10^3
Ho^{3+}	10	30.1	52.9	15.9	-1.24×10^3
Er^{3+}	11	10.5	62.3	20.6	-1.32×10^3
Tm^{3+}	12	−9.1	71.6	25.3	-1.40×10^3
Yb^{3+}	13	−28.68	80.9	29.9	-1.47×10^3

A comparison of these parameters with those found for the $[Ln(Pc)_2]^-$ and previous LnPOM families is in order. The most striking contrast appears for the A_2^0 parameter, which was positive for all the D_{4d} phthalocyaninato complexes and negative for all D_{4d} POM derivatives, while here it depends on the lanthanoid metal. This may be understood when taking into account the position of the ligands in the first coordination sphere (Figure 1): the lanthanoid is slightly between two pentagons formed by oxo atoms from the POM, while the water molecule is on the 5-fold symmetry axis. This means that there is a competition between the closest five oxo ligands from the POM, which are equatorial and contribute negatively to A_2^0, and the apical water molecule, which is axial and contributes to a positive A_2^0 value. The five furthest oxygen atoms are very close to the angular node ("magic angle", $\theta = 54.7°$) and their contribution should be smaller than the other two. It is likely that the evolution of this competition could result in a change of sign for the second-order uniaxial parameter. Indeed, a crystallographic and EXAFS study on the lanthanoid series in the Preyssler anion indicates that, as one advances in the series (from Tb^{3+} to Er^{3+}), the cations tend to move deeper between the pentagons.[24] Because of the angles involved, this can be expected to have a relatively minor effect on the contribution of the closest pentagon and a larger effect on the contribution of the furthest pentagon, resulting in an enhanced negative contribution to A_2^0. Moreover, the metal−water distance tends to grow, diminishing the positive contribution to A_2^0.

The sign of A_4^0 is also in contrast with that reported both in phtalocyaninate and in other POM derivatives. Such a difference can also be easily understood. Thus, sandwiched D_{4d} complexes have all ligands placed around the "magic angle", and hence they contribute negatively to A_4^0. In contrast, in Preyssler complexes, the closest-lying ligands are either axial or (almost) equatorial, which means dominating positive contributions to A_4^0. From this argument, one cannot predict the evolution of A_4^0 along the lanthanoid series, since the effects would be competing: decreasing because of the longer distance with both the axial water and the equatorial pentagon vs increasing as the furthest pentagon slips out of the negative lobe.

In a first approximation, the sign and evolution of A_6^0 would be similar to those of A_2^0. The fact that our fit produces the opposite result is an indication of the weak dependence of the magnetic data on A_6^0. Hence, these values should only be taken as approximate.

Another difference with the previous D_{4d} systems is, obviously, the fact that the main extra-diagonal parameter for the Preyssler systems is A_6^5 and not A_4^4. Its extremely high absolute value can be understood because, in contrast to what happens in the D_{4d} case, here the extra-diagonal parameter arises as a first-order effect and not of a small distortion of an ideal structure.

Electronic Structure of LnW_{30}. The electronic structure within the ground-state J multiplet of each lanthanoid is described here. Figure 3 shows the low energy part of the

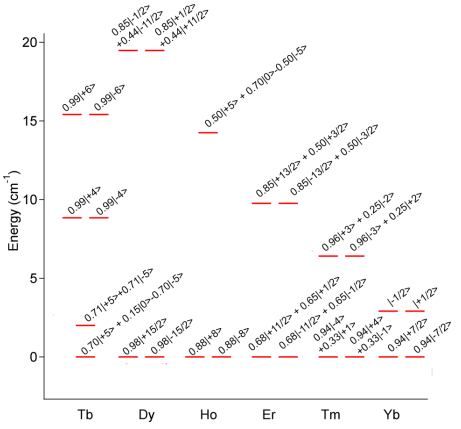

Figure 3. Low-lying levels of the different complexes in the LnW_{30} series (Ln = Tb, Dy, Ho, Er, Tm, or Yb).

scheme of the $2J + 1$ levels obtained by using the set of CF parameters derived from the simultaneous fitting method described above. These schemes are briefly discussed next for each compound in order to predict in which compounds a SMM behavior (i.e., the presence of a superparamagnetic blocking at low T with slow relaxation of the magnetization) has to be expected. Before entering into detail, it is important to notice that in contrast to what was observed for D_{4d} symmetry, for the C_5 symmetry the energy levels are, in general, characterized by a pronounced quantum mixture of M_J values (see Table 1, Supporting Information), which will favor the tunneling processes thus making difficult the observation of a SMM behavior. This is a direct consequence of the lowering of the crystal field symmetry (from D_{4d} to C_5) because it results in the appearance of non-negligible off-diagonal CF parameters (A_6^5 in the present case), which allow the mixing of functions with different M_J values.

TbW_{30}. In this case, the ground state doublet is the $M_J = \pm 5$, split by the mixture with $M_J = 0$. The next sublevel, at 9 cm^{-1}, is the $M_J = \pm 4$ doublet. Both groups are isolated from all the next levels by a 15 cm^{-1} gap. Despite having a high $|M_J|$ ground state, this strong quantum mixture should allow the system to relax and invert its spin, thus preventing the Tb^{3+} complex from behaving as a SMM.

DyW_{30}. The lowest Kramers doublet corresponds to the $M_J = \pm 15/2$, the first excited states $M_J = \pm 13/2$ and $M_J = \pm 1/2$ being placed very near to each other (at 20 cm^{-1}). These three doublets are well isolated from the next ones by a gap of about 40 cm^{-1}. This may provide a favorable situation for behaving as a SMM.

HoW_{30}. The ground doublet for this complex is $M_J = \pm 8$, and thus, it is favorable for exhibiting SMM behavior. Still, the first excited state, a mixture of $M_J = \pm 5$ with $M_J = 0$, is rather close in energy (only 14 cm^{-1} above it). Owing to this small energy

dx.doi.org/10.1021/ja305163t | J. Am. Chem. Soc. 2012, 134, 14982−14990

gap, the system is expected to magnetically block only at very low temperatures.

ErW$_{30}$. In this complex, the lowest lying doublet is an equally weighted quantum mixture of $M_J = \pm 11/2$ and $\pm 1/2$. The first excited doublet consists of mixtures of $M_J = \pm 13/2$ and $\pm 3/2$ and lies at 10 cm^{-1} over it. The $M_J = \pm 15/2$ doublet, responsible for the SMM behavior observed in other POM complexes,[11] is the highest in energy here. This energy scheme should prevent the blocking of its magnetic moment at low temperature.

TmW$_{30}$. For this complex, the ground doublet is mainly $M_J = \pm 4$ with a minor contribution of $M_J = \mp 1$. The next doublet is a mixture of $M_J = \pm 3$, ∓ 2, lying at 7 cm^{-1}. In this case, we would expect no direct tunneling, because in a first approximation there is no overlap between the two wave functions containing, respectively, {+4,−1} and {−4,+1}. The experimental lack of SMM properties therefore is in apparent contradiction with the theory and needs a rationalization. A likely explanation is that small distortions to the ideal symmetry can mix the $M_J = \pm 1$ contribution of the ground doublet, facilitating a rapid relaxation of the magnetization.

YbW$_{30}$. The lowest-lying Kramers doublet in this complex is $M_J = \pm 1/2$. Two excited doublets have energies close to 3 cm^{-1} above the ground state doublet, while the doublet associated with the highest M_J lies at about 87 cm^{-1}. The nearly constant value of $\chi_m T$ measured below room temperature is probably due to this particular energy level scheme and the ensuing small depopulation of the high CF sublevels. Of course, with the ground state being $M_J = \pm 1/2$, no blocking of the magnetization is possible.

Heat Capacity Measurements. In view of the above results, the only compounds that are expected to exhibit SMM behavior are the Dy and Ho derivatives. Let us study the molar specific heat, c_P, of these two compounds to get additional and independent information on the structure of the low-lying magnetic levels. Experimental data for these two compounds are shown in Figures 4 and 5 for different magnetic fields. We next describe the results obtained for each of these two separately.

Above 10 K, c_P for DyW_{30} is dominated by the contribution of lattice vibrations c_{latt}. Below 300 K, c_{latt} can be fitted reasonably well by the superposition of a Debye function, which accounts for the excitation of acoustic phonon modes with a Debye temperature $\theta_D = 29(1)$ K, plus two Einstein terms, with characteristic energies $\varepsilon_{E,1}/k_B = 45$ K and $\varepsilon_{E,2}/k_B = 108$ K, which account for the contributions of 159 and 321 vibration modes, respectively. At zero field, a magnetic contribution c_m shows up below 1 K. This contribution arises from the splitting of the magnetic energy levels associated with couplings to other electronic spins, probably of dipolar origin, and the hyperfine interactions with nuclear spins of Dy. This element has two stable isotopes, ^{161}Dy (natural abundance 18.9%) and ^{163}Dy (natural abundance 24.9%), with nuclear spin $I = 5/2$. A magnetic field further splits each doublet. The splitting of the ground doublet, with $M_J = \pm 15/2$, gives rise to the field-dependent Schottky-like anomaly that dominates the specific heat of **2** below 2 K. A second magnetic contribution, visible near 4−9 K, can be associated with the thermal population of the first excited doublet. As is shown in Figure 4, calculations performed with the same CF parameters derived from the magnetic susceptibility account well for the specific heat measured at all fields, therefore giving support to the electronic structure given in Figure 3.

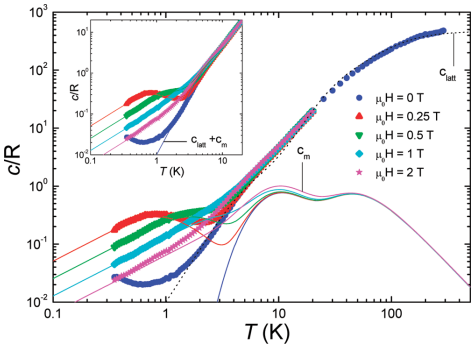

Figure 4. Specific heat of a powdered sample of DyW_{30} measured at several magnetic fields. The dotted line shows a fit of the lattice contribution c_{latt}, whereas the solid lines show the magnetic contribution c_m calculated with the Hamiltonian (1) using the CF parameters given in Table 2. The inset shows an enlarged view of the low-temperature region. The solid lines give the theoretical $c_P = c_{latt} + c_m$.

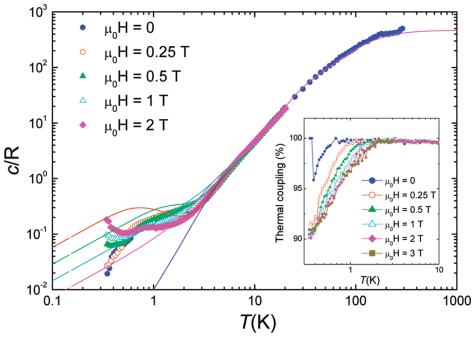

Figure 5. Specific heat of a powdered sample of HoW_{30} measured at several magnetic fields. The solid lines give the theoretical $c_P = c_{latt} + c_m$. The magnetic c_m was calculated with the Hamiltonian (1) using the CF parameters given in Table 2. The inset shows the thermal coupling parameters measured at the same field values. Its departure from 100% signals a deviation of the heat capacity from its thermal equilibrium value.

The specific heat of HoW_{30} is plotted in Figure 5. Like in the previous sample, lattice vibrations dominate c_P above 2 K. A good fit of c_{latt} is obtained for $\theta_D = 29(1)$ K, $\varepsilon_{E,1}/k_B = 45$ K (105 vibration modes), and $\varepsilon_{E,2}/k_B = 108$ K (375 vibration modes). Measurements performed at $H = 0$ show the rise of a magnetic contribution c_m already below 2.5 K. As can be seen by the comparison of Figures 4 and 5, this contribution is larger for the HoW_{30} complex than it is for the DyW_{30} complex, and furthermore, it shows up at higher temperatures. This is not unexpected, considering the strong hyperfine coupling between electronic and nuclear spins ($I = 7/2$) of ^{165}Ho (100% natural abundance). This coupling gives rise to a series of electro-nuclear energy levels defined by the electronic M_J and nuclear M_I spin projections along z, with approximate energies $E_{hf}(M_J,M_I) = M_J A_{hf} M_I/k_B$ where $A_{hf}/k_B = 0.04$ K is the

dx.doi.org/10.1021/ja305163t | J. Am. Chem. Soc. 2012, 134, 14982−14990

hyperfine coupling constant. The overall hyperfine splitting in the ground electronic doublet $M_J = \pm 8$ is $\Delta E_{hf}/k_B \approx 7M_J A_{hf}/k_B \approx 2.3$ K. By contrast, only 42% Dy atoms carry a nuclear spin, and the hyperfine coupling A_{hf} is nearly 8 times weaker than that of Ho.

Data measured under nonzero magnetic fields also show a magnetic contribution, which appears to gradually shift toward higher temperatures, as in DyW_{30}. However, the experimental c_m remains smaller than the expected electronic contribution (i.e., arising only from the electronic magnetic moments), which is shown by the solid lines in Figure 5. This effect suggests that the populations of electronic and nuclear spin levels are not able to fully attain their thermal equilibrium values within the experimental time scales. The time scale, on the order of 1.5 s at 1 K, is determined, in the present experiments, by the duration of the heat power pulses applied to the calorimeter. If c_m depends on time, the temperature changes that follow each pulse deviate from a pure exponential decay. This is observed here, indeed, as witnessed by the decrease of the effective thermal coupling, shown in the inset of Figure 5, with decreasing temperature. This parameter gives a measure of how closely the temperature decay follows an exponential decay, thus also of the presence of nonequilibrium effects in c_p. Therefore, these data show that the re-equilibration of electronuclear magnetic levels becomes relatively slow below 2 K, the more so as the magnetic field increases. These phenomena have been observed in polynuclear magnetic clusters, such as Mn_{12}, Fe_8, Mn_4, and others, where they are associated with the slow magnetic relaxation characteristic of the SMM behavior.[25−27] These aspects are considered in more detail in the following section.

Inelastic Neutron Scattering Experiments. INS was pursued in the instrument IN4 of the ILL for the compounds $K_{12}DyP_5W_{30}O_{110}$ and $K_{12}HoP_5W_{30}O_{110}$, because it is a technique that generally produces high-quality spectroscopic information on these excited magnetic levels. The measurements were done at wavelengths $\lambda = 1.1$, 2.2, and 3.6 Å, which correspond to energy windows of 5−60, 2−15, and 1−5 meV. Unfortunately, we found that the spectra are dominated by very intense phonon transitions that obscure any magnetic signal of the lanthanoid. Hence, INS has not provided in this case any information on this energy gap. The INS spectra are shown in Figures S1−3, Supporting Information.

Dynamic Susceptibility and Magnetization Hysteresis Measurements. Alternating current susceptibility measurements have been performed for the six members of the LnW_{30} series above 2 K. As expected, in this temperature region only the susceptibilities of samples with Dy^{3+} and Ho^{3+} depend on frequency. The dependences of χ' and χ'' are compatible with Cole−Cole functions[28] with $\alpha \leq 0.2$, as expected for a SMM relaxing its magnetic moment via a thermally activated mechanism. Yet, even in these two samples, a complete blocking of the susceptibility is not observed. In order to better understand the relaxation processes that govern the spin dynamics in these samples, ac susceptibility and magnetization hysteresis experiments have been extended to the region of very low temperatures. For the DyW_{30}, the in-phase χ' and out-of-phase χ'' components of the ac susceptibility are shown in Figure 6. Remarkably enough, the two curves increase with decreasing temperature down to 80 mK; that is, no complete superparamagnetic blocking occurs. This behavior indicates that the magnetic relaxation rate, τ^{-1}, depends very weakly on temperature.

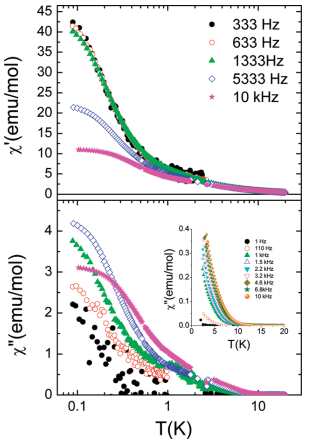

Figure 6. Alternating current susceptibility of a powdered sample of DyW_{30} vs temperature (in logarithmic scale): (top) in-phase component; (bottom) out-of-phase component. The inset shows an enlarged view of χ'' measured above 2 K.

The relaxation rate has been estimated as $\tau = \chi''/(\omega\chi')$. Strictly speaking, this relation holds only in the limit $\omega \to 0$. However, it provides a reasonably good approximation for frequencies that fulfill the condition $\omega\tau \ll 1$. Results obtained for $\omega/(2\pi) = 13.3$ kHz are shown in Figure 7. The magnetic

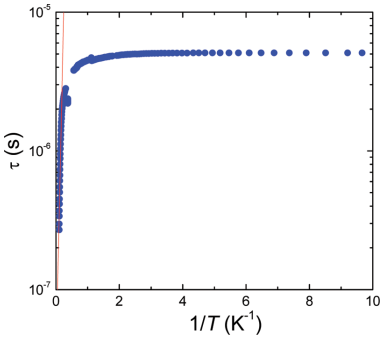

Figure 7. Relaxation-time plot used to fit an Arrhenius law for DyW_{30} at zero magnetic field.

relaxation is thermally activated above 2 K. Between 5 and 10 K, the Arrhenius fit of τ vs $1/T$ gives an activation energy $U/k_B = 24$ K. If we consider the electronic energy level spectrum of this complex (see Figure 2), these results suggest that, in this temperature region, magnetic relaxation takes place via thermal excitations to the first excited doublet. Between approximately 5 and 2 K, the relaxation time gradually flattens, finally saturating, below 2 K, to a very short value $\tau \approx 5$ μs, thus showing that relaxation becomes then dominated by pure quantum tunneling processes. The crossover to a new relaxation mechanism also leaves its mark on the distribution of relaxation times. Below 2 K, the parameter α of the Cole−

dx.doi.org/10.1021/ja305163t | J. Am. Chem. Soc. 2012, 134, 14982−14990

Cole functions increases to about 0.3−0.35. This increase can be assigned to the strong sensitivity of pure quantum tunneling events to the magnitude of the local magnetic bias acting on each spin.[29] At zero applied field, the bias is mainly associated with intercluster dipolar magnetic interactions. Because the molecular spins are oriented at random (the sample is paramagnetic), the dipolar bias changes from one lattice point to another, thus giving rise to a distribution of tunneling times.

The data of Figure 8 show that the relaxation time increases by at least 1 order of magnitude when low-intensity magnetic

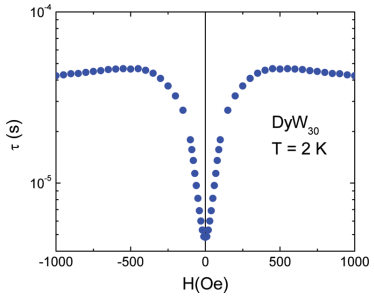

Figure 8. Magnetic relaxation time of a powdered DyW_{30} sample versus magnetic field.

fields are applied. This leads to observable magnetization hysteresis below 2 K, as is shown in Figure 9. These results confirm the SMM behavior and that spin−lattice relaxation occurs via pure quantum tunneling, as has recently been observed for ErW_{10}.[11]

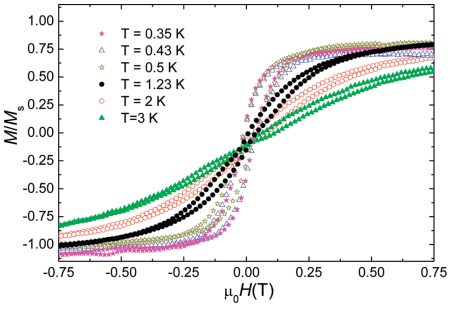

Figure 9. Hysteresis curves measured on powdered DyW_{30} at very low temperatures. The magnetic field sweeping rate was 2 T/min.

For HoW_{30}, the in-phase and out-of-phase susceptibility components are shown in Figure 10. They show evidence for a superparamagnetic blocking but only at very low temperatures. The relaxation time, shown in the inset of Figure 10, was determined from the maxima of χ'' vs T curves measured at different frequencies. The activation energy estimated from the Arrhenius plot is $U/k_B \approx 0.8$ K, much smaller than the energy separation between the first excited level and the ground level doublet $M_J = \pm 8$, which amounts to approximately 14 cm^{-1}.

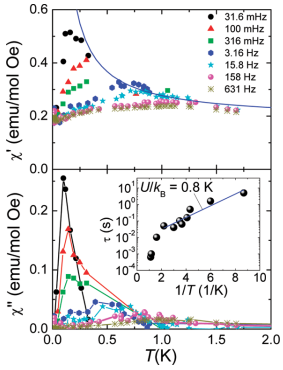

Figure 10. Alternating current susceptibility of a HoW_{30} single crystal having the magnetic anisotropy axis (C_S symmetry axis of the lanthanoid coordination shell, cf Figure 1) oriented at approximately 86.5° with respect to the excitation magnetic field: (top) in-phase component; the solid line is the equilibrium susceptibility χ_m calculated with eq 2 and the CF parameters given in Table 2; (bottom) out-of-phase component. The inset shows the Arrhenius plot of the relaxation time τ.

This shows that the low-T relaxation involves only transitions within the electronic ground state doublet.

The activated behavior, which contrasts with the nearly temperature-independent relaxation observed for DyW_{30}, can be associated with the strong hyperfine splitting present in Ho. Quantum tunneling takes place preferentially between states with the same nuclear spin projection M_I. Since the ground states of the electronuclear spin system have opposite M_I, the hyperfine interaction is to some extent equivalent to a bias field, blocking pure quantum tunneling. This effect has been observed in Ho-based phtalocyanines.[30] There, it was shown that quantum tunneling transitions between M_J and $-M_J$ states can be induced by the application of an external magnetic field, which generates level crossings between states of equal M_I. Our results add complementary information to this picture. They show that, at zero field, magnetic relaxation takes place by thermally activated transitions to excited nuclear spin states. Within this picture, the SMM behavior is dictated by hyperfine interactions rather than by the strength of the magnetic anisotropy. The prefactor $\tau_0 = 6 \times 10^{-3}$ s must then be associated with the lifetime of such excited nuclear spin states. The existence of such long-lived states is fully compatible with the weak coupling of nuclear spins to the lattice.

The SMM behavior is confirmed by the observation of magnetization hysteresis below 2 K (Figure 11). This temperature is much higher than the blocking temperatures determined from ac susceptibility experiments, which are all well below 1 K even for relatively high frequencies. The enormous differences between the spin dynamics measured by these two experimental techniques suggest that, similarly to what happens in the case of DyW_{30}, the magnetic relaxation time of HoW_{30} increases very strongly with H. The extreme sensitivity of τ to external magnetic fields seems to be a characteristic trait of mononuclear SMMs.[12,31]

Before closing this section, we shall consider the origin of the nonequilibrium phenomena observed in the specific heat of HoW_{30}. At zero field, c_m deviates from equilibrium below

dx.doi.org/10.1021/ja305163t | J. Am. Chem. Soc. 2012, 134, 14982−14990

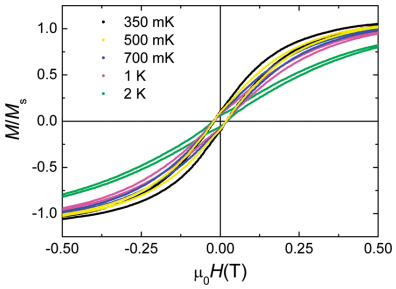

Figure 11. Magnetization hysteresis loops of HoW_{30} measured at different temperatures. The magnetic field sweeping rate was 0.54 T/min.

approximately 0.6 K, for experimental time scales on the order of 1 s. At the same temperature, the spin−lattice relaxation time obtained from the ac susceptibility is much shorter, on the order of 0.01 s. Since the two experiments are performed at zero field, the difference cannot be ascribed to the dependence of τ on H. Rather, it shows that both quantities are sensitive to different spin−lattice relaxation times: while the ac susceptibility gives mainly information about the relaxation of electronic spins, the low-T specific heat data depend on the re-equilibration of all electronuclear spin levels. Therefore, although both processes are intimately linked in Ho, our data suggest that the nuclear spin−lattice relaxation is much slower than the electronic spin−lattice relaxation.

CONCLUDING REMARKS

In this work, we have shown that POM-based mononuclear lanthanoid complexes with 5-fold symmetry can provide new examples of single-ion magnets that exhibit magnetic hysteresis at low temperatures in the case of Dy and Ho. This very unusual crystal field symmetry gives rise to remarkably large off-diagonal anisotropy parameters A_6^5, which mix magnetic states with different M_J values. The spin dynamics, especially at low temperatures, is then dominated by fast tunneling processes and strongly affected by hyperfine interactions and external magnetic fields. The fast spin−lattice relaxation associated with fast quantum tunneling seems to be detrimental for the use of these molecular single-ion magnets as magnetic memories. However, it can provide very attractive candidates for the application as solid-state spin qubits. In fact, most of these molecules possess a well-defined ground state doublet, which provides a good definition for the qubit state basis. The high tunneling rates should enable the coherent manipulation of these two states, for example, by using external electromagnetic radiation. In this respect, the existence, for some lanthanoids, of a manifold of electronuclear states can provide additional resources for the implementation of multiple qubit states within the same molecule.[32] This aspect is particularly relevant when dealing with POM molecules, because in this class of coordination complexes the main sources of quantum decoherence (hyperfine couplings and dipolar spin−spin interactions) can be minimized by preparing nuclear-spin free compounds and by diluting the magnetic centers while conserving the crystallinity. The ability of POMs to accommodate the lanthanoids in very different symmetries (D_{4d} vs C_S) offers also the possibility of tuning the magnetic anisotropy in these nanomagnets, while keeping them magnetically isolated (the magnetic ordering in these materials only occurs at very low temperatures; typically below 0.01 K). All these results allow us to emphasize that (i) mononuclear single-ion magnets offer very attractive possibilities to design new molecular nanomagnets with a control over their magnetic properties that is almost impossible to achieve with polynuclear clusters and dominant quantum effects and (ii) POM chemistry provides ideal examples of SIMs based on lanthanoids, which have shown to be useful as spin qubits[33] or, very recently, as magnetic coolers for ultralow temperatures.[34]

ASSOCIATED CONTENT

Supporting Information

Energies and modulus of the contribution of each M_J to the wavefunctions of the ground state multiplets and inelastic neutron scattering spectra. This information is available free of charge via the Internet at http://pubs.acs.org.

AUTHOR INFORMATION

Corresponding Author

eugenio.coronado@uv.es; fluis@unizar.es

Notes

The authors declare no competing financial interest.

ACKNOWLEDGMENTS

The present work has been funded through the EU (Project ELFOS and ERC Advanced Grant SPINMOL), the Spanish MINECO (Grants MAT2011-61584, MAT2009-13977-C03, MAT2007-61584, CTQ2008-06720 and the CONSOLIDER project on Molecular Nanoscience, CSD-2007-00010), the Generalidad Valenciana (Prometeo and ISIC Programmes of Excellence), and the Gobierno de Aragón (Project MOL-CHIP). The authors thank Dr. Hannu Mutka and the Institut Laue-Langevin for the INS measurements and the later discussion about the results. S.C.-S. also thanks the Spanish MECD for a FPU predoctoral grant.

REFERENCES

(1) (a) Clemente-Juan, J. M.; Coronado, E. *Coord. Chem. Rev.* **1999**, *193*−*195*, 361−394. (b) Kortz, U.; Muller, A.; van Slageren, J.; Schnack, J.; Dalal, N. S.; Dressel, M. *Coord. Chem. Rev.* **2009**, *253*, 2315−2327.

(2) (a) Suaud, N.; Gaita-Ariño, A.; Clemente-Juan, J. M.; Sánchez-Marín, J.; Coronado, E. *J. Am. Chem. Soc.* **2002**, *124*, 15134−15140. (b) Borrás-Almenar, J. J.; Clemente-Juan, J. M.; Coronado, E.; Tsukerblat, B. *Chem. Phys.* **1995**, *195*, 1−15.

(3) Calzado, C. J.; Clemente-Juan, J. M.; Coronado, E.; Gaita-Ariño, A.; Suaud, N. *Inorg. Chem.* **2008**, *47*, 5889−5901.

(4) (a) Coronado, E.; Gómez,-García, C. J. *Comments Inorg. Chem.* **1995**, *17*, 255−281. (b) Bassil, B. S.; Kortz, U., Z. *Anorg. Allg. Chem.* **2010**, *636*, 2222.

(5) Müller, A.; Peters, F.; Pope, M. T.; Gatteschi, D. *Chem. Rev.* **1998**, *98*, 239−271.

(6) Kögerler, P.; Tsukerblat, B.; Müller, A. *Dalton Trans.* **2010**, *39*, 21−36.

(7) Palii, A.; Tsukerblat, B.; Klokishner, S.; Dunbar, K.; Clemente-Juan, J. M.; Coronado, E. *Chem. Soc. Rev.* **2011**, *40*, 3130−3156.

(8) Lehmann, J.; Gaita-Ariño, A.; Coronado, E.; Loss, D. *Nat. Nanotechnol.* **2007**, *2*, 312−317.

(9) (a) Lehmann, J.; Gaita-Ariño, A.; Coronado, E.; Loss, D. *J. Mater. Chem.* **2009**, *19*, 1672−1677. (b) Clemente-Juan, J. M.; Coronado, E.; Gaita-Ariño, A. *Chem. Soc. Rev.* **2012**, DOI: 10.1039/c2cs35205b.

(10) Bertaina, S.; Gambarelli, S.; Mitra, T.; Tsukerblat, B.; Müller, A.; Barbara, B. *Nature* **2008**, *453*, 203−206.

(11) (a) AlDamen, M. A.; Clemente-Juan, J.; Coronado, E.; Martí-Gastaldo, C.; Gaita-Ariño, A. *J. Am. Chem. Soc.* **2008**, *130*, 8874−8875. (b) Aldamen, M. A.; Cardona-Serra, S.; Clemente-Juan, J. M.; Coronado, E.; Gaita-Ariño, A.; Martí-Gastaldo, C.; Luis, F.; Montero, O. *Inorg. Chem.* **2009**, *48*, 3467−3479.
(12) Luis, F.; Martínez-Pérez, M.; Montero, O.; Coronado, E.; Cardona-Serra, S.; Martí-Gastaldo, C.; Clemente-Juan, J. M.; Sesé, J.; Drung, D.; Schurig, T. *Phys. Rev. B* **2010**, *82*, No. 060403.
(13) Ishikawa, N.; Sugita, M.; Ishikawa, T.; Koshihara, S. Y.; Kaizu, Y. *J. Am. Chem. Soc.* **2003**, *125*, 8694−8695.
(14) Ishikawa, N.; Sugita, M.; Ishikawa, T.; Koshihara, S.; Kaizu, Y. *J. Phys. Chem. B* **2004**, *108*, 11265−11271.
(15) (a) Bertaina, S.; Gambarelli, S.; Tkachuk, A.; Kurkin, I. N.; Malkin, B.; Stepanov, A.; Barbara, B. *Nature Nano.* **2007**, *2*, 39−42. (b) Coronado, E.; Giménez-Saiz, C.; Recuenco, A.; Tarazón, A.; Romero, F. M.; Camón, A.; Luis, F. *Inorg. Chem.* **2011**, *50*, 7370−7372. (c) Jiang, S.; Wang, B.; Sun, H.; Wang, Z.; Gao, S. *J. Am. Chem. Soc.* **2011**, *133*, 4730−4733.
(16) Creaser, I.; Heckel, M. C.; Neitz, R. J.; Pope, M. T. *Inorg. Chem.* **1993**, *32*, 1573−1578.
(17) Martínez-Pérez, M. J.; Sesé, J.; Luis, F.; Drung, D.; Schurig, T. *Rev. Sci. Instrum.* **2010**, *81*, No. 0161198.
(18) Kim, K.-C.; Pope, M. T.; Gama, G. J.; Dickman, M. H. *J. Am. Chem. Soc.* **1999**, *121*, 11164−11170.
(19) Creaser, I.; Heckel, M.; Neitz, R.; Pope, M. *Inorg. Chem.* **1993**, *32*, 1573−1578.
(20) Stevens, K. W. H. *Proc. Phys. Soc. A* **1952**, *65*, 209−215.
(21) (a) Orbach, R. *Proc. Phys. Soc. A* **1961**, *264*, 458−484. (b) Rudowicz, C. *J. Phys. C: Solid State Phys.* **1985**, *18*, 1415−1430.
(22) Walter, U. *Phys. Rev. B* **1987**, *36*, 2504−2512.
(23) Ishikawa, N.; Sugita, M.; Okubo, T.; Takana, N.; Iino, T.; Kaizu, Y. *Inorg. Chem.* **2003**, *42*, 2440−2446.
(24) Chiang, M.-H.; Antonio, M. R.; Williams, C.; Soderholm, L. *Dalton Trans.* **2004**, *5*, 801−806.
(25) Sessoli, R.; Tsai, H.-L.; Schake, A.; Wang, S.; Vincent, J.; Folting, K.; Gatteschi, D.; Christou, G.; Hendrickson, D. N. *J. Am. Chem. Soc.* **1993**, *115*, 1804−1816.
(26) Delfs, C.; Gatteschi, D.; Pardi, L.; Sessoli, R.; Wieghardt, K.; Hanke, D. *Inorg. Chem.* **1993**, *32*, 3099−3103.
(27) Aliaga-Alcalde, N.; Edwards, R.; Hill, S.; Wernsdorfer, W.; Folting, K.; Christou, G. *J. Am. Chem. Soc.* **2004**, *126*, 12503−12516.
(28) Cole, K. H.; Cole, R. H. *J. Chem. Phys.* **1941**, *9*, 341−352.
(29) Wernsdorfer, W.; Ohm, T.; Sangregorio, C.; Sessoli, R.; Mailly, D.; Paulsen, C. *Phys. Rev. Lett.* **1999**, *82*, 3903−3906.
(30) Ishikawa, N; Sugita, M.; Wernsdorfer, W. *J. Am. Chem. Soc.* **2005**, *127*, 3650−3651.
(31) Car, P. E.; Perfetti, M.; Mannini, M.; Favre, A.; Caneschi, A.; Sessoli, R. *Chem. Commun.* **2011**, *47*, 3751−3753.
(32) Bertaina, S.; Gambarelli, S.; Tkachuk, A.; Kurkin, I. N.; Malkin, B.; Stepanov, A.; Barbara, B. *Nat. Nanotechnol.* **2007**, *2*, 39−42.
(33) Martínez-Pérez, M. J.; Cardona-Serra, S.; Schlegel, C.; Moro, F.; Alonso, P. J.; Prima-García, H.; Clemente-Juan, J. M.; Evangelisti, M.; Gaita-Ariño, A.; Sesé, J.; van Slageren, J.; Coronado, E.; Luis, F. *Phys. Rev. Lett.* **2012**, *108*, No. 247213.
(34) Martínez-Pérez, M. J.; Montero, O.; Evangelisti, M.; Luis, F.; Sesé, J.; Cardona-Serra, S.; Coronado, E. *Adv. Mater.* **2012**, *24*, 4301−4305.

Supplementary Material

Lanthanoid Single-Ion Magnets Based on Polyoxometalates with a Fivefold Symmetry: The series $[LnW_{30}O_{110}]^{12-}$ (Ln^{3+}=Tb, Dy, Ho, Er, Tm and Yb).

S. Cardona-Serra[1], J. M. Clemente-Juan[1], E. Coronado[1*], A. Gaita-Ariño[1], A. Camón[2], M. Evangelisti[2], F. Luis[2*], M. J. Martínez-Pérez[2], J. Sesé[3]

Energy (cm^{-1})	Wave function			
0	**0.70·|-5>**	0.15·|0>	**0.70·|5>**	
1.998	**0.71·|-5>**	**0.71·|5>**		
8.846	0.11·|-6>	0.11·|-1>	**0.99·|4>**	
8.846	**0.99·|-4>**	0.11·|1>	0.03·|6>	
15.414	**0.99·|-6>**	0.09·|-1>	0.12·|4>	
15.414	0.12·|-4>	0.09·|1>	**0.99·|6>**	
32.741	**0.99·|-3>**	0.11·|2>		
32.741	0.11·|-2>	**0.99·|3>**		
61.446	**0.99·|-2>**	0.11·|3>		
61.446	0.11·|-3>	**0.99·|2>**		
84.720	0.10·|-4>	**0.99·|1>**	0.10·|6>	
84.720	0.10·|-6>	**0.99·|-1>**	0.10·|4>	
93.403	0.10·|-5>	**0.99·|0>**	0.10·|5>	

Table S.1: Energies and modulus of the contribution of each M_J to the wave-functions of the ground state multiplets of TbW30.

Energy (cm^{-1})	Wave function		
0	**0.98·|-15/2>**	0.22·|-5/2>	
0	0.22·|5/2>	**0.98·|15/2>**	
19.483	0.44·|-11/2>	**0.85·|-1/2>**	0.28·|9/2>
19.483	0.28·|-9/2>	**0.85·|1/2>**	0.44·|11/2>
21.000	0.78·|-13/2>	**0.61·|-3/2>**	0.12·|7/2>
21.000	0.12·|-7/2>	**0.61·|3/2>**	0.78·|13/2>
80.159	0.59·|-13/2>	**0.67·|-3/2>**	0.43·|7/2>
80.159	0.43·|-7/2>	**0.67·|3/2>**	0.59·|13/2>
91.710	0.22·|-15/2>	**0.98·|-5/2>**	
91.710	**0.98·|5/2>**	0.22·|15/2>	
98.678	**0.79·|-11/2>**	0.22·|-1/2>	0.55·|9/2>
98.678	0.55·|-9/2>	0.22·|1/2>	**0.79·|11/2>**
115.488	0.18·|-13/2>	0.41·|-3/2>	**0.90·|7/2>**
115.488	**0.90·|-7/2>**	0.41·|3/2>	0.18·|13/2>
129.186	**0.78·|-9/2>**	0.47·|1/2>	0.41·|11/2>
129.186	0.41·|-11/2>	0.47·|-1/2>	**0.78·|9/2>**

Table S.2: Energies and modulus of the contribution of each M_J to the wave-functions of the ground state multiplets of DyW30.

Energy (cm^{-1})	Wave function			
0	0.05·|-7>	0.12·|-2>	0.45·|3>	**0.88·|8>**
0	**0.88·|-8>**	0.45·|-3>	0.12·|2>	0.05·|7>
14.249	0.50·|-5>	**0.70·|0>**	0.50·|5>	
22.538	0.40·|-4>	**0.70·|1>**	0.58·|6>	
22.538	0.58·|-6>	**0.70·|-1>**	0.40·|4>	
47.285	0.24·|-8>	0.20·|-3>	**0.82·|2>**	0.48·|7>
47.285	0.48·|-7>	**0.82·|-2>**	0.20·|3>	0.24·|8>
92.854	0.21·|-7>	0.20·|-2>	**0.87·|3>**	0.40·|8>
92.854	0.40·|-8>	**0.87·|-3>**	0.20·|2>	0.21·|7>
97.323	0.52·|-6>	0.35|-1>	**0.77·|4>**	
97.323	**0.77·|-4>**	0.35|1>	0.52·|6>	
104.207	**0.71|-5>**	**0.71|5>**		
182.661	0.08·|-3>	0.52·|2>	**0.85|7>**	
182.661	**0.85|-7>**	0.52·|-2>	0.08·|3>	
196.679	0.50·|-5>	**0.71·|0>**	0.50·|5>	
200.166	0.75·|-6>	**0.62·|-1>**	0.22·|4>	
200.166	0.22·|-4>	**0.62·|1>**	0.75·|6>	

Table S.3: Energies and modulus of the contribution of each M_J to the wave-functions of the ground state multiplets of HoW30

Energy (cm^{-1})	Wave function		
0	**0.69·|-11/2>**	0.65·|-1/2>	0.33·|9/2>
0	0.33·|-9/2>	0.65·|1/2>	**0.69·|11/2>**
9.767	**0.85·|-13/2>**	0.51·|-3/2>	0.13·|7/2>
9.767	0.13·|-7/2>	0.51·|3/2>	**0.85·|13/2>**
111.740	0.61·|-11/2>	0.27·|-1/2>	**0.75·|9/2>**
111.740	**0.75·|-9/2>**	0.27·|1/2>	0.61·|11/2>
139.792	0.48·|5/2>	**0.87·|15/2>**	
139.792	**0.87·|-15/2>**	0.48·|-5/2>	
141.494	0.42·|-13/2>	0.52·|-3/2>	**0.74·|7/2>**
141.494	**0.74·|-7/2>**	0.52·|3/2>	0.42·|13/2>
210.429	0.31·|-13/2>	**0.69·|-3/2>**	0.66·|7/2>
210.429	0.66·|-7/2>	**0.69·|3/2>**	0.31·|13/2>
221.269	0.58·|-9/2>	**0.71·|1/2>**	0.40·|11/2>
221.269	0.40·|-11/2>	**0.71·|-1/2>**	0.58·|9/2>
246.199	0.48·|5/2>	**0.88·|15/2>**	
246.199	**0.88|-15/2>**	0.48·|-5/2>	

Table S.4: Energies and modulus of the contribution of each M_J to the wave-functions of the ground state multiplets of ErW30

Energy (cm^{-1})	Wave function		
0	**0.94·|-4>**	0.33·|1>	0.11·|6>
0	0.11·|-6>	0.33·|-1>	**0.94·|4>**
6.408	**0.97·|-3>**	0.26·|2>	
6.408	0.26·|-2>	**0.97·|3>**	
52.061	**0.61·|-5>**	0.51·|0>	**0.61·|5>**
86.301	0.26·|-3>	**0.97·|2>**	
86.301	**0.97·|-2>**	0.26·|3>	
103.812	**0.71·|-5>**	**0.71·|5>**	
108.623	**0.85·|-6>**	0.46·|-1>	0.26·|4>
108.623	0.26·|-4>	0.46·|1>	**0.85·|6>**
207.207	0.52·|-6>	**0.82·|-1>**	0.22·|4>
207.207	0.22·|-4>	**0.82·|1>**	0.52·|6>
251.575	0.36·|-5>	**0.86·|0>**	0.36·|5>

Table S.5: Energies and modulus of the contribution of each M_J to the wave-functions of the ground state multiplets of TmW30

Energy (cm^{-1})	Wave function	
0	0.32·|-3/2>	**0.95·|7/2>**
0	**0.95·|-7/2>**	0.32·|3/2>
2.908	**1.00·|-1/2>**	
2.908	**1.00·|1/2>**	
171.523	**1.00·|-5/2>**	
171.523	**1.00·|5/2>**	
196.943	0.32·|-7/2>	**0.95·|3/2>**
196.943	**0.95·|-3/2>**	0.32·|7/2>

Table S.6: Energies and modulus of the contribution of each M_J to the wave-functions of the ground state multiplets of YbW30

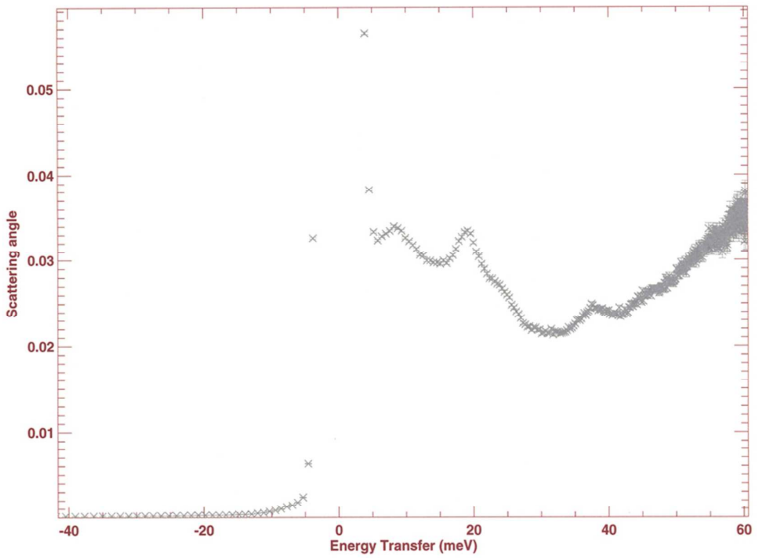

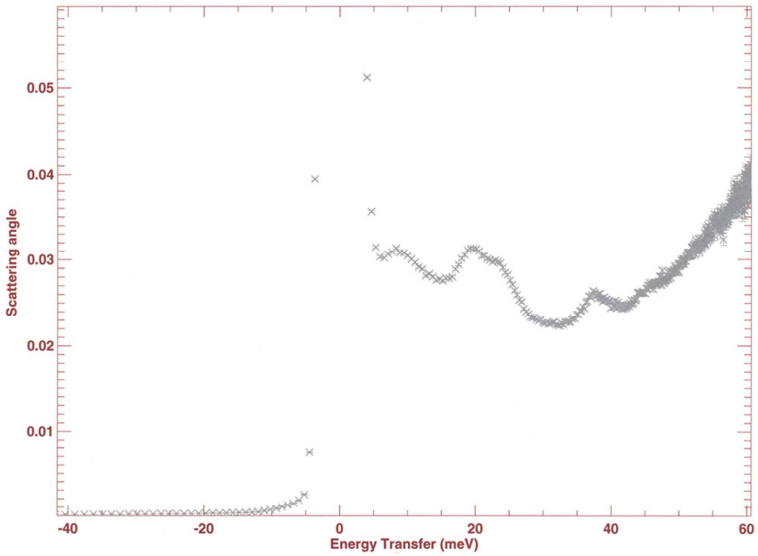

Figure S.1: Inelastic Neutron Scattering spectra of $K_{12}DyP_5W_{30}O_{110}$ (top) and $K_{12}HoP_5W_{30}O_{110}$ (down) the measurement were done at 1.5K and $\lambda = 1.1$Å.

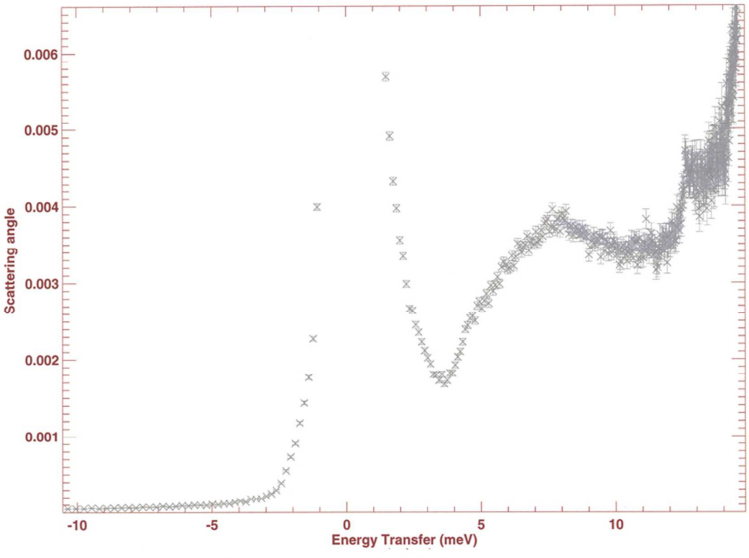

Figure S.2: Inelastic Neutron Scattering spectrum of $K_{12}DyP_5W_{30}O_{110}$, the measurement was done at 1.5K and λ = 2.2Å.

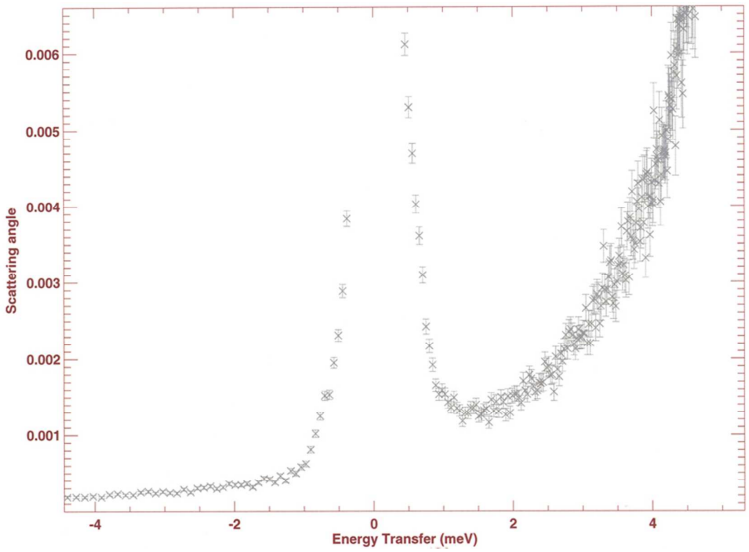

Figure S.3: Inelastic Neutron Scattering spectrum of $K_{12}DyP_5W_{30}O_{110}$, the measurement was done at 1.5K and λ = 3.6Å.

PAPER 5:
Rational Design of Single-Ion Magnets and Spin Qubits Based on Mononuclear Lanthanoid Complexes

Inorganic Chemistry, **2012**, *51*, 12565-12574.

Inorganic Chemistry

Article

pubs.acs.org/IC

Rational Design of Single-Ion Magnets and Spin Qubits Based on Mononuclear Lanthanoid Complexes

José J. Baldoví,[†] Salvador Cardona-Serra,[†] Juan M. Clemente-Juan,[†] Eugenio Coronado,*[,†] Alejandro Gaita-Ariño,*[,†] and Andrew Palii[‡]

[†]Instituto de Ciencia Molecular (ICMol), Universidad de Valencia, C/Catedrático José Beltrán 2, E-46980 Paterna, Spain

[‡]Institute of Applied Physics, Academy of Sciences of Moldova, Academy Street 5, MD 2028 Kishinev, Moldova

ABSTRACT: Here we develop a general approach to calculating the energy spectrum and the wave functions of the low-lying magnetic levels of a lanthanoid ion submitted to the crystal field created by the surrounding ligands. This model allows us to propose general criteria for the rational design of new mononuclear lanthanoid complexes behaving as single-molecule magnets (SMMs) or acting as robust spin qubits. Three typical environments exhibited by these metal complexes are considered, namely, (a) square antiprism, (b) triangular dodecahedron, and (c) trigonal prism. The developed model is used to explain the properties of some representative examples showing these geometries. Key questions in this area, such as the chemical tailoring of the superparamagnetic energy barrier, tunneling gap, or spin relaxation time, are discussed. Finally, in order to take into account delocalization and/or covalent effects of the ligands, this point-charge model is complemented with ab initio calculations, which provide accurate information on the charge distribution around the metal, allowing for an explanation of the SMM behavior displayed by some sandwich-type organometallic compounds.

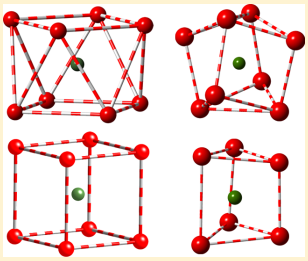

INTRODUCTION

For more than 15 years, single-molecule magnets (SMMs) have been a hot topic in molecular magnetism because of their rich physical behavior. Thus, crystals of these molecules exhibit a superparamagnetic blocking at T_B, characterized by slow relaxation of the magnetization at lower temperatures and by magnetic hysteresis.[1,2] On the other hand, they are among the most complex magnetic entities that show quantum phenomena like quantum tunneling of the magnetization,[3] quantum coherence, or quantum interference, and thus they have been postulated as candidates for spin qubits in quantum computing.[4]

The first generation of SMMs was based on polynuclear magnetic complexes (magnetic clusters) with strong magnetic coupling between d transition-metal ions, leading to a high-spin ground state, S, well separated in energy from the excited spin multiplets, and a negative uniaxial anisotropy, D, which causes a splitting of this ground state into $\pm S_z$ sublevels and creates a barrier for the spin reversal.[5] The major synthetic challenge in this case was to increase this energy barrier and, consequently, the blocking temperature T_B, by designing molecules having maximum values of S and D. However, the success of this approach has been very limited, as demonstrated by the fact that the first SMM, the so-called Mn_{12}, is still among the systems exhibiting the highest effective barriers (ca. 45−50 cm^{-1}) and hysteresis up to 4 K. More recently, magnetic clusters containing highly anisotropic lanthanoid ions have also been synthesized.[6] These complexes have shown effective barriers as high as 100 cm^{-1} and hysteresis up to 8 K.

In the past few years, a new generation of SMMs have appeared with the discovery that a mononuclear complex formed by a single magnetic center coordinated to ligands, usually an anisotropic lanthanoid ion, may also behave as a SMM. These compounds are known as single-ion magnets (SIMs) or mononuclear SMMs.[7] The first example of a molecular SIM was reported by Ishikawa et al. in 2003 in complexes of the general formula $[LnPc_2]^-$, with a "double-decker" structure and phthalocyanines as ligands.[8] Thus, the antiprismatic D_{4d} crystal field (CF) induced by the octacoordinated atoms around the Ln^{3+} ion splits its ground magnetic state, characterized by the total angular momentum, J, into $\pm M_J$ sublevels. In some cases, this leads to a sublevel scheme in which the levels with the higher $|M_J|$ values are stabilized with respect to the levels with the lower $|M_J|$ values. This creates a barrier that explains the SMM behavior observed in the terbium derivative for which the ground-state magnetic doublet corresponds to that with the maximum M_J value (=±6), being separated from the first excited level (M_J = ±5) by more than 300 cm^{-1}.

Later on, in 2008 our group showed that the concept of SIMs can be extended to other families of mononuclear lanthanide complexes. Thus, we discovered that polyoxometalate (POM) complexes encapsulating a lanthanoid ion do also exhibit SMM behavior for coordination sites close to the antiprismatic D_{4d} symmetry.[9] In this case, the different distortion of the

Received: September 24, 2012
Published: October 26, 2012

   dx.doi.org/10.1021/ic302068c | *Inorg. Chem.* 2012, 51, 12565−12574

antiprismatic site (axially compressed) compared to that shown by the $[LnPc_2]^-$ complexes (axially elongated) leads to a different splitting of the $\pm M_J$ levels. Thus, under this CF, the higher M_J values ($\pm^{13}/_2$) are stabilized in the erbium derivative, which behaves as a SMM, while in the terbium derivative, M_J = 0 is a ground state and the level with $M_J = \pm 6$ corresponds to an excited state; hence, it does not behave as a SMM.

Since then, many examples of mononuclear lanthanide complexes having different coordination geometries and different types of ligands have also shown SMM properties, thus demonstrating that the SIM concept is quite general. Some relevant examples are the organometallic double-decker Er^{3+} compound[10] and the acetylacetonate lanthanoid complexes,[11] both studied by Gao et al., and the DyDOTA complex reported by Sessoli et al.[12] In addition, some SIMs based on mononuclear uranium complexes have been reported.[13] Finally, mononuclear d transition metals have also shown to behave as SIMs, with the iron pyrrolide molecules[14] and a $Co(SPh)_4$ salt[15] being the most quoted cases. Note that the concept of SIMs is not restricted to the molecular world. In fact, the family of lanthanoid-substituted scheelites of the formulas $LiY_{1-x}Ho_xF_4$ and $Ca_{1-x}Er_xWO_4$ has also provided examples of SIMs. Thus, the former system behaves as a SMM showing a staircase-like hysteresis loop of the magnetization due to a nuclear-spin-driven quantum relaxation,[16] while the latter behaves as a spin qubit exhibiting coherent Rabi oscillations, which are indicative of high quantum coherence.[17]

The present work has been motivated by the need to find general criteria for the rational design of new mononuclear lanthanoid complexes behaving as SMMs or acting as spin qubits. Often, the same nanomagnet may be regarded as either a SMM or a molecular spin qubit, depending on the experiment performed. Still, some differences between these two aspects exist. Thus, the magnetization orientation of a molecule is utterly described by a classical bit. Instead, if we consider the molecule as a qubit, one additionally needs to address arbitrary superpositions between quantum states.

Nevertheless, in both cases, the final goal is to manipulate the quantum dynamics of a small number of levels, and in this regard, one needs the following:

(1) To know the mixing within our target subset of levels. This knowledge is required for the design of the system and, subsequently, for manipulation of the spin dynamics.

(2) To guarantee an effective isolation of the ground state from the rest of the spectrum, in the form of a large energy gap. Moreover, the optical, electric, or magnetic operations that one can perform on this subsystem should not cause leakage to excited states.

Previously, a qualitative approach to predicting the ligand disposition to obtain SMMs has been reported.[18] Here we will develop a general theoretical approach to calculating the energy spectrum and the wave functions of the low-lying magnetic levels of a lanthanoid ion submitted to the CF created by the surrounding ligands. We show that this model can allow us to predict which lanthanoids and geometries are more suited for obtaining SMMs or robust spin qubits. Key questions in this area, such as the chemical tailoring of the physical properties of these nanomagnets (superparamagnetic energy barrier, tunneling gap, spin relaxation time, etc.), are discussed. The computational approach, initially based on a point-charge model, can also incorporate delocalization and/or covalent effects of the ligands through ab initio calculations that give accurate information on the charge distribution around the metal.

RESULTS AND DISCUSSION

In a first approximation, a mononuclear lanthanoid-based complex will behave as a SMM, i.e., it will have a superparamagnetic energy barrier, if splitting of the ground state of the lanthanoid, J, caused by the CF created by the ligands is such that the ground-state magnetic doublet has a high M_J value, $\pm M_J$, which is well separated in energy from the excited-state M_J sublevels. Such a splitting will be dependent on the lanthanoid and on the symmetry and distortion of the coordination environment. The theoretical background of the CF calculation and the computational method will be presented in a separate section.

As far as the lanthanoid is concerned, we notice that J and the Stevens coefficients (α, β, and γ)[19] are fixed and are specific for each lanthanoid. It is obvious that the first condition to get a high-M_J ground-state doublet is to have a large J value. Hence, we should focus on the second half of the lanthanoid series because these ions possess a negative spin−orbit coupling, which stabilizes the states with maximum J values ($J = L + S$). According to this, Tb^{3+}, Dy^{3+}, Ho^{3+}, Er^{3+}, and Tm^{3+} will be the best choices, with Yb^{3+}, Pr^{3+}, and Nd^{3+} coming next.

The nuclear spin of the lanthanoid can also be relevant because it will determine the shape of the hysteresis loop, including whether there is quantum tunneling of the magnetization at zero field.[20]

As far as the coordination environment is concerned, the first condition for designing SIMs will be to have highly symmetric axial sites because they often provide the most favorable case to have pure M_J wave functions. The level splitting produced by strong diagonal terms can avoid the mixture with low M_J states even for nonideal geometries. Neglecting high-order parameters, one can expect that α-negative lanthanoids (Tb^{3+}, Dy^{3+}, Ho^{3+}, Pr^{3+}, and Nd^{3+}) will stabilize a high-M_J ground-state doublet when they are in an axially elongated coordination environment, whereas α-positive lanthanoids (Er^{3+}, Tm^{3+}, and Yb^{3+}) will need equatorial or axially compressed coordination environments to achieve this. This can be easily understood if we notice that the B_2^0 parameter is proportional to the axial zero-field-splitting parameter (D) and related to the A_2^0 parameter by the following expression: $B_2^0 = D/3 = \alpha\langle r^2\rangle A_2^0$. Thus, a negative B_2^0 will require a negative α (because A_2^0 is positive) for an elongation or a positive α for a compression (because in this case A_2^0 is negative). Finally, for particular symmetries where B_2^0 does not dominate (e.g., octahedral coordination geometry), the higher-order B_4^0 parameter usually does. In these cases, to favor stabilization of the medium-to-high M_J compared with the lowest M_J states, β-positive lanthanoids (Tb^{3+}, Er^{3+}, and Tm^{3+}) should have ligands on the z axis and/or on the xy plane, whereas β-negative lanthanoids (Pr^{3+}, Nd^{3+}, Dy^{3+}, Ho^{3+}, and Yb^{3+}) should have them at polar angles of around 50−60°. These behaviors are perhaps more easily understood through analysis of Figure 2.

In the following, we will study in detail the influence of the coordination environment on the splitting of the J ground state of the lanthanoid complex in three typical cases, namely, the (a) square antiprism, (b) triangular dodecahedron, and (c) trigonal prism. We will first assume both ideal and real structures to discuss the effect of these CFs and to give some general guidelines for the choice of the most adequate geometry.

a. Square-Antiprismatic versus Cubic Geometry. Herein, we compare the well-known square-antiprismatic geometry (D_{4d} ideal symmetry) and the cubic geometry (O_h ideal symmetry). POM chemistry provides nice examples of these two octacoordinated environments (Figure 1). In fact,

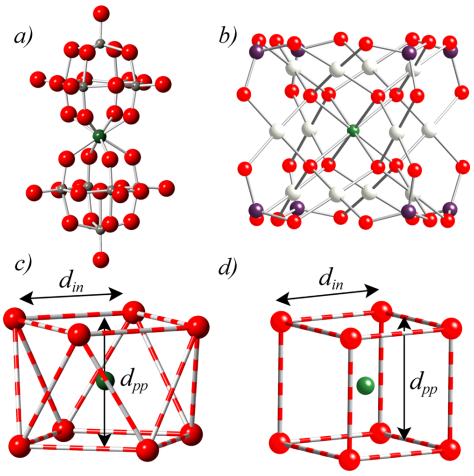

Figure 1. Schematic structures of two different POM complexes with interesting coordination symmetry, (a) **1** and (b) **2**, and their coordination polyhedra, (c) square antiprism and (d) cube. The d_{pp} parameter defines the average distance between the two oxygen-based square planes. d_{in} is the average O−O distance within the oxygen-based square planes.

these molecular metal oxides have rigid and stable structures that can impose highly symmetric CFs to the lanthanoid. In Figure 1, the structure of the square antiprism $[Ln(W_5O_{18})_2]^{9-}$ (**1**) is compared to the cubic structure of $[LnPd^{II}_{12}(As^{V}Ph)_8O_{32}]^{5-}$ (**2**) recently reported by Kortz et al.[21] Experimentally, the magnetic behavior of these two series shows that while for **1** some derivatives exhibit a SMM behavior, for **2** all of the derivatives exhibit a fast spin relaxation at low temperatures.[22] It seems therefore that the D_{4d} symmetry is more suitable for the design of SIMs than the O_h symmetry is.

Let us now discuss the origin of such a difference. The real geometry for the erbium derivative of the series **1** is plotted in Figure 1. In this compound, the ratio between the interplanar distance d_{pp} = 2.47(1) Å (calculated as the distance between the upper and lower planes containing the four oxygen atoms) and the average distance between the four neighboring oxygen atoms placed in each plane, d_{in} = 2.86(5) Å, is indicative of an axial compression of the square antiprism. Using this geometry, the main CF parameters to be considered are B^0_2, B^0_4, and B^0_6 (those allowed by an ideal D_{4d} system), but because of distortion of the site, nonnegligible values for B^3_4, B^4_4, and B^4_6 appear. The calculations lead to an isolated ground-state doublet, corresponding to that with the highest M_J value ($\pm^{15}/_2$), which is separated in energy from the first excited-state doublet $M_J = \pm^{13}/_2$ by 56.8 cm^{-1}. Such a feature explains the SMM behavior exhibited by this erbium compound. In fact, the energy gap between the ground state and the first excited state is close to the effective energy barrier determined experimentally (38.1 cm^{-1}). This indicates that relaxation will take place by quantum tunneling through the first excited state because the corresponding wave function is formed by a mixture of the $M_J = \pm^{13}/_2$ function and those having $M_J = \pm^{1}/_2$ and $\pm^{3}/_2$. Notice that, in this simple description, other factors, such as the presence of phonons or the effect of other nuclei, which are supposed to modify the effective barrier, have been neglected.

Experimental CF parameters can be obtained from the magnetic properties following the Ishikawa procedure.[23] For an isomorphic series of lanthanoid complexes, the CF parameters could be determined by a simultaneous fit of all of the $\chi_m T$ values under the assumption that each CF parameter shows a linear variation from the f^8 (Tb^{3+}) system to the f^{13} (Yb^{3+}) system.

This theoretical CF model can be extended to other lanthanoid derivatives of **1**, such as Ho^{3+}, Tb^{3+}, and Dy^{3+}. In this axially compressed geometry, both the erbium and holmium derivatives have high-spin ground states. Thus, they are both more likely SIM candidates than terbium and dysprosium, in contrast with the Pc_2Ln case. Nevertheless, according to our calculations summarized in Table 1,

Table 1. Calculated Low-Lying Energy Levels and Eigenvector Contributions with C_I^2 > 5% For $[Ln(W_5O_{18})_2]^{9-}$ (1; Ln = Er^{3+} and Ho^{3+}, up and down, Respectively)

energy (cm^{-1})	c_i^2 (M_J)
0.00	0.9996 ($-^{15}/_2$)
0.00	0.9996 ($^{15}/_2$)
56.82	0.9975 ($-^{13}/_2$)
56.82	0.9975 ($^{13}/_2$)
103.45	0.9316 ($-^{1}/_2$)
103.45	0.9316 ($^{1}/_2$)
energy (cm^{-1})	**c_i^2 (M_J)**
0.00	0.453 (−4), 0.453 (4)
0.11	0.451 (−4), 0.451 (4)
12.22	0.273 (−5), 0.217 (−3), 0.216 (3), 0.273 (5)
12.41	0.284 (−5), 0.205 (−3), 0.205 (3), 0.285 (5)
16.93	0.186 (−5), 0.249 (−3), 0.249 (3), 0.186 (5)
17.50	0.160 (−5), 0.284 (−3), 0.284 (3), 0.160 (5)

comparable minor deviations from the ideal geometry have markedly different effects on the erbium and holmium systems: the erbium derivative preserves a 99.96% purity of the (well-isolated) $M_J = \pm^{15}/_2$ ground state, while the holmium complex displays a thorough mixing, both in the ground state and in the low-lying excited states. This can be linked to the experimental behavior: for $[Er(W_5O_{18})_2]^{9-}$, the superparamagnetic blocking happens for frequencies as low as 100 Hz, while for $[Ho(W_5O_{18})_2]^{9-}$, the out-of-phase susceptibility only begins to arise at frequencies on the order of 10 kHz.

An important feature of these results is the sign of B^0_2, which is positive in Tb^{3+}, Dy^{3+}, and Ho^{3+} and negative for Er^{3+}. In general, the sign of B^0_2 for a given lanthanoid is determined by the combination of the axial ($\theta < 54.7°$) or equatorial character ($\theta > 54.7°$) of the sites, as defined by the ligand position. In fact, from Figure 2, it is easy to understand that at $\theta \approx 54.7°$, which corresponds to an axially nondistorted antiprism (defined by $d_{in} = d_{pp}$) or to a cube, a point charge is on a

dx.doi.org/10.1021/ic302068c | Inorg. Chem. 2012, 51, 12565−12574

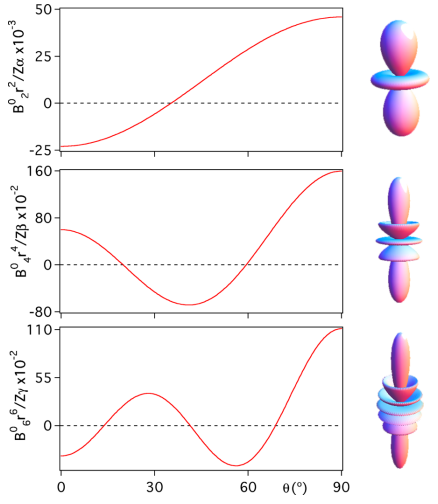

Figure 2. Magnetostructural correlation of B^0_2/α, B^0_4/β, and B^0_6/γ with the θ polar angle in the case of D_{4d}. Right side: shapes of Y_{20}, Y_{40}, and Y_{60}; in Y_{20}, one can recognize the shape of the d_{z^2} orbital.

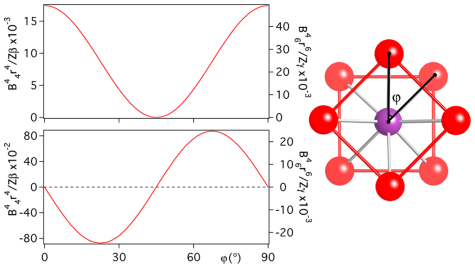

Figure 3. (left) Magnetostructural correlation of the real (top) and imaginary (down) parts of B^4_4/β and B^6_6/γ with φ. (right) Scheme depicting the torsion angle that describes the rotation of a cube from O_h to D_{4d} symmetries.

node, so that it contributes to B^0_4 and B^0_6, while B^0_2 is equal to zero.

An example with cubic symmetry is provided by the series **2**. Calculations performed on the Er^{3+} derivative using real coordinates show a mixed ground-state doublet, with the most important contribution being that of $M_J = \pm^1/_2$, followed by $\mp^{15}/_2$, $\mp^7/_2$, and $\pm^9/_2$. The first 4-fold degenerate excited state is located at 13.5 cm^{-1}, where the majority of the M_J values are contributing to the wave function. This low extensive mixing of the sublevels yields a fast quantum tunneling of the magnetization. On the other hand, the presence of $\pm^1/_2$ in the ground state explains why this molecule does not possess SIM behavior. Because of the well-known relations for cubic symmetry, $B^4_4/B^0_4 = 5$ and $B^6_6/B^0_6 = -21$, this system may be defined only by two CF parameters, B^0_4 and B^0_6. The absence of B^0_2 (meaning $D = 0$) reduces the possibilities of using a different lanthanoid (e.g., Tb^{3+}, Dy^{3+}, or Ho^{3+}) to obtain a higher barrier. In conclusion, D_{4d} symmetry (axially elongated for Tb^{3+}, Dy^{3+}, or Ho^{3+} or equatorially compressed for Er^{3+}) is much more favorable than cubic (O_h) symmetry for obtaining slow relaxation of the magnetization. This is better understood by performing a magnetostructural study in which the D_{4d} symmetry is taken as a distorted case of the O_h symmetry when the two squares are staggered rather than eclipsed. This situation is defined by the torsion angle between the upper and lower squares, φ, which goes from 0° in the O_h symmetry to 45° in the D_{4d} symmetry. To perform this calculation, the coordinates of the four point charges forming a square are rotated with respect to that of the other square around the z axis. A typical distortion of the D_{4d} symmetry can be obtained by slightly deviating φ from 45° (see Figure 3, left). The calculations indicate that the CF parameters B^0_4 and B^0_6 are invariant with respect to φ. Additionally, B^4_4 and B^4_6 are nonzero, except for $\varphi = 45°$, evolving as a function of φ (Figure 3, right). Thus, exact cancelation of these two parameters occurs for the D_{4d} symmetry, while the maximum values are reached for the O_h one. In conclusion, one can anticipate that for an ideal D_{4d} symmetry the wave functions will be described by pure $\pm M_J$ values, while for a cubic symmetry, the presence of the B^4_4 and B^6_6 CF parameters will result in an extensive mixing of functions with different M_J values (in particular, those differing by $\Delta M_J = 4$). On the other hand, as we have seen before, the B^0_2 parameter will be zero either for a cubic symmetry or for a nondistorted antiprismatic symmetry. This is the key parameter for creating a gap between the M_J ground-state doublet, and the excited states (and therefore a barrier) will only appear by axial distortion of the antiprism (elongation or compression). Using such a procedure, one is able to analyze real structures that are between these two symmetries, as determined by shape analysis.[24]

b. Triangular Dodecahedron. A triangular dodecahedron presents D_{2d} symmetry (Figure 4), closely related to S_4, with a

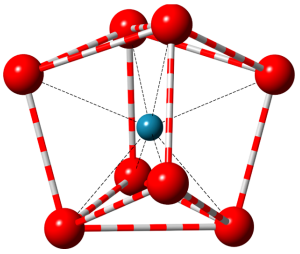

Figure 4. Schematic structure of a triangular dodecahedron site with D_{2d} symmetry, with 'axial' and 'equatorial' ligands.

coordination number of 8 around the lanthanoid ion. In this case, the most important examples are found in the salts $LiHo_xY_{1-x}F_4$ and $Er_xCa_{1-x}WO_4$, both showing a scheelite structure, with tetragonal distortion from the cubic symmetry arising from the displacement of two opposite edges in opposite directions. This yields a symmetry reduction from O_h to S_4. As a real example for this coordination symmetry, we have used the $LiHo_xY_{1-x}F_4$ compound, obtaining the following CF terms: B^0_2, B^0_4, B^0_6, B^3_4, B^4_4, and B^4_6. Because of the ionic character of F ions, this system provides an excellent scenario to test the point-charge model. The calculated splitting diagram for the $J = 8$ ground state of Ho^{3+} in this environment reveals a

ground-state doublet defined by two functions composed by the following M_J values: (+7, +3, −1, −5) and (−7, −3, +1, +5). Notice that, even if these two functions are formed by an extensive mixture of M_J, they cannot exhibit any tunneling because they do not present any overlap. On the contrary, the first excited-state doublet (lying at 10.8 cm^{-1} above the ground-state doublet) is formed by two functions composed by (+6, +2, −2, −6) and (−6, −2, +2, +6); these are mixed because both contain the same M_J values but different coefficients for the linear combination, thus allowing for tunneling. According to this, spin relaxation will take place by tunneling within the first excited-state doublet, but not within the ground state, explaining why this compound exhibits SMM behavior.

Notice that the extensive mixture of M_J calculated in the present case is a consequence of the presence of nonnegligible extradiagonal parameters B_4^4 and B_6^4. In particular, B_4^4 and B_6^4 parameters are 1 and 2 orders of magnitude larger than the corresponding diagonal terms (B_4^0 and B_6^0), respectively.[25] These ratios are even higher than those of cubic geometry. Figure 5 can be useful to understand the variation of these

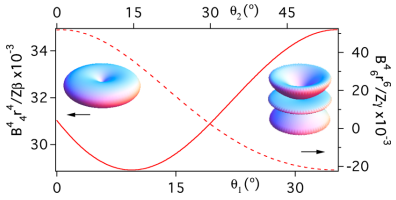

Figure 5. Variation of B_4^4/β and B_6^4/β for eight ligands submitted to a continuous D_{2d} distortion between an octahedron (left) and a cube (right). The four 'axial' ligands (see Figure 4) deviate from their initial positions at the z axis reaching the cubic disposition at $\theta_2 = 54.74°$, while the four 'equatorial' ligands leave the plane and complete the cube at $\theta_1 = 35.26°$. Insets: shapes of Y_{44} and Y_{64}.

extradiagonal parameters. As can be seen there, B_4^4 is almost constant for any degree of D_{2d} deformation between an ideal cube and an octahedron. For large deformations, B_6^4 can even suffer a sign reversal, but for realistic deformations (i.e., on the order of 15°), it is fairly stable. In contrast, both B_4^0 and B_6^0 display nodes in this region of intermediate angles (Figure 2), so moderate deformations can be expected to affect them more drastically.

c. Trigonal Prism. Trigonal prisms abound in lanthanoid coordination chemistry, either bare or with up to three apexes in the center of the rectangular faces. Some complexes having these kinds of coordination sites exhibit SMM behavior (Figure 6). This is the case of $[Tb(picNN)_3]$ (**3**),[26] where picNN = picolinate-based nitronylnitroxide, $[Dy_2(hfac)_6(H_2O)_2(L)]$ (**4**),[27] where hfac = 1,1,1,5,5,5-hexafluoroacetylacetonate anion and L = 4,4′,7,7′-tetra-*tert*-butyl-2,2′-bis(1,3-benzodithiole)-5,5′,6,6′-tetrone, and $[Ln(FTA)_3L]$ (**5**),[28] where FTA = 2-furyltrifluoroacetonate and L = *S*,*S*-2,2′-bis(4-benzyl-2-oxazoline).

It has to be remarked that, for these low-symmetry highly distorted geometries (often seen as distorted D_{4d} complexes), this result is not easy to predict. In any case, if one intends to approach this problem as a rational design process, one should first take into account that an ideal trigonal prism (D_{3h} symmetry) can only present B_2^0, B_4^0, B_6^0, and B_6^6 terms. The presence of the extradiagonal CF parameter B_6^6 means mixing between M_J values differing by ±6. It is crucial to note that this will produce direct tunneling only for doublets involving states with $M_J = \pm 3$ or ±6, and even in these cases, the compound may show SMM behavior if B_2^0 is large enough. This seems to be the case for the derivative **3**, where slow relaxarion of the magnetization has been exhibited, including magnetic hysteresis under 1 K.[25] Preliminary calculations have shown an $M_J = \pm 6$ ground-state doublet, which is clearly separated (around 200 cm^{-1}) with respect to the nearest excited-state doublet ($M_J = \pm 5$), in good agreement with the experiment. Another prediction is that for half-integer spins like Nd^{3+}, Sm^{3+}, Dy^{3+}, Er^{3+}, and Yb^{3+}, an ideal D_{3h} coordination symmetry may be as good as a pseudoaxial one for getting SMM behavior. In fact, even though actinoids cannot be precisely described by the Russell−Saunders scheme like lanthanoids, examples of U^{3+} ($J = {}^9/_2$) in this coordination environment have recently shown SMM properties.[29] The method reported in this work has recently been applied to describe such systems.[30]

Covalent Effects. Many-body effects that modify the simplest ionic picture are usually grouped under the catch-all term "covalent effects".[30] For simple halides, oxides, and other markedly ionic ligands, covalent effects are negligible and CF can be reproduced by simply substituting each atom in the coordination sphere by a point charge. In other molecules, where this assumption is no longer adequate, the point-charge model should be refined to include at least the effects of polarization and deformation of the electron clouds. In a first step, the use of partial charges, distributed among a larger number of centers and calculated by density functional theory (DFT), can account for some of these effects.

As an illustrative example, we have chosen the compound $[Dy^{III}(COT'')_2Li(THF)(DME)]$ [COT″ = 1,4-bis(trimethylsilyl)cyclooctatetraenyl dianion, THF = tetrahydrofuran, and DME = dimethyl ether], which has recently been reported to display SMM behavior.[22] This sandwich-type compound contains the metal complex $[Dy^{III}(COT'')_2]^-$ (Figure 7, right). It is clear that in this case the assumption of a purely ionic model, with a negative charge on each carbon atom, is totally unrealistic. In order to use the CF model, first, we have calculated the electronic density of an idealized COT ligand through DFT [Becke3LYP/6-31G(d)]. This calculation has provided the effective partial charges of the carbon ($q_1 = -0.175$) and hydrogen ($q_2 = -0.0742$) atoms on this ligand. Second, we have introduced these charges in the CF calculation code in order get the CF parameters. The distances $r_1 = 0.950$ Å, $r_2 = 1.415$ Å, and $r_3 = 3.794$ Å have been averaged from the crystallographic data. Using r_1, r_2, r_3, q_1, and q_2, we have obtained $B_2^0 = -15.3$ cm^{-1}, $B_4^0 = 3.31 \times 10^{-2}$ cm^{-1}, and $B_6^0 = -8.23 \times 10^{-5}$ cm^{-1}. The resulting energy-level scheme displays a high-spin M_J doublet = $\pm{}^{15}/_2$ as the ground state, with the first excited-state sublevel lying at 244 cm^{-1}, thus explaining the SMM properties.

Further improvements on the point-charge model reported here are easily conceivable. For instance, instead of a single charge centered on each nucleus, a larger number of smaller charges can be distributed around each atom. In this way, the actual electronic shape of the ligands can be mimicked. This extension allows us to consider the proper location of lone pairs and π clouds and to distinguish between markedly different anionic radii. Another possible refinement is to modify the coordinates of the partial charges to account for the coordination bond.[51] Such a treatment of the covalence effects was successfully used by us for the theoretical study of a d

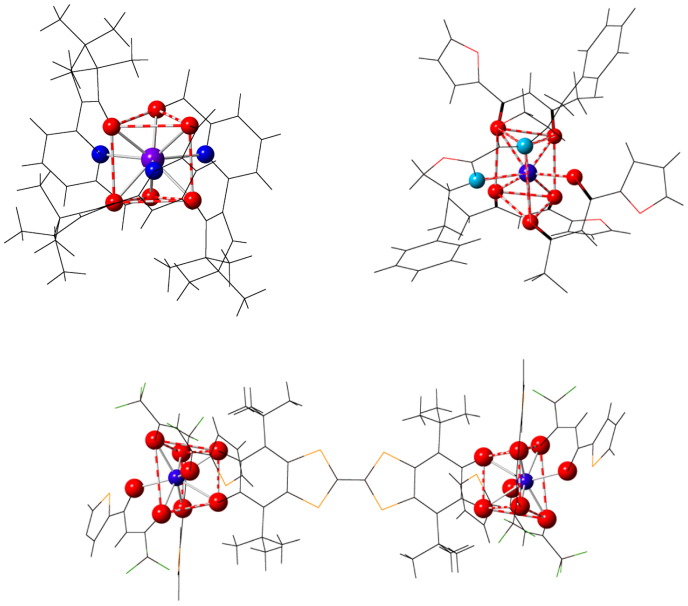

Figure 6. Structures of mononuclear lanthanoid complexes close to a trigonal prism that display SMM behavior: (top left) **3**; (top right) **4**; (bottom) **5**.

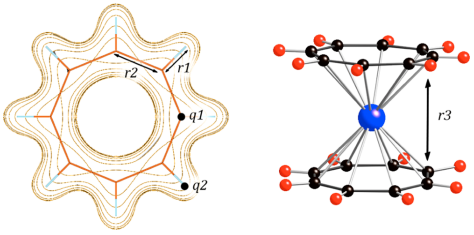

Figure 7. Left: Electronic density of COT calculated by DFT methods. Right: Idealized structure for a Dy(COT′′)$_2$ sandwich.

transition-metal SIM[31] and is somewhat similar to the effective-charge model proposed by Morrison.[32] An alternative possibility to taking into account the covalent effects is to apply the so-called "exchange-charge model".[33]

Remarks for the Design of Spin Qubits. Some special considerations need to be taken into account when designing a lanthanoid complex for its use as a spin qubit instead of just as a SIM, which mainly depend on (i) its nuclear spin, (ii) its tunneling gap, and (iii) its environment.

The first issue is the isotopic purity of the lanthanoid. At the very least, that is desirable and a need in most cases. Like a badly purified product, a sample with a natural distribution of isotopes contains a random mixture of quantum systems. In that sense, holmium, terbium, thulium, and praseodymium are especially adequate in this context because they only have one stable isotope each. Note that a nuclear spin accessible through contact hyperfine interaction has proven to be a very valuable resource because it can provide access to a larger number of well-defined states.[34] Nuclear spins are also of dramatic importance in determining the parity of the system, i.e., whether the ion is Kramers or non-Kramers. Elements with an even atomic number, like dysprosium, erbium, ytterbium, and neodymium, have half-integer J and some of their isotopes are $I = 0$, therefore being Kramers ions. In those cases, ligand-field extradiagonal parameters will potentially mix, but will not split, the components of the ground-state doublet. Hence, in those cases in which a degeneracy of the states is required, the best choice will be to use Kramers ions, while if a splitting is needed, non-Kramers ions will be preferred.

As a second consideration, the tunneling gap Δ in the ground state is critical for manipulation of the quantum state. Large tunneling gaps can be advantageous both for an easier spin manipulation[35] and for diminishing decoherence. In that sense, mononuclear lanthanoid-based qubits/SIMs (with gaps up to $\Delta = 0.1-1$ cm^{-1}) are vastly superior to cluster-type transition-metal-based SMMs (with the usual gaps in the range of $\Delta = 10^{-8}-10^{-4}$ cm^{-1}). A large tunneling gap results from a high-range extradiagonal parameter that mixes $+M_J$ with $-M_J$ in the ground state, either directly or by means of an intermediate M_J. In turn, large extradiagonal parameters can often be related to molecular high-symmetry axes. Hence, for the design of molecules with large tunneling gaps, we will need to have a M_J ground-state doublet that can be mixed by an extradiagonal term allowed by the symmetry of the molecule. Let us give two examples based on POM chemistry. The first concerns the series **1** with D_{4d} symmetry, which we mentioned earlier. In this case, the small distortion from an ideal D_{4d} symmetry allows the appearance of terms B_4^4 and B_6^4. This should facilitate the mixing

dx.doi.org/10.1021/ic302068c | Inorg. Chem. 2012, 51, 12565−12574

of a ground-state doublet containing $M_J = \pm 4$, which is exactly what happens for the holmium derivative, as can be seen in Table 1. For this compound, long coherence times have been detected.[36] The second example involves the Preyssler POM anion $[LnW_{30}O_{110}]^{12-}$. This anion shows an atypical geometry with a C_5 axis in such a way that a very high B_6^5 extradiagonal parameter can be estimated. Therefore, when the ground state contains a doublet with $M_J = \pm 5$, a very strong mixing through $M_J = 0$ is possible. This situation may occur for the terbium derivative, which, according to our calculations, should lead to a tunneling gap $\Delta > 2$ cm^{-1}.[37]

Last but not least, one needs to consider interactions taking place beyond the first coordination sphere. The more relevant ones for our purposes are the interaction with other spins (electronic or nuclear) and electron−phonon coupling. In fact, a recent work shows that environmental decoherence[38] in a SMM model can be tracked down to precisely these three sources: magnons, nuclear spins, and phonons.[38]

Unwanted interaction with neighboring spin qubits is a common source of decoherence. In lanthanoid ions, this problem can be easily addressed by diamagnetic dilution. Of course, under certain conditions, spin−spin coupling can also be used as a resource instead of just as a problem. This has been exploited to implement an intramolecular Controlled-NOT quantum gate.[39]

Nuclear spins are best kept away from the spin qubit. When the nuclear spin belongs to the lanthanoid, it is strongly coupled to its electronic spin so that it does not introduce any decoherence. The most critical region is the close vicinity of the lanthanoid ion. That means that coordination by oxygen (or sulfur), which are nuclear-spin-free, is much preferred over coordination by nitrogen or halogens, which have nuclear spins. Carbon would be a good option, but in the vast majority of the cases, it is bonded to hydrogen, which has the highest gyromagnetic ratio of all elements. In fact, when ^{1}H is present in the sample, deuteration is often the most effective way to minimize decoherence.

Finally, we also need to understand and estimate the state-dependent electron−phonon coupling. Phonons can cause leakage to excited states within the same molecule, and they can communicate qubits at long distances even in the absence of dipolar coupling. The solution for this is to design qubits that are almost transparent to phonons, i.e., qubits in which the phonon interactions do not affect the energy differences within the qubit or the response to experimental stimuli. This, of course, can only be achieved after deep magnetostructural analysis. A general recipe would be to have a very rigid coordination sphere for the qubit, while the crystalline environment in which the qubit is embedded is much softer. This requirement is naturally satisfied by molecular-based materials.

CONCLUSIONS

Let us start by making a comparison between the polynuclear cluster-type SMMs and the mononuclear SIMs. In the former case, the two major goals have been (i) to increase through chemical design the superparamagnetic barrier and, consequently, the blocking temperature, and (ii) to study the quantum effects exhibited by these nanomagnets. In the case of the SIMs, owing to the large magnetic anisotropy of the rare earths, superparamagnetic barriers with energies on the order of, or higher than, k_BT are not unusual. Still, at low temperatures, the spin relaxation of these systems has shown to be often dominated by a fast quantum tunneling, thus preventing their use as magnetic memories (classical spin bits). In fact, the quantum effects in the SIMs are much more pronounced than those in the polynuclear cluster-type SMMs. Hence, in this class of nanomagnets, the major focus of interest will deal with the study of quantum phenomena like tunneling, relaxation, and coherence. In this context, these simple molecules are better suited for their integration as reliable quantum bits (qubits) for quantum computing than the polynuclear SMMs are. The reason lies in the larger stability of SIMs against decoherence because the robustness of a quantum state decreases with the system's number of degrees of freedom. This idea is further supported by the possibility of chemically controlling the quantum coherence in these systems. Thus, the main sources of decoherence, namely, the dipolar spin−spin and hyperfine interactions, can be easily minimized by magnetic dilution, i.e., the synthesis of crystals containing both magnetic and nonmagnetic molecules, and by the preparation of nuclear-spin-free molecules.

In this work, we have shown that the major electronic features that determine the spin dynamics of SIMs based on lanthanoids can be directly correlated with the local coordination environment around the f metal ion. By using a relatively simple point-charge model, we have shown that the splitting of the ground state, J, of the lanthanoid into M_J sublevels, caused by the presence of the CF created by the surrounding ligands, is in good agreement with that experimentally calculated through a fit of the magnetic data. The power of this approach is that it allows us to predict the energy splitting as well as the nature of the resulting wave functions of a lanthanoid complex in any environment, in terms of the CF parameters. At this point, it is important to notice that, in the case of f electrons, the high-order CF terms arise from interaction between the electic field and ground state J, whereas for d-transition-metal SMMs, they appear as perturbative corrections. This difference underlines the key influence of these CF parameters on the magnetic properties of lantanoid complexes. Our method refines a purely electrostatic model through shielding corrections and has been applied to examine the most common lanthanoid geometries: square antiprism, trigonal prism, and triangular dodecahedron. Several real lanthanoid-based SIMs have been studied, and general magnetostructural correlations have been proposed. Also, we have illustrated the use of DFT calculations to extend such an electrostatic model to organometallic SIMs exhibiting marked covalency effects.

Let us now summarize the main rules that need to be known for the design of a SIM.

(i) As a general rule, SIMs require a high M_J ground state, to create an energy barrier leading to slow spin relaxation, and low mixing in the wave functions, to minimize fast spin relaxation through quantum tunneling processes. In the simplest case, this can be achieved with an ideal pseudoaxial symmetry such as D_{4d}, C_{5h}, D_{6d}, or any symmetry of order 7 or higher (such as, for example, in organometallic sandwich-type complexes). In all of these symmetries, the most suitable case is achieved when the second-order uniaxial anisotropy, accounted for by the B_2^0 parameter (also known as D), is maximized. Depending on the metal, this favorable situation can be reached by increasing the electron density either near the uniaxial axis (in the case of Tb, Dy, and Ho) or near the basal plane (in the particular case of Er but also for Tm and Yb). Notice that the chemical inequivalence of the ligands or chelating groups needs to be

dx.doi.org/10.1021/ic302068c | Inorg. Chem. 2012, 51, 12565−12574

taken into account because it will usually lower the overall symmetry. So, the first condition requires an axial coordination sphere around the lanthanoid, exhibiting small deviations from the ideal symmetry in order to avoid an additional undesired mixing of the M_J ground state.

(ii) Not all of the molecular symmetries are equally suited for favoring SIM behavior. For example, in the case of octacoordinated complexes, one can imagine either an antiprismatic D_{4d} symmetry or a cubic O_h symmetry. However, because the cubic coordination lacks second-order uniaxial anisotropy, B_2^0, this geometry is unfavorable to exhibit a large energy barrier for the magnetization reversal. On the contrary, an axially distorted D_{4d} symmetry has high B_2^0 values (either positive or negative), providing most of the known examples of SIMs. Thus, axially elongated sites are favorable for Tb^{3+}, Dy^{3+}, and Ho^{3+}, as exemplified by the double-decker bis-(phthalocyaninato) complexes, while axially compressed sites are favorable for Er^{3+}, as exemplified by POMs.

(iii) Not always does the presence of an extensive mixture of M_J values in the ground-state doublet lead to quantum tunneling. In fact, if the two wave functions do not present any overlap, relaxation through tunneling is forbidden. Additionally phonons allow transitions with $\Delta M_J = \pm 1$. For example, lanthanoid complexes exhibiting D_{2d} triangular dodecahedral geometry typically have extradiagonal CF terms of the type B_4^4 and B_6^4, whose values are higher than those of the diagonal terms. In some cases, the mixing generated by these terms, which involve functions with M_J values differing by 4 units, does not prevent the presence of an energy barrier.

For the rational design of molecular spin qubits, we have to exert control on two levels: the CF geometric effect and interaction with further electron spins, nuclear spins, and phonons. Interaction with the environment has already been commented on above. Let us now comment on the effect of the CF around the lanthanoid. Two minimal electronic features are required for having a spin qubit: (i) a controlled mixing of the wave functions in a well-defined level subset and (ii) sufficient isolation of this subset from the rest of the spectrum. These two requirements are the same as those needed for the design of SIMs. Hence, many SIMs will also be useful as spin qubits. Additionally, lanthanoid complexes can present a large tunneling gap in the ground state, Δ, which can minimize decoherence through nuclear spins.[40] In this sense, the tunneling gap in lanthanoid SIMs can be much higher than that exhibited by cluster-type SMMs (by a factor larger than 10^4). Hence, this favorable effect for minimizing decoherence is expected to be much more pronounced in the case of mononuclear SIMs. Taking into account this last effect, the three conditions that favor the design of a qubit will be (i) to use non-Kramers ions (for example, Tb or Ho), (ii) to choose a geometry for this lanthanoid allowing for a large extradiagonal CF term, and (iii) to have a $\pm M_J$ ground-state doublet such that $2M_J$ is a multiple on the range of this extradiagonal operator, q. Because the q value coincides, in general, with the order of the main symmetry axis of the molecule, an easy way to satisfy the third requirement is to find a molecular geometry having a q-range axis equal to $2M_J$. Two examples that illustrate this point are provided by the POMs $[Ho(W_5O_{18})_2]^{9-}$ (C_{4v}, $M_J = \pm 4$, and $\Delta > 0.1$ cm^{-1})[50] and $[TbW_{30}O_{110}]^{12-}$ (C_{5v}, $M_J = \pm 5$, and $\Delta \approx 2$ cm^{-1}), both of which have been experimentally found to show unusually long decoherence times.

THEORETICAL BACKGROUND AND COMPUTATIONAL METHOD

We consider a CF Hamiltonian, $\hat{H}_{cf}$, which parametrizes the electric field effect caused by the surrounding ligands acting over the central ion. $\hat{H}_{cf}$ generated by a charge distribution can be written in its most primitive form as the sum of Coulomb fields created by the charges. In order to determine the CF parameters, we adopt the point-charge electrostatic model,[41,42] in which N ligands are represented by their point charges (Z_i). Because of our interest in the magnetic properties, all of the excited levels are neglected and we consider only the splitting of the ground-state J multiplet.[43]

$\hat{H}_{cf}$ can be expressed in terms of different operators: spherical harmonics,[44] Stevens' operators,[20] or irreducible tensor operators.[45] The different notational conventions of this Hamiltonian are related to each other by equivalence coefficients. In this article, we use the extended Stevens operators, O_{qk}^k, which are the most extensively adopted operators in CF calculations.[46,47] For a given J multiplet, the CF Hamiltonian based on the Stevens formalism takes the general form

$$\hat{H}_{cf}(J) = \sum_{k=2,4,6}\sum_{q=-k}^{k} B_k^q O_k^q = \sum_{k=2,4,6}\sum_{q=-k}^{k} a_k(1-\sigma_k)A_k^q\langle r^k\rangle O_k^q \quad (1)$$

where k is order (also called rank or degree) of the Stevens operator equivalents O_k^q, and q is the operator range that varies between k and $-k$, a_k are the α, β, and γ Stevens coefficients for k = 2, 4, and 6, respectively, and σ_k are the Sternheimer shielding parameters of the 4f electronic shell and $\langle r^k\rangle$ are the moments of the 4f radial wave function.[48] α, β, and γ are tabulated and depend on the number off-electrons. Hence, the CF parameters A_k^q and B_k^q are referred to the ground state as well.

The CF parameters A_k^q can be calculated by the following expression:

$$A_k^q = \frac{4\pi}{2k+1} c_{kq}(-1)^q \sum_{i=1}^{N} \frac{Z_i e^2 Y_{k-q}(\theta_i, \phi_i)}{R_i^{k+1}} \quad (2)$$

where R_i, θ_i, and φ_i are the effective polar coordinates of the point charge and Z_i is the effective point charge, associated to the i-th ligand with the lanthanoid at the origin; e is the electron charge and c_{kq} is a tabulated numerical factor that relates spherical harmonics Y_{k-q} and Stevens operator equivalents. Note that, unless otherwise specified, Y_{kq}, A_k^q, and B_k^q are complex numbers. Because they have the same angular nodes, they can sometimes be used interchangeably. We use Y_{kq} to designate the mathematical shapes, A_k^q to discuss the field created by a set of ligands, and B_k^q for the final CF parameters.

This model has been implemented in a freely distributable computational code,[49] which has been used throughout this paper. The code, called SIMPRE, is written in portable Fortran 77 and calculates the full set of CF parameters, energy levels, wave vectors, and wave functions, as well as the magnetic properties for a mononuclear lanthanoid complex. This facilitates magnetostructural studies on real and ideal complexes, allowing the fitting and prediction of the magnetic properties.

AUTHOR INFORMATION

Corresponding Author

*E-mail: eugenio.coronado@uv.es.

Notes

The authors declare no competing financial interest.

ACKNOWLEDGMENTS

The present work has been partly funded through the EU (Project ELFOS and ERC Advanced Grant SPINMOL), the Spanish MINECO (Grants MAT2007-61584 and 2011-22785 co-financed by Feder, and the CONSOLIDER project on

Molecular Nanoscience), the Generalitat Valenciana (Prometeo and ISIC Programmes). A.G.-A. acknowledges funding by Project ELFOS under Contract UV-CI-12-009. J.J.B. and S.C.-S. thank the Spanish MINECO for a FPU predoctoral grant. A.P. thanks the Universitat de Valencia for a visiting research grant.

REFERENCES

(1) (a) Thomas, L.; Lionti, F.; Ballou, R.; Gatteschi, D.; Sessoli, R.; Barbara, B. *Nature* **1996**, *383*, 145−147. (b) Friedman, J. R.; Sarachik, M. P.; Tejada, J.; Ziolo, R. *Phys. Rev. Lett.* **1996**, *76*, 3830−3833.
(2) Wernsdorfer, W.; Ohm, T.; Sangregorio, C.; Sessoli, R.; Mailly, D.; Paulsen, C. *Phys. Rev. Lett.* **1999**, *82*, 3903−3906.
(3) Gatteschi, D.; Sessoli, R. *Angew. Chem., Int. Ed.* **2003**, *42*, 268−297.
(4) (a) Ardavan, A.; Blundell, S. J. *J. Mater. Chem.* **2009**, *19*, 1754−1760. (b) Troiani, F.; Affronte, M. *Chem. Soc. Rev.* **2011**, *40*, 3119−3129. (c) Stamp, P. C. E.; Gaita-Ariño, A. *J. Mater. Chem.* **2009**, *19*, 1718−1730. (d) Lehmann, J.; Gaita-Ariño, A.; Coronado, E.; Loss, D. *Nat. Nanotechnol.* **2007**, *2*, 312−317.
(5) Sessoli, R.; Tsai, H. L.; Schake, A. R.; Wang, S.; Vincent, J. B.; Folting, K.; Gatteschi, D.; Christou, G.; Hendrickson, D. N. *J. Am. Chem. Soc.* **1993**, *115*, 1804−1816.
(6) (a) Lin, P. H.; Burchell, T. J.; Ungur, L.; Chibotaru, L. F.; Wernsdorfer, W.; Murugesu, M. *Angew. Chem., Int. Ed.* **2009**, *48*, 9489−9492. (b) Guo, Y. N.; Xu, G. F.; Gamez, P.; Zhao, L.; Lin, S. Y.; Deng, R.; Tang, J.; Zhang, H. J. *J. Am. Chem. Soc.* **2010**, *132*, 8538−8539. (c) Rinehart, J. D.; Fang, M.; Evans, W. J.; Long, J. R. *Nat. Chem.* **2011**, *3*, 538−542. (d) Hewitt, I. J.; Tang, J.; Madhu, N. T.; Anson, C. E.; Lan, Y.; Luzon, J.; Etienne, M.; Sessoli, R.; Powell, A. K. *Angew. Chem., Int. Ed.* **2010**, *49*, 6352−6356. (e) Car, P. E.; Perfetti, M.; Mannini, M.; Favre, A.; Caneschi, A.; Sessoli, R. *Chem. Commun.* **2011**, *47*, 3751−3753. (f) Sessoli, R.; Powell, A. K. *Coord. Chem. Rev.* **2009**, *253*, 2328−2341.
(7) Sorace, L.; Benelli, C.; Gatteschi, D. *Chem. Soc. Rev.* **2011**, *40*, 3092−3104.
(8) Ishikawa, N.; Sugita, M.; Ishikawa, T.; Koshihara, S. Y.; Kaizu, Y. *J. Am. Chem. Soc.* **2003**, *125*, 8694−8695.
(9) (a) AlDamen, M. A.; Clemente Juan, J.; Coronado, E.; Martí-Gastaldo, C.; Gaita-Ariño, A. *J. Am. Chem. Soc.* **2008**, *130*, 8874−8875. (b) Aldamen, M. A.; Cardona-Serra, S.; Clemente-Juan, J. M.; Coronado, E.; Gaita-Ariño, A.; Martí-Gastaldo, C.; Luis, F.; Montero, O. *Inorg. Chem.* **2009**, *48*, 3467−3479.
(10) Jiang, S.; Wang, B.; Sun, H.; Wang, Z.; Gao, S. *J. Am. Chem. Soc.* **2011**, *133*, 4730−4733.
(11) Jiang, S.; Wang, B.; Su, G.; Wang, Z.; Gao, S. *Angew. Chem., Int. Ed.* **2010**, *49*, 7448−7451.
(12) (a) Car, P. E.; Perfetti, M.; Mannini, M.; Favre, A.; Caneschi, A.; Sessoli, R. *Chem. Commun.* **2011**, *47*, 3751−3753. (b) Cucinotta, G.; Perfetti, M.; Luzon, J.; Etienne, M.; Car, P. E.; Caneschi, A.; Calvez, G.; Bernot, K.; Sessoli, R. *Angew. Chem., Int. Ed.* **2012**, *51*, 1606−1610.
(13) (a) Rinehart, J. D.; Long, J. R. *J. Am. Chem. Soc.* **2009**, *131*, 12558−12559. (b) Rinehart, J. D.; Meihaus, K. R.; Long, J. R. *J. Am. Chem. Soc.* **2010**, *132*, 7572−7573.
(14) Harman, W. H.; Harris, T. D.; Freedman, D. E.; Fong, H.; Chang, A.; Rinehart, J. D.; Ozarowski, A.; Sougrati, M. T.; Grandjean, F.; Long, G. J.; Long, J. R.; Chang, C. J. *J. Am. Chem. Soc.* **2010**, *132*, 18115−18126.
(15) Zadrozny, J. M.; Long, J. R. *J. Am. Chem. Soc.* **2011**, *133*, 20732−20734.
(16) Bertaina, S.; Gambarelli, S.; Tkachuk, A.; Kurkin, I. N.; Malkin, B.; Stepanov, A.; Barbara, B. *Nat. Nanotechnol.* **2007**, *2*, 39.
(17) Giraud, R.; Wernsdorfer, W.; Tkachuk, A. M.; Mailly, D.; Barbara, B. *Phys. Rev. Lett.* **2001**, *87*, 057203.
(18) Rinehart, J. D.; Long, J. R. *Chem. Sci.* **2011**, *2*, 2078−2085.
(19) Stevens, K. W. H. *Proc. Phys. Soc. A* **1952**, *65*, 209−215.
(20) (a) Ishikawa, N.; Sugita, M.; Wernsdorfer, W. *Angew. Chem., Int. Ed.* **2005**, *44*, 2931−2935. (b) Ishikawa, N.; Sugita, M.; Wernsdorfer, W. *J. Am. Chem. Soc.* **2005**, *127*, 3650−3651.
(21) Barsukova, M.; Izarova, N. V.; Biboum, R. N.; Keita, B.; Nadjo, L.; Ramachandran, V.; Dalal, N. S.; Antonova, N. S.; Carbó, J. J.; Poblet, J. M.; Kortz, U. *Chem.—Eur. J.* **2010**, *16*, 9076−9085.
(22) Kortz, U.; Coronado, E. et al. Unpublished results.
(23) Ishikawa, N.; Sugita, M.; Okubo, T.; Takana, N.; Iino, T.; Kaizu, Y. *Inorg. Chem.* **2003**, *42*, 2440−2446.
(24) Alvarez, S.; Alemany, P.; Casanova, D.; Cibera, J.; Llunell, M.; Avnir, O. *Coord. Chem. Rev.* **2005**, *249*, 1693−1708.
(25) Bernal, E. G. *J. Chem. Phys.* **1971**, *55*, 2538−2549.
(26) Coronado, E.; Giménez-Saiz, C.; Recuenco, A.; Tarazón, A.; Romero, F. M.; Camón, A.; Luis, F. *Inorg. Chem.* **2011**, *50*, 7370−7372.
(27) Pointillart, F.; Klementieva, S.; Kuropatov, V.; Le Gal, Y.; Golhen, S.; Cador, O.; Cherkasovb, V.; Ouahab, L. *Chem. Commun.* **2012**, *48*, 714−716.
(28) Li, D.-P.; Wang, T.-W.; Li, C.-H.; Liu, D.-S.; Li, Y.-Z.; You, X.-Z. *Chem. Commun.* **2010**, *46*, 2929−2931.
(29) (a) Rinehart, J. D.; Long, J. R. *J. Am. Chem. Soc.* **2009**, *131*, 12558−12559. (b) Maria, L.; Campello, M. P.; Domingos, A.; Santos, I.; Andersen, R. *Dalton Trans.* **1999**, *43*, 2015. (c) Rinehart, J. D.; Meihauss, K. R.; Long, J. R. *J. Am. Chem. Soc.* **2010**, *132*, 7572. (d) Antunes, M. A.; Pereira, L. C. J.; Santos, I. C.; Mazzanti, M.; Marçalo, J.; Almeida, M. *Inorg. Chem.* **2011**, *50*, 9915. (e) Magnani, N.; Apostolidis, C.; Morgenstern, A.; Colineau, E.; Griveau, J. C.; Bolvin, H.; Walter, O.; Caciuffo, R. *Angew. Chem., Int. Ed.* **2011**, *50*, 1696. (f) Rinehart, J. D.; Long, J. R. *Dalton Trans.* **2012**, DOI: 10.1039/c2dt31352a. (g) Sun, Y.; McDonald, R.; Takats, J..; Day, V. W.; Eberspacher, T. A. *Inorg. Chem.* **1994**, *33*, 4433. (h) Coutinho, J. T.; Antunes, M. A.; Pereira, L. C. J.; Bolvin, H.; Marçalo, J.; Mazzanti, M.; Almeida, M. *Dalton Trans.* **2012**, DOI: 10.1039/c2dt31421e. (i) Magnani, N.; Colineau, E.; Eloirdi, R.; Griveau, J.-C.; Caciuffo, R.; Cornet, S. M.; May, I.; Sharrad, C. A.; Collison, D.; Winpenny, R. E. P. *Phys. Rev. Lett.* **2010**, *104*, 197202. (j) Mills, D. P.; Moro, F.; McMaster, J.; Van Slageren, J.; Lewis, W.; Blake, A. J.; Liddle, S. T. *Nat. Chem.* **2011**, *3*, 454.
(30) Baldoví, J. J.; Cardona-Serra, S.; Clemente-Juan, J. M.; Coronado, E.; Gaita-Ariño, A. In press.
(31) Palii, A. V.; Clemente-Juan, J. M.; Coronado, E.; Klokishner, S. I.; Ostrovsky, S. M.; Reu, O. S. *Inorg. Chem.* **2010**, *49*, 8073−8077.
(32) (a) Morrison, C. A. Lectures on Crystal Field Theory, HDL-SR-82-2, Harry Diamond Laboratories Report, 1982. (b) Porcher, P.; Dos Santos, M. C.; Malta, O. *Phys. Chem. Chem. Phys.* **1999**, *1*, 397.
(33) (a) Malkin, B. Z. Crystal field and electron−phonon interaction in rare-earth ionic paramagnets. In *Spectroscopy of Solids Containing Rare-Earth Ions*; Kaplyanskii, A. A., Macfarlane, R. M., Eds.; North-Holland: Amsterdam, The Netherlands, 1987; p 13. (b) Popova, M. N.; Chukalina, E. P.; Malkin, B. Z.; Saikin, S. K. *Phys. Rev. B* **2000**, *61*, 7421−7427. (c) Klokishner, S. I.; Ostrovsky, S. M.; Reu, O. S.; Palii, A. V.; Tregenna-Piggott, P. L. W.; Brock-Nannestad, T.; Bendix, J.; Mutka, H. *J. Phys. Chem. C* **2009**, *113*, 8573−8582.
(34) Fuchs, G. D.; Burkard, G.; Klimov, P. V.; Awschalom, D. D. *Nat. Phys.* **2011**, *7*, 789−793.
(35) Palii, A.; Tsukerblat, B.; Clemente-Juan, J. M.; Gaita-Ariño, A.; Coronado, E. *Phys. Rev. B* **2011**, *84*, 184426.
(36) Hill, S.; Coronado, E.; et al. Unpublished results.
(37) Cardona-Serra, S.; Clemente-Juan, J. M.; Coronado, E.; Gaita-Ariño, A.; Camón, A.; Evangelisti, M.; Luis, F.; Martínez-Pérez, M. J.; Sesé, J. *J. Am. Chem. Soc.* **2012**, *134*, 14982−14990.
(38) (a) Takahashi, S.; Tupitsyn, I. S.; van Tol, J.; Beedle, C. C.; Hendrickson, D. N.; Stamp, P. C. E. *Nature* **2011**, *476*, 76−79. (b) Stamp, P. C. E. *Phil. Trans. R. Soc. A.* **2012**, *370*, 4429−4453.
(39) Luis, F.; Repollés, A.; Martínez-Pérez, M. J.; Aguilá, D.; Roubeau, O.; Zueco, D.; Alonso, P. J.; Evangelisti, M.; Camón, A.; Sesé, J.; Barrios, L. A.; Aromí, G. *Phys. Rev. Lett.* **2011**, *107*, 117203.
(40) Stamp, P. C. E.; Tupitsyn, I. S. *Phys. Rev. B* **2004**, *69*, 014401.
(41) Hutchings, M. T. *Solid State Phys.* **1964**, *16*, 227−273.

(42) Figgis, B. W. *Introduction to ligand fields*; Wiley-Interscience: New York, 1966.
(43) Kahn, O. *Molecular Magnetism*; Wiley-VCH: Weinheim, Germany, 1993.
(44) Elliott, R. J.; Stevens, K. W. H. *Proc. R. Soc., Ser. A* **1952**, *215*, 437−453.
(45) Morrison, C. A.; Wortman, D. E.; Karayianis, N. *J. Phys. C: Solid State Phys.* **1976**, *9*, L191−194.
(46) (a) Buckmaster, H. A. *Can. J. Phys.* **1962**, *40*, 1670−1677. (b) Rudowicz, C. *J. Phys. C: Solid State Phys.* **1985**, *18*, 1415−1430.
(47) (a) Ryabov, I. D. *J. Magn. Reson.* **1999**, *140*, 141. (b) Ryabov, I. D. *Appl. Magn. Reson.* **2009**, *35*, 481−494.
(48) Edvarsson, S.; Klintenberg, M. *J. Alloys Compd.* **1998**, *275*−*277*, 230−233.
(49) Baldoví, J. J.; Cardona-Serra, S.; Clemente-Juan, J. M.; Coronado, E.; Gaita-Ariño, A.; Palii, A. To be submitted.
(50) Ghosh, S.; Datta, S.; Friend, L.; Cardona-Serra, S.; Gaita-Ariño, A.; Coronado, E.; Hill, S. *Dalton Trans.* **2012**, DOI: 10.1039/C2DT31674A.
(51) Baldoví, J. J.; Borrás-Almenar, J. J.; Clemente-Juan, J. M.; Coronado, E.; Gaita-Ariño, A. *Dalton Trans.* **2012**, DOI: 10.1039/C2DT31411H.

3

Electrically switchable magnetic molecules

"Nature, to be commanded, must be obeyed."
-Francis Bacon.

1. Introduction.

Switching magnetic molecular materials, that is, responsive molecular materials in which the magnetic properties can be reversibly tuned by applying an external stimulus, are attracting considerable interest in molecular magnetism. Typical examples are provided by spin-crossover solids based on molecules,[1] and bimetallic cyanide complexes. [2] In these materials, temperature light or pressure are commonly used as physical stimuli to control their spin states. Still, an electric field or an electric current can also be used in this context. Such a possibility has already been demonstrated on the macroscale in multiferroic materials[3] and semiconductor spintronics.[4] In fact, the use of an electric field, instead of a magnetic field, present some specific advantages on the nanoscale as it is easy to obtain (with gates or STM-tips) and undergoes fast switching (≈ ps) thus providing the possibility to address selectively a single molecule. Very recently it was proved that a static electric field can induce spin-crossover in nanodevices formed by a single nanoparticle of around 10 nm.[5]

Compared with other coordination compounds, polyoxometalates (POMs) present some advantageous chemical, structural and electronic features that make these molecular metal-oxide clusters suitable for nanospintronics. In particular, they are robust molecules which keep their cluster structure not only in solution but also in the solid state and when deposited on surfaces, thus facilitating their processing into devices. More importantly, most POMs are able to accept various numbers of electrons, while keeping their structure almost intact. This leads to mixed-valence systems in which the extra electrons are extensively delocalized over the whole framework, providing thus very versatile examples of MV magnetic molecules.[6]

A representative example has been provided by the $[PMo_{12}O_{40}(VO)_2]^{n-}$ di-capped Keggin anion, which has been proposed to be used for a quantum logical gate.[7] In this

1 (a) Gaspar, A. B.; Ksenofontov, V.; Seredyuk, M.; Gütlich, P. *Coord. Chem. Rev.* **2005**, *249,* 2661-2676. (b) Real, J. A.; Gaspar, A. B.; Niel, V., Muñoz, M. C. *Coord. Chem. Rev.* **2003,** *236,* 121 (c) Gütlich, P.; Hauser, A.; Spiering, H. *Angew. Chem. Int. Ed.* **1994**, *106*, 2109-2141. (d) Bousseksou, A.; Molnár, G.; Salmon, L.; NIcolazzi, W. *Chem. Soc. Rev.* **2011**, *40*, 3313-3335. (e) Clemente-León, M.; Coronado, E.; López-Jordá, M.; Desplanches, C.; Asthana,, S.; Wang, H.; Létard, J.-F. *Chem. Sci.* **2011***, 2,* 1121-1127.

2 (a) Sato, O.; Iyoda, T.; Fujishima, A.; Hashimoto, K. *Science*, **1996**, *272*, 704-705. (b) Coronado, E.; Gimenez-Lopez, M. C. Levchenko, G.; Romero, F. M.; Garcia-Baonza, V.; Milner, A; Paz-Pasternak, M. P. *J. Am. Chem. Soc.* **2005**, *127*, 4580-4581. (c) Sato, O.; Tao, J.; Zhang, Y. Z. *Angew. Chem. Int. Ed.* **2007,** *119,* 2200-2236. Ibid, **2007***, 46*, 2152-2187. (d) Ohkoshi, S.; Tokoro, H.; Hashimoto, K.; *Coord. Chem. Rev.* **2005***, 249*, 1830-1840. (e) Coronado, E.; Gimenez-Lopez, M. C.; Korzeniak, T.; Levchenko, G.; Romero, F. M.; Segura, A.; Garcia-Baonza, V.; Cezar, J. C.; de Groot, F. M.; Milner, A; Paz-Pasternak, M. P. *J. Am. Chem. Soc.* **2008**, *130,* 15519-15532.

3 (a) Cheong, S. W.; Mostovoy, M. *Nat. Mater.* **2007**, *6*, 13-20. (b) Ikeda, N.; Ohsumi, H.; Ohwada, K.; Ishii, K.; Inami, T.; Kakurai, K.; Murakami, Y.; Yoshii, K.; Mori, S.; Horibe, Y.; Kito, H. *Nature*, **2005**, *436*, 1136-1138. (c) Hur, N.; Park, S.; Sharma, P. A.; Ahn, J. S.; Guha, S.; Cheong, S. W. *Nature*, **2004**, *429*, 392-395. (d) Mostovoy, M.; *Nat. Mater.* **2008**, *7*, 269-270.

4 Awschalom, D. D.; Flatté, M. E. *Nat. Phys.* **2007***, 3*, 153-159.

5 Prins, F., Monrabal- Capilla, M.; Osorio, E. A.; Coronado, E.; van der Zant, H. S. J. *Avd. Mat.* **2011**, *23*, 1545-1549.

6 (a) Stamp, P.; Gaita-Ariño, A. *J. Mater. Chem.* **2009**, *19*, 1718–1730. (b) Bertaina, S.; Gambarelli, S.; Mitra, T.; Tsukerblat, B.; Müller, A.; Barbara, B. *Nature* **2008**, *453*, 203–206.

7 (a) Lehmann, J.; Gaita-Ariño, A.; Coronado, E.; Loss, D. *Nat. Nanotech.,* **2007**, *2*, 312-317. (b) Lehmann, J.; Gaita-Ariño, A.; Coronado, E.; Loss, D. *J. Mater. Chem.*, **2009**, *19*, 1672-1677.

POM the spins of two electrons, each one localized on a vanadyl ion, which represent the qubits, could be coupled when an 'extra' electron is injected in the central mixed-valence Mo12 cluster through an electrical gate provided by a STM setup.

In this thesis an example of mixed-valence POM, $K_2Na_6[GeV_{14}O_{40}]\cdot 10H_2O$,[8] which contains two "extra" electrons delocalized over the POM framework is discussed. The compound contains 12 spin-less V^V ions and 2 S=1/2 V^{IV} ions. The unique feature of this POM is that it has a paramagnetic behaviour down to 1.7K. This behavior is in sharp contrast with what has been typically observed in other 2e-reduced POMs, which are diamagnetic at room temperature meaning that the two "extra" electrons are strongly antiferromagnetically coupled (see Chapter 1 for a detailed explanation).[9]

The key to explain this apparently anomalous behaviour lies in the central square $[GeV_4O_{12}]$ of the cluster, which is sandwiched between the two square pyramids $[V_5O_{14}]$ (Figure 1). Because of a combination of poor electron transfer between the two square pyramids and a high orbital energy of the central square, the spins of the two electrons are effectively independent because they preferentially reside in distant V4 positions to minimize the Coulomb repulsion.[10] As this is essentially an electrostatic effect, one can expect that an electric field applied along the main axis of the molecule will eventually overcome the Coulomb repulsion thus enabling the electrons to approach each other and to strongly interact antiferromagnetically. The motivation for the present work is precisely this: to test whether this magnetic molecule switches its ground spin state from two independent S =1/2 spins to a total S = 0 when an external electric field is applied along the main molecular axis. A communication describing the preliminary results of this work has been published.[11]

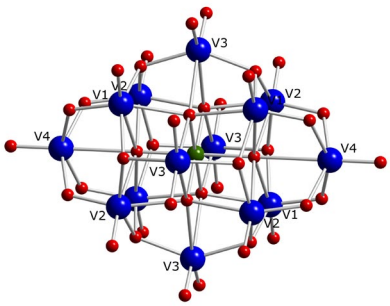

Figure 1. The V14 POM. In red the O ions, in yellow the V ions and in white at the center the Ge ion. Molecular coordinates: x is along V1-V1, y along V2-V2 and z along V4-V4.

8 Bi, L.-H.; Kortz, U.; Dickman, M. H.; Nellutla, S.; Dalal, N. S.; Keita, B.; Nadjo, L.; Prinz, M.; Neumann, M. *J. Clus. Sci.* **2006**, *17*, 143–165.

9 Kozik, M.; Hammer, C. F.; Baker, L. C. W. *J. Am. Chem. Soc.* **1986**, *108*, 2748-2749. Kozik, M.; Baker, L. C. W. J. *Am. Chem. Soc.* **1987**, *109*, 3159-3160. Kozik, M.; Casañ-Pastor, N.; Hammer, C. F.; Baker, L. C. W. *J. Am. Chem. Soc.* **1988**, *110*, 7697-7701. Kozik, M.; Baker, L. C. W. *J. Am. Chem. Soc.* **1990**, *112*, 7604-7611. Casañ-Pastor, N.; Baker, L. C. W. *J. Am. Chem. Soc.* **1992**, *114*, 10384-10394.

10 Suaud, N.; Masaro, Y.; Coronado, E.; Clemente Juan, J. M.; Guihéry, N. *Eur. J. Inorg. Chem.* **2009**, 5109–5114.

11 Cardona-Serra, S.; Clemente Juan, J. M.; Gaita-Ariño, A.; Suaud, N.; Svobodab, O.; Coronado, E.; *Chem. Comm.* **2013**, DOI: 10.1039/C3CC44859B

2. *Results and discussion*

In absence of electric field, the singlet-triplet energy gap obtained from the diagonalization of the t-J model Hamiltonian (explained in Chapter 1) is almost zero (0.02 meV ≈ 0.2K), in agreement with the paramagnetic behavior observed experimentally. In this parametrized Hamiltonian the transfer and exchange parameters - t_{ij} and J_{ij}, respectively - are extracted from ab-initio calculations on embedded fragments. The density matrices of the lowest singlet and triplet states are very similar. They show a large occupation on each V4 ion by an 'extra' electron (0.87), so that these electrons remain in distant sites. In fact, the configuration in which the two electrons are located on the two V4 ions has a weight of 87%, while 11% of the weight in the wave functions come from configurations with one electron on a V4 ion from a $[V_5O_{14}]$ moiety and the other on a V1 or V2 ion from the other moiety. The total weight of the configurations with 2 electrons on the same $[V_5O_{14}]$ moiety is negligible (less than 0.003%).

From the analysis of the wave functions, when an electric field is applied along z (the

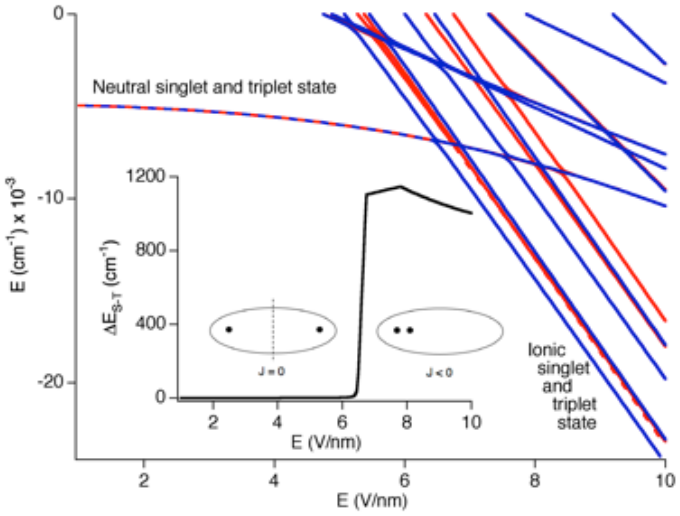

Figure 2. Energy level scheme as a function of the external electric field (Red: singlet states, blue: triplet states). Inset: Energy gap between the ground singlet and the lowest triplet state, with an schematic representation of the electron distribution.

molecular axis), 4 regions can be distinguished. For a field lower than 6.2 V/nm, the singlet ground state and the lowest triplet state are essentially based on configurations where one electron is localized on each moeity of the POM (called "neutral" configurations). The weight of these configurations decreases from about 100% for both states in absence of electric field to about 98.1% for the singlet and 99.3% for the triplet state for a field of 6.2 V/nm. Then, for a field in the range 6.2 V/nm – 6.74 V/nm the nature of the singlet

state completely changes whereas the triplet state does not. Indeed, a strong mixing between the neutral configurations of the singlet state and the "ionic" ones (those where the 2 electrons are on the same moiety) occurs. As a result, just below 6.74 V/nm, the singlet is almost completely ionic (99.5%) whereas the triplet state is still neutral (92%). Note that a step-like feature appears at ca. 6.5 V/nm, which corresponds to the opening of a large singlet-to-triplet energy gap of ca.130 meV (≈ 1500K), i.e, to the appearance of a very strong antiferromagnetic coupling between the two S = ½ spins. Interestingly, this spin switching appears for a very weak intensity change in the electric field (with a increase of about 0.3V/nm the energy gap is multiplied by about 10^4!). At higher fields a

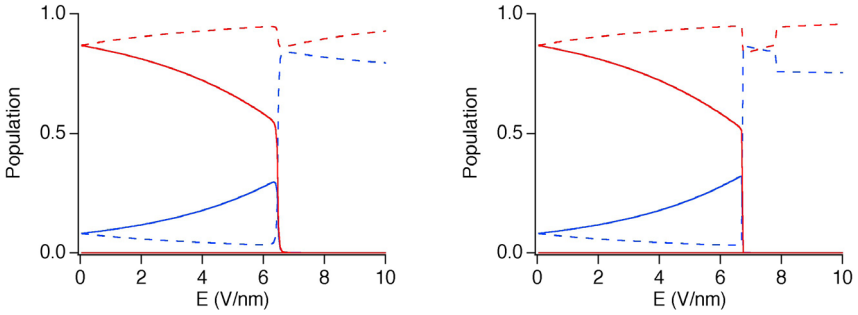

Figure 3. Single site electronic population as a function of the external electric field for singlet (left) and triplet (right). (Red line: V4, blue line: V1 and V2)

crossing between two triplet states occurs in such a way that just above 6.74 V/nm, both the singlet ground state and lowest triplet state are ionic (more than 99.5%). For a higher electric field, no significant change in the ionic nature of the two states is observed. Finally, the value of 7.81 V/nm is characterized by the crossing between two triplet states differing by the location of the electrons on the base of the pyramid.

The population of the initially equivalent atoms begins to imbalance at both sides of the molecule as soon as an electric field is applied. As can be seen in Figure 3, the two V4 are differentiated when a minimum field is applied (red solid line versus red dotted line). One of them is strongly stabilized, and therefore its population increases, while the other is destabilized in the same proportion. As the electric field is increased, an abrupt jump occurs in the population of the different sites (at 6.5 V / nm for the singlet states and 6.8V/nm for triplet states). The population of one of the apical vanadium ions goes straight to zero as its electron density is transferred to the V1 and V2 centres on the other side. In this region where the two electrons are in the same half of the molecule, the energy levels are slightly different for the singlet and triplet due to the exchange interaction (Figure 3).

It is interesting to study whether a singlet-to-triplet energy gap is also induced when the electric field is applied in the perpendicular direction, i.e., along x and y axis. In fact an electric field along a direction that is perpendicular to the molecular axis also has dramatic electric and magnetic effects. One observes that, in contrast to what happens when the field is applied along z, in the transversal case a gradual transition with smaller

energy gaps is predicted. (see Figure 4). Thus, a gap of around 0.6 meV or 1.6 meV is observed when increasing the applied electric field from 0 to 20 V/nm along x or y, respectively. Notice that the quantitative differences between x and y orientations are

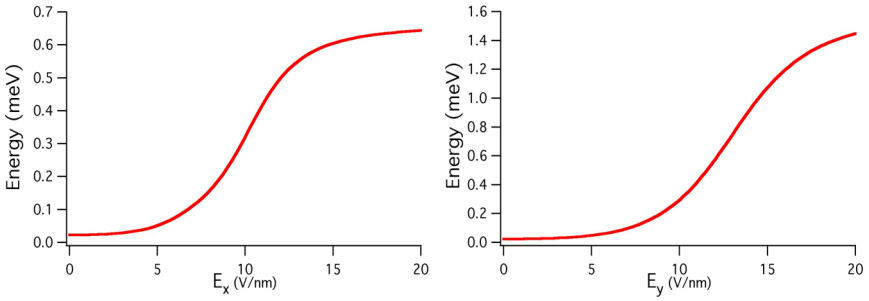

Figure 4. Energy gap between the singlet ground state and the lowest triplet state as a function of the intensity of the electric field along x (left) or y (right).

due to the position of the counter-cations in the crystal as they induce a D_{2h} symmetry for the molecule, instead of the ideal D_{4h} symmetry predicted in the absence of counter-ions, and important differences between the microscopic parameters involving V1 or V2. Nevertheless, the general shape of the two curves is the same.

In conclusion, this model Hamiltonian allows to predict a transition from a paramagnetic to a diamagnetic behaviour, which is very abrupt when the electric field is applied along the z-axis of the $[GeV_{14}O_{40}]^{8-}$ molecule.

Such a prediction has been nicely confirmed by density functional theory (DFT) calculations. DFT provides a completely different framework to verify the phenomenon. Without the need to isolate molecular fragments DFT is performed on the whole molecule and can also provide information on the spin distribution. We used GAUSSIAN 09 software package.[12] All the calculations have been done at B3LYP[13] functional and CREMBL basis set level.[14] The simplest DFT calculations are based on the crystallographic structure of the bare anion, ignoring the countercations. As the fine details of the anion structure are influenced by the cations, in a second step we have optimized the only-anion structure by the means of a standard DFT calculation. In order to check whether the countercations have some influence on the calculations, we have explicitly considered the neighbouring cations surrounding the polyanion. First we have used the crystallographic positions of the eight nearest cations (2 K^+ and 6 Na^+) stoichiometrically needed to compensate the negative charge of the anion. Second, we have taken into account in the calculation the shell of all the nearest cations around the POM. For simplicity, these cations have been treated as point monopositive charges.

Above a critical value of the electric field of 11.5 V/nm, DFT predicts that the singlet state is suddenly stabilized as one electron crosses the tunneling barrier and interacts

12 GAUSSIAN 98 - Gaussian Inc., Pittsburgh, PA, **1998**.

13 Becke, A. D.; *J. Chem. Phys.* **1993**, *98*, 5648-5652.

14 (a) Pacios L.F.; Christiansen, P. A.; *J. Chem. Phys.* **1985**, *82*, 2664-2671. (b) Hurley M.M.; Pacios L.F.; Christiansen, P. A.; Ross, R. B.; Ermler, W. C. *J. Chem. Phys.* **1986**, *84*, 6840-6853.

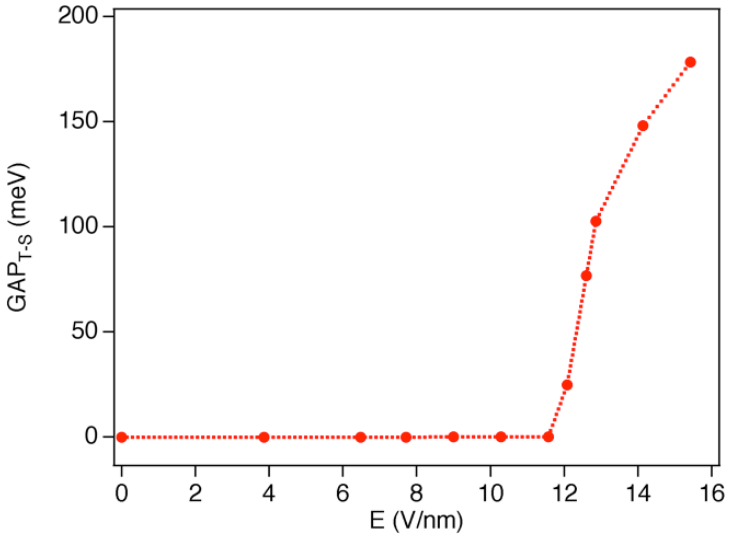

Figure 5. Energy gap between the singlet ground state and the lowest triplet states (Calculated by DFT, see text) as a function of the intensity of the electric field along z.

antiferromagnetically with its neighbor (see Figure 5). The calculated singlet-to-triplet gap is also very strong (it sharply increases to 100 meV at 12.5 V/nm reaching a value of 175 meV at 15 V/nm). The spin distribution can be seen in Figure 6. At zero field, both singlet and triplet have their spin density distributed along the extreme vanadium ions, V4. For the singlet states (left) the transition already occurs at 12 V/nm, while the triplet maintains distributed its density over the two apical vanadium ions. At higher fields (15 V/nm), both states have their electronic distribution completely displaced over one of these two apical vanadium atoms.

One major difference between the results of DFT and the previously detailed spin Hamiltonian is the behaviour at high fields. Indeed, for the model Hamiltonian (Figure 2, inset) the triplet-singlet gap seems to reach a plateau of around 120 meV immediately after the sudden jump, while for DFT calculations (Figure 5) the triplet-singlet gap keeps rising after the jump, albeit with a much smaller derivative. This may be rationalized if one considers the fundamentally different assumptions of the two models. In the model Hamiltonian, at high electric fields the electron has been displaced from V4 on one end of the molecule to V2/V1 on the other end, but it absolutely cannot go further, as configurations with double occupation are not included. This is the case both for the singlet and for the triplet, so at high fields the energy difference mostly corresponds to the effective magnetic exchange i.e. close to 120 meV. In the DFT calculation, double occupation is permitted, but with an important energy difference between singlet and triplet. In the case of the singlet, double occupation can happen by paying the pairing energy; in the case of the triplet, it is necessary to promote the electron to the next energy level. This means that at high but reasonable fields, the electric dipole of the ground state will always be higher in the case of the singlet, as the contribution of the double occupancy of V4 will be more significant in that case. A higher value of the electric

dipole translates into more stabilization of the singlet by the electric field, and thus into a triplet-singlet energy gap that rises with rising electric field, exceeding 180 meV.

Another important difference is that the critical field value (11.5 V/nm) is higher than the one formerly calculated by combination of a model Hamiltonian and ab initio calculations (6.75 V/nm). Again this difference can be rationalized if one considers the different assumptions of the two models, in particular how or whether shielding effects are taken into account. Obviously, the displacement of the moving electron caused by applying an external electric field, E_{ext} , should be hindered by the shielding effects caused by the local electric dipoles induced in the molecule. Therefore, the local dipoles generated by polarizing the electronic clouds around the nuclei will contribute to generate a shielding electric field that will be opposed to the external electric field in such a way that the effective field felt by the molecule, E_{eff}, will be smaller than E_{ext}. Notice that these effects are implicitly taken into account by DFT calculations but not by the model Hamiltonian calculations.

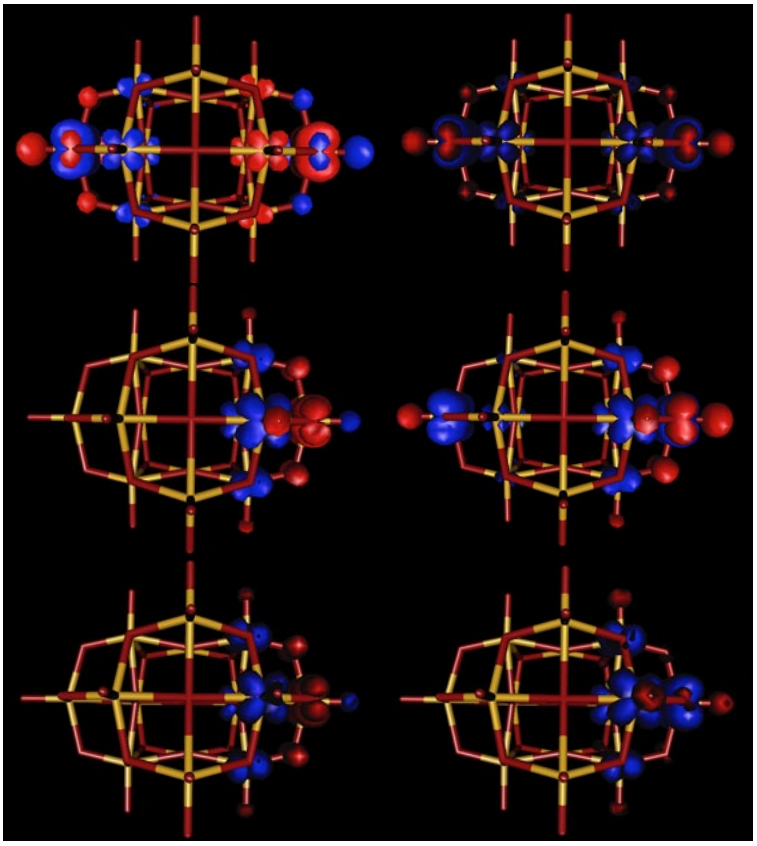

Figure 6. Spin density distribution for the singlet (left) and triplet (right) states for increasing values of the external electric field (up to down 0, 12.5 and 15 V/nm).

To quantify the shielding effect we have carried out a simplified calculation at different external fields, E_{ext}. From DFT calculations we can calculate the total electric

dipole moment induced in the molecule, p_{mol}, for different values of E_{ext}. Independently, we have estimated the electric dipole coming from the two extra electrons in the two extreme situations, i.e., when the two electrons are located at the two V4 apical positions, and when the two electrons are on the same side of the molecule and a dipole is induced. In the neutral case, the dipole is zero, $p_{el}=0$, while in the "ionic" case $p_{el} = q \cdot d \approx 28$ Debye, considering that the horizontal displacement of the moving electron roughly corresponds to the distance between V4 and V1 (or V2) projected along the molecular axis. Thus, the difference between the so estimated electric dipole and the DFT dipole will account for the local dipoles induced by the electric field. As V^{5+} and Ge^{4+} are "hard" cations, barely polarizable, we have further assumed that these local dipoles are caused by the 40 oxygen atoms, which for simplicity have been assumed to be equally polarizable. The results, although very limited in accuracy, seem to go into the right direction (Table 1). Indeed, the external electric field that forces the localization of the electron on adjacent sites, which has been estimated by DFT to be in the range of 10 to 15 V/nm, corresponds to an "unshielded" effective field of just 5.4 to 11.5 V/nm, in qualitative agreement with the results obtained by diagonalizing the model Hamiltonian.

To check if these assumptions are reasonable at least in the order of magnitude, we compared the obtained electrical dipoles for the oxo anions with the ones that would appear for water molecules in an equivalent electric field. For this we will assumed the value calculated by Nir et al.[15] for the contribution of the electronic motions (i.e. the electronic energy levels) to the polarizability at infinite wavelength of a water molecule, as it is in accordance with experimentally determined values. In an electric field of 10 V/nm, this polarizability results in an electrical dipole of 0.48 Debye per H_2O molecule. This value has the same order of magnitude as the approximately 0.55 Debye that we assign to each oxo anion when the polyoxoanion is in a field of 10 V/nm (Table 1).

Eext [V/nm]	pmol (Debye)	pmol - pel (Debye)	Eeff [V/nm]
5.0	17	17	1.4
10.0	22	22	5.4
15.0	44	16	11.5

Table 1. Summary of the dipolar electric shielding estimation.

3. Conclusions

In this work we have evaluated the influence of an electric field on the magnetic coupling and spatial distribution of two delocalized electrons in a V14 mixed-valence polyoxometalate. We have shown that both a model Hamiltonian coupled with *ab initio* calculations on fragments and DFT calculations on the whole molecule predict that, in absence of an electric field, the compound is paramagnetic down to very low temperatures since the 2 electrons are located on different parts of the POM.

Very different theoretical approaches predict an abrupt change of the magnetic coupling between the two delocalized electrons after the application of an electric field

15 Nir, S.; Adams, S.; Rein, R. *J. Chem. Phys.*, **1973**, *59*, 3341-3355

along the main molecular axis. Indeed, the field can force the 2 spins S = ½ to localize on nearest-neighbor metal centers, leading to a very strong antiferromagnetic coupling. The results of the different DFT calculations give similar results: After including these eight new atoms in the model, the results were not essentially different from the ones of the bare anion; both the critical electric field and the magnitude of the singlet-to triplet gap are maintained. As a result, DFT confirms that the sharp spin transition induced by an electric field in the V14 system is a robust phenomenon, intramolecular in nature and which can only slightly be modified by explicitly considering the surroundings.

This electric control of the spin state may be relevant for molecular spintronics and quantum computing.

From the experimental point of view, two problems are limiting the applicability of this molecule. The first one concerns the high electric field needed to reach the switching of the spin state (of the order of 10 V/nm). A way to reduce this critical value would be replacing the apical V4 ions by Mo or W as the orbital energies of these ions are higher than that corresponding to V. Thus, in Figure 7, one can see that the critical electric field significantly decreases when ε increases, varying from 6 V/nm for Mo_2V_{12} ($\Delta\varepsilon = \varepsilon Mo - \varepsilon V = \approx 0.3$ eV) to 4.5 5.5 V/nm for W_2V_{12} ($\Delta\varepsilon = \varepsilon W - \varepsilon V = \approx 1.1$ 0.6eV).[16] The second problem concerns the high negative charge of this type of mixed-valence molecules. This can limit the electronic stability of the cluster when it is contacted to metallic electrodes.

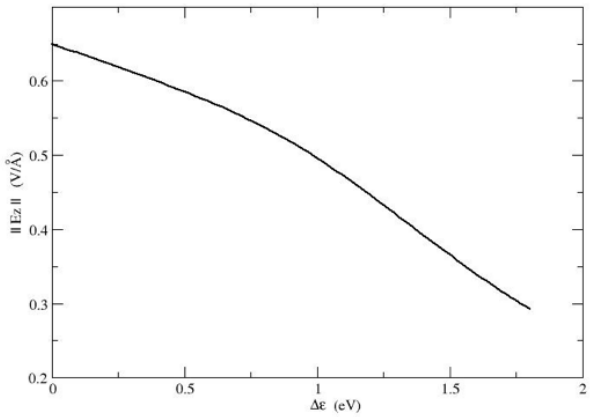

Figure 7. Evolution of the intensity of the electric field necessary for the transition when changing the orbital energy of the apical vanadium ions. Δε=0 corresponds to the case of the V14 POM.

16 (a) Lopez, X.; Bo, C.; Poblet, J.M.; *J. Am. Chem. Soc.* **2002**, *124*, 12574-12582 (b) Lopez, X.; Carbo, J. J.; Bo, C.; Poblet, J.M.; *Chem. Soc. Rev.* **2012**, *41*, 7537-7571.

4
Resumen de la tesis doctoral

"La conquista propia es la más grande de las victorias."
-Platón.

1. Introducción.

El magnetismo molecular es un campo de investigación en rápida expansión y cuyo objetivo central es el diseño y estudio de moléculas y materiales magnéticos con propiedades que puedan ser ajustadas a voluntad. Esta disciplina empezó a desarrollarse en la decada de 1980 cuando el principal interés era obtener sólidos magnéticos basados en moléculas que se ordenasen a altas temperaturas. Esta propiedad se mostró en primer lugar en dos tipos de materiales: El primero basado en tetracianoetileno (TCNE) y el segundo de base cianuro. Como curiosidad, los Azules de Prusia, $Fe_4[Fe(CN)_6] \cdot H_2O$, fueron el primer complejo de coordinación así como el primer imán de base molecular descubierto, hace casi 300 años.

Las tendencias actuales en magnetismo molecular se basan en dos tipos de materiales principalmente: Materiales magnéticos multifuncionales y nanoimanes moleculares. Los primeros son aquellos materiales que combinan el magnetismo con al menos otra propiedad de interés. Estos sólidos son prometedores para la obtención de algunas propiedades tecnológicas importantes que se creían exclusivas de materiales no-moleculares, por ejemplo la combinación de ordenamiento magnético con conductividad, superconductividad o ferroelectricidad.

El otro tipo de materiales, los nanoimanes moleculares, ha mostrado una importancia crucial en el campo. Estos compuestos, generalmente llamados Imanes Monomoleculares, son capaces de mostrar comportamiento superparamagnético a escala molecular. De hecho, a cierto rango de temperaturas los imanes monomoleculares muestran histéresis magnética con un origen puramente molecular, junto con unos efectos cuánticos muy marcados. Así, contrariamente a lo que ocurre en los imanes tradicionales, en estas moléculas no es necesario tener orden magnético a largo alcance para mostrar efectos de memoria.

Existen muchos ejemplos de este tipo de imanes basados en moleculas polinucleares de metales de transición. Sin embargo, la molécula mas citada sigue siendo la primera en ser caracterizada como tal: $[Mn_{12}O_{12}(O_2CMe)_{16}(H_2O)_4]$ (Mn12ac)[1]. Esta molécula combina una gran anisotropía axial con un elevado momento magnético. Debido a esta anisotropía, caracterizada por un término D negativo, el estado de espín fundamental S se desdobla en sus componentes M_S, de tal forma que el doblete $M_S = \pm 10$ es estabilizado mientras que el resto de estados se encuentran progresivamente a energías mayores según $|M_S|$ disminuye. Este desdoblamiento de los niveles magnéticos explica la barrera térmica experimental que se debe superar para invertir el momento magnético.

Poco después de la caracterización de este compuesto, se encontraron las mismas propiedades de imán monomolecular en un complejo octanuclear de hierro, el $([Fe_8O_2(OH)_{12}(tacn)_6]^{8+}$ siendo *tacn* el 1,4,7-triazaciclononano).[2] Este sistema ha sido también estudiado a fondo, siendo preferido en concreto por la comunidad física. Tras

1 Sessoli, R.; Tsai, H. L.; Schake, A. R.; Wang, S.; Vincent, J. B.; Folting, K.; Gatteschi, D.; Christou, G.; Hendrickson, D. N.; *J. Am. Chem. Soc.* **1993**, *115*, 1804-1816.

2 (a) Delfs, C.; Gatteschi, D.; Pardi, L.; Sessoli, R.; Wieghardt, K.; Hanke, D. *Inorg. Chem* **1993**, *32*, 3099–3103. (b) Barra, A. L.; Debrunner, P.; Gatteschi, D.; Schulz, C. E.; Sessoli, R.; *Europhys. Lett*.; **1996**, *35*, 133-138.

él, han sido estudiados muchos otros ejemplos de complejos metálicos. Generalmente se perseguía la posibilidad de combinar en el mismo compuesto una gran anisotropía axial junto al mayor momento magnético total posible. Desgraciadamente, el éxito de esta aproximación es más bien limitado, y de hecho se ha demostrado que aumentar el espín del sistema lleva inherente la disminución de la anisotropía del complejo.

Afortunadamente, surgió una aproximación completamente nueva con el descubrimiento de los imanes moleculares monoatómicos. Esta innovación resultó ser un paso crucial en la miniaturización de los nanoimanes, de forma que la anisotropía que muestra un solo átomo magnético bajo el efecto de un campo cristalino es una condición suficiente para la aparición de la barrera térmica necesaria para la inversión de la magnetización.

Estos nanoimanes moleculares poseen aplicaciones tan variadas como: refrigerantes magnéticos (gracias a su enorme variación de la entropía de espín debido a su elevado momento magnético), agentes de contraste para resonancia magnética nuclear o tratamento hipertérmico de tumores. Adicionalmente, la capacidad de modificar a voluntad las propiedades de estos sistemas sigue siendo un objetivo tras esta linea de investigación.

La habilidad de diseñar y obtener moléculas magnéticas y controlar sus propiedades con un estímulo externo, como un campo eléctrico, es uno de los objetivos principales de la espintrónica molecular. Así esta disciplina se encarga de explorar la interacción entre el espín de una molécula y un campo eléctrico externo. Existen dos objetivos prioritarios en esta nueva area, el primero consiste en el diseño de análogos moleculares de las estructuras espintrónicas mientras que el segundo se basa en estudiar la fenomenología utilizando para ello una sola molécula.

En esta segunda aplicación, espintrónica unimolecular, casi todo el trabajo realizado ha sido teórico, con muy pocos ejemplos experimentales. Estas medidas están todavía en una fase inicial, donde están apareciendo ciertos problemas inherentes a la naturaleza de las moléculas (tales como estabilidad química o el control de la deposición sobre una superficie) que deben ser solucionados antes de obtener resultados fiables.

La evolución del magnetismo molecular desde especies simples hasta intrincados sistemas con propiedades interesantes en nanomagnetismo e incluso hasta el diseño de materiales moleculares aplicados a la espintrónica, demuestra la extraordinaria multidisciplinariedad del campo. De hecho, las colaboraciones entre químicos y físicos han sido absolutamente esenciales para el desarrollo de la magnetoquímica y en general se han extendido para abarcar la investigación en ciencia de materiales, ingeniería, medicina, biofísica y bioquímica.

2. Motivación.

El proyecto descrito en esta tesis está motivado por un interés particular en el Magnetismo Molecular desde un punto de vista principalmente teórico.

Esta tesis está dividida en tres capítulos. En cada uno de ellos, se describe el estado del campo cuando se comenzó la tesis, las contribuciones principales derivadas de este trabajo y una explicación detallada sobre la aportación del autor en cada apartado.

En el primer capítulo, **"Métodos computacionales en Magnetismo Molecular"**, se introduce el trabajo del autor sobre dos herramientas desarrolladas para la comprensión de las propiedades de las moléculas magnéticas. El primer artículo "*Implementación paralela de MAGPACK para el analisis de 'clusters' de spin de alta nuclearidad*" resultó de una activa colaboración entre el autor y el departamento DSIC de la Universidad Politécnica de Valencia. La segunda contribución "*MVPACK, un código para calcular niveles de energía y propiedades magnéticas en 'clusters' de valencia mixta de alta nuclearidad*" fue escrita mientras el autor comenzaba su tesis y su contribución consistió en añadir la computación de la variación de las propiedades magnéticas al aplicar un campo eléctrico sobre la molécula.

En el segundo capítulo, **"Imanes moleculares monoatómicos basados en polioxometalatos"** se describen tres familias de moléculas con estas propiedades magnéticas. De hecho, estas moleculas fueron las que efectivamente abrieron el campo a la actual variedad de ligandos y estructuras que presentan este comportamiento. En este capítulo se presentan tres contribuciones en este aspecto. La primera es "*Imanes Mononucleares basados en complejos de polioxometalatos con lantánidos* $[Ln(W_5O_{18})_2]^{9-}$ *y* $[Ln(\beta_2\text{-}SiW_{11}O_{39})_2]^{13-}$ *(*Ln^{III} *= Tb, Dy, Ho, Er, Tm and Yb)*" y presenta las dos series iniciales de compuestos, su síntesis, caracterización y estudio. La siguiente es "*Imanes Mononucleares basados en polioxometalatos con simetría pentagonal: La serie de* $[LnP_5W_{30}O_{110}]^{12-}$ *(*Ln^{III} *= Tb, Dy, Ho, Er, Tm y Yb)*", donde un complejo de lantánido de simetría pentagonal se estudió por completo. Esto fue muy importante porque constituyó una alternativa a las ya conocidas estructuras de antiprisma cuadrado y de hecho motivó la última contribución en este capítulo: "*Diseño racional de imanes moleculares monoatómicos y 'espín-qubits' basados en complejos mononucleares de lantánidos*". En este último artículo se muestra una aproximación teórica basada en cargas puntuales para la predición del comportamiento magnético de estos sistemas, así como sugerencias para el correcto diseño de las mismas.

En el tercer capítulo, **"Moléculas interruptor controladas por un campo eléctrico"**, se presenta la aplicación de MVPACK al estudio del control eléctrico del estado magnético fundamental en estas moléculas. En este capítulo se varía la estructura general de la tesis y se presenta el estudio completo de la molécula $K_2Na_6[GeV_{14}O_{40}]\cdot 10H_2O$ descrito detalladamente.

A continuación se presenta una descripción detallada de cada capítulo, donde se explicarán resumidamente los resultados más relevantes así como la contribución

original del autor.

3. Capítulo 1: *"Métodos computacionales en Magnetismo Molecular".*

3.1. Implementación paralela de MAGPACK. Consideraciones Generales.

El código secuencial MAGPACK es una poderosa y eficiente herramienta computacional utilizada para resolver el problema del canje en complejos polinucleares de espín considerando la anisotropía local y los canjes isótropo, anisótropo, bicuadrático y antisimétrico. Desde su publicación en 2001 ha sido extensamente utilizado por muchos grupos dentro de la comunidad científica, de hecho, en julio de 2013, la publicación original cuenta con 482 citas en campos tan diversos como los imanes nanomoleculares, las interacciones entre metales 3d-4f y las cadenas monodimensionales anisótropas.

Pese a sus capacidades, el código presenta un "cuello de botella" importante: la diagonalización de la matriz de energía. Este obstáculo se concreta en dos problemas: el primero es la ocupación de la memoria RAM, lo cual presenta un límite físico al tamaño del sistema, y el segundo es el tiempo de diagonalización el cual puede llegar a ser una traba para cálculos con restricción temporal. Esto marca un límite a partir del cual el sistema ya no puede ser calculado. Para las especificaciones de un procesador estándar (1 microprocesador +2 Gb RAM) el código es capaz de calcular matrices con trazas del orden de 30 000 elementos.

Para incrementar el tamaño del cálculo, una propuesta podría consistir en aumentar la memoria RAM del sistema. Esto ha demostrado no ser una solución, ya que en ese caso, el factor limitante es la velocidad del procesador. Esto ocurre porque la subrutina que se encarga de la diagonalización de la matriz de energía (DSPEV / ZHPEV) trabaja de forma secuencial, esto es, un solo microprocesador realiza todo el trabajo. De este modo, los cientos de nodos de los que dispone un supercomputador no son accesibles para programa.

El código podría ser mejorado añadiendo la funcionalidad que aporta la paralelización. Esto es, la distribución de la carga computacional sobre un numero de microprocesadores, realizando cada uno una pequeña parte del trabajo. Por suerte, en la Universidad Politecnica de Valencia se encuentra el Departamento de Sistemas Informáticos y Computación (DSIC), donde se ha desarrollado una librería que permite la diagonalización paralela de matrices dispersas de tamaños considerables. Este código, llamado SLEPc, parecía la contribución óptima a la mejora paralela de MAGPACK. Por este motivo, se inició una extensa colaboración entre los dos grupos ICMOL-DSIC, para la elaboración de una versión paralela de MAGPACK.

En esta contribución, el código original se reescribió parcialmente con el objeto de paralelizar su flujo de trabajo así como el proceso de diagonalización. Esto se realizó enriqueciendo el código original escrito en FORTRAN77 con una serie de directivas en C++ que controlan el uso de la librería SLEPc que está basada en PETSc, un marco de cálculo matemático también paralelo. SLEPc aporta una rutina basada en métodos de proyección para la diagonalización parcial de la matriz de energías. Esto quiere decir que, en el proceso, solo se obtienen una cantidad concreta de valores propios (o bien los más altos o bien los más bajos) y no todo el espectro. Esto puede significar un

problema a la hora de calcular propiedades termodinámicas, ya que si el espectro de niveles es un cuasi-continuo, no es trivial elegir la cantidad de niveles donde truncar la matriz. Esto puede ser solucionado calculando de forma precisa la propiedad a bajas temperaturas (considerando la anisotropía del sistema) mientras que el resto del espectro sería calculado mediante otros métodos efectivos (por ejemplo, por la aproximación de espín gigante). En cuanto a la posibilidad de reproducir propiedades ópticas (como la Dispersión Inelastica de Neutrones, INS), el tamaño de los vectores propios seguiría haciendo lento y costoso el proceso.

3.2. Implementación paralela de MAGPACK. Breve resumen de los resultados obtenidos.

El desarrollo del código paralelo fue testeado utilizando para ello varias matrices con trazas de alrededor de 60 000 elementos. Estas pruebas pueden ofrecer, en un tiempo razonable, información sobre la exactitud del cálculo así como dar una idea sobre la escalabilidad con el número de procesadores. En este aspecto, se llegó a las siguientes conclusiones:

- La paralelización del programa ha permitido reducir drásticamente el tiempo de cálculo en comparación con el código secuencial original. Esto supone un gran avance para la solución de problemas de tamaño moderado con unos pocos procesadores, pero aun más, porque permite resolver sistemas de tamaños mucho mayores que serían imposibles de tratar por culpa de limitaciones ya sea en memoria o simplemente en capacidad computacional.
- El uso de diagonalizadores parciales específicamente diseñados para matrices dispersas permitió la obtención de los valores propios adecuados para el cálculo de la propiedad termodinámica, desechando así aquellos valores que no aportan información y ahorrando esfuerzo computacional.
- El rendimiento paralelo obtenido fue razonablemente bueno para los casos obtenidos (especialmente para los cálculos que incluyen anisotropía). Esto confirmó la correcta distribución de la carga de trabajo, así como el funcionamiento distribuido de la librería SLEPc.
- Se pusieron a punto distintos métodos de almacenamiento de matrices dispersas y se comprobó la eficiencia de cada uno de ellos. Del mismo modo la operación entre matrices del tipo $A + \gamma B$ se optimizó de forma interna dentro de SLEPc. Como conclusión a este paso, se comprobó que el almacenamiento simétrico combinado con una representación implícita de las matrices parece ser el método más efectivo.

3.3. Sistemas de Valencia Mixta, MVPACK. Consideraciones Generales.

Los sistemas de valencia mixta son aquellos que poseen varios iones de un metal de transición en distinto estado de oxidación. Existe una enorme variedad de estos compuestos, entre los cuales se encuentran complejos de relevancia biológica y manganatos de tierras raras con magnetorresistencia gigante.

Bajo ciertas condiciones, los electrones extra que poseen estas estructuras pueden

deslocalizarse sobre toda la estructura metálica. Esta deslocalización fue históricamente estudiada en el complejo de Creutz-Taube $[(NH_3)_5Ru^{II}(pirazina)Ru^{III}(NH_3)_5]$. En este caso, un solo electrón se encuentra deslocalizado sobre los dos metales diamagnéticos. La sencillez de este sistema permitió estudiar a nivel molecular el acoplamiento de los electrones con el movimiento de los nucleos (interacciones vibrónicas). Estas interacciones son inherentes a los sistemas de valencia mixta debido a la considerable deformación de la esfera de coordinación inducida por la presencia de un electrón adicional. La teoría vibrónica para dímeros de valencia mixta fue desarrollada por Piepho, Krausz y Schatz y se la conoce como la teoría PKS.

La deslocalización electrónica afecta también al canje magnético entre los metales. Por ejemplo, dando lugar al fenómeno del doble canje, el cual acopla el momento magnético de cada ion a través de los electrones que se encuentran deslocalizados ya que la orientación de su espín se mantiene mientras se mueven. Erróneamente se puede pensar que esto conllevaría siempre la estabilización del estado ferromagnético, pero no es así para ciertas nuclearidades o topologías. Los primeros cálculos realizados para sistemas con canje tipo Heissenberg-Dirac-Van Vleck y doble canje mostraron que, incluso en los casos más simples (dímeros, trímeros o tetrámeros), la deslocalización electrónica podría tener distintos efectos. Como consecuencia, las conclusiones extraídas de modelos simples no pueden ser extrapoladas con facilidad a sistemas de alta nuclearidad donde se acoplan espines deslocalizados y localizados. En este contexto, se observó que sería necesario desarrollar una teoría que tuviera en cuenta las interacciones magnéticas así como la transferencia electrónica entre iones. Esta teoría fue publicada en 1996 por Borrás-Almenar *et al*.

Una decada más tarde, este teoría fue modificada para incluir "dominios" de deslocalización que delimitan la posibilidad de transferencia de cada uno de los electrones extra. Esto añade dos ventajas: La primera es que, considerando estos dominios, las posibilidades de deslocalización de los electrones son menores, generando de este modo un número menor de distribuciones y permitiendo el cálculo de sistemas de mayor tamaño. La segunda es la posibilidad de asignar distintos momentos de "core" a los centros magnéticos de cada dominio, permitiendo así el cálculo de sistemas de valencia mixta heteronucleares.

Esta aproximación teórica fue implementada como un código computacional llamado MVPACK, que permitía el cálculo de las propiedades termodinámicas de sistemas de alta nuclearidad. Este código incluye el efecto de la transferecia electrónica, así como el canje isótropo, las energías orbitales de los distintos iones y la repulsión de Coulomb.

3.4. Sistemas de Valencia Mixta, MVPACK. Breve resumen de los resultados obtenidos.

Este código fue ampliamente usado incluso antes de su publicación. De hecho, permitió el calculo de polioxometalatos reducidos de nuclearidad creciente como:

$[W_{10}O_{32}]^{6-}$.[3], $[PW_{12}O_{40}]^{5-}$,[4] y $[V_{18}O_{48}]^{n-}$ (n=4-12).

En el primer caso, experimentalmente se observa que el sistema birreducido se comporta como un diamagneto. Esto parecía difícil de interpretar ya que, a priori, se podría esperar que los dos electrones deslocalizados se encontrasen en los extremos de la molécula para reducir la interacción de Coulomb. Gracias a los cálculos teóricos se descubrió que los electrones prefieren deslocalizarse entre los 2 anillos centrales de W de forma que se acaba generando una interacción antiferromagnética entre ellos.

De forma parecida se dedujo en el caso de $[PW_{12}O_{40}]^{5-}$ que, por la interacciones entre la repulsión de Coulomb y la transferencia electrónica las rutas de deslocalización eran distintas para el estado singlete y triplete. Y de este modo mantener ambos electrones lomás separados posibles, conllevaba una fuerte estabilización del estado singlete.

Por último en el caso del polioxovanadato $[V_{18}O_{48}]^{n-}$, tenemos una familia de compuestos que van desde el completamente reducido (n=12, 18 electrones extra) hasta el que posee 10 electrones extra (n=4). En estos compuestos se presentaba una fenomenología magnética inusual: según la cantidad de electrones deslocalizados disminuye, aumenta el acoplamiento antiferromagnético entre los electrones restantes. Para entender este comportamiento, se realizó un estudio completo de la influencia del canje y la transferencia electrónica sobre los niveles de spin más bajos.

Adicionalmente a estos cálculos, el código MVPACK fue modificado para añadir la posibilidad de incluir el efecto de aplicar un campo eléctrico. Este efecto fue añadido durante esta tesis y ha sido la principal contribución del autor a este código.

El campo electrico se añadió mediante la inclusión de una subrutina que se encarga de tomar las coordenadas del sistema así como del número de campos eléctricos, junto a su dirección, sentido e intensidad. Con estos datos, las energías orbitales de los distintos centros metálicos se modifican acordes con su posición en la dirección del campo eléctrico. De hecho, si un metal se encuentra sometido a un potencial mayor, su energía orbital es estabilizadas respecto a otro metal que sufra el efecto de un potencial menor.

Esta adición se realizó para conseguir simular la estabilización o desestabilización de ciertas distribuciones electrónicas usando para ello un campo eléctrico. Esta característica básica puede proveer información útil sobre el control del estado de espín del sistema mediante su manipulación con un estímulo externo tal como la aplicación de un potencial eléctrico. Entender el efecto de dicho potencial en la localización / deslocalización electrónica es uno de los puntos fuertes de esta nueva subrutina.

3 Clemente Juan, J. M.; Coronado, E.; Gaita-Ariño, A.; Suaud, N. *J. Phys. Chem.* **2007**, *111*, 9969–9977.

4 Suaud, N.; Gaita-Ariño, A.; Clemente Juan, J. M.; Sánchez-Marín, J.; Coronado, E. *J. Am. Chem. Soc.* **2002**, *124*, 15134–15140.

4. Capítulo 2: "*Imanes moleculares monoatómicos basados en polioxometalatos*".

4.1. Estudios iniciales sobre nanoimanes de lantánidos.

Durante mucho tiempo desde el descubrimiento del primer SMM, la comunidad de químicos ha seguido una estrategia para incrementar la temperatura de bloqueo de estos nanoimanes. Este procedimiento pretende combinar dos requerimientos, (a) incrementar la nuclearidad del sistema y por tanto su espín total S y (b) incrementar la anisotropía axial *D*. Finalmente, se sugirió que estos requerimientos no podrian ser optimizados simultaneamente. Pero antes de que esta afirmación se comprobase formalmente, apareció un nuevo camino con el descubrimiento de los imanes moleculares monoatómicos (SIMs).

Los SIMS son moléculas con un solo ión magnético que muestran relajación lenta de la magnetización a bajas temperaturas. De hecho, se comportan como análogos mononucleares de los bien conocidos SMMs. En estos nanoimanes, el comportamiento magnético viene determinado por el desdoblamientos de los niveles magnéticos más bajos. De este modo, el estado fundamental (*J*) de un ión de lantánido se desdobla en sus componentes M_J por el efecto de un campo de ligandos (LF) producido por su esfera de coordinación. Si la simetría es axial, el LF suprime la mezcla de M_J en la función de onda y por tanto elimina la rápida relajación de la magnetización por túnel cuántico.

Para la mayor parte de simetrías de coordinación, el LF introduce una anisotropía con términos de orden superior así que el desdoblamiento de niveles magnéticos no sigue la típica regla de DS_z^2 tal y como ocurre con muchos de los SMMs de metales de transición. En estos casos la anisotropía es mucho más difícil de visualizar y solo puede ser estimada considerando la simetría completa de la coordinación. Es importante tener en cuenta que en estos sistemas la barrera no puede ser calculada como la diferencia energética entre los estados de mayor y menor espín.

El primer ejemplo de SIM fue el bis-ftalocianinato de terbio ($TbPc_2$) de coordinación D_{4d} (antiprisma de base cuadrada) descrito por Ishikawa. La caracterización magnética de este compuesto se basó en el mismo procedimiento que se usa para los SMMs, es decir, medidas de susceptibilidad dinámica de campo alterno. En esta técnica se aplica un campo magnético oscilante a una cierta frecuencia de forma que la orientación del momento magnético de la muestra oscila para seguir a este campo. A bajas frecuencias, el sistema tiene suficiente tiempo para invertir su espín, ya sea bien por efecto tunel o bien simplemente sobrepasando la barrera. Cuando la temperatura es lo suficientemente baja y la frecuencia es alta, el sistema va poco a poco siendo incapaz de seguir el campo externo de forma que la oscilación de la magnetización adquiere una fase en comparación con el campo oscilante. Según disminuye la temperatura, o a mayores frecuencias existe un punto en el cual la frecuencia natural de la relajación del sistema es la misma que la frecuencia del campo externo. En este punto, aparece un máximo en la susceptibilidad fuera de fase. Si posteriormente se sigue disminuyendo la temperatura, solo se podrá observar una disminución en la señal tanto en fase como fuera de fase hasta que la magnetización esta completamente bloqueada y permanece invariable con el campo alterno. Este mecanismo de relajación de espín has sido muy estudiado en SMMs y

comúnmente se asume que sigue una ley de Arrhenius.

En el caso de $TbPc_2$, las medidas de susceptibilidad fuera de fase mostraron que este complejo bloquea su momento magnético a 40 K y que posee una barrera efectiva de unos 400 cm^{-1}. Además se han preparado varios derivados de este compuesto con el fin de incrementar su temperatura de bloqueo. De hecho, se consiguió un derivado especialmente prometedor oxidando el ligando, de forma que se incrementa el LF sentido por el ión metálico.

Estas contribuciones de Ishikawa constituyeron un cambio de rumbo en la investigación de nanoimanes. A partir de este momento, comenzaron a aparecer otros compuestos de simetría pseudoaxial con este tipo de comportamiento. De hecho, una de estas primeras contribuciones consistió en un complejo de polioxometalato-lantánido con comportamiento de SIM. Este compuesto $[Er(W_5O_{18})_2)]^{9-}$ posee simetría D_{4d} tal y como era el caso en $TbPc_2$.

Las medidas magnéticas demostraron que en el caso de los complejos POM-Ln, el derivado de Er es el que daba el mejor comportamiento SIM. Esto está en claro contraste con lo observado en el caso de los complejos de bis-ftalocianinato en los cuales era Tb el que tenía este comportamiento. Esta divergencia se atribuyó a las diferencias en la coordinación de ambos compuestos. La comprensión de dichas diferencias motivó el estudio teórico de distintos esquemas de coordinación para racionalizar la correlación entre estructura y propiedades.

4.2. Estudios teóricos sobre SIMs

Los primeros estudios sobre nanoimanes fueron empíricos. Simplemente intentaban analizar la susceptibilidad dinámica con el objetivo de parametrizar el comportamiento. La aproximación más simple considera un único proceso de relajación posible el cual está impedido por una barrera de activación térmica. Dentro de esta aproximación, el comportamiento puede ser ajustado mediante una ley de Arrhenius y así, ser descrito mediante dos parámetros: la altura efectiva de la barrera (U_{eff}) y el factor preexponencial (τ_0). Un paso más allá, aunque dentro de las aproximaciones empíricas, se encuentra la determinación de múltiples procesos de relajación. En este caso se utiliza el parámetro de Cole-Cole (α), el cual es una magnitud que relaciona las señales en fase y fuera de fase y que contiene información sobre la cantidad de procesos de relajación activos.

Por su lado, la teoría del campo de ligandos trata el efecto de la coordinación sobre el desdoblamiento del estado fundamental *J* del lantánido. Inicialmente, se realizaron estudios simples para obtener los parámetros de LF ideales para el caso del complejo $TbPc_2$. Algunos años después, se crearon modelos basados en cargas puntuales para precedir el valor de los parámetros de LF únicamente considerando la estructura del complejo. Estas descripciones cualitativas no pueden ofrecer detalles precisos sobre la estructura de los niveles magnéticos pero pueden ser usadas como punto de partida para aclarar qué derivados son aquellos de los que se espera el mejor comportamiento de SIM. La conclusión final sobre los modelos teóricos es que incluso con los cálculos más complejos posibles, no existe una descripción unimolecular que sea capaz de predecir

por si sola los fenómenos de relajación.

De este modo, gran parte de la teoría desarrollada sobre imanes moleculares está centrada en la comprensión de los procesos de relajación. Este fenómeno causó un gran interés en la comunidad física, la cual intentó desarrollar una teoría general para entender el efecto del resto del cristal en el bloqueo magnético. Un ejemplo interesante fue el estudio de la decoherencia en un baño de espines.

4.3. Breve resumen de los resultados obtenidos.

El objetivo de este trabajo es obtener SIMs basados unicamente en complejos de polioxometalatos (POMs) con lantánidos y analizar sus propiedades magnéticas. Estos complejos pueden ser muy interesantes por el aislamiento que produce la parte diamagnética, que minimiza la interacción dipolar directa. Además, es posible diluir magneticamente el sistema utilizando como matriz un derivado diamagnético (como Y^{3+}) y estudiar las propiedades de un solo ión. Finalmente, los POMs presentan una enorme variedad de simetrías de coordinación que puede ser explorada para construir nuevos SIMs.

En esta tesis se presentan tres familias de polioxowolframatos que han sido sintétizadas, caracterizadas y teoricamente explicadas. Son: $Na_9Ln(W_5O_{18})_2$ [LnW10], $K_{13}Ln(\beta_2\text{-}SiW_{11}O_{39})_2$ [LnW22] and $K_{12}LnP_5W_{30}O_{110}$ [LnW30]. Ln = Tb^{3+}, Dy^{3+}, Ho^{3+}, Er^{3+}, Tm^{3+},Yb^{3+}. Este trabajo se completa con un análisis teórico exhaustivo y una racionalización de las propiedades magnéticas de los SIMs.

La síntesis de estos productos se realizó siguiendo la receta previamente publicada por sus autores originales. Todos ellos fueron caracterizados por EPMA (Microanalisis por sonda electrónica), espectrometría infrarroja, y difracción de rayos X.

Las medidas de susceptibilidad magnética se llevaron a cabo con un magnetómetro comercial equipado con un sensor SQUID y un PPMS. Las medidas de susceptibilidad *dc* se realizaron en un rango de 2-300 K con un campo aplicado de 1000 G. Estos datos fueron corregidos utilizando las tablas de constantes de Pascal para eliminar la contribución diamagnética. Las medidas de corriente alterna (*ac*) se realizaron en un rango de 2-15 K con un campo alterno de 3.95 G a distintas frecuencias en el rango de 1-10000 Hz.

Para algunos de los compuestos, la caracterización magnética se extendió a temperaturas muy bajas utilizando una combinación de instrumentos no comerciales. En este aspecto, se hicieron medidas de histéresis magnética entre 350 mK y 7 K utilizando una sonda micro-Hall casera junto a un refrigerador de ^{3}He. En estas condiciones se realizaron también medidas ac desde 333 Hz a 13 kHz, acoplando el susceptómetro a la camara de mezcla de un refrigerador de dilución de ^{3}He-^{4}He. Esto permite acceder a temperaturas en el rango desde 0.09 K hasta 3.5 K. Por último las medidas de calor específico se realizaron entre 350 mK y 20 K en un PPMS comercial.

Para el caso de LnW10, medidas *ac* del complejo de Er^{3+} muestran una dependencia con la frecuencia en su señal a baja temperatura. Según se va enfriando esta muestra, se puede observar un pico a altas frecuencias (1000-10000 Hz) sobre 4-6 K. En el caso del

derivado de Ho^{3+} también aparece una señal interesante, que muestra un hombro a 5 K.

Para el caso de LnW22, no solo Er^{3+} sino también Dy^{3+}, Ho^{3+} e Yb^{3+} muestran dependencia con la frecuencia en su señal fuera de fase. Desafortunadamente, en estos casos solo se pudo detectar un ligero hombro y no un pico. Esto nos muestra que los procesos de relajación en LnW22 son bastante más rápidos que en LnW10.

Por último, en el caso de LnW30, el compuesto de Dy^{3+} es aquel que muestra una dependencia más definida, mientras que Ho^{3+} muestra una señal peor resuelta. En estos compuestos no se puede observar un pico al bajar la temperatura hasta 80 mK, esto quiere decir que no llegamos a tener un bloqueo superparamagnético en ningún momento.

Adicionalmente se realizaron experimentos de dispersión inelástica de neutrones (INS) en las muestras de LnW10 (Ln=Er^{3+}, Ho^{3+}) y LnW30 (Ln=Dy^{3+}, Ho^{3+}). Muestras deuteradas de estos compuestos se midieron en el IN4 en el Instituto Laue-Langevin en Grenoble, Francia. Estas medidas se realizaron a longitudes de onda de λ = 1.1, 2.2 y 3.6 Å lo cual corresponde con ventanas de energía de 5-60, 2-15 y 1-5 meV respectivamente. INS es una técnica que puede ofrecer información muy precisa sobre los niveles magnéticos de un sistema. Desgraciadamente para estos compuestos, las medidas estaban dominadas por una transiciónes fonónicas muy intensas que oscurecian cualquier tipo de señal magnética que pudiera aparecer.

4.4. Conclusiones generales.

En general, los complejos Ln-POM han demostrado ser unos prometedores candidatos al estudio del comportamiento de los SIMs. Han sido usados para obtener muestras diluidas en forma de cristales robustos que han podido ser estudiados con una gran cantidad de técnicas experimentales. Además, estos compuestos pueden ser sintetizados variando el espín nuclear del lantánido (si procede), un factor que influye en la relajación tunel del sistema. Esto ha resultado provechoso en muchos otros trabajos tanto teóricos como experimentales sobre estos mismo sistemas. Además se ha realizado un extenso estudio en el uso de estos compuestos como espín-qubits. En concreto, se realizaron experimentos de EPR con el fin de determinar el "tuneling gap" para el caso de HoW10, un parámetro clave para realizar manipulaciones cuánticas en el sistema.

Además, experimentalmente se han propuesto derivados de Gd^{3+} para implementar refrigerantes magnéticos a muy bajas temperaturas. Sobre el desarrollo de dispositivos basados en Ln-POM, se ha utilizado nanolitografía DIP-PEN para obtener nanoestructuras cristalinas que pueden ser depositadas con precisión con la punta de un microscopio de fuerza atómica (AFM).

Finalmente, se pueden extraer algunas últimas ideas del análisis teórico de los resultados experimentales.

- **El esquema de coordinación determina qué lantánido se comporta como SIM.** Existe una gran diferencia entre los complejos de bis-ftalocianinato y los de POMs. En el caso de los $LnPc_2$, es el ión Tb^{3+} el que ofrece un mejor comportamiento magnético (temperatura de bloqueo más alta y barrera de energía mayor). mientras que en el caso de LnW10, el candidato más prometedor es Er^{3+} . Tb^{3+} y Er^{3+} tienen signo opuesto del coeficiente de Stevens α (α<0 para

Tb^{3+} y $\alpha>0$ para Er^{3+}). Así, la estabilización de los subniveles de alto M_J en ambos casos debe ser debe ser consecuencia de sus distintos esquemas de coordinación. Tal y como se muestra en la descripción del cristal, las distancias entre los planos de coordinación de los oxígenos (Ln-POM) es mas pequeña que la distancia entre los planos de los nitrógenos ($LnPc_2$). Esto se podría considerar como un efecto de "compresión" para el caso del POM frente al bis-ftalocianinato. Este sería el causante del cambio en el signo del término de segundo orden del campo de ligandos, que a su vez explica la diferencia en el comportamiento magnético.

- **Esquemas de coordinación muy distintos y no necesariamente axiales pueden dar lugar a SIMs.** Comparando las dos series de LnW10 y LnW30 se puede observar que ambos sistemas tienen comportamiento de SIM pese a las enormes diferencias en su estructura (alargada frente a achatada). En el caso de LnW10, la principal contribución a la estabilización del máximo MJ es el término de segundo orden B_2^0 (proporcional al conocido 'desdoblamiento a campo cero', *D*). A diferencia de esto, en la serie de LnW30 es un término de orden superior (q=5) aquel que define sus propiedades magnéticas. Este parámetro que produce la mezcla de funciones magnéticas con distinto M_J no es suficiente para suprimir la capacidad del sistema de bloquear su momento magnético a bajas temperaturas. La explicación de este fenómeno, consiste en el hecho de que la mezcla no es siempre "activa" de forma que el estado fundamental no tiene porqué contener ambas contribuciones $+M_J$ y $-M_J$. En este aspecto, el sistema no puede encontrar una vía para relajar por efecto tunel dentro de su misma función de onda y solo puede hacerlo mediante un proceso térmicamente activado de tipo "Orbach".

- **Dentro de un mismo esquema de coordinación, pequeñas diferencias estructurales se pueden correlacionar con las distintas tasas de relajación obtenidas.** Pese a las estructuras de coordinación similares que se muestran entre las familias de LnW10 y LnW22, se puede observar que su comportamiento magnético es bastante distinto, teniendo la segunda serie tiempos de relajación más rápidos que en el primer caso. Esto puede ser explicado si se tiene en cuenta que la hipótesis inicial que consideraba ambos sistemas con simetría D_{4d} perfecta no es estrictamente correcta si no que en el segundo caso, la estructura esta bastante distorsionada, cosa que añade términos extra que pueden producir un aumento en la relajación del sistema.

- **Las divergencias en las señales *ac* a baja temperatura revelan un proceso túnel muy eficiente.** La divergencia observada en la señal fuera de fase de la susceptibilidad dinámica por debajo de la temperatura de bloqueo no se había observado nunca para SMMs de metales de transición. Este fenómeno muestra la existencia de un proceso de relajación túnel muy rápido que tiene lugar a bajas temperaturas. Este comportamiento fue muy estudiado en colaboración con la Universidad de Zaragoza. Resumiendo brevemente estos resultados, se puede concluir que a altas diluciones, la interacción dipolar es casi inexistente en estos sistemas y que dicho proceso de relajación tiene que venir de un fenómeno de

relajación spín-red cooperativo. Para este trabajo, la contribución experimental consistió en aportar muestras magnéticamente diluidas utilizando para ello una matriz diamagnética de YW10 la cual se cocristalizaba junto al complejo magnético en la proporción deseada.

5. Capítulo 3: *"Moléculas interruptor controladas por un campo eléctrico".*

5.1. Introducción a los materiales magnéticos de tipo interruptor.

Los materiales magnéticos de tipo interruptor son aquellos en los cuales sus propiedades magnéticas pueden ser reversiblemente modificadas aplicando un estímulo externo. Como ejemplos de base molecular de este tipo de materiales se tendrían, los solidos de transición de espín moleculares y los complejos bimetálicos de cianuros. En este tipo de materiales, la luz o la presión pueden ser usadas como estímulos externos que controlen su estado de espín. Sin embargo, el campo eléctrico o la corriente eléctrica también pueden ser usados con este fin. Esta posibilidad ha sido demostrada macroscopicamente mendiante estudios en materiales multiferroicos o en espintrónica de semiconductores. De hecho, el uso de un campo eléctrico en lugar de un campo magnético presenta ciertas ventajas en la nanoescala. Este campo es fácil de obtener (por ejemplo con el uso de una punta de un microscopio de efecto túnel STM) y puede ser encendido/apagado de una forma muy rapida (del orden de picosegundos) ofreciendo así la posibilidad de ser aplicado con precisión sobre una sola molécula durante un tiempo muy controlado. Estudios recientes muestran que es posible obtener transición de espín en nanopartículas de 10 nm mediante un campo eléctrico.

En este ámbito y comparando con el resto de compuestos moleculares, los POM presentan ciertas ventajas químicas, estructurales y electrónicas que les permiten ser adecuados para aplicaciones en espintrónica. En particular, estas moléculas son especialmente robustas y mantienen su estructura no solo en disolución si no también en estado sólido o cuando se encuentran depositadas en superficies, facilitando su procesado. Más importante si cabe es la posibilidad de los POM de aceptar un número variable de electrones "extra" manteniendo su estructura prácticamente intacta. Esto da lugar a sistemas de valencia-mixta en los cuales los electrones se encuentran (típicamente) deslocalizados sobre el entramado de iones metálicos. Un ejemplo representativo de este comportamiento es la molécula $[PMo_{12}O_{40}(VO)_2]^{n-}$ la cual ha sido propuesta para ser usada como puerta lógica cuántica.

En este POM, los espines de los iones vanadilo pueden ser acoplados mediante la inyección de un electrón "extra" en la cavidad central de Mo12 mediante la aplicación de un potencial con un STM.

En esta tesis se presenta el estudio del POM de valencia-mixta de fórmula $K_2Na_6[GeV_{14}O_{40}]\cdot 10H_2O$, el cual se encuentra reducido por dos electrones "extra". De este modo el compuesto posee 12 iones V^V (S=0) y 2 iones V^{IV} (S=1/2). La característica más peculiar de este sistema es que experimentalmente mantiene el paramagnetismo hasta

1.7 K. Este comportamiento esta en clara contradicción con lo que se había observado en otros POM direducidos que son diamagnéticos incluso a temperatura ambiente, mostrando así un fuerte acoplamiento antiferromagnético entre ambos electrones. (Ver el Capítulo 1 para una explicación mas detallada).

La clave para explicar este comportamiento aparentemente anómalo subyace en el cuadrado central de la estructura de la molécula [GeV_4O_{12}] que separa dos pirámides de base cuadrada de tipo [V_5O_{14}]. La combinación de una mala transferencia electrónica entre las dos pirámides, con la elevada energía orbital del cuadrado central, da lugar a que ambos electrones estén situados en extremos opuestos de la molécula minimizando así la repulsión de Coulomb. Tomando como base este comportamiento es posible imaginar que un campo eléctrico aplicado en la dirección del eje molecular principal pueda sobrepasar la repulsión interelectrónica, permitiendo que ambos electrones se acerquen e interactuen de forma fuertemente antiferromagnética. Así pues, la motivación de este trabajo consistión en el interés por comprobar si esta molécula magnética puede funcionar como interruptor y modificar su estado de espín fundamental desde dos espines 1/2 independientes a un estado S=0 diamagnético mediante la aplicación de un campo eléctrico.

5.2. Breve resumen de los resultados obtenidos.

Inicialmente, se realizó un cálculo utilizando un modelo de valencia mixta como el descrito en el Capítulo 1 (modelo efectivo de Hamiltoniano t-J). En este tipo de cálculo, los parámetros de transferencia y canje son extraidos previamente de calculos *ab initio* sobre fragmentos de la molécula original. Este modelo nos confirmó la fenomenología observada experimentalmente: en ausencia de campo eléctrico externo, la diferencia entre el estado singlete y triplete es prácticamente nula (0.02 meV ≈ 0.2 K). En estas condiciones la ocupación de los iones vanadio extremos es de un 87% mientras que el 13% restante se encuentra fundamentalmente deslocalizado entre los cuatro vanadios restantes de la pirámide.

Cuando se aplica un campo eléctrico en dirección z (eje molecular principal), aparece un comportamiento en escalón a 6.5 V/nm, en la separación entre los estados singlete y triplete. Esta apertura entre los niveles es de una gran magnitud (130 meV ≈ 1500 K) y se debe al acoplamiento de los dos electrones en un mismo extremo de la molécula. Además, este salto es tan abrupto que con solo un cambio de 0.3 V/nm, la diferencia de energía entre los dos estados aumenta en cuatro ordenes de magnitud.

Además de esto, se realizaron estudios sobre el comportamiento del sistema cuando el campo eléctrico se aplica en la dirección de los ejes x e y. En estos dos casos se puede observar que la transición que aparece es mucho menos abrupta y que las diferencias de energía entre estados son menores (0.6 y 1.6 meV para x e y respectivamente). Las diferencias que aparecen entre aplicar el campo en el eje x o y proviene de la posición de los contracationes en el cristal, ya que inducen la reducción de la simetría a un grupo D_{2h} en lugar del ideal D_{4h}.

En conclusión, el modelo de Hamiltoniano efectivo predice la transición del estado paramagnético a un estado fuertemente acoplado antiferromagnéticamente S = 0

mediante la aplicación de un campo eléctrico.

Esta predicción ha sido confirmada utilizando cálculos basados en la teoría del funcional de la densidad (DFT). Utilizando DFT se consigue un marco completamente distinto donde verificar este fenómeno. Sin la necesidad de aislar fragmentos de moléculas, DFT se presenta como una herramienta capaz de cálcular la molécula por completo y ofrecer información sobre su distribución electrónica. Estos cálculos se realizaron sobre la estructura cristalina del anión ignorando, en principio, los contracationes. Para mejorar esta primera aproximación se optimizó esta estructura aniónica según un cálculo típico DFT y se repitieron los cálculos. Por último, para comprobar el efecto que pudieran tener los contraiones, se consideraron, primero los ocho cationes más cercanos que estequiométricamente completan una estructura neutra y posteriormente toda una corteza de contraiones con el fin de simular el campo de Madelung Para simplificar estos cálculos, los contraiones se han considerado como cargas puntuales monopositivas.

Todos estos cálculos se han llevado a cabo utilizando el programa comercial GAUSSIAN 09 junto al conocido funcional B3LYP y la base atómica CREMBL. Mediante esta aproximación se realizaron multitud de cálculos a distintas magnitudes de campo eléctrico hasta encontrar el campo crítico donde se produce la transición. En este caso se obtuvo un campo de 11.5 V/nm, a partir del cual el estado antiferromagnético se estabiliza abruptamente. La separación de niveles predicha en este caso es de 100meV a 12.5 V/nm y continua avanzando hasta alcanzar un valor de 175 meV a 15V/nm.

Una de las grandes diferencias entre los comportamientos predichos por el modelo de Hamiltoniano efectivo y por DFT es el comportamiento del sistema a elevados campos eléctricos. De hecho, en el modelo de Hamiltoniano efectivo, la separación de niveles alcanza un "plateau" de alrededor de 120 meV inmediatamente despues del salto mientras que en el cálculo DFT esta separación continua aumentando progresivamente. Esto puede ser explicado si se consideran las aproximaciones fundamentales de cada modelo. En el Hamiltoniano efectivo, a altos campos, el electrón se ha desplazado de una pirámide hasta la contraria quedando deslocalizado en la base ya que los estados de doble ocupación están prohibidos. Por el contrario, en el cálculo DFT este microestado está permitido, pero con una importante diferencia entre sus posibilidades singlete y triplete. En el caso del singlete, la doble ocupación puede ocurrir simplemente pagando el coste energético de la energía de apareamiento. En el caso del triplete es necesario promover a este electrón hasta un orbital superior. De esta forma, el dipolo eléctrico del estado fundamental siempre será mayor para el caso del singlete ya que la contribución del estado doblemente ocupado es mucho más significativa que en el triplete.

Otra diferencia muy importante entre ambos modelos es el campo crítico al cual se produce la estabilización del singlete (11.5 V/nm para DFT y 6.75 V/nm para el modelo de Hamiltoniano efectivo). De nuevo, esta diferencia puede ser racionalizada mediante la comparación directa de ambos métodos, en este caso fijándonos en cómo se considera el apantallamiento de los electrones al aplicar el campo eléctrico. Como es obvio, el desplazamiento de los electrones producido por el campo externo (E_{ext}) produce la aparición de unos pequeños dipolos locales en la molécula. De este modo, estos dipolos creados por la polarizacion de las nubes electrónicas contribuirán a generar un efecto

de apantallamiento que será opuesto al campo externo de forma que el campo efectivo experimentado por la molécula (E_{eff}) será menor que E_{ext}. Nótese que estos efectos se consideran implicitamente en un cálculo DFT pero no en un cálculo de Hamiltoniano efectivo.

Para cuantificar el efecto del apantallamiento, se llevó a cabo un cálculo simplificado considerando varios campos eléctricos externos y cuya conclusión principal es que un E_{ext} de un rango de 10-15 V/nm corresponde a un E_{eff} en un rango de 5.4-11.5 V/nm. Estos valores están cualitativamente de acuerdo con los que se esperan según los cálculos de Hamiltoniano efectivo.

5.3. Conclusiones generales.

En este trabajo se ha evaluado la influencia de un campo eléctrico en el acoplamiento magnético y en la distribución espacial de los dos electrones deslocalizados en un polioxometalato de valencia-mixta. Se ha mostrado que dos aproximaciones distintas (Hamiltoniano efectivo y DFT) predicen que en ausencia de campo eléctrico, el compuesto muestra un comportamiento paramagnético con los dos electrones situados en posiciones opuestas en los extremos de la molécula. Ambas aproximaciones predicen además, que a cierto campo aplicado sobre el eje molecular principal se produce un cambio abrupto en las propiedades magnéticas. De hecho, este campo es capaz de forzar a los dos electrones a situarse en metales vecinos, dando lugar a un fuerte acoplamiento antiferromagnético entre ellos. Este control eléctrico del estado de espín puede ser muy importante en espintrónica molecular o computación cuántica.

Annex 1:
Polyoxometalates

"We may brave human laws, but we cannot resist natural ones."
-Jules Verne.

1. History of Polyoxometalates:

A polyoxometalate (abbreviated POM) is a polyatomic ion, usually an anion, that consists of three or more transition metal oxyanions linked together by shared oxygen atoms to form a large and closed framework. Many reviews have been published about these compounds due to their interesting properties and their applications in molecular science.[1,2]

POMs have been described as molecular oxide clusters formed by different transition metals, with Vanadium, Molybdenum and Wolfram as the most quoted examples. Typically, two main types of Polyoxoanions are described, Isopolyanions and Heteropolyanions. The former ones contain only oxygen and the main metal ion, while the later also contains other elements like P, Si, As, etc in a small proportion.

Historically, the discovery of POMs can be assigned to two Spanish scientists, the Delhuyar brothers. In 1783,[3] José and Fausto Delhuyar found on their experiments a yellow, spicy tasting salt. The first POM was synthesized and their main metal ion was named "Wolfram" as it was extracted from the mineral "Wolframite". Berzelius rediscovered and reported this compound in 1826.[4] But until 1862, the composition of this yellow salt was not resolved. It was identified as the ammonium salt of the 12-wolframosilicate by Marignac[5] in the course of the study of the wolframosilicic acids. The crystalline structure of this POM was determined in 1933 by Keggin,[6] who identified the polyanion $[PW_{12}O_{40}]^{3-}$ by an x-ray difraction study (See Fig. 1).

Initially, the structure of POMs was understood using Werner's coordination theory. Following this principles, Miolati and Pizzighelli in 1908 developed a theory later adapted by Rosenheim.[7] Within this approach, the heteropoly acids were based on six-coordinate heteroatoms with $[MO_4]^{2-}$ or $[M_2O_7]^{2-}$ anions as ligands or bridging groups. Here is presented a brief introduction to the history of the best-known POM structures.

---

1 (a) Pope, M. T.; Müller, A. *Polyoxometalate Chemistry, From Topology via Self-Assembly to Applications.* Kluwer Academic Publishers, Netherlands, 2001. (b) Yamase, T.; Pope, M. T. *Polyoxometalate Chmistry for Nano-composite Design* Kluwer Academic/ Plenum Publishers, New York, 2002. (c) Borrás-Almenar, J. J.; Coronado, E.; Müller, A.; Pope, M. T. *Polyoxometalate Molecular Science* Kluwer Academic Publishers, Netherlands, 2003. (d) Pope, M. T. *Heteropoly and Isopoy Oxomtalates* Springer. Berlin**,** 1983. (e) Souchay, P. *Polyanions et Polycations* Gautier-Villars, Paris, 1963. (f) Baker, L. C. W.; Kirschner, S. *In Advances in the Chemistry of the Coordination Compounds* Macmillan, New York, 1961.

2 (a) Special issue on polyoxometalates, Hill, C.; *Chem. Rev.* **1998**, *98*, 1 and reviews therein. (b) Evans, H. T.; *Perspectives on Structural Chemitry* **1971,** *4*, 1. (c) Weakley, T. J. R.; *Structure and Bonding (Berlin)*, **1974**, *18*, 131. (d) Pope, M. T. ; Müller, A.; *Angew. Chem. Int. Ed.*, **1991**, *30*, 29. (e) Day, V. W.; Klemperer, W. G.; *Science* **1985**, *228*, 533. (f) Coronado, E.; Gómez-García, C. J. *Chem. Rev.* **1998**, *98*, 273–296. (g) Clemente Juan, J. M.; Coronado, E. *Coord. Chem. Rev.* **1999**, *193-195*, 361–394.

3 de Luyart Lubice, J. J.; de Luyart Lubice, F. D. *Extractos de las Juntas Generales celebradas por la Real Sociedad Bascongada*; **1783**, 46-88.

4 Berzelius, J.; *Poggendorffs Annalen*; **1862**, *6*, 369-380.

5 (a) Marignac, C. C. *Russian Academic of Science* **1862**, *55*, 888; (b) Marignac, C. C. *Russian Annual of Chemistry* **1862**, *25*, 362; (c) Marignac, C. C. R. *Ann. Chem. Phys.* **1863**, *69*, 41.

6 (a) Keggin, J. F.; *Nature* **1933**, *131*, 908. (b) Keggin, J. F.; *Proceedings of the Royal Society* **1934**, *A144*, 75. (c) Illingworth, J. W.; Keggin, J. F.; *J. Chem. Soc.* **1935**, 575.

7 Rosenheim, A.; Pieck, M.; *Zeitschrift für anorganische und allgemeine Chemie;* **1916**, *96*, 139.

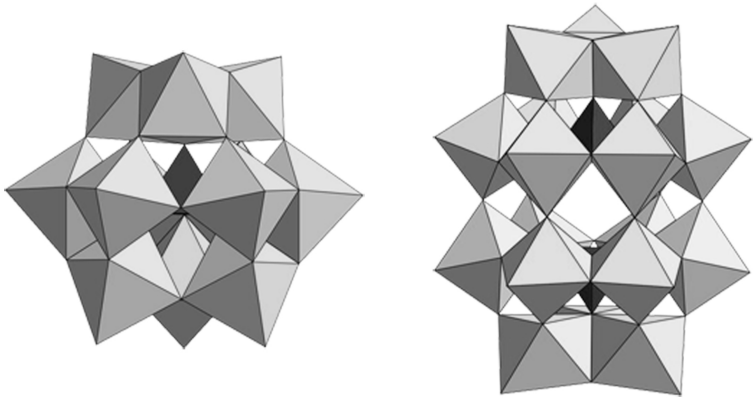

Figure 1. Molecular stucture of: left $[PMo_{12}O_{40}]^{3-}$ (*Keggin anion*) and right α-$[P_2W_{18}O_{62}]^{6-}$ (*Dawson-Wells anion*)

In 1915, Rosenheim and Traube synthesized a new compound, the ammonium 18-molybdophosphate.[8] It was extensively studied by Wu,[9] who found that the compound could exist in two geometrical isomers. Wells, in 1945, suggested the structure for the wolfram isomorph based on Pauling's principles.[10] The single crystal X-ray study of the $[P_2W_{18}O_{62}]^{6-}$ was done in 1953 by Dawson (See Fig.1).[11] Later Strandberg and D'Amourd, reported respectively the structure of α-$[P_2Mo_{18}O_{62}]^{6-}$ and α-$[P_2W_{18}O_{62}]^{6-}$.[12] The chirality of these compounds was ultimately confirmed by the studies of Pope et al. by mutarotation;[13] and by Acerete's work using NMR techniques.[14]

In 1948, Evans[15] published the POM crystallographic structure of the $[TeMo_6O_{24}]^{6-}$ (see Fig.2). Anderson previously suggested this structure for the 6:1 compounds and for heptamolybdate anions in 1937.[16]

The synthesis and characterization of POMs continued in the 1950's, starting with the contribution of Lindqvist who solved other structures based on the Anderson compound (See Fig. 2).[17] The study of the coordination POM compounds was developed in the next

8 Rosenheim, A.; Traube, A.; *Zeitschrift für anorganische und allgemeine Chemie*; **1915**, *91*, 75.
9 Wu, H. J.; *J. Biol. Chem.;* **1920**; *43*, 183.
10 Wells, A. F. *Structural Inorganic Chemistry*. 1st Ed.; Oxford University Press; Oxford, **1945**, 344.
11 Dawson, B.; *Acta Cryst.* **1953**, *6*, 113.
12 (a) Strandberg, R.; *Acta Chem. Scand. Sect. A* **1975**, *29*, 350. (b) D'Amour, H.; *Acta Cryst. Sect. B.*; **1976**, *B32*, 729.
13 Garvey, J. F.; Pope, M. T.; *Inorg. Chem.* **1978**, *17*, 1115.
14 Acerete, R.; et al.; *J. Chem. Soc. Chem. Commun.***1979**, 777.
15 Evans, H. T.; *J. Am. Chem. Soc.* **1948**, *70*, 1291.
16 Anderson, J. S.; *Nature* **1937**, *140*, 850.
17 Lindqvist, I.; *Arkiv Kemi 2* **1950**, 325.

decade by the contributions of Weakley[18] and the group of Tourné.[19] Also in the 1960's L. C. W. Baker and his postdoctoral student M. T. Pope published some studies about physical properties of heteropolyanions.[20] Decades later, in the 1980's, M. T. Pope started a new research group which was very successful in the study of POMs.

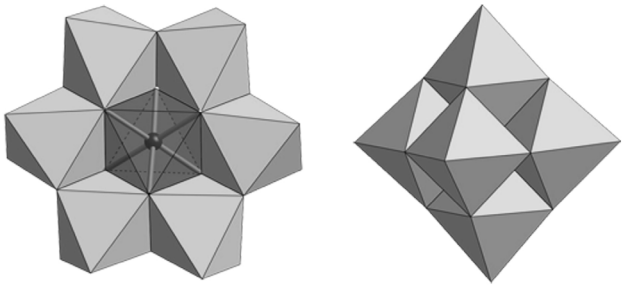

Figure 2. Molecular stucture of: left $[TeMo_6O_{24}]^{6-}$ (*Anderson anion*) and right $[Mo_6O_{19}]^{2-}$ (*Lindqvist anion*)

Almost one generation before, in the early 1940's, Pierre Souchay, had also started a research group focused on POMs at the Sorbonne. His work was focused on determining the POM formulas in solution. His main tools were electrochemistry methods (polarography, potentiometric titration, controlled potential electrolysis, etc), usually accompanied with spectrophotometry, magnetochemistry and NMR. After his death in the mid-1970's, his group continued publishing and covering a extensive range of research in POMs. Many important French scientists were trained in this group, e.g. Pierre Gouzerh, Gilbert Hervé, Yves Jeannin, Jean-Pierre Launay, Andre Tezé and René Thouvenot.

In 1970, Preyssler assigned the formula $[HP_3W_{18}O_{66}]^{8-}$ to a recently discovered wolframophosphate anion.[21] Later, on 1985, a crystallographic investigation revealed that the compound has a fivefold structure with formula $[NaP_5W_{30}O_{110}]^{14-}$.

More recently, a growing number of research groups have concentrated their attention on POMs. The groups doing topmost research in this topic are nowadays too numerous to list comprehensively and include those led by Müller, Klemperer, Papaconstantinou, Hill, Secheresse, Coronado, Proust, Kortz, Cronin, Poblet, and Mialane.

The main part of the work of Coronado's group focuses in molecular magnetism and, specially, in magnetic POMs. Its major contributions so far have been to show the

18 (a) Weakley, T. J. R., Malik, S. A.; *J. Inorg. Nucl. Chem.* **1967**, *29*, 2935. (b) Malik, S. A.; Weakley, T. J. R., *Chem. Comm. 1967*, 1094.; (c) *J. Chem. Soc. A* **1968**, 2647.

19 (a) Tourné, C. M. C.; *R. Acad. Sci. Ser. C.* **1968**, *266*, 702. (b) Tourné, C. M. C.; Tourné, G. C. *R. Acad. Sci. Ser. C.* **1968**, *266*, 1363.

20 (a) Pope, M. T.; Baker, L. C. W.; *J. Phys. Chem.* **1959**, *63*, 2083. (b) Baker, L. C. W.; Pope, M. T.; *J. Am. Chem. Soc.* **1960**, *82*, 4176.

21 Preyssler, C.; *Bull. Soc. Chim. Fr.* **1970**, *30.*

relevance of POMs in molecular magnetism and the use of these molecules as inorganic components of organic/inorganic hybrid materials showing multifunctional properties.[22]

In the next section, a brief discussion about the most common structures of POMs is made.

2. Structural description of POMs.

As mentioned above, Vanadium, Molybdenum or Wolfram in their highest oxidation states are the main metal components of most POMs but other metal polyoxoanions are also known: Niobium, Tantalum and Chromium can give rise to similar structures. In the case of the heteropolyoxometalates, over 60 different ions, including metals and non-metals, are known to be able to play the heteroatom role.

Using wolfram as an example, the formation of a POMs is described as a polymerization (condensation) in acidic conditions of individual wolframate entities (WO_4^{2-}). The reaction can be exemplified by equation 1.

$$8H^+ + 7[WO_4]^{2-} \rightarrow [W_7O_{24}]^{6-} + 4H_2O \quad (1)$$

The final structure is defined mainly by the so-called Lipscomb rules[23]:

•Each metal forms an MO_x polyhedron (typically an octahedron or square pyramid) with the metal displaced toward the free vertex that is located at the surface of the structure (usually forming a double bond with that oxygen).

•Structures with MO_6 moieties that contain three or more free vertices are not observed (in general).

The last rule has been found not to be strict, as some anti-Lipscomb polyoxomolybdates have been characterized.[24] Despite this, those structures remain uncommon.

The effect of the first rule polarizes external oxygen atoms of the polyoxoanion strongly towards the metal, giving rise to a less negative charged surface. This forms a shell-like structure usually with the heteroatom in the inner part.

Heteropolyoxometalates grow by a mechanism that requires the attachment of protons to the oxygen atoms; once the shell structure is defined this oxygen becomes polarized and avoids any further polymerization. This is the main driving force that results in small discrete moieties instead of large solid polymers. Thus, the pH is going to play an important role to control which species can appear in solution. Also we need

22 (a) Coronado, E.; Giménez-Saiz, C.; Gómez-García, C. J. *Coord. Chem. Rev.* **2005**, *249*, 1776–1796. (b) Clemente Juan, J. M.; Coronado, E.; Gaita-Ariño, A. *Chem. Soc. Rev.* **2012**, *41*, 7464–7478.

23 Lipscomb, W. N.; *Inorg. Chem.* **1965**, *4*, 132.

24 (a) Ma, L.; Liu, S.; Zubieta, J.; *Inorg. Chem.* **1989**, *28*, 175. (b) Müller, A.; Krickemeyer, E.; Penk, M.; Wittneben, V.; Döring, J.; *Angew. Chem. Int. Ed.* **1990**, *102*, 85; (c) *Ibid.*, *29*, 88.

to notice that the compound isolated in crystalline form may not be the most abundant one in solution.

Here it is presented a summary of the most common POM structures.

2.1. Usual POM lacunary structures.

Depending on the spatial distribution of the MO_x polyhedra, POM can present multiple isomers. See Figure 3 for some important isomeric compounds of $[SiW_{12}O_{40}]^{4-}$ and α-$[P_2W_{18}O_{61}]^{6-}$. There POM basic structures can then be chemically modified to produce vacancies by the elimination of some metal octahedra. The new species are called "lacunary derivatives". Depending on the removed octahedra, different structures can be found.

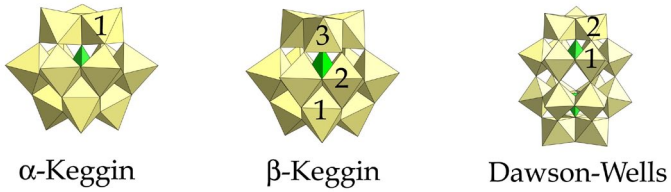

Figure 3. α–(T_d) and β-(C_{3v}) isomers of the $[SiW_{12}O_{40}]^{4-}$ and α-$[P_2W_{18}O_{62}]^{6-}$. The number in the figure represents the octahedron removed to give each vacant isomer.

In Figure 4 some lacunary structures for the α-Keggin polyoxometalate (monovacant and trivacant) are displayed. These derivatives have produced a rich chemistry owing to their ability to act as chelating ligands.These lacunary structures are usually working as inorganic rigid ligands able to encapsulate transition metal or even lanthanoid and actinoid ions. Also these structures can be combined among themselves or with others to create new ones.[25]

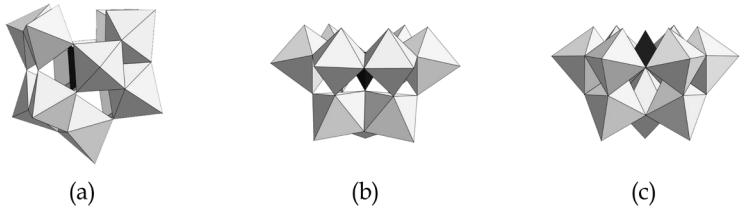

Figure 4. Example of Lacunary species derivated from α-Keggin structure $[XMo_{12}O_{40}]^{3-}$. (a)$[XW_{11}O_{39}]^{8-}$, (b)A-$[XW_9O_{34}]^{9-}$, (c)B-$[XW_9O_{34}]^{9-}$.

25 Fuchs, J.; Hartl, H.; Schiller, W.; Gerlach, U.; *Acta Cryst., Sect. B: Struct. Sci.* **1976**, *32*, 740-749

There are many systems in molecular magnetism that use POMs as coordinating agents. Some of the best-known are those with transition metals; i.e. the series $[M_4(H_2O)_2(PW_9O_{34})_2]^{10-}$ (M=Mn, Fe, Ni, Co, Cu and Zn) reported by Tourné et al. in 1973.[26] The related compounds $[M_4(H_2O)_2(P_2W_{15}O_{56})_2]^{16-}$ were also reported for Co, Cu, Zn, Mn and Ni.[27] In both cases, two trivacant POMs act as a sandwich to a rhombic M_4 structure, with two water molecules completing the coordination.

A main focus of interest in this area was to obtain molecular spin clusters with interesting magnetic coupling between these ions. Increasing the nuclearities of these clusters has been a challenge that was successfully solved in the case of Ni-POMs and Co-POMs in Prof. Coronado's group.[28] The methodology was to use slight variations of the experimental conditions, notably the pH, to isolate different compounds of the POM-TM complexes. In one example, up to three molecules were obtained with different magnetic nuclearities. See Figure 5.

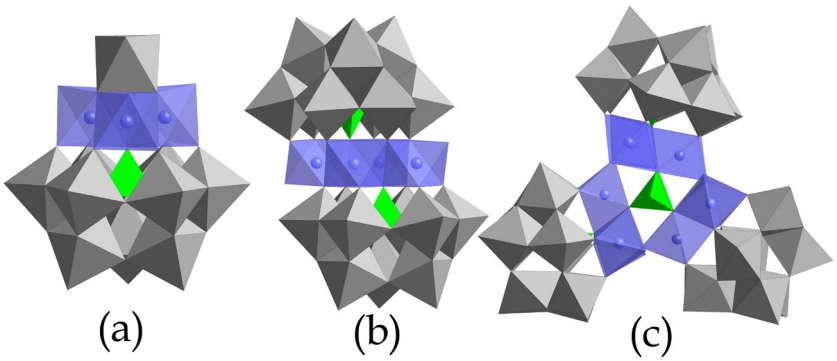

Figure 5. From left to right: (a)$[Ni_3(H_2O)_3(PW_{10}O_{39})H_2O]^{7-}$, (b)$[Ni_4(H_2O)_2(PW_9O_{34})_2]^{10-}$, and (c)$[Ni_9(OH)_3(H_2O)_6(HPO_4)_2(PW_9O_{34})_3]^{16-}$.

The $[Ni_3(H_2O)_3(PW_{10}O_{39})H_2O]^{7-}$ cluster is formed by three edge-sharing NiO_6 octahedra located in the position of one wolfram triad. An additional WO_4 octahedron is capping the whole structure. The $[Ni_4(H_2O)_2(PW_9O_{34})_2]^{10-}$ cluster follows the general structure for $[M_4(H_2O)_2(PW_9O_{34})_2]^{10-}$ POMs described above. $[Ni_9(OH)_3(H_2O)_6(HPO_4)_2(PW_9O_{34})_3]^{16-}$ is obtained by the condensation of three Keggin anions with one of their triads substituted with three NiO_6 octahedra. In these large anions the magnetic clusters are well isolated from the environment due to the presence of the diamagnetic POM moieties.

To conclude, the condensation of several units of substituted Keggin anions is a versatile route to vary the nuclearity of the magnetic clusters.

26 Weakley, T. J. R.; Evans, H. T.; Showell, J. S.; Tourné, G. F.; Tourné, C. M.; *J. Chem. Soc. Chem. Comm.* **1973**; 139.
27 Gómez-García, C. J.; Borrás- Almenar, J. J.; Coronado, E.; Ouahab, L.; *Inorg. Chem.*; **1994**, *33*, 4016.
28 Clemente-Juan, J. M.; Coronado, E.; Galán-Mascarós, J. R.; Gómez-García, C. J.; *Inorg. Chem.* **1999**; *38*, 55-63.

These Transition-Metal POM complexes have been very important in the two last decades. In Molecular Magnetism, they were (and still are) used as models for studying many properties (spin transition, slow-relaxation of the magnetization, etc.) They were also studied with "exotic" experimental techniques (like Inelastic Neutron Scattering).[29] Many of these studies use POMs instead of other polynuclear complexes due, mainly, to their ability to isolate the magnetic moiety from other magnetic molecules in the same crystal.

In the last years, lanthanoid complexes have become a hot focus of interest in magnetism.[30] For this reason, the next section will be the presentation of the lanthanoid-POM systems.

3. Polyoxometalate – Lanthanoid complexes.

3.1. Introduction:

Peacock and Weakley did the first systematic studies of lanthanoid-POM complexes in 1971.[31] The first compounds studied were the full series of $[LnW_{10}O_{36}]^{9-}$ (Ln = La, Pr, Nd, Sm, Ho, Er, Yb, Y and Ce). The direct reaction of WO_4^{2-} with a suitable lanthanoid salt rapidly yielded crystals which were stable in the pH range between 5.5-8.5. More recent ^{183}W-NMR studies indicate that in solution the anions containing the heaviest rare earths (Tm, Yb and Lu) are partially decomposed.[32] The structural analysis of the Ce(IV) complex shows two POM moieties $[W_5O_{18}]^{6-}$ that are encapsulating the lanthanoid in square antiprismatic symmetry (See Fig. 6a).[33]

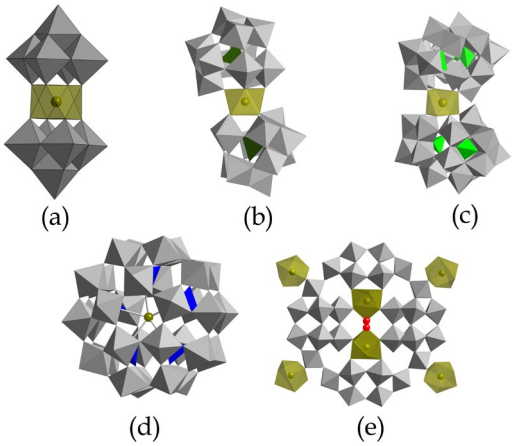

Figure 6. Up, from left to right: (a)$[Ln(W_5O_{18})_2]^{9-}$, (b)$[Ln(\alpha\text{-}SiW_{11}O_{39})_2]^{13-}$ and (c)$[Ln(\alpha_1\text{-}P_2W_{17}O_{61})_2]^{17-}$. Down, from left to right: (d)$[LnP_5W_{30}O_{110}]^{12-}$ and (e) $\{Ln_4(H_2O)_{28}[K\text{-}P_8W_{48}O_{184}(H_4W_4O_{12})_2Ln_2(H_2O)_{10}]^{13-}\}$

29 Andres, H.; Clemente Juan, J. M.; Aebersold, M.; Güdel, H. U.; Coronado, E.; Büttner, H.; Kearly, G.; Melero, J.; Burriel, R.; *J. Am. Chem. Soc.*; **1999**, *121*, 10028-10034.

30 Sorace, L.; Benelli, C.; Gatteschi, D.; *Chem. Soc. Rev.;* **2011**, *40*, 3092-3104

31 (a) Peacock, R. D.; Weakley, T. J. R.; *J. Chem. Soc. A;* **1971**, 1836-1839. (b) *J. Chem. Soc. A;* **1971**, 1937-1940.

32 Inoue, Y.; Yamase, T.; Kazansky, L. P.; *Polyhedron;* **2003**, *22*, 1183-1189.

33 (a) Iball, J.; Low, J. N.; Weakley, T. J. R.; *J. Chem. Soc., Dalton Trans.*; **1974**, 2021-2024. (b) Rosu, C.; Weakley, T. J. R.; *Acta Cryst. Sect. C: Cryst. Struct. Commun. Online* **1998**, *C54*, IUC9800047. (c) Sawada, K.; Yamase, T.; *Acta Cryst. C* **2002**, *58*, 149–151. , (b) Yamase, T.; Ozeki, T.; Ueda, K.; *Acta Cryst. C* **1993**, *49*, 1572–1574.

As described in the previous section, the Keggin anion displays two lacunary derivatives, either monovacant moieties that encapsule one lanthanoid ion (See Fig. 6b),[34] or trivacant moieties, which can coordinate up to three. The so-called Dawson-Wells compounds shares part of its structure with the Keggin anion thus giving rise to similar coordination compounds (See Fig. 6c).

Other polyoxometalates, like the "Preyssler" structure ($[NaP_5W_{30}O_{110}]^{14-}$) have an inner position that can be occupied by ions with the correct charge/radii ratio (See Fig. 6d).[35]

Furthermore, it is possible to find polylanthanoid complexes. This the case of $[P_8W_{48}O_{184}]^{40-}$ (reported by Contant and Tézé),[36] which can react with lanthanoid salts to produce a structure with formula: $Ln_4(H_2O)_{28}[K\text{-}P_8W_{48}O_{184}(H_4W_4O_{12})_2Ln_2(H_2O)_{10}]^{13-}$.[37] (See Fig. 6e) The diamagnetic initial structure is derived from the Dawson-Wells structure $[P_2W_{18}O_{62}]^{6-}$ but removing four octahedra. Thus, the $[H_2P_2W_{12}O_{48}]^{12-}$ anion is condensed controlling the pH to form the product. It is important to note that, in this case, the lanthanoid is coordinated by the $[P_8W_{48}O_{184}]^{40-}$ anion in two different positions.

3.2. Bis(pentawolfra)metalates, $[LnW_{10}O_{36}]^{n-}$.

As mentioned above, the crystalline structure of $[LnW_{10}O_{36}]^{n-}$ anion was reported by Iball et al. for the Ce^{4+} derivative. One of the most important characteristics of this structure is the D_{4d} symmetry coordination around the lanthanoid cation as will be discussed later on. In solution NMR studies show that this structure os mantained.[38]

In adition, other groups developed the syntheses for most of the lanthanoid ions, also exchanging the cations of the final crystal structure.[39] Some of these compounds were found interesting in photoluminescence, and the influence of the counterion was studied by Prof. Yamase et al.[40]

NMR spectroscopy has been established as a valuable method to determine the solution structure and coordination of lanthanoid-POM complexes. This is mainly because of the relationship between electron density transferred by the paramagnetic ion and the observed chemical shifts. With these data it is possible to know whether the compound is stable in solution or if it decomposes.

34 Bassil, B. S.; Dickman, M. H.; Von der Kammer, B.; Kortz, U.; *Inorg. Chem.;* **2007**, *46*, 2452-2458.

35 Creaser, I.; Heckel, M. C.; Neitz, R. J.; Pope, M. T.; *Inorg. Chem*. **1993**, *32*, 1573-1578.

36 Contant, R.; Tézé, A.; *Inorg. Chem.* **1985**, *24*, 4610-4614.

37 Zimmermann, M.; Belai, N.; Butcher, R.J.; Pope, M. T.; Chubarova, E. V.; Dickman, M. H.; Kortz, U.; *Inorg. Chem.;* **2007**, *46*, 1737-1740.

38 (a) Fedotov, M. A.; Samokhvalova, E. P.; Kazansky, L.; *Polyhedron*; **1996**, *15*, 3341-3351. (b) Shiozaki, R.; Inagaki, A.; Nishino, A.; Nishio, E.; Maekawa, M.; Kominami, H.; Kera, Y.; *J. Alloys Compd.*; **1996**, *234*, 193-198.

39 (a) Yamase, T.; Ozeki, T.; Ueda, K. *Acta Cryst.* **1993**, *C49*, 1572–1574.; (b)*Acta Cryst.* **1993**, *C49*, 1574-1577; (c) *Acta Cryst.***1993**, *C49*, 1574-1577.

40 Ozeki, T.; Yamase, T.; *J. Alloy. Compd.* **1993**, *192*, 28-29.

3.3. $[Ln(XM_{11}O_{39})_2]^{n-}$, $[Ln(X_2M_{17}O_{61})_2]^{n-}$ and related derivatives.

Peacock and Weakley first reported these complexes. Other authors later extended this series. The main difference with the previous ones is a great variability of compounds in this case. Ln, X and M can be almost any combination and this is coupled with the different isomers of the POM matrix.

The most common monolacunary isomers are the α–Keggin and α_2-Dawson-Wells. But the β_2-Keggin and the α_1-Dawson-Wells also receive attention for the chirality of their lacunary complexes. These systems have a global symmetry of C_s at most, but the specific lanthanoid coordination still is quasi-D_{4d}.

3.4. Fivefold symmetry complex $[LnP_5W_{30}O_{110}]^{12-}$.

The case of $[LnP_5W_{30}O_{110}]^{12-}$ exhibits a remarkable difference with the previous ones. Instead of showing the typical sandwich structure, it exhibits a cryptate type coordination. In these compounds, an internal cavity is occupied by a Na^+ cation and a molecule of water. To get the Ln^{3+} derivative, the inner Na^+ cation is replaced with a lanthanoid ion. This provides an exotic coordination around the lanthanoid with a fivefold symmetry scheme.

The chemistry of this series uses harder methods compared with the previous lacunary ones because it needs higher temperature and pressure to substitute the central ion by the lanthanoid. Usually these reactions are carried in a high-pressure reaction vessel under hydrothermal conditions.

3.5. Other Lacunary-Lanthanoid Complexes.

The formation of 1:1 species of $[XW_{11}O_{39}]^{n-}$ and α_2-$[P_2W_{17}O_{61}]^{10-}$ can also produce either dimers or polymeric species. There is a limited quantity of examples with crystallographic data, so it is risky to generalize about these systems, but the usual assumption is that the 1:1 complexes of the W_{11} ligands crystallize as one-dimensional polymers while the complexes of W_{17} anion form dimers (with some exceptions like Kholdeeva et al.) [41]

The existence and formation of dimeric (2:2) species in solution has been detected for Ce(III) complexes in α_1 and α_2 isomers.[42] The dimerization of the 1:1 species has been followed by ^{31}P-NMR measurements, which concluded that α_1 species present a greater tendency to dimerize fthan α_2.

In addition to the previously described complexes, other multivacant moieties exist. The trivacant species of the Keggin and Wells-Dawson are well known to give complexes

41 Kholdeeva, O. A.; Timofeeva, M. N.; Maksimov, G. M.; Maksimovskaya, R. I.; Neiwert, W. A.; Hill, C. L.; *Inorg. Chem.;* **2005**, *44*, 666-672.

42 (a) Sadakane, M.; Dickman, M. H.; Pope, M. T.; *Inorg. Chem.;* **2001**, *40*, 2715-2719. (b) Sadakane, M.; Ostuni, A.; Pope, M. T.; *J. Chem. Soc. Dalton Trans.;* **2002**, 63-67.

with one or more lanthanoid ions.[43] The tendency in this case is to form more complex structures. In general a large number of these compounds have been described in literature. Here, one of the most important examples is presented.

43 Liu, J.; Liu, S.; Qu, L.; Pope, M.T.; Rong, C. *Transition Met. Chem.* **1992**, *17*, 311-313.